

Nontrivial and topological magnetic states in Mn-rich In-based ferrimagnetic systems

By

Bimalesh Giri

Enrolment No: PHYS11201704001

National Institute of Science Education and Research,
Bhubaneswar

*A thesis submitted to the
Board of Studies in Physical Sciences*

*In partial fulfillment of requirements
for the Degree of*

DOCTOR OF PHILOSOPHY

of

HOMI BHABHA NATIONAL INSTITUTE



December, 2022

STATEMENT BY AUTHOR

This dissertation has been submitted in partial fulfillment of requirements for an advanced degree at Homi Bhabha National Institute (HBNI) and is deposited in the Library to be made available to borrowers under rules of the HBNI.

Brief quotations from this dissertation are allowable without special permission, provided that accurate acknowledgement of source is made. Requests for permission for extended quotation from or reproduction of this manuscript in whole or in part may be granted by the Competent Authority of HBNI when in his or her judgment the proposed use of the material is in the interests of scholarship. In all other instances, however, permission must be obtained from the author.

Bimallesh Giri
Bimallesh Giri

DECLARATION

I, hereby declare that the investigation presented in the thesis has been carried out by me. The work is original and has not been submitted earlier as a whole or in part for a degree / diploma at this or any other Institution / University.

Bimalesh Giri
Bimalesh Giri

List of Publications arising from the thesis

Journal

• Published

1. “Robust antiskyrmion phase in bulk tetragonal Mn–Pt (Pd)–Sn Heusler system probed by magnetic entropy change and ac-susceptibility measurements”, Sk Jamaluddin, Subhendu K Manna, **Bimalesh Giri**, PV Prakash Madduri, Stuart SP Parkin, Ajaya K Nayak, **Adv. Funct. Mater.** **29**, 1901776 (2019).
2. “Robust topological Hall effect driven by tunable noncoplanar magnetic state in Mn-Pt-In inverse tetragonal Heusler alloys”, **Bimalesh Giri**, Arif Iqbal Mallick, Charanpreet Singh, PV Prakash Madduri, Françoise Damay, Aftab Alam, Ajaya K Nayak, **Phys. Rev. B** **102**, 014449, (2020).
3. “ac susceptibility study of magnetic relaxation phenomena in the antiskyrmion-hosting tetragonal Mn-Pt (Pd)-Sn system”, P. V. Prakash Madduri, Subir Sen, **Bimalesh Giri**, Dola Chakrabartty, Subhendu K. Manna, Stuart S. P. Parkin, and Ajaya K. Nayak, **Phys. Rev. B** **102**, 174402, (2020).
4. “Intra-unitcell cluster-cluster magnetic compensation and large exchange bias in cubic alloys”, **Bimalesh Giri**, Bhawna Sahni, C. Salazar Mejía, S. Chattopadhyay, Uli Zeitler, Aftab Alam, and Ajaya K. Nayak **Phys. Rev. B** **104**, 014413, (2021).

• Manuscript under preparation

1. “Effect of non-collinear magnetic ordering on stabilisation of anti-skyrmion phase in Mn-Pt(Pd)-Sn-In inverse Heusler system ”, **Bimalesh Giri** D. Chakrabartty, A. Das, D. Das, Sreeparvathy P C, S.S.P. Parkin, A. Alam

Giri and Ajaya K. Nayak. Under preparation

Conferences

1. **Bimalesh Giri**, Presented Poster "Annul Condensed Matter Physics Meeting", 26th -27th February, 2018, National Institute of Science Education and Research (NISER), Bhubaneswar, India
2. **Bimalesh Giri**, "XVIII School on Neutrons as Probes of Condensed Matter (NPCM-XVIII)" October 28-November 1, 2018, BARC, Mumbai, India
3. **Bimalesh Giri**, "International Conference on Magnetic materials and Application (ICMAGMA-2018)", Presented Poster 9th -13th December, 2018, National Institute of Science Education and Research (NISER), Bhubaneswar, India
4. **Bimalesh Giri**, Presented Poster (virtual platform) "7-th Conference on Neutron Scattering (CNS-2021)", 25th -27th November, 2021, Bhabha Atomic Research Centre (BARC), in Association with Neutron Scattering Society of India, Mumbai, India
5. **Bimalesh Giri**, Presented Poster (virtual platform) "Symposium on Magnetism and Spintronics (SMS-1) 2021" 25th -27th November, 2021, School of physical Sciences, National Institute of Science Education and Research (NISER), Bhubaneswar, India

Bimalesh Giri

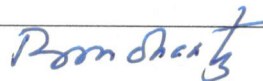
Bimalesh Giri

Homi Bhabha National Institute¹

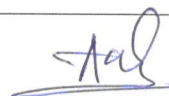
Recommendations of the Viva Voce Committee

As members of the Viva Voce Committee, we certify that we have read the dissertation prepared by Bimalesh Giri entitled "Nontrivial and topological magnetic states in Mn-rich In-based ferrimagnetic systems" and recommend that it may be accepted as fulfilling the thesis requirement for the award of Degree of Doctor of Philosophy.

Chairman – Prof. Bedangadas Mohanty

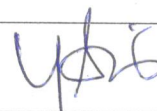


Guide / Convener – Dr. Ajaya K. Nayak

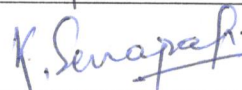


Co-guide - Name & Signature with date (if any)

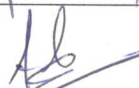
Examiner – Dr. Yogesh Singh



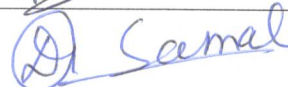
Member 1- Dr. Kartikeswar Senapati



Member 2- Dr. Anamitra Mukherjee



Member 3- Dr. Debakanta Samal



Final approval and acceptance of this thesis is contingent upon the candidate's submission of the final copies of the thesis to HBNI.

I/We hereby certify that I/we have read this thesis prepared under my/our direction and recommend that it may be accepted as fulfilling the thesis requirement.

Date: 22.05.2023

Place: NISER

Signature

Co-guide (if any)



Signature

Guide

¹ This page is to be included only for final submission after successful completion of viva voce.

DEDICATIONS

Dedicated to

My

Parents

Rabindranath Giri and Tulsi Giri

ACKNOWLEDGEMENTS

I would like to thank my supervisor, Dr. Ajaya Kumar Nayak, for giving me the opportunity to work on this topic. I appreciate his constant support and encouragement throughout my Ph.D. tenure. I am very thankful to him for his valuable suggestions and guidance in improving my skill and knowledge. I am also grateful for his critical advice to improve this thesis manuscript. I want to thank Prof. Bedangadas Mohanty, chairman of my doctoral committee. His critical comments and suggestion in evaluating the annual progress report always motivated me to improve basic physics in line with the practical consideration. I would also like to thank the rest of my doctoral committee members, Dr. Anamitra Mukherjee and Dr. Kartikeswar Senapati, for their continuous assessment of my work. I want to thank Dr. Debakanta Samal from IOP, Bhubaneswar, for his kind evaluation of my work as an external doctoral committee member. Their inquiries during the annual progress evaluation helped me to realize the other aspects of particular problems. No doubt, their scrutiny helped a lot to improve my understanding of the topic. I am thankful to my collaborators Prof. Aftab Alam, Mr. A.I. Mallik, and Ms. Bhawna Sahni from IIT Bombay, India, for their support in theoretical calculations. I would also like to thank our collaborators, Dr. Amitabh Das, BARC, Mumbai, India, and Dr. Franoise Damay at Laboratoire Leon Brillouin-Orphee, CEA-CNRS, Saclay, France, for providing the neutron diffraction data. Thanks to my collaborator Dr. C. Salazar Meja, and Dr. S. Chattopadhyay from HLD-EMFL, Dresden, Germany, and Dr. Uli Zeitler, HFML-EMFL, Radboud University, Nijmegen, Netherlands, for providing the high magnetic field data. I also want to thank former postdocs of our lab Dr. Suvendu K. Manna, Dr. P.V.P. Madduri, and Dr. Prachi Mohanty. I am also like to thank my colleagues from our lab Mr. Charanpreet Singh, Mr. Subir Sen, Ms. Dola Chakrabartty, Mr. Sk Jamaluddin, Mr. Mahadev Dey, and Ms. Kshanaprava Pradhan, for the fruitful discussion on several occasion. The Financial

assistance provided by NISER during my Ph.D. tenure is highly acknowledged.

Finally, my most valued thanks to my family members: my parents for their affection and love. I am very grateful to my parents for their blessing and support throughout my Ph.D. tenure. I am also thankful to my brothers (Amalesh and Kamalesh) for their unconditional support in pursuing higher studies. I would also like to thank my sisters (Susama and Lilima) for their blessings and loves.

Contents

Title page	i
SUMMARY	xiii
List of Figures	xviii
1 Introduction	1
1.1 Brief introduction about topology in magnetism	4
1.2 Berry phase	7
1.3 Scalar spin chirality (SSC)	11
1.4 Various magnetic interaction	12
1.4.1 Heisenberg exchange	14
1.4.2 Indirect exchange	14
1.4.3 Dzyaloshinskii–Moriya interaction (DMI)	16
1.4.4 Magnetic anisotropy	17
1.5 Ferrimagnets	18
1.6 Domain and domain wall	21
1.7 Non-trivial magnetic states	24
1.8 Magnetic skyrmion and antiskyrmion	25
1.8.1 Brief history	25
1.8.2 Topological spin texture and stabilization mechanism	26
1.8.3 Spintronics and skyrmionic prospect	29
1.9 Emergent phenomena of nontrivial and topological materials	30

1.9.1	Topological Hall effect (THE)	31
1.10	Exchange bias	33
1.10.1	Nontrivial interfacial spin structure and EB	35
1.11	Inter-metallic Heusler compounds	37
1.11.1	Mn-rich In-based ferrimagnetic systems	38
1.12	Conclusion	43
2	Experimental methodology	45
2.1	Introduction	45
2.2	Arc melting furnace	46
2.3	X-Ray diffraction (XRD)	47
2.4	Scanning electron microscope (SEM) and focussed ion beam (FIB)- dual beam platform	50
2.5	SQUID vibrating sample magnetometer (VSM)	55
2.6	Hall effect measurement	56
2.7	Lorentz transmission electron microscope (LTEM)	58
2.8	Neutron diffraction (ND)	62
3	Tunable topological Hall effect in inverse tetragonal Mn-Pt-In fer- rimagnetic system	67
3.1	Introduction	67
3.2	Sample preparation	70
3.3	Characterisation	70
3.3.1	Structural analysis (XRD)	70
3.3.2	SEM and EDS study	72
3.3.3	Magnetic properties study	73
3.4	Tunable topological Hall	77
3.5	Probing the non-collinear magnetic ordering in $\text{Mn}_{1.5}\text{PtIn}$	82
3.6	Origin of THE	85
3.7	Summary	88

4	Role of non-collinear magnetic ordering on antiskyrmion phase in Mn-Pt(Pd)-Sn-In	89
4.1	Introduction	89
4.2	Motivation	92
4.3	Experimental details	93
4.4	Structural characterisation	96
4.5	Magnetic properties study	98
4.6	Lorentz transmission electron microscopy study	99
4.6.1	Spontaneous meron and antimeron formation	101
4.7	Neutron diffraction (ND) study	103
4.7.1	Neutron diffraction study of $\text{Mn}_{1.4}\text{PtSn}_{0.8}\text{In}_{0.2}$	103
4.7.2	Neutron diffraction study of $\text{Mn}_{1.4}\text{PtSn}_{0.4}\text{In}_{0.6}$	106
4.8	Discussion	107
4.9	Conclusion	110
5	Large exchange bias and non-trivial interface spins in compensated ferrimagnets	113
5.1	Introduction	113
5.2	Motivation	115
5.3	Experimental details	116
5.4	Characterisation	119
5.4.1	Structural characterization	119
5.4.2	Homogeneity and composition study	120
5.5	Theoretical understanding	120
5.6	Magnetic properties	121
5.7	Tunable EB	123
5.8	Transport measurement and discussion	128
5.9	Conclusion	133
6	Summary and future perspective	135
6.1	Summary of the thesis work	135

6.2	Future perspective	138
-----	------------------------------	-----

SUMMARY

The main goal of this thesis work is the experimental observation of the non-trivial and topological magnetic states and related emergent phenomena in Mn-rich In-based ferrimagnetic systems. The non-triviality of the spin structure is considered to be one beyond the conventional co-linear spin ordering. In particular, it focuses on the Mn-rich In-based family of ferrimagnetic materials because of their flexible tuning of the magnetic properties, such as magnetization, magnetic anisotropy, and Curie temperature (T_C). Therefore, the realization of complex spin states and their effective manipulation is achieved by tuning the sublattice magnetic moments. Moreover, it introduces three different types of non-trivial magnetic states. Details study of their magnetic and magneto-transport properties is performed. The powder neutron diffraction study is carried out to uncover the underlying magnetic ground states in the system. The notion of topology is invoked along with the non-trivial spin textures to describe the exotic phenomena related to magnetic and magneto-transport properties. Lorentz Transmission Electron Microscopy (LTEM) measurement is performed to observe real space images of topological magnetic objects, e.g., skyrmion (skx) and anti-skyrmion (askx). Even the study extended to see the effect of the formation of non-trivial magnetic states at the interface of exchange coupled systems. The different mechanisms which materialized such states are also dug out in detail with the help of theoretical understanding. Moreover, the whole work in this thesis can be divided into three parts.

Part-1: The first part of this thesis comprises the tuning of the exotic topological Hall (THE) effect in the $\text{Mn}_{2-x}\text{PtIn}$ system. For this purpose, a series of polycrystalline $\text{Mn}_{2-x}\text{PtIn}$ materials are synthesized. After confirming the structural and chemical phase purity, detailed magnetic measurements are performed. A systematic decrement of the saturation magnetization and Curie temperature is

found. In fact, a completely compensated ferrimagnetic state is obtained for the MnPtIn. The density functional theory (DFT) calculations show the stabilization of a non-collinear magnetic ground state for Mn₂PtIn and Mn_{1.5}PtIn. Large non-collinearity with canting angles of $180^\circ \pm 40^\circ$ and $180^\circ \pm 15^\circ$ are found for Mn₂PtIn and Mn_{1.5}PtIn, respectively. For the MnPtIn system, a completely compensated collinear ferrimagnetic ground state is found, which is consistent with the experimental result. The non-collinearity arises as a result of exchange frustration, i.e., the competition between nearest and next-nearest neighbor anti-ferromagnetic exchange interaction. The powder neutron diffraction experiment performed on the Mn_{1.5}PtIn sample also confirms the non-collinear magnetic state. The reflection of variation in the degree of non-collinearity in Mn_{2-x}PtIn system is captured through the rigorous Hall resistivity measurements. A robust signature of THE in Mn₂PtIn is found and extracted to be $\sim 0.9 \mu \Omega \text{ cm}$. Similarly, the extracted THE is about $0.3 \mu \Omega \text{ cm}$ and a vanishingly small for Mn_{1.5}PtIn and Mn_{1.2}PtIn, respectively. Magnetic ac susceptibility data do not show any kink/dip kind of feature, thereby exclude the possibility of the skx/askx phase in the current system. The observed THE in the present systems is attributed to the non-vanishing scalar spin chirality governed by the non-coplanar spin structure formed by three nearest neighbor moments. The effective tuning of the degree of non-collinearity between the magnetic moments results in the observed tunable THE in the present system.

Part-2: The second part details the effect of non-collinear magnetic ordering on the stabilization of asks phase in the Mn-Pt(Pd)-Sn-In system. The askx are topological magnetic objects; unlike circular symmetry in skyrmion, they hold twofold rotational symmetry about the perpendicular central axis. The first experimental observation of askx was found in the inverse tetragonal Heusler Mn_{1.4}Pt_{0.9}Pd_{0.1}Sn material belonging to the D_{2d} crystallographic class. It was evident that the askx could be stabilized above the spin re-orientation temperature (T_{SR}) only. Therefore,

it is interesting to find the underlying magnetic ordering above and below T_{SR} and correlate it with the stability of askx. Moreover, a large value of magnetic moment in this compound causes a significant dipolar field effect which leads to the different shapes and sizes of asks depending on the lamellae thickness. The dipolar effect can be reduced by reducing the system's magnetic moment. The substitution of the Tin (Sn) by Indium (In), which has one less valence electron, can lead to a significant decrement in the magnetization. Also, the $Mn_{1.4}PtIn$ shows non-collinear magnetic ordering without any evidence of the askx phase. With this objective, prepared a series of samples $Mn_{1.4}Pt_{0.9}Pd_{0.1}Sn_{1-x}In_x$ without altering the magnetic element Mn and heavy metal element Pt, to tune the underlying interactions. The structural characterization confirms that all the samples ($x=0.1-0.6$) form in the inverse tetragonal crystal structure. The magnetic study reveals a systematic decrease in the saturation magnetization and T_C . All the samples show a spin re-orientation temperature of around 100 K. The ac susceptibility data shows the feature of the existence of asks phase only above the T_{SR} for $x=0.1-0.4$. Lorentz transmission electron microscopy (LTEM) measurement is performed to confirm the presence of askx in this system. It is found that the askx and Bloch skx stabilize above T_{SR} . Below T_{SR} , non-topological bubbles can be found. Powder neutron diffraction analysis reveals that the askx is stabilized only when there is a collinear ordering of the background spin. They do not stabilize in the temperature region where there is a non-collinear ordering of the spin. For further understanding, the powder neutron diffraction experiment is performed on higher In doped samples. It is found that the sample (higher In doped) shows a non-collinear magnetic ordering throughout the temperature range in their ordered phase. The LTEM measurements and ac-susceptibility data of this sample exclude the evidence of asks. Therefore, the combined ac susceptibility results, LTEM imaging, and ND study establish that the formation of the asks phase requires a collinear arrangement of background

spin for the present systems. Most possibly, the exchange frustration-driven non-collinearity hinders the formation of skyrmions in the Mn-Pt(Pd)-Sn-In system. Furthermore, we observe the formation of merons and antimerons chains sideways within the helical stripe in $\text{Mn}_{1.4}\text{Pt}_{0.9}\text{Pd}_{0.1}\text{Sn}_{0.6}\text{In}_{0.4}$. It is noteworthy to mention that the meron/antimeron chain formation is spontaneous and at a temperature below T_{SR} . Merons (antimerons) is a distinctive type of topological non-coplanar objects with a topological charge of $-1/2$ ($+1/2$). The formation of merons and antimerons within the helical stripe possesses great possibility from the application point of view. The observation of fractional topological objects like meron/antimeron in the inverse Heusler system is the first of its kind.

Part-3: The third part is concentrated on the role of the non-coplanar spin structure of the uncompensated interfacial spins in exchange coupled systems. The $\mu_0 H$ measurement is utilized to reveal the existence of a non-trivial interfacial spins state. The formation of such an interfacial spin structure results from the interfacial DMI and symmetric exchange. The presence of symmetric exchange and anti-symmetric (DMI) at the interface endorse a large exchange bias field in the special type of compensated FiM. For the experimental realization, a series of $\text{Mn}_{3-x}(\text{Pt}, \text{Ni})_x\text{In}$ polycrystalline samples are prepared. All the samples form in the cubic structure belonging to the space group $P\bar{4}3m$. The magnetic properties are rigorously studied and inferred a nearly compensated FiM state in the systems. The experimental conjecture is supported by the DFT calculations. A fully compensated FiM (FCF) state is found to be energetically most stable. The magnetic compensation arises as a consequence of anti-ferromagnetic coupling between the effective moment of two cluster moments situated at $(0, 0, 0)$ and $(0.5, 0.5, 0.5)$. Also, it is found that there can be formation of an uncompensated FiM state due to a small energy difference to the FCF state. Due to the magnetic phase coexistence, this system shows a very large exchange bias field. Hall measurements are performed in $\text{Mn}_{2.8}\text{Ni}_{0.2}\text{In}$ to

understand the nature of exchange interactions between the FCF background and the FiM cluster. The absence and presence of THE in a zero field and field-cooled measurement indicates that it is an interfacial phenomenon. The resultant THE arises as a result of the non-coplanar spin state stabilized by the interfacial DMI. Therefore, the large exchange bias phenomena in this system are assigned to the combined effect of symmetric exchange and interfacial DMI.

This thesis introduces different types of non-trivial magnetic states in Mn-rich FiM systems. The first part presents a details study of the non-collinear magnetic ground states in multi-sublattice $\text{Mn}_{2-x}\text{PtIn}$ system. It is a classic example of a large and robust THE, which can be effectively tuned by modifying the canted magnetic state. The second part accounts for the effect of non-collinear magnetic ordering on the stability of askx phase in the Mn-Pt(Pd)-Sn-In system. In the third part, THE measurement is utilized to map out the presence of a non-coplanar spin state stabilized by the interfacial DMI along with symmetric exchange. This leads to the observation of a large exchange bias field in a special type of compensated ferrimagnet Mn_3In . Moreover, the non-trivial magnetic materials showcase various exotic phenomena which possess a very rich physics.

List of Figures

- 1.1 (Color online) (a) Connecting the two ends of an 1-D line form a circle.
 (b) Joining the edges of the rectangular sheet along the x direction to form a cylinder, and then joining the two sides of the cylinder along the Y direction resulting in a torus. (c) Möbius strip is a result of joining the two end of a rectangular sheet along x direction after a single twist. 5
- 1.2 (Color online) (a) The description of the mapping of the order parameter from real space to order parameter space. The blue arrows show the order parameter in real space (a 2-D plane). The angle $\phi(r)$ of the order parameter in \mathcal{R} space falls on the close loop (red color, taken in the counter clockwise direction) mapped onto a close circle (shown in black color) in \mathcal{O} space. The number of times the loop (yellow color) wraps around the circle (black color) in \mathcal{O} space is the winding number w . Different winding number for (a) uniform order parameter, $w = 0$; (b) an unstable defect, $w = 0$; (c) and (d) radial configuration around a singularity point (red dot), $w = 1$. The angle of the order parameter in \mathcal{R} space marked by the numbers 1 to 4 are also indicated in \mathcal{O} space. The red dot in order parameter configuration ((c) and (d)) corresponds to the singular point. 8

- 1.3 (Color online) (a) A long rectangular bar with unit vector \mathbf{a} (black arrow) is along the axis and \mathbf{n} (red arrow) perpendicular to one surface. (b) The bar is bending into several steps. In each step the direction of \mathbf{a} and \mathbf{n} vector are shown. A change in the orientation of the \mathbf{n} vector by $\pi/2$ can be seen as \mathbf{a} reach to its initial state. (c) Joining the tip of the three non-coplanar spins (S_i, S_j, S_k) forms a umbrella. (d) Projecting these three vectors on a unit sphere subtends a solid angle Ω at the center of the sphere. 9
- 1.4 (Color online) (a) Two spatially separated magnetic ions A and B. (b) Overlapping of the electronic wave function for two nearby atoms in spatially symmetric (bonding) and antisymmetric manner (anti-bonding). (c) Super exchange: two magnetic ions interact through a nonmagnetic ion. (d) RKKY: two localized moments interact through conduction electron. (e) DMI: two magnetic atoms interact through the nonmagnetic heavy metal atom. 13
- 1.5 (Color online) Schematic representation of the Moriya rules for the resultant DM vector direction between two atoms under various symmetry conditions. The direction of \mathbf{D} is shown by thick black arrows. Blue balls represent atoms, and they are situated at points P and Q and separated by a distance of PQ. 1. $\mathbf{D}=0$, when there is a center of symmetry at point B marked by the yellow cross. 2. when there exists a perpendicular two-fold rotational axis pass through the center point B of the line PQ. 3. $n (\geq 2)$ -fold rotation axis contains the line PQ. 4. A mirror plane perpendicular to PQ, and 5. Mirror plane contains PQ. 15

- 1.6 (Color online) (a)-(c) Spin ordering in FM, AFM, and FiM, respectively. (d) A graphical representation of the temperature variation of the sub-lattices (black open square (m_I) and red open circle (m_{II})) moment. A compensated state is marked by the zero value of the net moment (blue open triangle). Note: the moment value of sub-lattices and the compensation temperature are made arbitrary. (e) An uncompensated and (f) completely compensated state achieve by extracting one of the sub-lattice. 19
- 1.7 (Color online) (a) Schematic representation of domain state in the magnetic material. The direction of magnetization in each domain is shown by a set of blue arrows. The black line separating different domains is called domain wall. The spin rotation within the domain wall (marked by a yellow dashed rectangle) between 180° domain states can be a Bloch type (b) or Néel type (c). In Bloch type, spin rotates parallel to the domain wall, and in Néel case, they rotate perpendicular to the domain wall. 22

- 1.8 (Color online) (a) An in-plane non-collinear triangular spin structure as observed in Mn_3Sn , Mn_3Ge . Green balls represent Mn atoms, and the yellow arrows show the magnetic moment direction. (b) Nd (green circles) and Mo (blue circles) atoms sit at the corner of a tetrahedron [16]. (c) The moment at each corner pointed towards the center of the tetrahedron due to strong anisotropy and forming 2-in 2-out non-coplanar spin structure. (d) The relative orientation of the sub-lattice Mn moment sitting at Wyckoff position 2b (Mn_I , blue balls) and 2d (Mn_{II} , red balls) [48]. (e) A schematic description of exchange frustration inducing a non-collinear magnetic state as observed in Mn_2RhSn [48]. (f) Cycloid: spins are rotated in a plane parallel to the plane containing propagation vector \vec{q} . (g) Helicoid: spins are rotated in a plane perpendicular to the plane containing \vec{q} . . 23

- 1.9 (Color online) (a) Schematic spin texture of Bloch, (b) Néel, and (c) anti-skyrmion. Helicity (γ) of each spin structure is mentioned below. (d) In the upper row: the Néel and Bloch skyrmion structure with different helicity for a given vorticity $w = +1$. Lower row: anti-skyrmion with different helicity for $w = -1$. The central black and peripheral white correspond to the down and up spin with zero in-plane moments, respectively. The color wheel is shown on the right side, where n_x and n_y correspond to the two orthogonal axes. The black arrows indicate the direction of the in-plane magnetic moment. Image (a)-(c) and (d) taken from ref-[57] and ref-[2], respectively. . . 26

- 1.10 (Color online) (a)-(c) Schematic of the in-plane magnetic moments (black arrows) and the Lorentz deflections of the transmitted electrons (orange arrows) in a Bloch, Néel, and anti-skyrmion respectively. The corresponding simulated LTEM images as a result of the deflected electrons is shown below the respective schematic. Lower panel images are taken from ref-[57]. The schematic spin texture of these three types of skyrmion is shown in the Fig. 1.9(a)-(c). 27
- 1.11 (Color online) (a) Large room temperature anomalous Hall effect (red square symbols) observed in AFM Mn_3Sn . Blue circle symbols correspond to the magneto-resistance (MR) [49]. (b) The different color symbols indicate direction-dependent magnetization ($M(H)$) at 300 K in AFM Mn_3Sn [49]. (c) Cartoon description of the electron path through skyrmion [70]. (d) Observation of extra Hall contribution in the A-phase (skyrmion phase) of the MnSi system [11]. (e) Schematic depiction of electron deflection due to the fictitious magnetic field (violet arrow) in a finite SSC. 31
- 1.12 (Color online) (a) Graphical representation of a usual (upper one) and shifted (lower one) magnetic hysteresis loop. (b) Schematic description of a shifted hysteresis of an FM-AFM bilayer system measured after field cooled. The cartoon spin texture in (b) corresponds to a different portion of the hysteresis marked with open ellipses are just for illustration and not necessarily the exact scenario of the magnetization. (c) An FM-AFM bilayer system with compensated AFM interface spin. The effective inter-facial energy is zero due to alternate FM (+j) and AFM (-j) coupling. (d) An FM-AFM bilayer system with un-compensated AFM interface spin. In this case, there is non-zero inter-facial energy. 34

- 1.13 (Color online) (a) Stacking of bilayer Co and Mn_3Ir . The red, blue, and green balls are Ir, Mn, and Co atoms. (b) Depiction of the magnetic arrangement at the (111) interface. The Mn moments (blue arrows) lie in the plane, forming triangular AFM ordering. J_1 and J_2 are the two kinds of isotropic exchange interactions between Co-Mn NNs. DM vectors (\mathbf{D}_{ij}) between Co-Mn nearest neighbors are shown in orange arrows. The h_{dmi} (violet arrows) and h_{dm} (magenta arrows) is the DM interface field and DM field per unit cell acting on the Co atoms, respectively. Image (a)-(c) is taken from ref.-[23]. 36
- 1.14 (Color online) Crystal structure of various types of Heusler compounds. (a) Half Heusler. (b) Regular full Heusler with Cu_2MnAl (L_{21}) as prototype. (c) Inverse full Heusler with CuHg_2Ti as a prototype. (d) Mn_2NiSn type inverse tetragonal full Heusler. The nomenclature of the different color balls is shown on the right side of (d). Tetrahedral and octahedral coordination is shown by the connection of long cylindrical line in (a) and by polyhedra in (b) and (c), respectively. 39
- 2.1 (Color online) Various parts of the Arc melting furnace. The copper hearth is the bottom part of the closed vacuum chamber. 47
- 2.2 (Color online) (a) Schematic representation of X-ray diffraction measurement. (b) Ray diagram of Bragg law of diffraction. θ is the angle between the incident ray and the crystal plane. d is the separation between the two parallel crystal planes. The resultant path difference between the two rays is marked with red color. 48
- 2.3 (Color online) A pictorial description of the different components of the Scanning Electron Microscope (SEM). 52

2.4	(Color online) The dual-beam platform of SEM and focus ion beam (FIB) column is equipped with a Gas Injection system (GIS). The FIB column is arranged at an angle of 54° with respect to the SEM column.	53
2.5	(Color online) Different steps of preparation of TEM lamella. (a) One micrometer width and a thick layer of PtC_x protection cap. (b) Trench out of the material from two sides of the capped portion. (c) One side of the thick lamella is attached to the bulk portion of the sample. (d) Joining of the micromanipulator with the floating lamella. (e) Detachment and lift off of the lamella by the manipulator. (f) Joining of one side of the lamella with TEM grid. (g) Detaching the manipulator after joining the lamella with the TEM grid. (h), (i) Side and top view of the thinned lamella taken with SEM. The images taken using SEM or FIB at a particular angle are mentioned in the respective images.	54
2.6	(Color online) (a) Arrangement of second-order gradiometer superconducting coils. The sample space is within the gradiometer coil, and the whole system is placed within the liquid Helium bath.	57
2.7	(Color online) Circuit diagram for the five probe Hall effect measurement on a rectangular sample. A potentiometer is used to nullify the offset voltage due to misalignment of the voltage lead. The lower inset shows the circuit fabrication of such rectangular Hall bar on a ACT puck.	58

- 2.8 (Color online) Two basic modes of operation of a TEM (a) Diffraction mode, and (b) Image mode. In case of diffraction pattern (DP) and image mode the objective aperture at the back focal plane (BFP) is removed and inserted, respectively. Selected area diffraction (SAD) aperture is inserted for DP mode only. This is simplified ray diagram of DP and image formation. Real TEM may contains more number of intermediate lenses for greater flexibility of focusing and magnification purpose for DP and image formation. Image taken from ref-[103]. . . 59
- 2.9 (Color online) Schematic ray diagram of electron through the magnetic sample in Fresnel mode of Lorentz TEM. The domain wall contrast appears as a dark and bright line in over and under focused condition, respectively. \otimes and \odot represent the magnetization direction into and out of the plane of the page, respectively. The color bar represents two oppositely magnetization directions (blue and red). . . 61
- 2.10 (Color online) (a) Incident neutrons with wave vector \mathbf{K} gets scattered by the crystal planes and propagate with wave vector \mathbf{K}' through a scattering angle of 2θ . (b) For elastic scattering; the scattering vector is defined as $\mathbf{Q} = \mathbf{K} - \mathbf{K}'$. (c) A schematic picture of the neutron diffraction experimental set up. 64
- 3.1 (Color online) Powder XRD patterns for $\text{Mn}_{2-x}\text{PtIn}$ for $x = 0.0$ to 0.4 taken at room temperature. The open black circles in the figure represent the experimental data, and the red color solid lines are the simulated data. The solid blue line shows the difference between the experimental and simulated lines. The $(h\ k\ l)$ value for all major reflections is shown for $x = 0$ by vertical dark green lines. The magenta square boxes in the top three panels represent the extra Bragg peak outside $\bar{1}\bar{4}m2$ 69

- 3.2 (Color online) Room temperature powder XRD patterns for $\text{Mn}_{2-x}\text{PtIn}$ for $x = 0.5$ to 1.0 . The open black circles represent the experimental data, and the red solid lines are the simulated data. The solid blue line shows the difference between the experimental and simulated lines. The $(h\ k\ l)$ values for all major reflections are shown only for $x=0.5$ and 1.0 . The * marked $(h\ k\ l)$ indexes for $x = 1.0$ belongs to the MnPt secondary phase. 71
- 3.3 (Color online) (a) Crystal structure of Mn_2PtIn belongs to $I\bar{4}m2$ space group. (b) Crystal structure of $\text{Mn}_{1.5}\text{PtIn}$ belongs to $I\bar{4}2m$ space group. The distinctive atoms occupy the different Wyckoff positions are mentioned and represented by different color balls in each figure. . 72
- 3.4 SEM images of (a) Mn_2PtIn , (b) $\text{Mn}_{1.5}\text{PtIn}$ and (c) $\text{Mn}_{1.2}\text{PtIn}$ 73
- 3.5 (a)-(g) Temperature dependence of magnetization $M(T)$ measured in zero field cooled (ZFC, open symbols) and field cooled (FC, filled symbols) modes in an applied field of 0.1 T for $\text{Mn}_{2-x}\text{PtIn}$. (h) Variation of Curie temperature (T_C) with Mn concentration (x) in $\text{Mn}_{2-x}\text{PtIn}$. 74
- 3.6 (a)-(g) Field dependence of magnetization loops measured at 2 K for $\text{Mn}_{2-x}\text{PtIn}$. (h) The composition-dependent saturation magnetization (M_S) taken at a field of 5 T 75
- 3.7 (a)-(c) Plot of ac-susceptibility data with respect to the applied DC-magnetic field at a constant temperature of 5 K for Mn_2PtIn , $\text{Mn}_{1.5}\text{PtIn}$, and $\text{Mn}_{1.2}\text{PtIn}$, respectively. 76

- 3.8 (Color online) (a)-(g) Experimentally obtained and calculated Hall resistivity plot of Mn_2PtIn at different constant temperatures. The experimental data are shown in open and filled blue circles, and the solid red lines correspond to the fitted data. Open and filled symbols correspond to the +5 T to -5 T and -5 T to +5 T, respectively. (h) Extracted topological Hall resistivity at different temperatures. Open and filled symbols corresponds to same meaning as stated before. The inset of (d) and (g) shows the usual field reversal of Hall resistivity data. 78
- 3.9 (Color online) (a)-(e) Experimental and fitted Hall resistivity data of $\text{Mn}_{1.5}\text{PtIn}$ at different constant temperatures. The experimental data are shown in open and filled blue circles, and the solid red lines correspond to the fitted data. Open and filled symbols represent the field sweep direction of +5 T to -5 T and -5 T to +5 T, respectively. (f) Extracted topological Hall resistivity for different temperatures. . . 79
- 3.10 (Color online) (a)-(c) Experimental Hall resistivity plot of $\text{Mn}_{1.2}\text{PtIn}$ at different temperatures. The experimental data are shown in open and filled blue circles, and the solid red lines correspond to the fitted data. Open and filled symbols correspond to the +5 T to -5 T and -5 T to +5 T, respectively. (d) Extracted topological Hall resistivity at different temperatures. 80
- 3.11 (Color online) (a) The temperature variation of THE (for three different samples as mentioned by different colors and symbols. (b)-(d) The external magnetic field dependence of longitudinal Hall resistivity of Mn_2PtIn , $\text{Mn}_{1.5}\text{PtIn}$, and $\text{Mn}_{1.2}\text{PtIn}$ respectively. The temperature values are indicated in the respective plot. 81

- 3.12 (Color online) (a) Intensity plot of the powder neutron diffraction performed on $\text{Mn}_{1.5}\text{PtIn}$ sample. The x- and y-axis correspond to the diffraction angle (2θ) and temperature (T). (b) Temperature dependence of the normalized integrated intensity for Bragg peaks (101), (200), and (004). (c) The respective Bragg planes are indicated in the unit cell of $\text{Mn}_{1.5}\text{PtIn}$ 83
- 3.13 (Color online) (a), (b) Reitveld refinement of 300 K and 1.5 K ND pattern, respectively. The open black circles correspond to the experimental data, and the solid red line represent the calculated intensity. The solid blue line is the difference between experimental and calculated intensity. The green vertical lines are Bragg peak positions. The magnetic structure obtained from the refinement is shown in the inset of (b). 84
- 3.14 (Color online) (a) Temperature dependence of the sub-lattice moment in $\text{Mn}_{1.5}\text{PtIn}$ indicated by different color symbols. Here, $\text{Mn}_Y(8i)$ is the absolute value of the y component of the $\text{Mn}(8i)$ sub-lattice moment. (b) Variation of lattice constant a and c with temperature. . . 85
- 3.15 (Color online) (a) Non-collinear magnetic ordering of Mn_2PtIn system. (b) Non-collinear magnetic ordering in $\text{Mn}_{1.5}\text{PtIn}$ as obtained from powder ND experiment. The black dashed loop connecting different Mn sub-lattice moments in (a) and (b) is used to calculate SSC. (c) Upper panel: cancellation of fictitious magnetic field directed in both upward and downward directions (purple arrows) due to the absence of any chiral DMI. The fictitious magnetic field associated with the solid angle subtended by three noncoplanar spins \mathbf{S}_i , \mathbf{S}_j , \mathbf{S}_k . Lower panel: Fixed chirality and non-vanishing fictitious field in the presence of DMI. 87

- 4.1 (Color online) Powder XRD patterns for $\text{Mn}_{1.4}\text{Pt}_{0.9}\text{Pd}_{0.1}\text{Sn}_{1-x}\text{In}_x$ where $x = 0.1$ to 0.5 . The open green circles in the figure represent the experimental data, and the black color solid lines are the simulated data. The blue color solid line shows the difference between the experimental and simulated lines. The (h k l) value for all major reflections is shown only for $x=0.1$ 91
- 4.2 (Color online) (a) Variation of lattice parameters with the Indium concentration (x) in $\text{Mn}_{1.4}\text{Pt}_{0.9}\text{Pd}_{0.1}\text{Sn}_{1-x}\text{In}_x$. The inset is the unit cell volume with Indium concentration (x). The lines are guides to the eye. (b) Crystal structure of $\text{Mn}_{1.4}\text{PtSn}$. The distinct atoms in the unit cell are represented by different color balls, as mentioned on the right side. 92
- 4.3 (Color online) (a) Magnetization plot with respect to varying temperature (T) measured at a constant field of 1000 Oe for different compositions of x as indicated by different colors and symbols. The solid and open symbols correspond to the zero field-cooled (ZFC) and field-cooled (FC) data. The light gray shaded region mark the temperature region below T_{SR} 93
- 4.4 (Color online) (b) Isothermal magnetization data taken at a constant temperature of 5 K. The inset shows the M_{sat} with respect to x. . . . 94
- 4.5 (Color online) Ac susceptibility data of $\text{Mn}_{1.4}\text{Pt}_{0.9}\text{Pd}_{0.1}\text{Sn}_{1-x}\text{In}_x$ for $x= 0.1$ to 0.5 . (a)- d) Plot of the real part of ac susceptibility data with respect to dc magnetic field. The measurements are taken at selective constant temperatures above T_{SR} as mentioned in each plot. (e) χ (H) plot for $x=0.5$ at temperature 200 K, which is above the shoulder kind of feature [see $M(T)$ plot of $x=0.5$ in Fig. 1(a)]. (f)-(j) χ (H) plots taken at 2 K well below T_{SR} 95

- 4.6 (Color online) (a) Side view of TEM lamella of $\text{Mn}_{1.4}\text{Pt}_{0.9}\text{Pd}_{0.1}\text{Sn}_{0.8}\text{In}_{0.2}$ sample with three different thickness regions as can be understood from the brightness contrast. (b) Selected area electron diffraction pattern for one of the regions. (c)-(e) Over focused LTEM images taken from the three different thickness regions. Helical modulation of the magnetic structure propagating along either (100) or (010). Right corner insets in (c)-(e) represent the intensity profile of the line scan marked in each figure. The scale bar in figure (c)-(e) is set to 500 nm. 96
- 4.7 (Color online) Field evolution of non-topological bubble phase at 100 K temperature of $\text{Mn}_{1.4}\text{Pt}_{0.9}\text{Pd}_{0.1}\text{Sn}_{0.8}\text{In}_{0.2}$ sample. (a)-(e) Over-focused LTEM images captured under different magnetic fields as mentioned in each figure. (f) Zoomed view of a NT bubble selected from the marked area of (e). (g) The schematic spin texture of the NT [ref-[94]]. (h) Tilting angle from the pole position at which the images are taken. The angle α and β is the tilting angle about the X and Y axis from the pole position. The scale bar in each figure is set to 500 nm. 97
- 4.8 (Color online) Temperature and field evolution of skx and askx phase in $\text{Mn}_{1.4}\text{Pt}_{0.9}\text{Pd}_{0.1}\text{Sn}_{0.8}\text{In}_{0.2}$. (a)-(d) LTEM images taken at 200 K and different values of the magnetic fields as mentioned in each figure. (e)-(i) and (j)-(m) LTEM images of the askx phase and their field-dependent transformation at 250 K and 300 K, respectively. All the images presented here are captured in over-focused mode. The scale bar in each figure corresponds to 500 nm. The angle α and β is the tilting angle about the X and Y axis from the pole position. 98

- 4.9 (Color online) (a) Core down skyrmion. (b) Core down meron. (c) Over focus LTEM image taken at 102 K. The chain of meron and antimeron evident in the $\text{Mn}_{1.4}\text{Pt}_{0.9}\text{Pd}_{0.1}\text{Sn}_{0.6}\text{In}_{0.4}$ sample are indicated by yellow and red arrow, respectively. (d) Enlarge view of the highlighted region in yellow dashed rectangle of (c). 103
- 4.10 (Color online) Field evolution of two pairs of chain of meron and anti-meron. (a)-(h) OF LTEM images taken at $T = 102$ K and at different field value as mentioned in the each figure. The meron anti-meron chain pair are indicated by blue and red dashed lines for visual guidance. Scale bar in each figure is $1 \mu\text{m}$ 104
- 4.11 (Color online) (a) Intensity plot of powder neutron diffraction data with respect to diffraction angle 2θ . The various color lines represents ND data recorded at different constant temperature indicated in the inset. For a clear view of the major magnetic reflections, the patterns are magnified in the range of 3 to 35 degrees. The Bragg peak (101) is highlighted by a magenta color dash line ellipse. (b) and (c) Rietveld refinement of the 5 K and 300 K ND data by taking the magnetic contribution into account. 105
- 4.12 (Color online) (a) and (b) Simulated magnetic structure of $\text{Mn}_{1.4}\text{PtSn}_{0.8}\text{In}_{0.2}$ at 5 K and 300 K, respectively. 106
- 4.13 (Color online) (a) and (b) Variation of component of the sub lattice moment with temperature. (c) Temperature variation of lattice constant (a and c). 107

- 4.14 (Color online) (a) Intensity plot of powder neutron diffraction data of $\text{Mn}_{1.4}\text{PtSn}_{0.4}\text{In}_{0.6}$ sample with respect to diffraction angle 2θ . The various color lines represent ND data recorded at the different constant temperatures indicated in the inset. For a clear view of the major magnetic reflections, the patterns are magnified in the range of 3 to 35 degrees. The Bragg peak (101) is highlighted by a magenta color dash line ellipse. (b) and (c) Rietveld refinement of the 5 K and 200 K ND data by taking the magnetic contribution into account. The inset magnetic structure corresponding to 5 K ND data. 108

- 4.15 (Color online) (a) and (b) Variation of component of the sub lattice moment with respect to temperature. (c) Temperature variation of lattice constant a and c 109

- 5.1 (Color online) Mn_3In crystal structure. (a) Four Mn atoms (blue balls) connected to each other, forming an inner tetrahedron (IT). (b) Four Mn atoms (yellow balls) form an inverted outer tetrahedron (OT), which is rotated by 30 degrees with respect to the IT. (c) Six Mn atoms (violet balls) form an octahedron (OH) in a way such that each OH atom is close to two IT and two OT atoms. (d) The IT, OT, and OH atoms held inside the cuboctahedron (CO) are formed by twelve Mn atoms (orange spheres). Altogether, the arrangement of IT + OT + OH + CO is called cluster-A. (e) cluster-B: It is also formed in a similar way to that of cluster-A. The only difference is that here the CO contains eleven In atoms (light-green balls) and one Mn atom (orange ball), and the OH is composed of four Mn atoms (violet balls) and two In atoms (light-green balls). Atomic composition/geometry for the IT and OT are the same as of cluster-A. (f) Extended view of Mn_3In unit cell with cluster-A centered at (0, 0, 0) and cluster-B at (0.5, 0.5, 0.5). 116
- 5.2 (Color online) Room temperature powder XRD patterns for $\text{Mn}_{3-x}\text{Pt}_x\text{In}$ and $\text{Mn}_{3-y}\text{Ni}_y\text{In}$ for $x = 0.1$ to 0.3 . and $y = 0.1$ and 0.2 . The open black circles in the figure represent the experimental data, and the red solid lines correspond to the simulated data. The difference between the experimental and simulated data is shown by the blue color solid line. The green vertical lines indicate the Bragg positions. The (h k l) values for all major reflections are shown for $\text{Mn}_{2.9}\text{Ni}_{0.1}\text{In}$ the sample. 117
- 5.3 (Color online) Zoomed view of the variation of (211) peak intensity for the substitution of Pt atoms at distinctive/combinations of Wyckoff positions in $\text{Mn}_{2.7}\text{Pt}_{0.3}\text{In}$ 118

- 5.4 (Color online) (a)- c) SEM images of $\text{Mn}_{3-x}\text{Pt}_x\text{In}$ for $x = 0.1$ to 0.3 .
 (d) and (e) SEM images of $\text{Mn}_{3-y}\text{Ni}_y\text{In}$ where $y = 0.1$ and 0.2 119
- 5.5 (Color online) Temperature-dependent magnetization plot, $M(T)$,
 measured at an applied field of 0.1 T. (a) For $\text{Mn}_{3-x}\text{Pt}_x\text{In}$ and (b)
 for $\text{Mn}_{3-y}\text{Ni}_y\text{In}$. Solid (open) symbols represent the ZFC (FC) data.
 The data for $x = 0.2$ and $x = 0.3$ are multiplied by factors of 1.3 and
 1.5 , respectively, for visual clarity. 123
- 5.6 (Color online) Temperature dependent magnetisation $M(T)$, mea-
 sured at different value of constant magnetic fields. (a) For $\text{Mn}_{2.8}\text{Pt}_{0.2}\text{In}$
 and (b) for $\text{Mn}_{2.8}\text{Ni}_{0.2}\text{In}$. Solid (open) symbols represent the ZFC
 (FC) data. 124
- 5.7 (Color online) Temperature-dependent real part of ac susceptibility
 (χ') taken at different ac field frequencies for (a) $\text{Mn}_{2.8}\text{Pt}_{0.2}\text{In}$ and (b)
 $\text{Mn}_{2.8}\text{Ni}_{0.2}\text{In}$ sample. An ac drive field of 10 Oe amplitude is used. . . 125
- 5.8 (Color online) $M(H)$ loops measured at $T = 2$ K in ZFC (open symbol)
 and $+5$ T FC (solid symbol) mode. (a) For $\text{Mn}_{3-x}\text{Pt}_x\text{In}$ and (b) for
 $\text{Mn}_{3-y}\text{Ni}_y\text{In}$ sample. The $M(H)$ loops corresponding to the sample x
 $= 0.2$ and 0.3 are shifted by 0.75 and $1.5 \mu_B/\text{f.u.}$, respectively, along
 the magnetization axis. $M(H)$ loops for $y = 0.2$ is shifted by 0.35
 $\mu_B/\text{f.u.}$ 126
- 5.9 (Color online) Dependence of exchange bias fields (H_{EB}) and coercive
 fields H_C on Pt concentration (x) for $\text{Mn}_{3-x}\text{Pt}_x\text{In}$ systems. The inset
 plot shows the dependence of H_{EB} and H_C on Ni concentration (y)
 in $\text{Mn}_{3-y}\text{Ni}_y\text{In}$ 127

- 5.10 (Color online) (a) ZFC pulsed field magnetisation data ($M(H)$) measured up to 60 T for $\text{Mn}_{3-x}\text{Pt}_x\text{In}$. Magnetization data for the sample $x = 0.2$ and 0.3 are shifted along M axis by 0.5 and $1.5 \mu_B/\text{f.u.}$, respectively. (b) 15 T FC $M(H)$ loops measured up to ± 30 T. The $M(H)$ loops of $x = 0.2$ and 0.3 are vertically shifted by 0.8 and $1.6 \mu_B/\text{f.u.}$, respectively. 128
- 5.11 (Color online) (a) Cluster-A and cluster-B with finite staggered magnetization M_1 and M_2 aligned anti-parallel. (b) Left panel: fully compensated FiM background as a result of cancellation between the staggered magnetization M_1 and M_2 of cluster-A (orange arrows) and cluster-B (violet arrows). Right panel: Possible FiM cluster due to a finite magnetic moment; as one of the uncompensated magnetic state has small energy difference with the FCF ground state. The dashed line stands for the interface between the FCF background and the FiM cluster with finite moment. 129
- 5.12 (Color online) (a) Temperature dependence of longitudinal resistivity (ρ) for $\text{Mn}_{3-x}\text{Pt}_x\text{In}$, and (b) for $\text{Mn}_{3-y}\text{Ni}_y\text{In}$ 130

- 5.13 (Color online) Field dependence of Hall resistivity (ρ_{yx}) measured at 5 K for $\text{Mn}_{2.8}\text{Ni}_{0.2}\text{In}$. The open circles and open squares represent the ρ_{yx} measured after field cooling the sample in an applied field of +7 T and -7 T, respectively. The solid lines correspond to the total calculated Hall resistivity. The schematic spin configuration at the top and bottom panels represent the possible interfacial FCF magnetic texture at the field reversal point, which are marked in dotted circles and dotted squares, respectively. The solid angle subtended by the noncoplanar spins in the schematic diagrams is marked by a shaded dark grey region, and the red arrows indicate the direction of the fictitious magnetic field. 131
- 5.14 (Color online) Field dependence of ZFC Hall resistivity (ρ_{yx}) measured at 5 K for $\text{Mn}_{2.8}\text{Ni}_{0.2}\text{In}$. The open circles and solid lines correspond to the experimental data points and calculated Hall resistivity, respectively. 132

Chapter 1

Introduction

“You can’t cross the sea merely
by standing and staring at the
water.”

Rabindranath Tagore

Magnetism is one of the the most extensively studied topics in condensed matter physics that covers the work on both theoretical and experimental perspectives of different related phenomena in magnetic materials. In the modern days, several advance technologies extensively employ the phenomena of magnetism to facilitate and ease human life in several ways. Furthermore, the rapidly evolving digital world demands future energy harvesting and information storage devices. Especially for the storage media, the effort has been put forward to find new magnetic materials with exotic properties to fulfill the requirement of high density and fast processing of the information. Moreover, conceptualizing a new framework to enhance the capacity and functionality of every aspect of a storage device is still open and challenging. In this direction, the discovery of spin-dependent electrical resistivity of magnetic materials gives birth to a new branch in condensed matter physics, namely *spintronics*. The main focus of this field is to implement the spin degree of freedom in the nano-electronics devices. Trivially, the ferromagnetic materials that are good source of spin-polarized current have been extensively used for the said purpose. However,

nontrivial magnetic states are at the center of present research interest, as different exotic phenomena can be derived from these states. Here, the nontrivial magnetic states are considered to be ones beyond the conventional collinear ferromagnetic (FM), ferrimagnetic (FiM), and antiferromagnetic (AFM) ordering.

In general, competing magnetic interactions in magnetic materials have led to the findings of many non-trivial complex spin states outside the collinear ordering [1]. For example, the frustrated magnetic ordering obtained due to specific geometric arrangement of the lattice sites, exchange frustration, higher-order exchange, and spin-orbit coupling induced Dzyloshinskii-Moriya interaction (DMI) are the sources of interactions that lead to non-collinear or non-coplanar spin textures. Including the notion of topology along with the non-trivial spin textures enables the description of many exotic phenomena related to magnetic, electrical, optical, and thermal properties. The unconventional response of these properties in quantum topological materials (non-trivial magnetic materials, topological insulator, high- T_C superconductor, Weyl semi-metal, etc.) are the key driving forces in developing next-generation energy harvest and storage media [2, 3, 4]. In this regard, Parkin et al. have proposed the concept of race track memory, a 3-D solid-state device based on the domain wall motion [5]. However, the large current density required for the domain wall motion causes unwanted heating of the device. Jonietz et al. have shown that inserting the skyrmion hosting materials in the race track devices could solve the heating problem as skyrmion needs very low current density to be non-stationary [6]. The magnetic skyrmions are localized swirling spin textures with topological protection, which makes them stable against weak fluctuation [7, 8, 9]. Owing to their topologically non-trivial spin textures and integer topological charge (± 1), they showcase topological Hall effect (THE) [10, 11, 12, 13, 14, 15]. The origin of THE is the effective fictitious magnetic field, which can be interpreted in terms of Berry curvature, experienced by the conduction electrons when travel through the skyrmion.

In this scenario, the concept of the Berry phase is the crucial notion for the origin of THE. Moreover, the dissipation-less anomalous and topological Hall current can

play an important role in spin-based electronics. Therefore, topological magnetism is one of the intense fields of research in spintronics.

The concept of THE is mainly employed to distinguish the topological spin texture in the system. However, it can arise in a system with a non-coplanar spin texture which can be topologically trivial [16, 17, 18, 19]. Therefore, THE can be used as a tool to uncover the uncompensated spins in the interface of the exchange coupled system [20]. Such uncompensated interfacial spins are the critical requirements for inducing strong exchange field at the interface. Also, it has been proposed that the magnitude of the exchange bias (EB) field can attain several Tesla by considering anisotropic Dzyaloshinskii–Moriya interaction [21, 22, 23]. Due to inter-facial Dzyaloshinskii–Moriya interaction, the interface spin can form a non-coplanar spin structure with particular chirality. Therefore, revealing the interface spin ordering of the exchange coupled system can provide the type of interaction responsible for the observed exchange bias effect. It is noteworthy that, in modern times, almost all spintronic devices essentially employ the phenomenon of exchange bias. As a result of EB, a large magneto-resistance can be achieved even with a small magnetic field in the giant magneto-resistance (GMR) [24, 25, 26, 27] and tunnelling magneto-resistance (TMR) [28] based sensors, mainly used as read and write head.

This thesis mainly focuses on the nontrivial and topological spin structures and related emergent phenomena in Mn-rich In-based ferrimagnetic systems. The underlying magnetic interactions are manipulated by tuning the chemical composition to realize complex spin states in three different systems. In the first case, a non-collinear magnetic ground state as a result of exchange frustration in $\text{Mn}_{2-x}\text{PtIn}$ system is attained to showcase the tunable THE. The effect of such exchange frustration on formation of topological antiskyrmion is investigated in $\text{Mn}_{1.4}\text{Pt}_{0.9}\text{Pd}_{0.1}\text{Sn}_{1-x}\text{In}_x$ systems. Also, the presence of non-coplanar spin at the interface of an exchange coupled system is highlighted for the realization of a large exchange bias effect in a special type of compensated ferrimagnetic system Mn_3In . The complex spin states under study arise due to the competition between different interactions, as discussed in

the subsequent chapters.

This chapter is organized as follows. First, a short introduction to the role of topology in magnetism is introduced. Then a brief discussions of the magnetic interactions is presented, as they are the main pillar of achieving nontrivial magnetic states. In addition a brief discussion about ferrimagnetic materials and their importance from the application point of view is given. A short literature review of nontrivial and topological magnetic systems is also presented. How the different emergent properties arise due to the topology is also mentioned. A brief discussion on the role of uncompensated spin in exchange coupled systems is highlighted. Finally, a discussion about the inter-metallics and Heusler materials in the context of Mn-rich In-based composition is included.

1.1 Brief introduction about topology in magnetism

Topology is the abstract study of continuity in mathematics [29]. It deals with the geometry of the objects that remains unchanged under smooth deformation, such as stretching, twisting, bending, etc. The idea of topology is applied to describe different 'invariant properties' in different branches of physics, such as condensed matter physics, quantum field theory, and physical cosmology. The application of boundary conditions on the wave function becomes the source of topological properties. Let's consider three simple examples to understand how the boundary condition can turn a simple geometry into geometry with a hole or twist. The application of periodic boundary conditions leads to a 1-D line into a circle [Fig. 1(a)]. Similarly, a flat rectangle sheet can be converted into a torus by applying periodic boundary conditions along the x and y direction [Fig. 1(b)]. A Möbius strip can emerge if we join the flat sheet in one direction after a twist [Fig. 1(c)]. Therefore, a consistency condition can be applied to a well-defined space of torus or twisted strip to that of the flat sheet. In the same way, in condensed matter physics, an ordered state can be a crystalline structure or magnetic order defined by an order parameter. The associated symmetry element corresponding to the ordered state

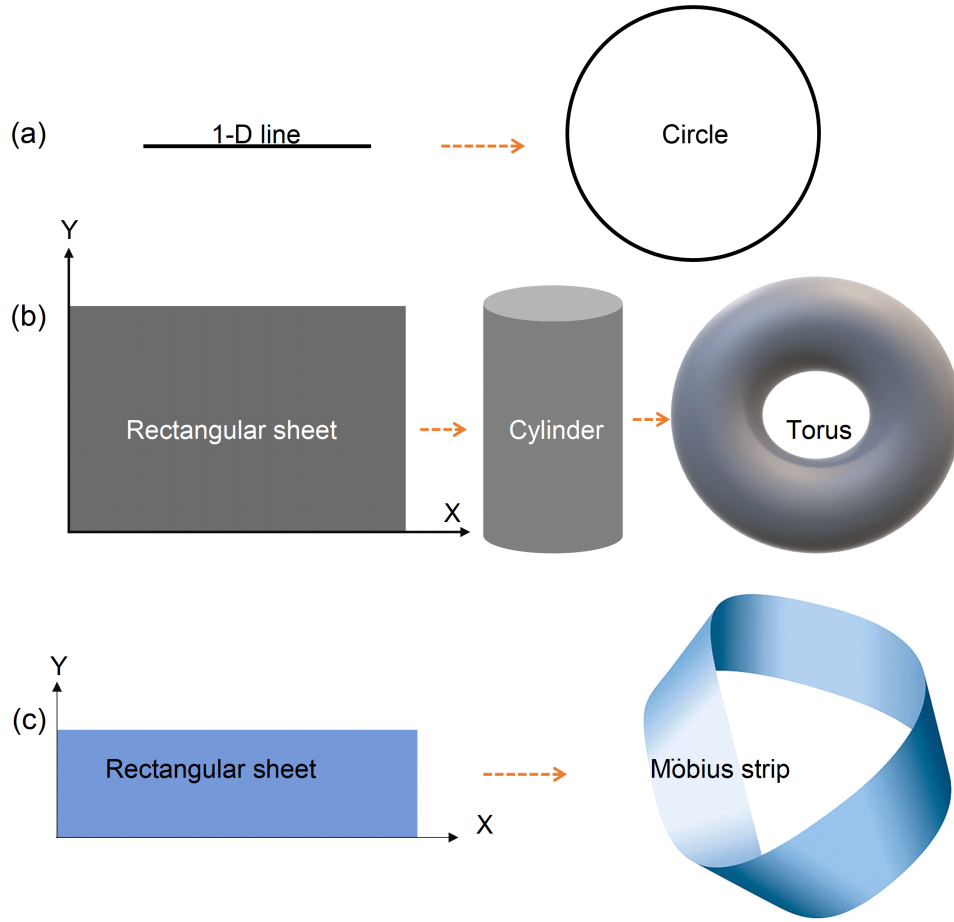


Figure 1.1: (Color online) (a) Connecting the two ends of an 1-D line form a circle. (b) Joining the edges of the rectangular sheet along the x direction to form a cylinder, and then joining the two sides of the cylinder along the Y direction resulting in a torus. (c) Möbius strip is a result of joining the two end of a rectangular sheet along x direction after a single twist.

form a group (G) which is expected to be a subgroup of the group of the disordered state. Moreover, the allowed values of the order parameter form a topological space called the order parameter space (\mathcal{O}). For example, magnetization (M) is the order parameter for a magnetically ordered state. The $M = 0$ and $M \neq 0$ (constant) correspond to the paramagnetic and ferromagnetic states. However, M can take different directions depending on the type of magnet it belongs to. For example, in an Ising magnet M can only attain up or down direction. For XY magnet, M is a two-dimensional vector; for Heisenberg magnet, M is a 3-D vector. So, the order

parameter space corresponds to Ising, XY, and Heisenberg magnet are set of integer $(0, 1)$, circle, and the surface of a 3-D sphere, respectively. It can be understood that the point on the circle and sphere in \mathcal{O} space corresponds to the different value of angle (ϕ) and (θ, ϕ) in \mathcal{R} space, respectively. A mapping of the ordered parameter from \mathcal{R} space to \mathcal{O} space can be defined suitably. Mapping of the ordered parameter from \mathcal{R} space of d ($d=2$) dimension i.e., \mathcal{R}^2 to \mathcal{O} is shown for four different planar spin configurations of magnetization. A mapping function is defined by $f_n(\mathbf{r}) = \mathbf{i} \cos \phi(\mathbf{r}) + \mathbf{j} \sin \phi(\mathbf{r})$ for different configuration of real space spin. Here, \mathbf{i} and \mathbf{j} is the unit vector in the Cartesian coordinate system. All the spin (blue arrow) in real space have constant magnitude, but their orientation can be different and considered as the ordered parameter here. The order parameter on a close loop (taken in the counter clockwise direction) in \mathcal{R} space is mapped to \mathcal{O} space (circle). Basically, it is the different orientation of the spin (denoted by angle $\phi(\mathbf{r})$) that falls on the loop in \mathcal{R} space to circle on the \mathcal{O} space. From Fig. 1.2(a), it can be seen that the ordered parameter is uniform over the 2-D plane. So, the mapping of the order parameter sitting on a close loop (red circle) will lead to a single dot in the \mathcal{O} space. In Fig. 1.2(b)-(d), the spins are continuous over the space except for the point mark by the red dot in \mathcal{R} space. From Fig. 1.2(b), it can be seen that the spins on the upper half (point $1 \rightarrow 2 \rightarrow 3$) and for the lower half (point $3 \rightarrow 4 \rightarrow 1$) of the loop rotated in an anti-clockwise and clockwise manner, respectively. The corresponding points of mapping on the circle of \mathcal{O} space is shown by yellow lines. The upper and lower yellow lines traverse a half circle corresponding to point $1 \rightarrow 2 \rightarrow 3$ and point $3 \rightarrow 4 \rightarrow 1$ in \mathcal{R} space, respectively. From Fig. 1.2(c) and (d), the mapping of order parameters from \mathcal{R} space to \mathcal{O} form a complete loop in an anti-clockwise and clockwise way, respectively. The close loop encircles the circle of the \mathcal{O} space once in an anti-clockwise and clockwise manner denoted by the winding number $(w) +1$ and -1 , respectively. These two loops are topologically in-equivalent, and a continuous transformation between them is not possible. That means the smooth variation of the order parameter in \mathcal{R} space of Fig. 1.2(c) can not be transformed into the spin configuration as shown in Fig. 1.2(d) or vice versa. However, a smooth variation of

the order parameter can transform the spin configuration into each other, as shown in Fig. 1.2(a) and (b), as they are topologically equivalent and characterized by the same winding number ($w = 0$).

It should be noted that the direction of the spin in the center of \mathcal{R} space (marked by red dot) of Fig. 1.2(c) and (d) is not well defined hence creating a singular point. If we take the close loop in real space with a very small radius $r \rightarrow 0$, and mapped into \mathcal{O} space will cause the shrunk of the loop. In this case, the point is called a topological defect. There can be topological defects, which do not possess a singularity. That means the order parameter is continuous everywhere in \mathcal{R} space. An example of such structural defects is skyrmions. A brief introduction about the skyrmions shall be provided in a dedicated section in this chapter. Nevertheless, the mapping of a close loop in real space when creating a close loop in ordered parameter space can be non-trivial, and their feature is determined by the fundamental group $G: \pi_1(S^1)$. These close loops have various topological aspects, such as any continuous deformation of the parameter can not change the consistency condition imposed on the loop in order parameter space. Furthermore, the physics associated with a close path can be very interesting and can have wide implications in condensed matter physics.

1.2 Berry phase

In 1984, M. V. Berry showed that a quantum system traversing slowly (adiabatically) over a closed circuit acquires an extra phase in its wave function description [30]. Consider a quantum mechanical system evolving adiabatically around a close loop. For such a system, the eigenstate can be derived from the equation-

$$H(t)\psi_n(x, t) = E_n(t)\psi_n(x, t). \quad (1.1)$$

Adiabatic theorem allows the particle remains in the starting state (say in n -th eigenstate) and at most pick up a time-dependent phase factor in the wave function.

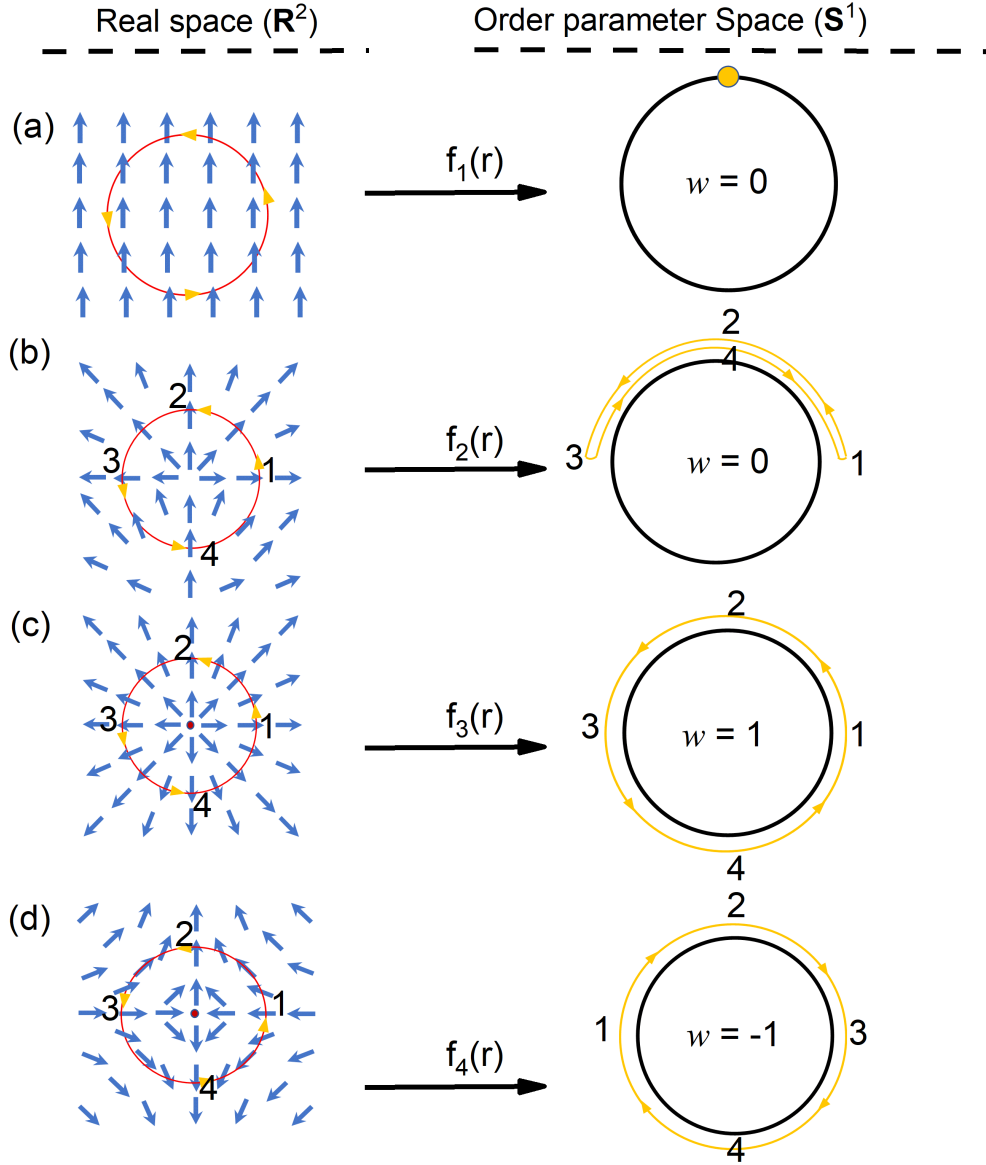


Figure 1.2: (Color online) (a) The description of the mapping of the order parameter from real space to order parameter space. The blue arrows show the order parameter in real space (a 2-D plane). The angle $\phi(r)$ of the order parameter in \mathcal{R} space falls on the close loop (red color, taken in the counter clockwise direction) mapped onto a close circle (shown in black color) in \mathcal{O} space. The number of times the loop (yellow color) wraps around the circle (black color) in \mathcal{O} space is the winding number w . Different winding number for (a) uniform order parameter, $w = 0$; (b) an unstable defect, $w = 0$; (c) and (d) radial configuration around a singularity point (red dot), $w = 1$. The angle of the order parameter in \mathcal{R} space marked by the numbers 1 to 4 are also indicated in \mathcal{O} space. The red dot in order parameter configuration ((c) and (d)) corresponds to the singular point.

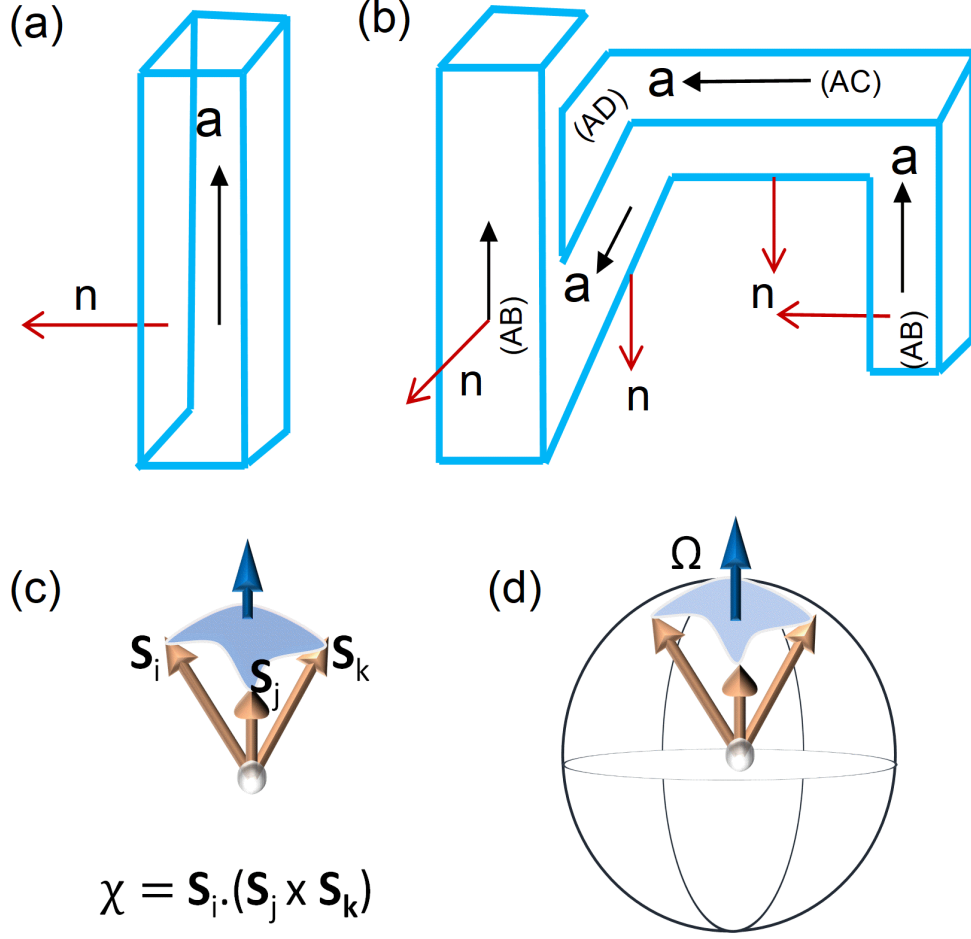


Figure 1.3: (Color online) (a) A long rectangular bar with unit vector \mathbf{a} (black arrow) is along the axis and \mathbf{n} (red arrow) perpendicular to one surface. (b) The bar is bending into several steps. In each step the direction of \mathbf{a} and \mathbf{n} vector are shown. A change in the orientation of the \mathbf{n} vector by $\pi/2$ can be seen as \mathbf{a} reach to its initial state. (c) Joining the tip of the three non-coplanar spins (\mathbf{S}_i , \mathbf{S}_j , \mathbf{S}_k) forms an umbrella. (d) Projecting these three vectors on a unit sphere subtends a solid angle Ω at the center of the sphere.

Therefore, ψ_n can be written in the below form-

$$\psi_n(x, t) = \psi_n(x, t) e^{i\theta_n(t)} e^{i\gamma_n(t)} \quad (1.2)$$

where,

$$\theta_n(t) = -\frac{2\pi}{h} \int_0^t E_n(t') dt' \quad (1.3)$$

is the dynamical phase term. The ‘extra phase’ term $\gamma_n(t)$ is called the geometric phase. One can consider a parameter $R(t)$ in the Hamiltonian, which evolves slowly with time. For example, let’s say the width of a 1-D potential well expands with time. Then, we can write the wave function in terms of $R(t)$. And for close loop case, if the particle comes back to its initial position, then the form of $\gamma_n(t)$ can be given by-

$$\gamma_n(t) = i \oint \langle \Psi_n | \nabla_R \Psi_n \rangle dR. \quad (1.4)$$

The term,

$$i \langle \Psi_n | \nabla_R \Psi_n \rangle = A_n(R) \quad (1.5)$$

is called Berry connection. It can be shown that the Berry connection plays the same role as that of magnetic vector potential ($\mathbf{A}(\mathbf{r})$). Before Berry, in 1959, Yakir Aharonov and David Bohm showed that the math of quantum mechanics allows a charged particle to feel the effect of magnetic field in a region without physical magnetic fields [31]. Consider a charged particle moving along a close path circulating around a thin solenoid of infinite length. The magnetic field (\mathbf{B}) is only inside the solenoid, and there will be no effect of the magnetic field on the charged particle. However, there can be the effect of vector potential \mathbf{A} on the wave function and causes a complex phase shift. The Berry phase is not only a quantum issue. To understand how this extra phase appears for a quantum mechanical system evolving around a closed path. Let’s consider a classic example of a long rectangular bar with a unit vector along its long axis [Fig. 1.3(a)]. The normal of the one surface is marked red arrow [Fig. 1.3(b)]. Then the bar is bent in several steps and brought back to its initial direction [Fig. 1.3(b)]. It can be seen that the perpendicular vector (\mathbf{n}) now makes an angle $\pi/2$ with its initial direction. This phase shift is very similar to that of the Berry phase. Generally, the Berry phase is a geometrical phase and depends on the path. Sometimes it can be independent of the path or geometry of

the loop hence considered the topological origin.

1.3 Scalar spin chirality (SSC)

In recent times the concept of Berry phase has immense importance in distinguishing different phenomena related to the topological phase in quantum materials like Weyl semimetals [32], topological insulators (TIs) [33], magnetic skyrmions, etc. Particularly, magnetic materials with topologically nontrivial spin textures enable showcasing the topological Hall effect (THE). The origin of THE is the effective fictitious magnetic field which can be constructed in the system with finite scalar spin chirality given by $\mathbf{S}_i \cdot (\mathbf{S}_j \times \mathbf{S}_k)$, where \mathbf{S}_i , \mathbf{S}_j , \mathbf{S}_k are the three nearest neighbor spin [see Fig. 1.3(c)] [16, 17, 18]. The non-coplanar spin structure can be mapped onto a unit sphere. The area enclosed by joining any three spins subtend a solid angle at the center [Fig. 1.3(d)]. The solid angle 2π can be obtained when the three spin lie on the equatorial plane. However, the SSC becomes zero when they are co-planar. There are only limited examples of nonzero SSC originating from the non-coplanar spin structures [16, 34, 35]. In most of the cases, these systems display a special type of lattice structures, e.g., pyrochlore, triangular lattices, etc., with distinctive types of spin configurations. So, the systems exhibits a non-vanishing scalar spin chirality, which can appear in magnetic materials with non-coplanar spin structures, ideal for the realization of THE [16, 17, 19]. However, the absence of chiral magnetic symmetry can lead to a net vanishing THE in most of the systems. Due to the strong coupling between charge and spin degrees, the electronic wave function attains the Berry phase while hopping from one site to another in a non-collinear or non-coplanar spin texture. As the Berry phase related to the magnetic vector potential, a fictitious magnetic field ($\mathbf{B} = \nabla \times \mathbf{A}$) can be constructed from this. This fictitious magnetic field causes the extra Hall contribution in Hall resistivity measurement. Since, the dissipation-less nature of the anomalous and topological Hall current is suitable for spin-based electronic devices. Therefore, tuning of THE is one of the most intense fields of research in the field of spintronics. So, designing

nontrivial topological magnetic materials and their electrical detection is a key challenge. In recent times nontrivial topological magnetic materials are the center of research because of their utmost importance in developing future spintronic devices [4].

1.4 Various magnetic interaction

It is understood that all solids are formed by atoms, and the atoms are governed by the nucleus (proton, neutron) surrounded by electrons. The electrons are fermions with spin $1/2$ particles. This spin degree of freedom of the electrons results in a spin moment to the individual atoms consistent with Hund's rule. These individual atomic moments collectively showcase the magnetization in the materials. Magnetization is defined as the amount of magnetic moment per unit volume of the magnetic materials. As the magnetic moment is a vector, the magnetization value is solely determined by how they are arranged among themselves. If they are arranged in the same direction, then the magnetization will be simply the sum of all the individual moments divided by the volume of the materials. However, it is also possible, in fact, to occur with the various other arrangement provided the energy cost is minimum to form the particular order. Like solids can be either ordered, i.e., crystalline or amorphous, the magnetic system also shows similar behaviors. An order state from a disorder state followed by a temperature induce second-order phase transition. Above the critical temperature, spins are randomly arranged and called as paramagnetic state. In case of ferromagnet (FM), all spins are arranged in a parallel manner, whereas for antiferromagnet (AFM), an antiparallel alignment of spins is formed. In ferrimagnets (FiM), the moments are arranged antiparallel manner; however, the magnetic moment of the two sub-lattices is different. Such collinear ordering of the magnetic moment within the magnetic materials can not be explained by dipolar interaction because the strength of coupling due to dipolar interaction is too weak to account for the ordering temperature of many magnetic materials. An alternative root that can describe long-range magnetic ordering is the

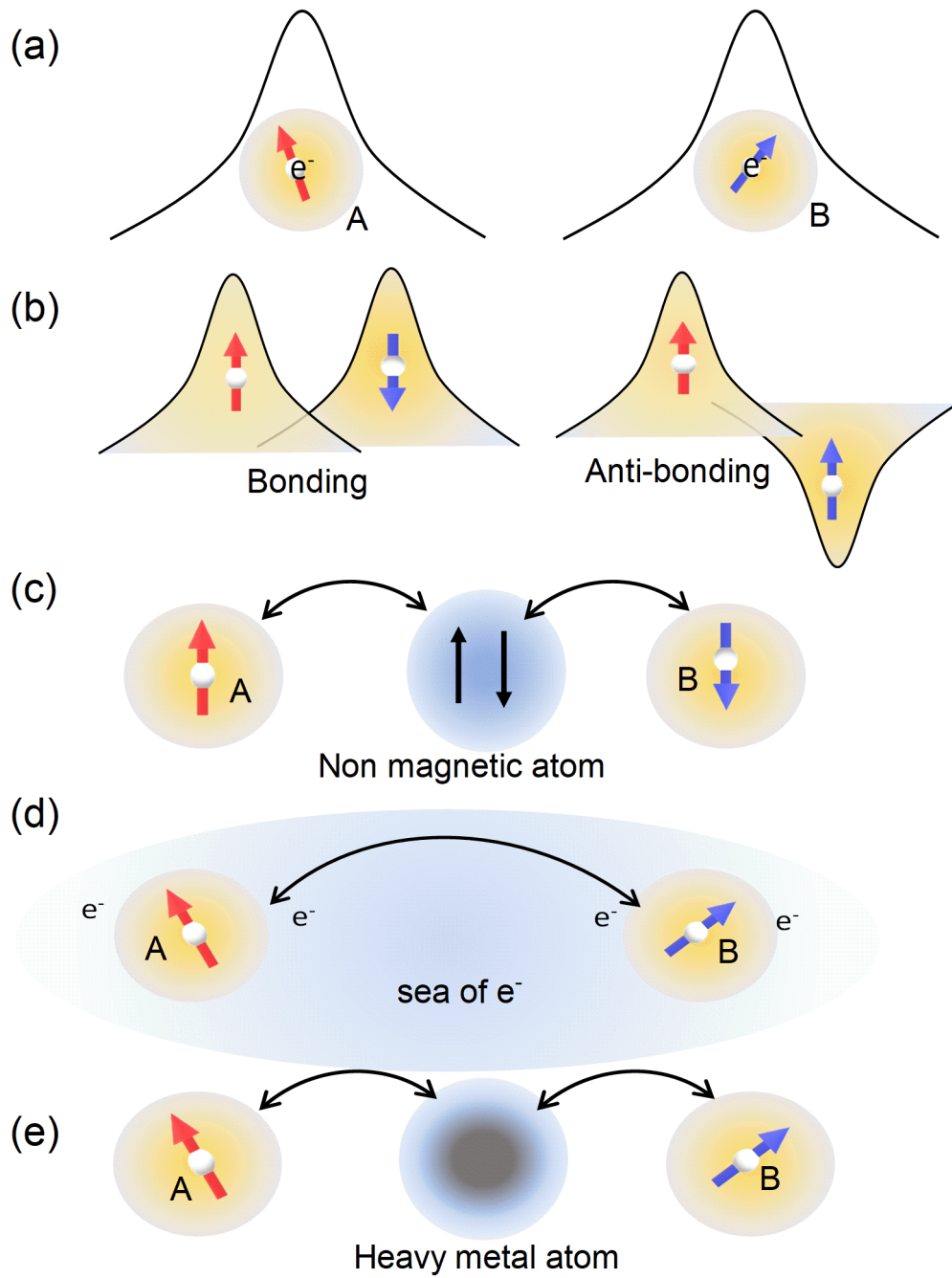


Figure 1.4: (Color online) (a) Two spatially separated magnetic ions A and B. (b) Overlapping of the electronic wave function for two nearby atoms in spatially symmetric (bonding) and antisymmetric manner (anti-bonding). (c) Super exchange: two magnetic ions interact through a nonmagnetic ion. (d) RKKY: two localized moments interact through conduction electron. (e) DMI: two magnetic atoms interact through the nonmagnetic heavy metal atom.

Heisenberg exchange interaction.

1.4.1 Heisenberg exchange

In 1926, W. Heisenberg gave the microscopic origin of the FM or AFM alignment of the localized spin of electrons of spatially separated magnetic ions [Fig. 1.4(a)]. Suppose the distance between two ions is small enough. In that case, a spatially symmetric (bonding) or anti-symmetric (anti-bonding) overlap between the electronic wave function of the two atoms is possible [Fig. 1.4(b)]. Electron hopping from one atom to another atom happens through the direct overlapping of the orbitals of the atoms. As a result, a singlet (AFM) or triplet spin states (FM) occur between the two nearby magnetic atoms. The Hamiltonian describes the interaction between two nearest spins as given by-

$$H = -JS_i.S_j \quad (1.6)$$

, where J is the exchange integral and i , and j are the spin at the i -th and j -th lattice sites. The Heisenberg exchange always favors the parallel or anti-parallel, i.e., collinear alignment of the nearest spin depending on the sign of the exchange integral J .

1.4.2 Indirect exchange

Exchange interaction can be categorized into two types, i.e., direct and indirect interactions. Heisenberg exchange belongs to the former class due to the direct overlapping of the electronic wave function. However, in some magnetic ions, the electronic wave function is strongly localized, so it is hard to imagine a direct overlapping of the wave function. In such conditions, an indirect exchange interaction with hopping of electrons from one site sets up the magnetic ordering in many systems. Through such hopping, the electron minimizes its kinetic energy, and the resultant spin ordering in this way follows Pauli's exclusion principle. There are

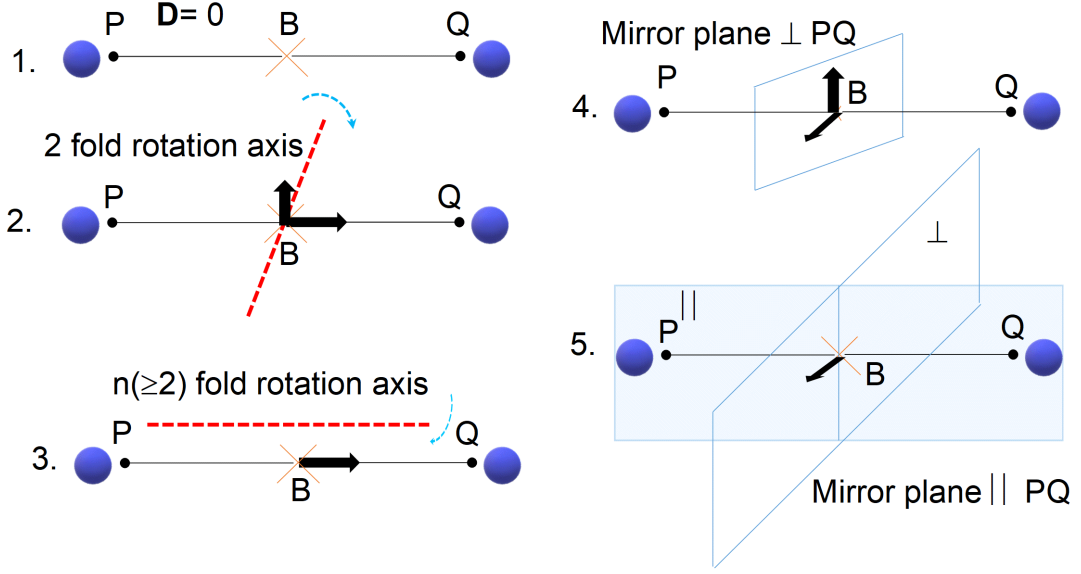


Figure 1.5: (Color online) Schematic representation of the Moriya rules for the resultant DM vector direction between two atoms under various symmetry conditions. The direction of \mathbf{D} is shown by thick black arrows. Blue balls represent atoms, and they are situated at points P and Q and separated by a distance of PQ. 1. $\mathbf{D} = 0$, when there is a center of symmetry at point B marked by the yellow cross. 2. when there exists a perpendicular two-fold rotational axis pass through the center point B of the line PQ. 3. $n (\geq 2)$ -fold rotation axis contains the line PQ. 4. A mirror plane perpendicular to PQ, and 5. Mirror plane contains PQ.

different types of indirect exchange interaction, namely superexchange, double exchange, asymmetric exchange, etc. In super exchange, the interaction between two magnetic ions occurs through nonmagnetic ions [Fig. 1.4(c)]. The appearance of AFM ordering in MnO is caused by super exchange mediated by Oxygen ion [36]. In some rare cases, the super exchange can give weak FM ordering depending on the electron filling in the orbitals of the magnetic ions. Double exchange is another kind of super exchange that led to observing FM ordering in some oxide systems. When two magnetic ions of the same atoms have different oxidation states, their interaction does not follow the usual root of super exchange. The overall energy minimization through hopping of the electron favors an FM alignment of the spin of the magnetic ions. This kind of interaction occur in $\text{La}_{1-x}\text{Sr}_x\text{MnO}_3$ system [37], where for $x = 0$ and 1, the system stabilizes in an AFM state due to super exchange.

However, doping of divalent Sr (Sr^{2+}), in place of trivalent La (La^{3+}) causes part of the Mn atoms adopts to Mn^{4+} and the rest in Mn^{3+} oxidation states. As a result, a metallic FM state in this system can be observed due to the double exchange.

The RKKY (named after four scientists, Ruderman, Kittel, Kasuya, and Yosida) interaction is another type of indirect exchange interaction. In the metallic system, the conduction electron mediates the coupling between two moments sitting at a sufficiently large distance where the direct overlapping of the atomic wave function is not possible. In such a system, the conduction electron became polarized at each local site's moment and coupled to the other local moment situated at distance r [Fig. 1.4(d)]. This interaction is oscillatory in nature and depends on the distance between the two interacting atoms. The exchange interaction is written in the form-

$$J_{RKKY} \propto \frac{\cos(2K_F r)}{r^3} \quad (1.7)$$

where, K_F is the wave vector that corresponds to the Fermi surface. So, depending on the distance r , the J_{RKKY} can be positive or negative; hence a ferromagnetic and anti-ferromagnetic ordering will occur. In some metallic materials, the nearest neighbor (nn) interaction is Heisenberg type, and the next nearest neighbor (nnn) is due to RKKY.

1.4.3 Dzyaloshinskii–Moriya interaction (DMI)

The DMI interaction was first introduced by Dzyaloshinskii in 1958 to describe the weak ferromagnetism in some of the antiferromagnetic materials [38]. Later, T. Moriya provided the microscopic origin and connected it to the relativistic spin-orbit coupling [39]. Usually, heavy metals show strong spin-orbit interaction in the system. In this case, the interaction between two magnetic atoms given by the equation $\mathbf{D} \cdot (\mathbf{S}_i \times \mathbf{S}_j)$, where \mathbf{D} is the Dzyaloshinskii- Moriya vector which determines the strength and sign of the DMI. \mathbf{S}_i and \mathbf{S}_j are the spin moments of the two nearby sites located at the i -th and j -th atomic positions. The DMI is often referred to as

the antisymmetric because any small deviation of the \mathbf{S}_i spin moment account for some energy gain, and this is unequal in magnitude if the same amount of deviation happened with \mathbf{S}_j spin moment. Unlike Heisenberg exchange interaction that favors a collinear spin ordering, the DMI favors canted spin ordering. Basically, in the collinear case spins are either parallel or antiparallel, whereas the DMI rotates the spin in a perpendicular direction. Also, it favors a particular sense of rotation of the constituted spin, i.e., anisotropic. The sense of rotation of the constituent spin solely depends on the symmetry between the atoms. Moriya tabulated the direction of the effective \mathbf{D} vector existing between two atoms based on the symmetry analysis [39]. The five symmetry configuration and their resultant \mathbf{D} vector is schematically shown in Fig. 1.5. In the modern theory of magnetism, most of the nontrivial magnetic states of the magnetic materials are often described with the help of the DMI. However, a prerequisite of this interaction to persist in any materials is the breaking of the inversion symmetry in the structure. For thin film heterostructure, the broken space inversion symmetry at the interface and the presence of heavy metal elements induce the DMI. The competition between Heisenberg exchange, DMI leads to various unconventional magnetic states which have a special interest in rapidly growing data storage and information processing in the field of spintronics.

1.4.4 Magnetic anisotropy

Under the application of an external magnetic field, the magnetic moments align in the field direction. Therefore magnetization occurs in this direction. However, in some materials, the magnetization has some preferential direction, i.e., in some directions it will be easily magnetized, whereas in the other directions are hard to magnetize the materials. Such a directional-dependent magnetization process is called magnetic anisotropy. The origin of such behavior of magnetic materials can have several reasons. For example, magneto crystalline anisotropy (depends on the underlying crystal structure), shape anisotropy, exchange anisotropy (arises from the interface exchange coupling), magneto-elastic effect, etc. The directions along

which the materials get easily magnetized/hard to magnetized are called the easy axis/hard axis. Also, some materials show an easy plane of magnetization. Easy axis anisotropy is essential to observe magnetic hysteresis. The energy required to switch the magnetization from easy axis to hard axis direction is the measure of the anisotropy energy (E_a). The form of E_a is usually written in a series expansion and depends on the crystal class. For example, in case of a hexagonal crystal system the following relation can be obtained.

$$E_a = K_1 \sin^2 \theta + K_2 \sin^4 \theta + \dots, \quad (1.8)$$

where, K_1 and K_2 are anisotropy constants, and θ is the angle between the magnetization and the high symmetry axis. K_1, K_2, \dots depends on the temperature, pressure, etc. For a uniaxial anisotropic system, the magnetization shows two easy and equivalent directions separated by a 180° angle. In an exchange coupled system, for instance, a composite system of FM and AFM interacting through a common interface has only one easy direction and is denoted as unidirectional anisotropy. Such a system shows a shifted magnetic hysteresis loop (along the field axis) at a temperature $T < T_N < T_C$, in the presence of an external magnetic field. The shift in the loop is called exchange bias (H_{EB}).

1.5 Ferrimagnets

Ferrimagnets are the class of magnetic materials that exhibits antiferromagnetic coupling between two different magnetic sublattices. Since the magnetic moments belong to two different sublattices, they are unequal in magnitude, and hence a net uncompensated magnetic moment is found. The schematic representations of FM, AFM, and FiM are shown in Fig. 1.6(a)-(c). In contrast AFM materials show one type of sublattice with equal magnitude of magnetic moment. The sublattices in FiM systems can be different elements, even the same element in a different environment having a different magnitude of the moment. For example, an atom

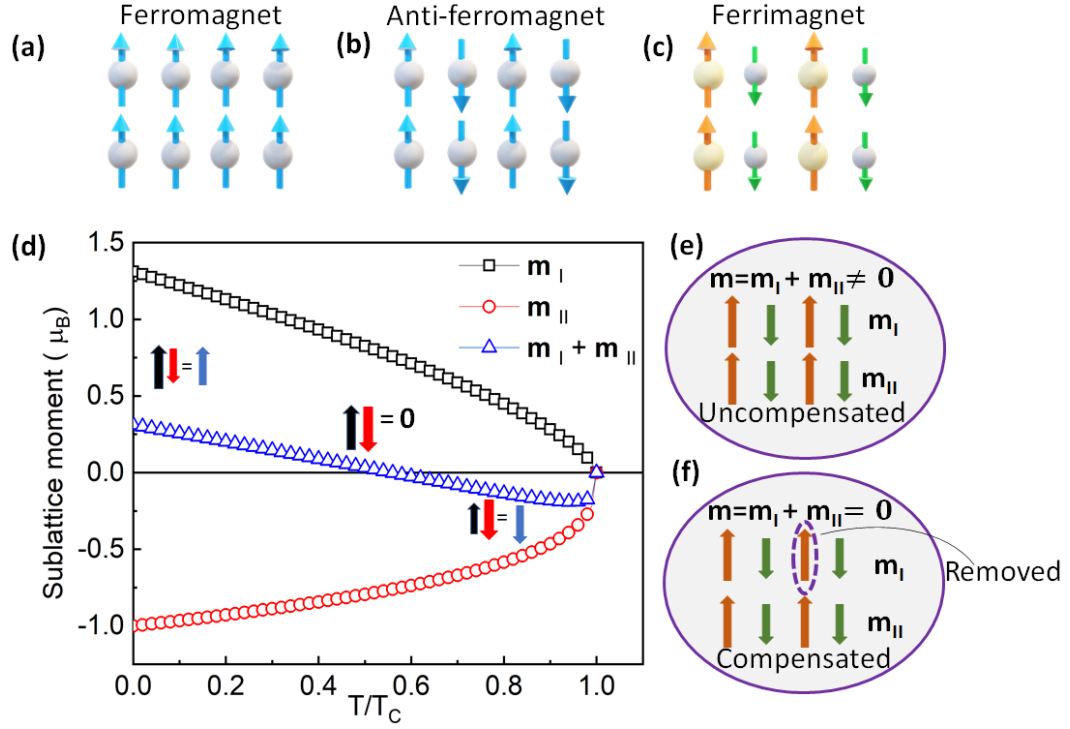


Figure 1.6: (Color online) (a)-(c) Spin ordering in FM, AFM, and FiM, respectively. (d) A graphical representation of the temperature variation of the sub-lattices (black open square (m_I) and red open circle (m_{II})) moment. A compensated state is marked by the zero value of the net moment (blue open triangle). Note: the moment value of sub-lattices and the compensation temperature are made arbitrary. (e) An uncompensated and (f) completely compensated state achieve by extracting one of the sub-lattice.

coordinated in octahedral and tetrahedral atmospheres shows different magnitude of the moments. The inequality in the sublattice moment results in a spontaneous magnetic moment in FiM materials same as that of FM materials. Therefore, it is believed that the FiM materials have the potential to replace the FM materials for magnetic storage media. Apart from various applications, the flexibility of tuning magnetization, magnetic anisotropy, and Curie temperature (T_C) makes them special. Most importantly, the realization of a completely compensated state in the FiM system is in centre of attraction. In case of fully compensated magnetic state the net magnetization becomes zero. Such a state can be achieved by varying temperatures, chemical engineering, etc. In this direction, rare earth (RE)- transition metal (TM) based systems are well studied. CoTb, CoGd, GdFeCo etc., are some

of the example of RE-TM materials which showed temperature-dependent magnetic compensation [40, 41, 42]. In these RE-TM materials, the moment of the RE and TM atoms originates from the f and d orbital electrons, respectively, and coupled antiferromagnetically. With increasing the temperature, the moment of individual sub-lattices varies differently. At a particular temperature, the magnitude of both the sublattices moments becomes equal, resulting into a zero-moment state. Apart from RE-TM based systems, rare-earth iron garnet like $\text{Gd}_3\text{Fe}_5\text{O}_{12}$ [43], $\text{Tm}_3\text{Fe}_5\text{O}_{12}$ [44], etc., and Heusler compound $\text{Mn}_{1.5}\text{FeV}_{0.5}\text{Al}$ also show temperature-dependent magnetic compensation [45]. A graphical representation shown in Fig. 1.6(d) depicts the variation of two sub-lattice (m_I by black, m_{II} by red) moments with temperatures. The resultant magnetization shown in blue becomes zero at a certain temperature hence marking the zero moment state. The other way of achieving a completely compensated state is engineering with chemical composition. The FiM materials can contain two or more sublattices. Therefore, it is possible to extract the magnetic atom contributing to excess moment by substituting a nonmagnetic atom. Basically, a suitable balance between the constituent elements contributing toward the magnetization can ultimately result in a compensated state. An uncompensated state resulting from the imbalance between two sublattices m_1 and m_2 is shown schematically in Fig.1.6(e). The extraction of some of the sublattices results in a complete compensation [46]. Another way of reaching a compensated point is to proportionate mixing of oppositely magnetized materials [47].

Fully compensated FiM materials have a wide range of applications in the field of spintronics. Besides this, the compensated ferrimagnets have great importance for the fundamental study. The realization of exotic spin textures, magneto transport properties, interface phenomena, etc., requires thorough and rigorous studies. Furthermore, the finding of new materials bases of compensated FiM state in insulating, metallic, semiconducting materials, etc., is essential for extending the multi-purpose functionality. In this thesis, observation of various non-trivial magnetic states in Mn-based In-rich FiM systems are mostly achieved through tuning the chemical composition. As a result, an effective change in the underlying interaction

can be stabilized, resulting in the observation of different exotic magnetic states.

1.6 Domain and domain wall

Spontaneous magnetization is a signature feature for any FM materials. However, in general the magnetization is zero in the absence of a magnetic field in the virgin state. Another important behavior of the FM materials is the observation of large magnetization value in a weak magnetic field. Such a large value of magnetization can be equivalent to a very large magnetic field. Therefore, it is hard to imagine an expensive ferromagnetic exchange interaction between the paramagnetic spin with such a small field. The weak field just acts as a trigger to respond in the field direction for an already magnetized system. In 1907 Weiss first proposed the macroscopic picture of magnetization in ferromagnetic material called ‘domain theory’. Domains are small areas of uniform magnetization as shown Fig. 1.7(a). Ferromagnetic materials consist of a large number of such domains. The formation of multiple domains is preferable to the single domain state. Breaking of multiple domains causes a reduction in magneto-static energy or dipolar energy by forming a flux closure. For a single domain system, the magnetization occurs through coherent rotation of spin and alignment along the magnetic field. In the case of domain state, the domain wall motion and the expansion of the domain align along the field direction, causing a net magnetization. Generally, the direction of the magnetization varies from domain to domain. Two nearby domains are separated by a narrow cylindrical region called domain wall. The spins within the domain wall are rotated by some angle with respect to its nearest neighbor. Depending on the plane of rotation of the spin within the domain wall, there are two fundamental domain walls, namely Bloch and Néel walls. For the Bloch wall, the spin rotate within the plane parallel to the wall, and for the Néel case, the spin rotation is perpendicular to the wall. Figure 1.7(b) and (c) show a typical π Bloch and Néel wall. Despite the reduction in magneto static energy by the formation of the domains, the domain wall costs some energy to the system. Let’s consider a π domain wall in a ferromagnet. The energy between

two spins twisted by an angle θ is $-2JS_1.S_2$. For finite and small value of θ , the energy cost is $JS^2 \theta^2$. For a π domain wall, the π angle is the rotation taken over N number of spin. So, the angle $\theta = \pi/N$. Therefore, the total energy cost for such a single chain of spin within the domain wall is $JS^2 \pi^2/N$. This indicates that the energy cost can be reduced by the participation of more and more spin, i.e., the system will tend to unwind its spin and grow in size. However, this unwinding can be stopped if some other energies favor the twist. For a normal domain wall, it is magnetic anisotropy that competes with the exchange energy and causes a finite width for the domain wall. This idea of the finite width domain wall is necessary to describe the formation of nanometric size ‘ 2π domain wall’ or ‘skyrmion’. However, unlike in the 1-D dimensional domain wall, the twist in the spin can be governed by the competition of different energy such as exchange energy, perpendicular magnetic anisotropy, and antisymmetric DMI subject to the underlying crystal symmetry.

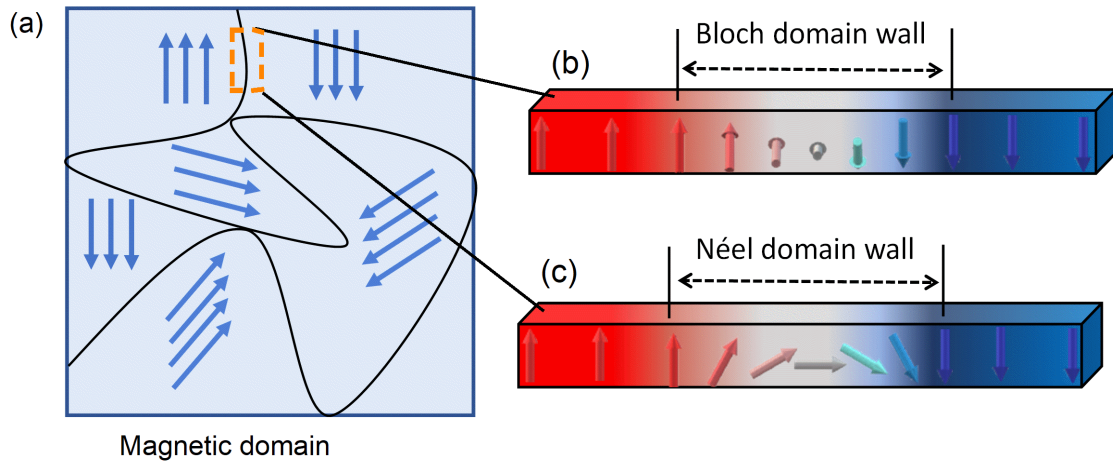


Figure 1.7: (Color online) (a) Schematic representation of domain state in the magnetic material. The direction of magnetization in each domain is shown by a set of blue arrows. The black line separating different domains is called domain wall. The spin rotation within the domain wall (marked by a yellow dashed rectangle) between 180° domain states can be a Bloch type (b) or Néel type (c). In Bloch type, spin rotates parallel to the domain wall, and in Néel case, they rotate perpendicular to the domain wall.

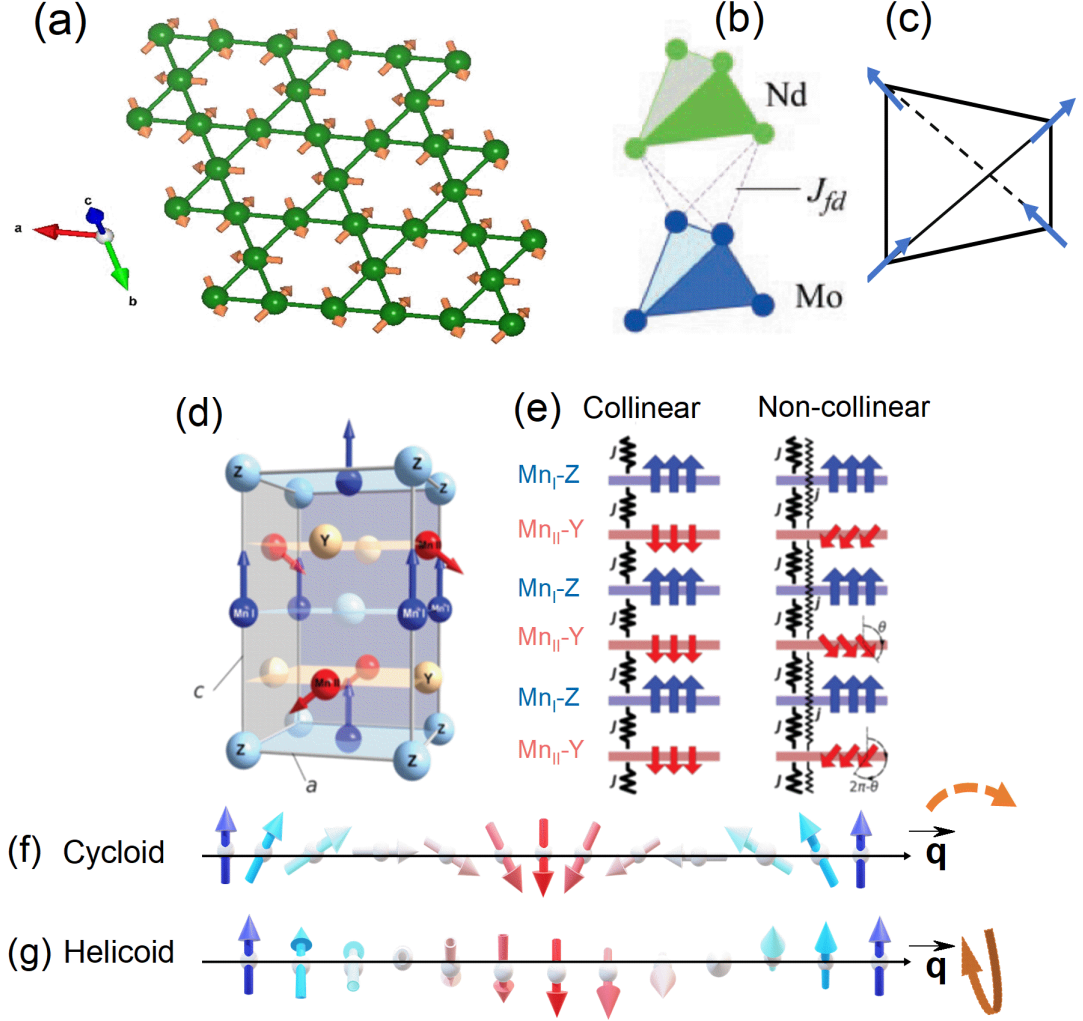


Figure 1.8: (Color online) (a) An in-plane non-collinear triangular spin structure as observed in Mn_3Sn , Mn_3Ge . Green balls represent Mn atoms, and the yellow arrows show the magnetic moment direction. (b) Nd (green circles) and Mo (blue circles) atoms sit at the corner of a tetrahedron [16]. (c) The moment at each corner pointed towards the center of the tetrahedron due to strong anisotropy and forming 2-in 2-out non-coplanar spin structure. (d) The relative orientation of the sub-lattice Mn moment sitting at Wyckoff position 2b (Mn_I , blue balls) and 2d (Mn_{II} , red balls) [48]. (e) A schematic description of exchange frustration inducing a non-collinear magnetic state as observed in Mn_2RhSn [48]. (f) Cycloid: spins are rotated in a plane parallel to the plane containing propagation vector \vec{q} . (g) Helicoid: spins are rotated in a plane perpendicular to the plane containing \vec{q} .

1.7 Non-trivial magnetic states

The nontrivial magnetic states are those beyond the known magnetic structures, e.g. FM, AFM, and FiM. The early development in magnetism mainly dealt with such magnetic ordering. For a simple system, the defining energy contribution comes from the exchange interaction and magnetic anisotropy. Limiting the exchange interaction for the nearest neighbor pair gives the collinear FM and AFM depending on the type of interactions. However, this mechanism is unable to explain the weak ferromagnetism in AFM α -Fe₂O₃, MnCO₃ and CoCO₃. Later on I. Dzyaloshinskii explains the weak FM state in terms of spin-orbit coupling mediated DMI [38]. In exception, even with the nearest neighbor Heisenberg type interaction can generate a non-collinear magnetic ordering for certain geometric arrangements. For example, a triangular lattice with AFM interaction only has a magnetic ground state 120° rotated from each other [see Fig. 1.8(a)] [49, 50]. A recent study shows that the inclusion of higher-order exchange terms leads to the incommensurate as well as non-coplanar spin state for triangular lattice in the Mn₃Sn system [51]. Even for an FM-type interaction, a non-coplanar FM ordering has been observed in a geometrically frustrated system of pyrochlore type Nd₂Mo₂O₇ [Fig. 1.8(b) and (c)] [16]. A non-collinear magnetic ordering can be formed as a result of exchange frustration [Fig. 1.8(d)]. For example, the ground magnetic state of Mn₂RhSn shows a large non-collinearity as the nearest neighbor exchange is AFM and the next nearest is also AFM [Fig. 1.8(e)] [48]. Such non-collinear/non-coplanar structures mainly appear within the crystallographic unit cell and are termed as a commensurate state. However, the incommensurate states are the magnetic ordering, while the repetition of the magnetic ordering contains more than one to several crystallographic unit cells. Also, it should be mentioned that the length cannot be scaled with an integer multiple of the unit cell. There are different incommensurate magnetic ordering categorized based on the rotation of the spin with respect to the direction of propagation (\vec{q}). Figure 1.8(f) and (g) represents a cycloidal and helical spin modulation, respectively. In the helical case, the spin is rotated in a plane perpendicular to the

\vec{q} . Whereas for cycloid, the spin rotates to the plane containing the \vec{q} . The conical spin structure is also often observed in rare-earth-based compounds. In this case, the spin rotation is not exactly perpendicular to the \vec{q} . A constant finite angle is present between each moment and the \vec{q} vector. As a result, some finite moments are generated along the direction of the \vec{q} . Such a scenario can be realized when applying a small magnetic field along the \vec{q} in a helical system. In that case, all the spin will be tilted towards the field direction. Most of the cases, the helical or cycloid states arise as competition between various energy terms like exchange interaction, and DMI. Some of the rare earth materials show incommensurate modulated magnetic structure due to the exchange frustration [52]. This kind of modulated spiral states are different from the chiral helical structure. The formers are typically very short period spirals and follows arbitrary sense of rotation of spin.

1.8 Magnetic skyrmion and antiskyrmion

1.8.1 Brief history

The term ‘skyrmion’ was first utilized by Tony Skyrme in 1962 in nuclear physics to describe topologically stable field configuration used in the modelling of nucleon [53]. Later on, the idea of skyrmion started to be used to distinguish the uncommon phase of the systems (turing pattern of classical liquid [54], blue phase of the liquid crystal [55], integer quantum Hall magnet [56], etc.) in a different branch of condensed matter physics. In 1989 A. N. Bogdanov and D. A. Yablonskii showed that the inhomogeneous magnetic states consist of ‘magnetic vortices’ energetically more favorable than the uniform magnetic state in certain classes of magnetic systems [7]. In 2006, U.K. Rößler et al. established that the formation of the spontaneous skyrmionic ground state is also possible same as the generally occurred ordered state of FM and AFM [8]. In 2008, the first experimental evidence of magnetic skyrmion was observed by S. Mühlbauer et al. Since then skyrmion phase appeared as a new ordered state of magnetic material [9].

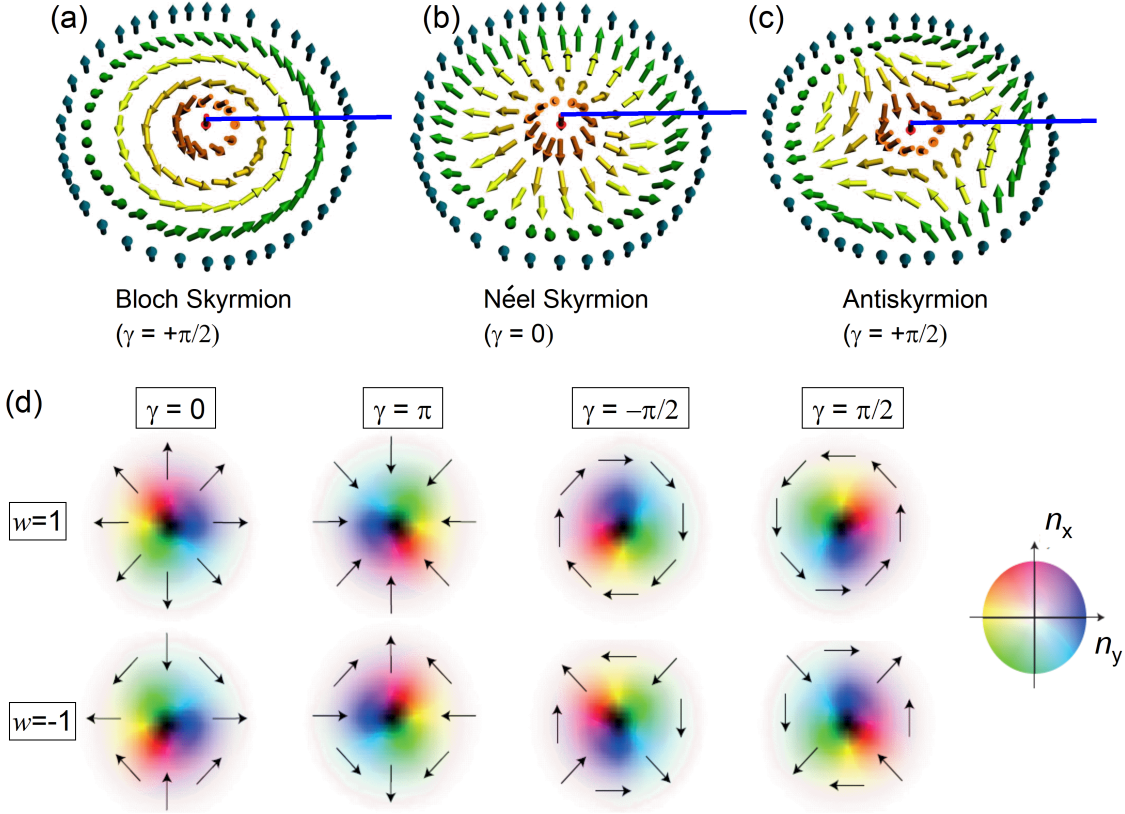


Figure 1.9: (Color online) (a) Schematic spin texture of Bloch, (b) Néel, and (c) anti-skyrmion. Helicity (γ) of each spin structure is mentioned below. (d) In the upper row: the Néel and Bloch skyrmion structure with different helicity for a given vorticity $w = +1$. Lower row: anti-skyrmion with different helicity for $w = -1$. The central black and peripheral white correspond to the down and up spin with zero in-plane moments, respectively. The color wheel is shown on the right side, where n_x and n_y correspond to the two orthogonal axes. The black arrows indicate the direction of the in-plane magnetic moment. Image (a)-(c) and (d) taken from ref-[57] and ref-[2], respectively.

1.8.2 Topological spin texture and stabilization mechanism

There are three distinct types of magnetic skyrmions (skx) found in different classes of magnetic materials, namely Bloch, Néel, and antiskyrmion [Fig. 1.9(a)-(c)]. The nomenclature of the Bloch and Néel type of skyrmions follows in analogy with the spin rotation in Bloch and Néel domain walls. The antiskyrmion (askx) contains both the Bloch and Néel types of spin rotation. It can be seen from Fig. 1.9(a)-(c), that the spin at the center and periphery is directed oppositely while the in-between

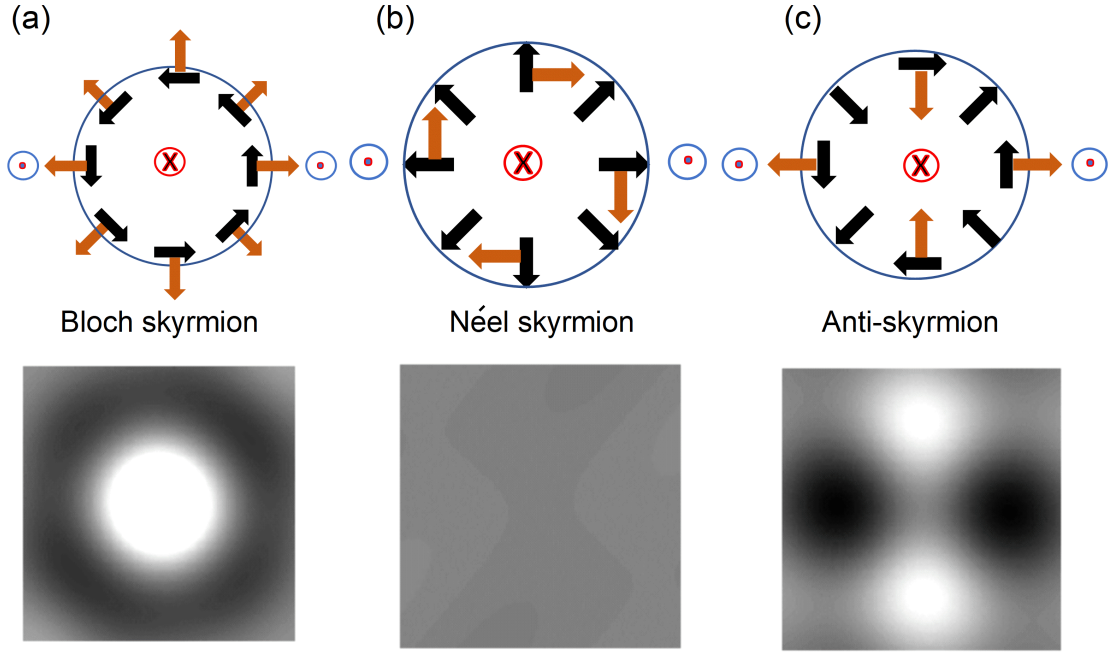


Figure 1.10: (Color online) (a)-(c) Schematic of the in-plane magnetic moments (black arrows) and the Lorentz deflections of the transmitted electrons (orange arrows) in a Bloch, Néel, and anti-skyrmion respectively. The corresponding simulated LTEM images as a result of the deflected electrons is shown below the respective schematic. Lower panel images are taken from ref-[57]. The schematic spin texture of these three types of skyrmion is shown in the Fig. 1.9(a)-(c).

spins rotate in a continuous manner. So, going diametrically, it looks like a 360° domain wall. Magnetic skx are characterized by topological charge (Q) given by-

$$Q = \frac{1}{4\pi} \iint \mathbf{n} \cdot \left(\frac{\partial \mathbf{n}}{\partial x} \times \frac{\partial \mathbf{n}}{\partial y} \right) dx dy \quad (1.9)$$

where, \mathbf{n} is normalized local magnetic moment. For skx, Q can be any integer number depending on how many times \mathbf{n} wraps a unit sphere. This is basically the mapping of the order parameter (\mathbf{n}) from real space to order parameter space as described earlier. Also, it can be noted that the center spin align in a particular direction, so the origin is not a singular point. The direction of center spin defined the polarity ($p = \pm 1$). For the up and down directions, it is conventionally taken as

+1 and -1, respectively. Another quantity that distinguishes the rich spin structure in skx is the helicity (γ). The helicity of the skx is defined as the direction of spin rotation with respect to the reference radial plane as marked by blue thick line in Fig. 1.9(a)-(c). The angle is $\frac{\pi}{2}$ with respect to the outward radial plane for Bloch skx. So, helicity is $\frac{\pi}{2}$ considering anti-clockwise rotation. In a similar manner for Néel skx, it will be either 0 or π [see Fig. 1.9(d)]. Four different helicity configurations are shown for an askx with vorticity ($w = -1$) in the lower row of Fig. 1.9(d). As it contains both type of helicity ($0, \pi$) and $(+\frac{\pi}{2}, -\frac{\pi}{2})$ due to Néel and Bloch part within it, respectively. The first experimental report of skx was in the chiral MnSi system and detected utilizing small angle neutron scattering (SANS) [9]. Later, Yu et al. demonstrated the real space observation of the magnetic skx using Lorentz transmission electron microscopy (LTEM) [58]. LTEM is extensively used for detecting the magnetic skx/askx, including the present thesis. Figure 1.10(a)-(c) describe the images of the above-mentioned three distinct types of skx under LTEM.

Magnetic skyrmions are found in a wide range of materials with sizes from sub-nanometer to microns. Their stability/formation in different systems depend upon the underlying crystal symmetry and magnetic interaction present in the system. In chiral MnSi system, the DMI and Heisenberg exchange govern the helical state, which transforms into the skyrmion lattice under a magnetic field. The energy hierarchy in this system is as follows, Heisenberg, DMI, and uni-axial anisotropy energy. Some thin film systems with perpendicular easy-axis anisotropy exhibit skyrmionic state [59, 60, 61]. In this case, competition between long-range magnetic dipolar interaction and anisotropy governs the skyrmion state. The dipolar interaction tries to align spin in the in-plane direction, while anisotropy favors an out-of-plane orientation. A recent study shows that some of the centrosymmetric bulk materials also stabilize skx lattice due to the same mechanism [62, 63]. The formation of isolated atomic size skx and lattice of skx in mono-layer Fe on Ir is described in terms of four spin exchange interactions [64]. Also, the evidence of nano-metric size skx in lattice form is reported in a geometrically frustrated system of Gd_2PdSi_3 [15]. So, it is clear that the modulation length scale for a system with DMI and non-DMI

is different. Also, the energy of the skx in the frustrated system is independent of their helicity, i.e., a degenerate helicity state is possible. Whereas, a DMI-assisted skx often follows a particular helicity depending on the sign of the DM vector. Recently, the center of focus is to find skx/askx in the frustrated magnetic systems. It is important to mention here that these frustrated magnetic systems do not always favor the spin spiral state with an in-commensurate period. The minimization of the energy can be achieved through a commensurate non-collinear/non-coplanar spin state. In such a situation, temperature-driven exchange variation can be a key parameter to be taken into account.

1.8.3 Spintronics and skyrmionic prospect

In 2004, the idea of ‘race track’ memory was proposed by S.S.P Parkin as an alternative to MRAM storage devices [5, 65]. The race track memory is a completely solid state device consisting of magnetic nanowires patterned with alternate magnetic domains separated by a thin magnetic domain wall. Driving the domain walls by passing electrical current through it can be used to transfer of information in it. With the application of spin polarised current through the wire, the electron transfers its spin angular momentum to the spin of the domain wall, thereby causing the motion of the domain wall. It is noteworthy that the movement of the domain walls requires a very high current density $\sim 10^{12}$ A/m², which is not suitable from the perspective of consumption of power [66]. In subsequent studies, it has been revealed that the speed of the domain walls can be improved for thin film systems with PMA [67, 68] instead of in-plane soft magnetic materials [66]. Further studies on the heterostructure of PMA based magnetic material deposited on heavy metals reveals the presence of an interfacial DMI. This helps in the modification of the domain wall structure and enhances the domain wall velocity. The strength of the DMI is related to the magnitude of proximity induced moment within the heavy metal layer [67]. The gist of the above discussion is that the modification in the domain wall structure and the new materials with dynamic properties are in the center of the present

time, which can help to reach the goal of non-volatile high-density memory devices. The skx can be regarded as a circular 360° chiral domain wall with rotational symmetry, and very robust against external perturbation. These magnetic skyrmions are rich in spin texture, and their topological protection makes them unique from any trivial ordering of spin states. Soon after the first experimental observation, several groups have rigorously studied their different physical properties to explore the potential use in the field of spintronics. Jonietz et al. have shown that spin transfer torque induced magnetization dynamics can be instigated with a relatively smaller current density in the skyrmionic phase of MnSi bulk crystal [6]. Most importantly, a maximum domain wall velocity of 750 m/s has been reported for a synthetic antiferromagnetic system (SAF) where two FM layers were separated by a spacer layer coupled antiferromagnetically [69]. Therefore, a search for materials with both features i.e, skyrmion phase in zero magnetic moment systems, is highly desirable.

1.9 Emergent phenomena of nontrivial and topological materials

As discussed above, different types of topologically trivial and non-trivial magnetic states can be realized in the range of materials including metal, semiconductors, and insulators. They are non-trivial not only because of their complex spin ordering but also showcase exotic magnetic/transport properties. For example, consider the discovery of AHE [71], which was found in FM materials and is therefore believed to be a consequence of the magnetization of the system. An empirical formula has been provided by Pugh and Lippert (1932) for the observed Hall signal in ferromagnetic materials where the Hall signal scales with magnetization [72]. Therefore, the AFM materials are not expected to show any anomalous Hall effect (AHE) as they have zero magnetic moment. In contrast, the triangular AFM Mn_3Sn [49] and Mn_3Ge [50] show a large AHE. As can be seen from Fig. 1.11(a) and (b), the Mn_3Sn has

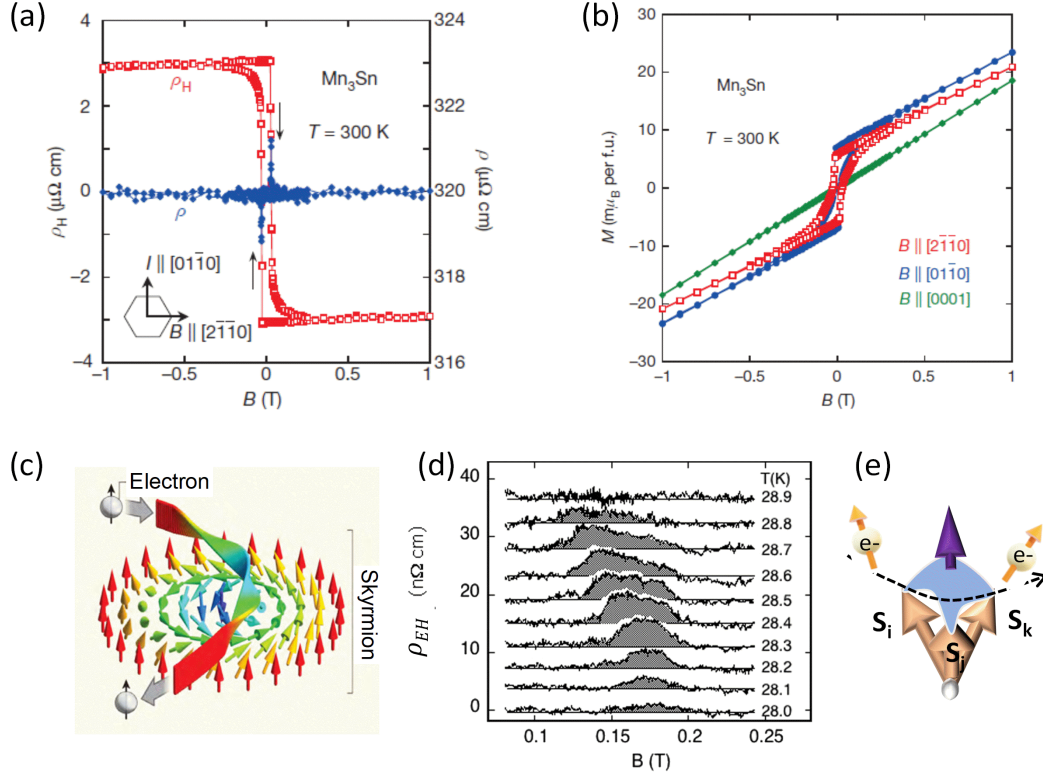


Figure 1.11: (Color online) (a) Large room temperature anomalous Hall effect (red square symbols) observed in AFM Mn_3Sn . Blue circle symbols correspond to the magneto-resistance (MR) [49]. (b) The different color symbols indicate direction-dependent magnetization ($M(H)$) at 300 K in AFM Mn_3Sn [49]. (c) Cartoon description of the electron path through skyrmion [70]. (d) Observation of extra Hall contribution in the A-phase (skyrmion phase) of the MnSi system [11]. (e) Schematic depiction of electron deflection due to the fictitious magnetic field (violet arrow) in a finite SSC.

large anomalous Hall resistivity, although the magnetic moment is extremely small $\sim 0.002 \mu_B/\text{f.u.}$ The origin of AHE in these systems is understood in terms of the non vanishing Berry curvature arises due to the non-collinear spin structure.

1.9.1 Topological Hall effect (THE)

A non-coplanar spin structure with finite SSC can be described by a gauge field. This gauge field results in an electromagnetic field in the system, which can results into

various emergent electromagnetic phenomena. For instance, THE in the skyrmionic system is one such example. In metals, when the conduction electrons move through the complex spin texture, like skx , the spin of the conduction electron tries to align locally to each spin direction according to Hund's rule. Therefore, on traversing the skyrmion texture, the e^- will acquire an extra phase, called the Berry phase [Fig. 1.11(c)]. The Berry phase has the connection to the gauge field, which act as a source of the fictitious magnetic field in the materials. Due to this fictitious magnetic field, an extra Hall ρ_{EH} contribution known as THE appears along with the ordinary (OHE) and anomalous Hall Effect (ρ_{AH}). Total Hall (ρ_H) resistivity in conventional FM and FiM materials is given by

$$\rho_H = \rho_{OHE} + \rho_{AHE} \quad (1.10)$$

where

$$\rho_{OHE} = \mu_0 R_0 H \quad (1.11)$$

and

$$\rho_{AHE} = b\rho^2 M. \quad (1.12)$$

R_0 and H are the ordinary Hall coefficient and external magnetic field, respectively. ρ and M are the longitudinal resistivity and magnetization of the sample, respectively. b is the scale factor/constant. Therefore ρ_{EH} can be extracted by subtracting the ρ_H [Eqn. 1.10] from the experimentally obtained Hall resistivity ($\rho_{EXPT} = \rho_H + \rho_{EH}$). It can be seen in Fig. 1.11(d) that an ρ_{EH} appears in the A phase of the MnSi system [11].

It can be mentioned here that different origin of ρ_{AHE} evolves with time since its discovery. It can be mainly classified into two mechanisms (i) intrinsic and (ii) extrinsic [73]. The notion of Berry curvatures comes under the intrinsic mechanism, whereas the 'skew scattering' and 'side-jump' belongs to the extrinsic mechanism. It is noteworthy that the ρ_{AHE} arise from the intrinsic mechanism varies as a square of the longitudinal resistivity ρ and directly scales with the magnetization of the

sample. However, the extrinsic contribution from the skew scattering (ρ_{AHE}^{skew}) and side jump (ρ_{AHE}^{sj}) to the ρ_{AHE} given as $\rho_{AHE}^{skew} \propto \rho$ and $\rho_{AHE}^{sj} \propto \rho^2$ [73]. Also, a new scaling relation is demonstrated for ρ_{AHE}^{skew} and ρ_{AHE}^{sj} for high conductivity materials ($\sigma_{xx} \sim 10^6 \Omega^{-1} \text{ cm}^{-1}$) in terms of the residual resistivity (ρ_0) instead of ρ [74]. Furthermore, different regimes of conductivity can have different contribution from the intrinsic or skew scattering process [73]. The anomalous Hall effect due to skew scattering and side jump is irrelevant even at low temperatures in materials with moderate conductivity ($\sim 10^4 - 10^6 \Omega^{-1} \text{ cm}^{-1}$) with negligible magneto-resistance [75, 76, 77].

As discussed above, the finite value of THE is only possible when three spins becomes non-coplanar. In this case the solid angle subtended by these three non-coplanar spins over a unit sphere act as source of magnetic field [Fig. 1.11(e)]. In fact, a system with such non-coplanar spin structure can be used to manipulate the THE by changing the relative spin canting angle. In the third chapter it is shown that changing the degree of non-collinearity of the alignment of the magnetic can be utilized to control the THE in the system.

1.10 Exchange bias

Exchange bias field (EB) or unidirectional exchange anisotropy is the measure of the asymmetrical offset of the magnetic hysteresis loop ($M(H)$) along the magnetic field axis [Fig. 1.12(a)]. Meiklejohn and Bean first discovered the phenomena of exchange bias in 1956 in a core-shell system of ferromagnetic Co and antiferromagnetic CoO [78]. Since then, it has been believed that the EB is related to the interfacial exchange interaction between an FM and AFM coupled system. A cartoon picture describing various stages of the conventional EB system is shown in Fig. 1.12(b). For an FM-AFM bilayer system, when the field is applied at temperature $T_N < T < T_C$, the FM spins align along the field direction. However, the AFM spins remain randomly oriented [top schematic in Fig. 1.12(b)]. In this condition, further decreasing the temperature below T_N , the top layer spins from the AFM side

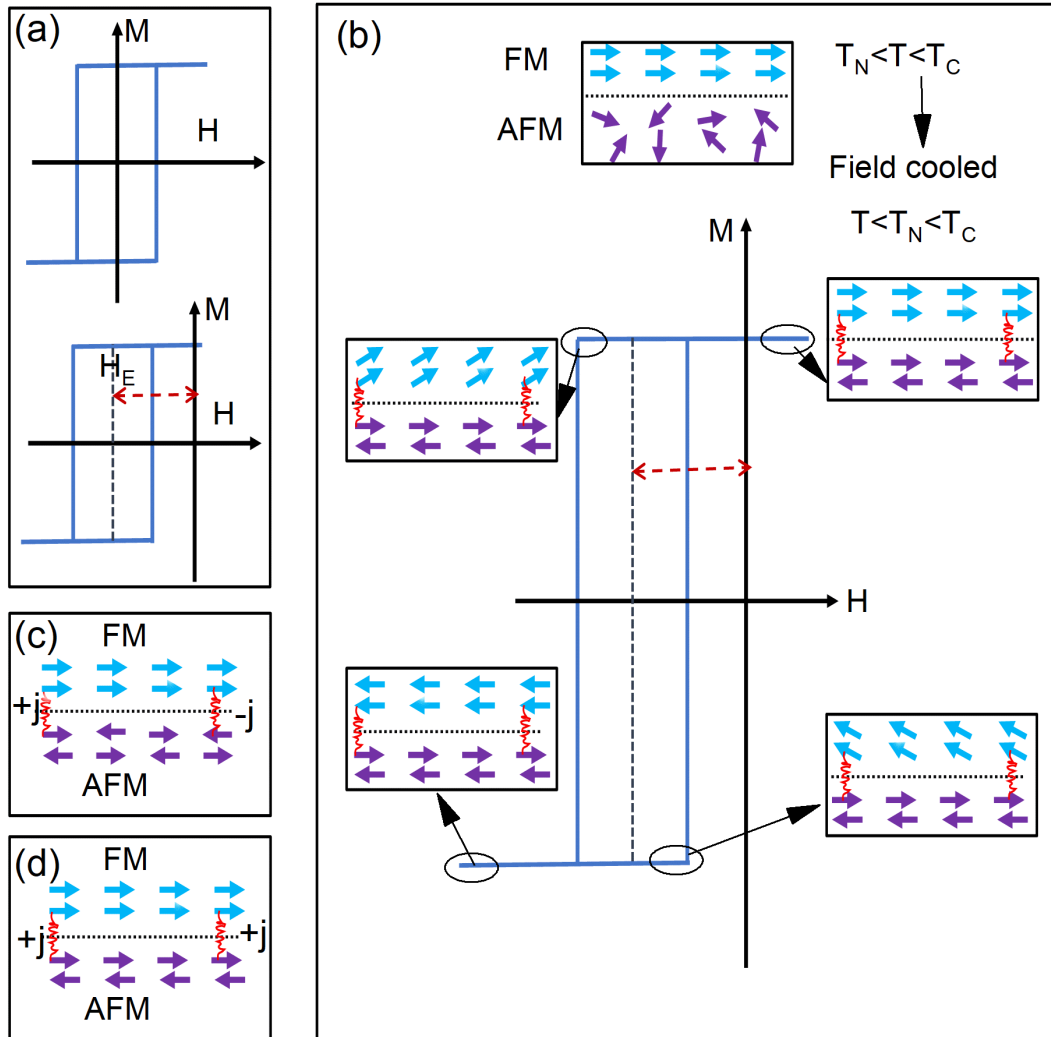


Figure 1.12: (Color online) (a) Graphical representation of a usual (upper one) and shifted (lower one) magnetic hysteresis loop. (b) Schematic description of a shifted hysteresis of an FM-AFM bilayer system measured after field cooled. The cartoon spin texture in (b) corresponds to a different portion of the hysteresis marked with open ellipses are just for illustration and not necessarily the exact scenario of the magnetization. (c) An FM-AFM bilayer system with compensated AFM interface spin. The effective inter-facial energy is zero due to alternate FM ($+j$) and AFM ($-j$) coupling. (d) An FM-AFM bilayer system with un-compensated AFM interface spin. In this case, there is non-zero inter-facial energy.

will align ferromagnetically (here considering ferromagnetic coupling) due to the exchange interaction with the bottom layer spin from the FM side. The bulk part of

the AFM spins follow the top layer spin in such a way as to make the net magnetization zero. The anisotropy axis of the AFM layer gets oriented in the field direction. The FM spins start following the magnetic field when reversing the field direction. However, the AFM spin configuration remains unchanged due to strong anisotropy. As a result, the bottom layer spin from the FM side, which is coupled to AFM spin, tries to remain in the initial direction of the field. Thus, the AFM spins provide a microscopic torque to keep the FM spins in their initial direction. Therefore, an extra field is required to fully reverse the direction of FM spins to overcome the torque that arises from the interface exchange coupling. Now, bringing back the FM spins in their original position requires less field as the torque is now acting in favor. Therefore, the lower and upper cut-off field (where magnetization becomes zero) is not symmetric about the origin of the field coordinate. Hence an asymmetric hysteresis occurs, and the resultant offset (marked with a double-headed arrow) is the measure of the EB field.

1.10.1 Nontrivial interfacial spin structure and EB

Although the EB effect was first observed in FM-AFM core-shell arrangement, subsequent studies show the existence of the effect in FM-FiM [79], FM-Spin Glass (SG) [80], AFM-FiM [81], and AFM-SG [82] systems. Therefore, the microscopic origin of the EB phenomena is the subject of intense discussion. In this regard, different microscopic models are proposed to describe the EB phenomena. Among them, rough interface model [83], uncompensated interface spin model [84], and domain state model [85] mainly concentrate on the magnetic properties of bulk and the interfacial spins of the AFM part. For example, A. P. Malozemoff proposes the concept of random field arising from the randomness in the exchange coupling due to the rough interface in the FM-AFM bilayer system [83]. This random field act on the AFM part and create the domain wall perpendicular to the FM-AFM interface. The formation of the domain wall occurs during the field cooling process in the presence of FM magnetization. Therefore, a finite moment arises from the AFM

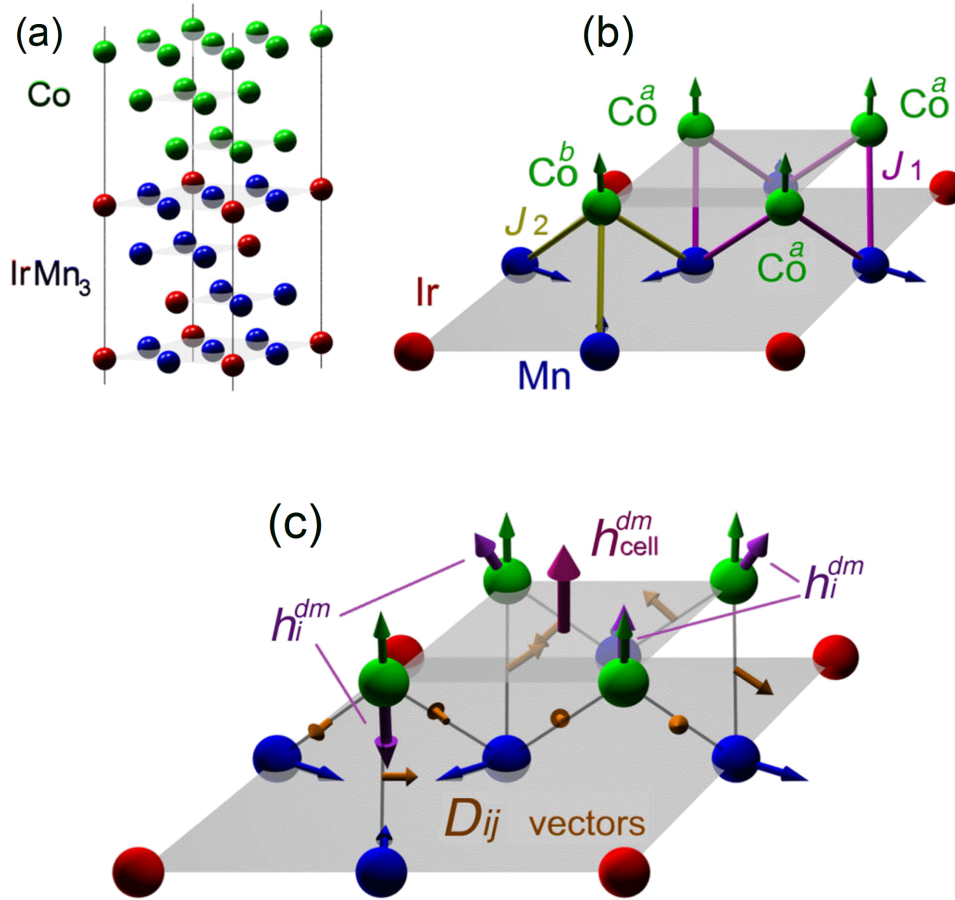


Figure 1.13: (Color online) (a) Stacking of bilayer Co and Mn_3Ir . The red, blue, and green balls are Ir, Mn, and Co atoms. (b) Depiction of the magnetic arrangement at the (111) interface. The Mn moments (blue arrows) lie in the plane, forming triangular AFM ordering. J_1 and J_2 are the two kinds of isotropic exchange interactions between Co-Mn NNs. DM vectors (D_{ij}) between Co-Mn nearest neighbors are shown in orange arrows. The h_{dmi} (violet arrows) and h_{dm} (magenta arrows) is the DM interface field and DM field per unit cell acting on the Co atoms, respectively. Image (a)-(c) is taken from ref.-[23].

side couples to FM spins at low temperatures. Takano et al. have experimentally shown the role of uncompensated spin from the AFM layer to the EB effect [84]. In this study, they measure the thermoremanent magnetization of the interface spin of CoO/MgO, which shows the same feature and temperature dependency as that of the exchange bias field obtained from $Ni_{81}Fe_{19}/CoO$ bilayer. P. Miltényi et al., establish the role of AFM domain state in the volume part to describe the increase

in the EB in the Co/CoO bi-layers [85]. Moreover, all these models consider only the isotropic exchange coupling between the FM-AFM layer. Thus, the finite magnetization at the interface from the AFM part becomes the essential requirement. This can be understood from the simple schematic picture of an FM-AFM bilayer system with the isotropic exchange, as shown in Fig. 1.12(c) and (d). With compensated interface spins from the AFM layer resulting into an alternate (+ve and -ve) exchange interaction, a net zero interface energy is expected [Fig. 1.12(c)]. For uncompensated cases, there is only one kind of exchange interaction [Fig. 1.12(d)], which results in finite inter-facial energy. However, some recent studies show that the antisymmetric DMI can be the main source of EB effect in case of perpendicular bilayer system even with the compensated AFM interface spin [see Fig. 1.13(a)-(c)] [23].

As mentioned before, the DMI requires broken inversion symmetry. Therefore, in some systems, it is possible to exist interfacial DMI at the FM-AFM interface. Therefore, an unconventional interface spin texture may result from this as well. Until recently, the observation of THE like signal in manganese nitride (Mn_4N) films system conjectured to be the presence of chiral skx [86]. Chen et al., show that the presence of chiral 90 degree domain wall at the interface of a Dy-Co/Ni-Fe (FiM-FM) bilayer system induces exchange-bias effect [87]. The chiral interfacial domain wall arise from the competition between the exchange coupling of Ni-Fe and Dy-Co at the interface and the DMI in the Dy-Co layer [87]. Therefore, combined effect of symmetric and antisymmetric interactions at the interface can causes the non-trivial interfacial spin textures in the system which can be very strongly pinned. In such a situation, a large EB field may arise.

1.11 Inter-metallic Heusler compounds

Inter-metallic compounds are the stoichiometric mixture of more than one element resulting into some defined crystal structure. Most interestingly, these compounds neither hold the structure nor follow the physical properties of any of the constituent

elements. Heusler compounds (discovered in 1903 by Fritz Heusler) are one such example of inter-metallics with growing interest in different branches of condensed matter physics. The Heusler compounds are generally expressed by the formula X_2YZ (full Heusler), and XYZ (half Heusler), where X and Y are mainly transition metals and appear as ascending order of electro-negativity and Z is the main group element from the second half of the periodic table [88]. The half Heusler compounds crystallize in a non-centrosymmetric cubic structure $F\bar{4}3m$ (space group (SG) no. 216). The full Heusler compounds (X_2YZ) are generally formed in the cubic space group $Fm\bar{3}m$ (SG no. 225). The corresponding prototype of $C1_b$ and $L2_1$ structure of XYZ and X_2YZ , respectively, are shown in Fig. 1.14(a) and (b). However, a different permutation and combination of the XYZ in the distinct position is also possible based on several factors like atomic size, type of interaction i.e., metallic or covalent between the atoms, etc. [88]. An inverse Heusler structure of $CuHg_2Ti$ type prototype forms when the atomic number (Z) of one of the X atoms is less than that of the Y atom from the same period, even for transition metal element from different periods also possible. In a conventional Full Heusler system, the Y and Z atoms are octahedrally coordinated, and X atoms fill all the tetrahedral positions. Whereas, for inverse Heusler [see Fig. 1.14(c)], one of the X atoms and Z form the octahedral coordination, and the remaining X and Y fill all the tetrahedral positions. The tetrahedral coordination is shown in Fig. 1.14(a). Mn_2 -based materials with $Z(Y) > Z(Mn)$ often show this inverse Heusler structure as illustrated below.

1.11.1 Mn-rich In-based ferrimagnetic systems

The first two parts of the thesis highlight some interesting results based on the Mn-rich In-based inverse tetragonal Heusler compounds. Mn is a transition metal element with $[Ar]3d^54s^2$ electronic configuration, and in bulk, it shows AFM ordering. Indium (In) is the main group element from the second part of the periodic table with electronic configuration $[Kr]5s^25p^1$. The use of non-magnetic Platinum (Pt) as a Y element is based on the fact that it has a large atomic number and

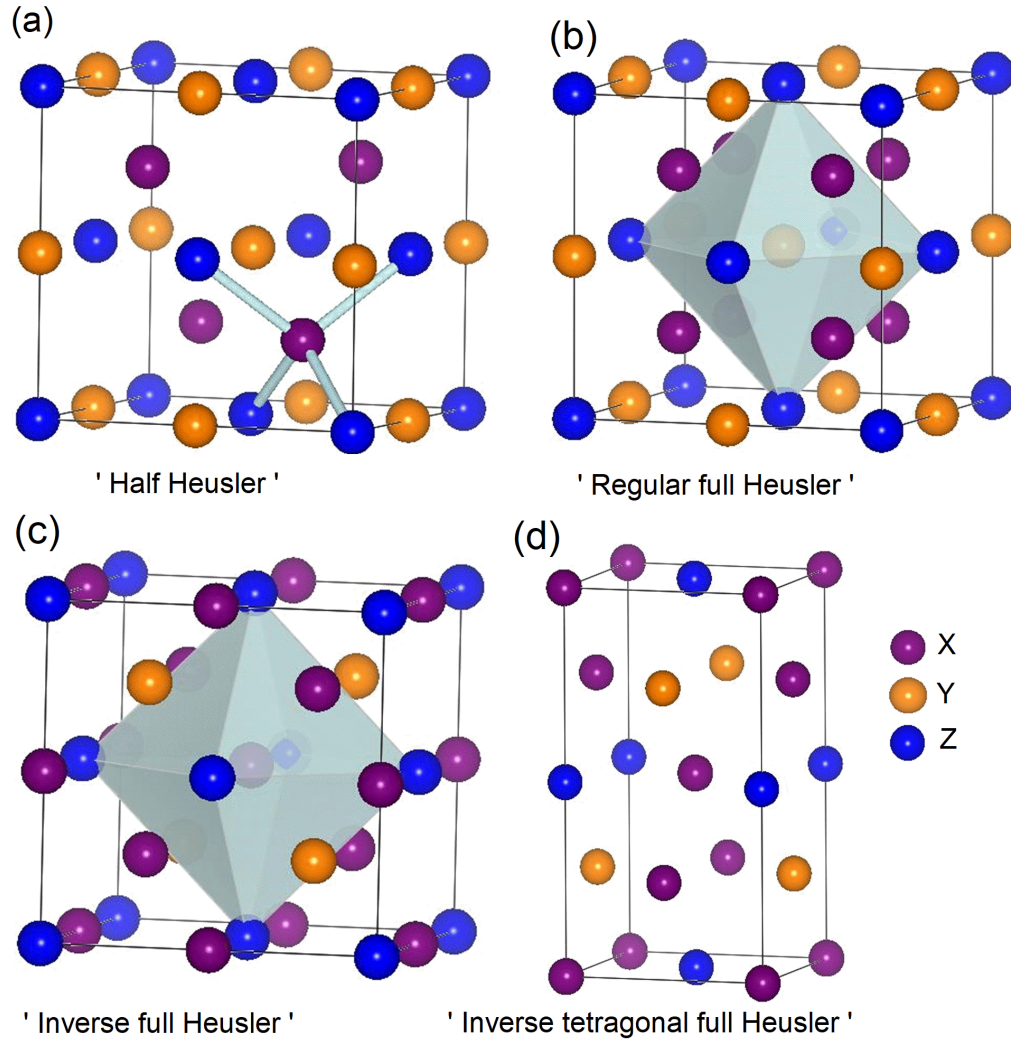


Figure 1.14: (Color online) Crystal structure of various types of Heusler compounds. (a) Half Heusler. (b) Regular full Heusler with Cu_2MnAl ($L2_1$) as prototype. (c) Inverse full Heusler with CuHg_2Ti as a prototype. (d) Mn_2NiSn type inverse tetragonal full Heusler. The nomenclature of the different color balls is shown on the right side of (d). Tetrahedral and octahedral coordination is shown by the connection of long cylindrical line in (a) and by polyhedra in (b) and (c), respectively.

strong spin-orbit coupling suitable for inducing DMI in the system with broken inversion symmetry. Moreover, Mn-based Heuslers stabilized in the tetragonal phase are promising candidates from the application point of view in the field of spintronics. Figure 1.14(d) depicts an inverse tetragonal Heusler structure belonging to the space group $I\bar{4}m2$ (SG no. 119). The tetragonal structure can be interpreted as a distortion of the cubic structure, i.e., squeezing/elongation in the basal plane

axis and elongation/squeezing along a perpendicular direction. For such kind of distortion, the system costs elastic energy, which is compensated by the energy gain due to the crystal field effect. This phenomenon is popularly known as the ‘band Jahn-Teller effect’. The ordering of the Mn moment strongly depends on the coordination and type of atoms that take part in it. The geometry of the arrangement of magnetic atoms and the type of interaction among the spins govern the magnetic ordering in the system.

1.11.1.1 Non-collinear ferrimagnet: Mn_2PtIn

The functionality of the spintronic devices based on the spin transfer torque (STT) phenomena focuses on perpendicular magnetic anisotropy (PMA). The materials are mainly explored to satisfy the stringent requirement of spintronic devices, like minimizing the switching current and switching time while maintaining thermal stability. A list of pre-requisite to achieve an optimal switching current and switching time can be derived for the materials as per the Slonczewski–Berger equation [89, 90]. Magnetic materials with high spin polarization, large Curie temperature (T_C), low saturation magnetization (M_S), low Gilbert damping, and considerable PMA are very useful for the said purpose. Also, the magnetic multi-layers are the backbone of future spintronic devices. Especially, the spin valve configuration plays a central role in the easy electrical reading and writing process. One must remember that the alteration of the magnetically stable state of the free layer requires sufficient energy to trigger the switching. For the miniaturization of this difficulty, Berger et al., proposed a special geometry of the spin valve configuration, called ‘dual spin valve’ [91]. In which the free ferromagnetic layer is enclosed between two other fixed ferromagnetic layers separated by a spacer layer. In this scenario, the spin polarized electrons gets accumulated at the metal-ferromagnet interface on both sides of the free layer, enhancing the effect of STT. Further, considering the non-collinear spin arrangement of the free and fixed layer results in a significant decrement of the critical switching current density [92].

Hence, the non-collinear magnets are equally important from application and

fundamental physics points of view. The Density functional theory (DFT) calculations have shown that Mn_2PtIn exhibits a non-collinear magnetic ground state [48]. The non-collinearity arises as a consequence of exchange frustration in the system. In fact, the powder neutron diffraction experiment provides concrete evidence of non-collinear magnetic ordering in the isostructural compound Mn_2RhSn [48]. In addition, it shows high Curie temperature ($T_C \sim 350$ K) and low magnetic moment ($\sim 1.6 \mu_B/\text{f.u.}$) [93]. As we aim to find a system whose degree of non-collinearity can be manipulated to observe the change in the emergent properties, Mn_2PtIn can be a good starting point to showcase the desired effect.

1.11.1.2 Antiskyrmion: D_{2d} inverse Heusler Mn-Pt-Sn

The first experimental observation of magnetic antiskyrmion was found in $\text{Mn}_{1.4}\text{Pt}_{0.9}\text{Pd}_{0.1}\text{Sn}$ [57]. This is a member of the inverse tetragonal Heusler compounds. $\text{Mn}_{1.4}\text{Pt}_{0.9}\text{Pd}_{0.1}\text{Sn}$ shows large Curie temperature (~ 400 K) and a spin re-orientation transition at the low temperature (~ 130 K) region. The presence of heavy metal element Pt leads to a strong spin-orbit coupling and magneto-crystalline anisotropy. A magnetic moment of about $5 \mu_B/\text{f.u.}$ has been reported at 5 K. Due to the large magnetic moment of the system, dipolar energy appears as one of the key energy contributors to stabilizing the sky in this system. Also, it plays a crucial role in controlling the shape and size of the sky in this system [94]. It is reported that the sky size increases with increasing the film thickness. As mentioned earlier, this compound crystallizes in D_{2d} point symmetry, which restricts the opposite sign of DM vector ($D_x = -D_y$) lie along the two principal axes within a tetragonal basal plane. Such anisotropic DMI generates an opposite sense of twisting in the spins along two orthogonal directions in the basal plane. The anisotropic DMI competes with the isotropic exchange interaction that governs the helical modulation propagation along (100) and (010) directions. Under the application of a magnetic field in the direction of the tetragonal axis (001), which is an easy axis of magnetization, transform the helical phase into sky phase. It is important to mention here that the sky phase is found only above the spin re-orientation temperature ($T_{SR} \sim 130$ K [57]).

The absence of the DM vector along the tetragonal axis ensure the almost constant magnetic field -temperature (B-T) phase boundary for askx for different thickness sample. Powder neutron diffraction study shows a collinear and a non-collinear spin ordering above and below (T_{SR}), respectively [95]. However, it is not clear the effect of thermal and exchange fluctuation in this system.

1.11.1.3 Compensated ferrimagnet: Mn_3In

Binary intermetallic compounds Mn_3Z ($\text{Z} = \text{Sn, Ge, Ga, Sb, Si, In}$) form in the different types of crystal structures and exhibit various exotic properties [88]. The Mn_3Sn , Mn_3Ge crystallizes in the hexagonal structure (DO_{19}) and shows a triangular AFM spin ordering [49, 50]. Mn_3Sb forms in the cubic (L1_2 -type) structure and exhibit weak ferromagnetism. Whereas, Mn_3Si forms in the cubic structure and shows a complex incommensurate AFM magnetic ordering. Among these families of binary compounds, Mn_3Ga draws great attention as it can be stabilized in both tetragonal [96] and hexagonal [97] form depending on the heat treatment. Also, Mn_3Ga can be prepared in thin film form [98] which shows PMA, an important characteristic of the magnetic device. Mn_3In form in the cubic structure with a large number of atoms within a unit cell [99, 100]. A ferrimagnetic state with a small net magnetic moment was predicted using a powder neutron diffraction study by Brown et al. [99]. Later on, Zhang et al. show a possible spin glass-like state in the low-temperature range for this compound [100]. The mixed occupancy between the magnetic (Mn) and non-magnetic (In) at different Wyckoff positions intrinsically introduces a disorder in the system. In such a system, a change in the electronic environment around the magnetic ions can cause a spatial imbalance of the magnetic interaction. This can lead to the formation of a small size magnetic cluster with frozen interface spin. Therefore this kind of system may be interesting in studying interface phenomena such as EB.

1.12 Conclusion

This chapter introduces the idea of topology in the context of magnetism. The concept of the Berry phase is a key pillar of understanding the various exotic phenomena associated with nontrivial magnetic states. The different fundamental magnetic interactions are also discussed, as they are the primary source of nontrivial magnetic ordering. Then, a discussion about ferrimagnetic materials and their consequences on magnetic compensation is given. Different type of complex magnetic states and their origin is highlighted. Among them, especially the focus is given to topological magnetic skyrmion/antiskyrmions. Also, the presence of a nontrivial interface spin structure is discussed regarding the exchange bias effect. In the end, a short review of the materials system under the study of this thesis is presented. The discussions in this chapter are relevant to the work contained in this thesis. The third chapter of the present thesis discusses about the tunable topological Hall effect in the non-collinear $\text{Mn}_{2-x}\text{PtIn}$ system. The fourth chapter is focused on the effect of non-collinear magnetic states on the stabilization of antiskyrmions. The fifth chapter discusses the role of the non-coplanar spin structure on the uncompensated interfacial spins in the exchange-coupled system.

Chapter 2

Experimental methodology

“Take risks in your life.

If you win, you can lead.

If you loose, you can guide.”

Swami Vivekananda

2.1 Introduction

In this chapter, a brief discussion on different experimental techniques that are being mainly used in the present thesis is presented. Most of the instruments are custom built; however, a basic understanding of the working principle of the different instruments are summarized here. In experimental condensed matter physics, the successful synthesis of desired materials is a crucial part. After that, systematic characterization experiments need to be done to ensure structural phase purity, quality of structural ordering, etc. Subsequently, thorough experiments are performed to probe and obtain various physical properties. For the sample synthesis, arc-melt technique is used to prepare bulk polycrystalline samples. For structural and phase purity identification, X-ray diffraction, Scanning Electron Microscopy (SEM) equipped with an Energy Dispersive X-ray spectroscopy (EDS) detector are

used. The magnetic structure is obtained using neutron diffraction experiments at different temperature ranges. The magnetic properties are measured using Vibrating Sample Magnetometer (VSM) in Quantum design SQUID magnetometer. The magneto-transport measurements are carried out using a Physical Properties Measurement System (PPMS, Quantum Design). The dual beam platform of SEM and focused ion beam (FIB) is used to prepare the electron transparent thin lamella for transmission electron microscope (TEM) study. Lorentz TEM is used to observe the real space image of the topological magnetic objects, skyrmions and antiskyrmions.

2.2 Arc melting furnace

All the samples studied in this thesis are prepared using an arc melt furnace as depicted in Fig. 2.1. The samples use in the present thesis consist of mainly selective combination of Mn, Pt, Pd, Ni, In, and Sn as the constituent elements. All individual metals show different melting temperature ranging from the room temperature to several thousand Kelvin. Therefore, for the preparation of a homogeneous sample of the constituent elements it is important to mix these elements above the melting temperature in an evacuated environment to protect from oxidation. Arc melting is a technique that generates a very high temperature by confined arc produced in between the electrode and metal surface as shown in Fig. 2.1. The complete system can be divided into three parts: power source, chiller, and vacuum unit. The power source delivers a high current through the tungsten electrode tip to generate an arc. Circulation of cold water from the chiller helps to cool down the electrode and the metal crucible. The arc melting chamber is purged with argon gas and evacuated several times using a rotary pump to avoid oxidation of the as melted compound. The chamber is again filled with argon gas so that melting is performed in an argon atmosphere. Finally, the produced arc melts the elemental metals, which solidify quickly into an ingot. The solidified ingots are melted 3-4 times by flipping them upside down to ensure better homogeneity of the samples.

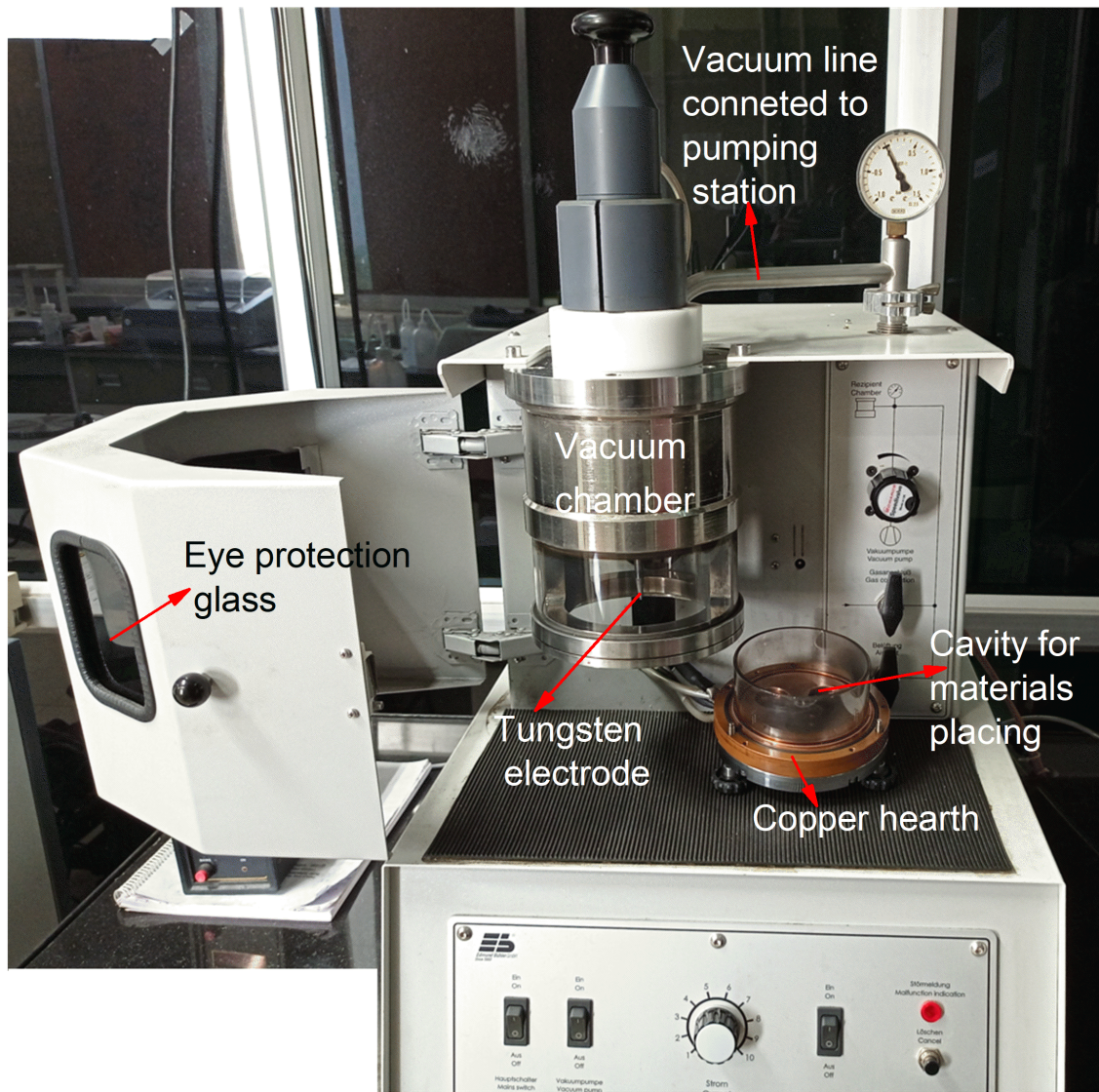


Figure 2.1: (Color online) Various parts of the Arc melting furnace. The copper hearth is the bottom part of the closed vacuum chamber.

2.3 X-Ray diffraction (XRD)

X-ray diffraction (XRD) is a widely used tool to characterize samples in almost all fields of experimental science. It is commonly used to identify the crystal structure, phase purity, and average quantification of the phase of the materials [101]. The basic principle of operation of XRD is the constructive interference of the diffracted X-ray from the parallel lattice plane of the crystalline materials and detection of

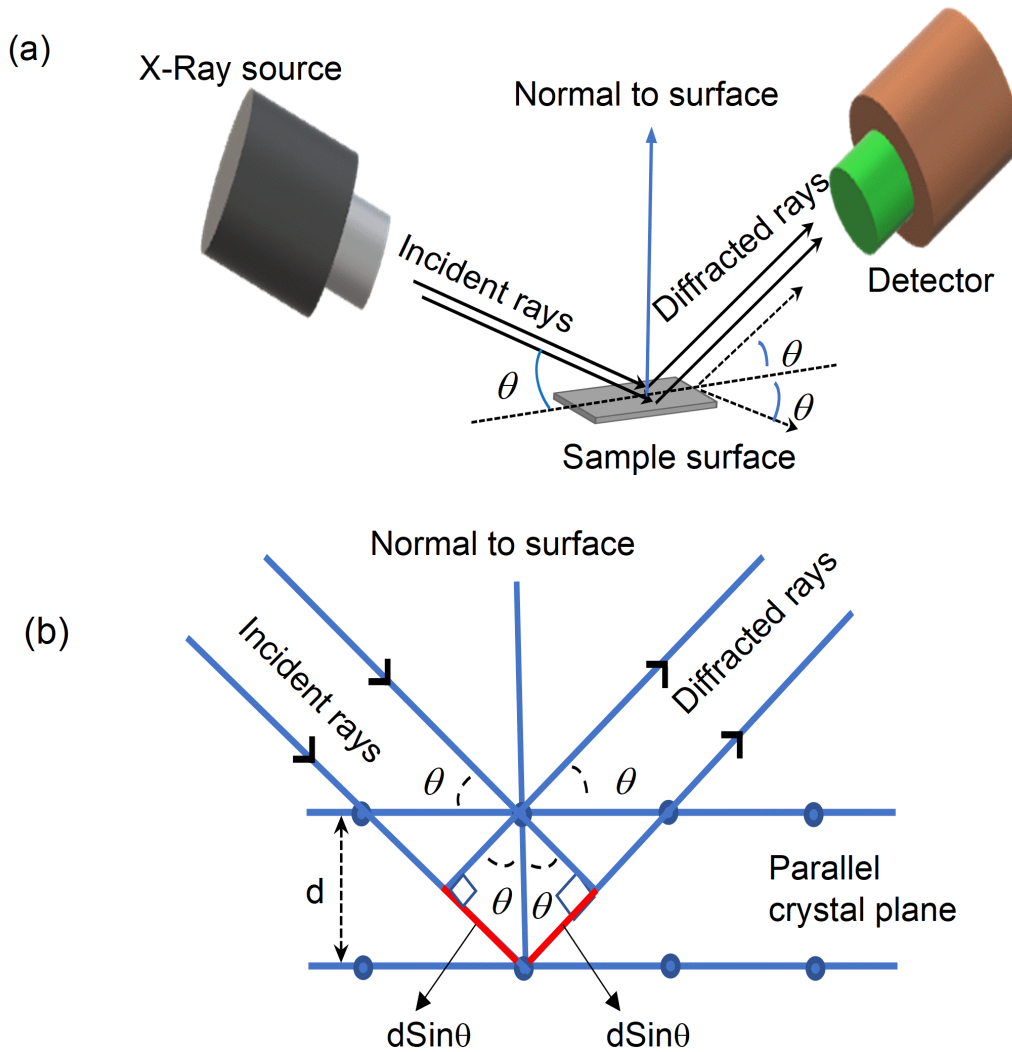


Figure 2.2: (Color online) (a) Schematic representation of X-ray diffraction measurement. (b) Ray diagram of Bragg law of diffraction. θ is the angle between the incident ray and the crystal plane. d is the separation between the two parallel crystal planes. The resultant path difference between the two rays is marked with red color.

the diffracted rays. The whole experimental system can be split into three parts: generation or source of X-ray, collimation directed to specimen, and detection of the diffracted rays from the sample. The X-rays are generated in a cathode ray tube where the electrons are produced by heating a filament. The emitted electrons are

then accelerated by applying high voltage and bombarded to a target material. The bombarded electron possesses enough energy to dislodge an inner core shell electron. Now, the electron sitting in the high-energy shell jumps to occupy the vacant position, and a photon of energy equal to the difference between the two energy levels of the atom is emitted as a characteristic X-ray. The wavelength of the generated X-ray depends on the energy level between which the transition of the electron happens and on the type of atom. Generally, Cu, Fe, Mo, and Cr are used as the target material. Typical wavelength of $\lambda = 1.54016 \text{ \AA}$ for Cu- K_α radiation. The radiation is then filtered to produce a monochromatic ray. Using an incident slit box, the angular divergence of the directed beam is controlled and exposed to the specimen. A simple schematic ray diagram of XRD measurement is shown in Fig. 2.2(a). The specimen can be a chunk of single crystal, powder of polycrystalline material, thin film, etc. For polycrystalline materials, a few tenths of milligram sample are crushed into a fine powder and spread over a few mm^2 areas on a glass slide with a smooth top surface. The incident rays are scattered from the materials and interfere to produce the diffraction pattern. The mechanism of X-ray diffraction from the atoms sitting on the parallel lattice plane of the crystalline material is shown in Fig. 2.2(b). The scattered rays from the atoms produce constructive interference when they satisfy Bragg's law $n\lambda = 2d \sin \theta$ [see Fig. 2.2(b)]. Here, d is the spacing between the parallel lattice plane, and θ is the glancing angle between the incident ray and the lattice plane, also known as the 'diffraction angle', and n is the order of diffraction. The diffracted rays are then detected using a detector. The detected signal is then processed and converted into counts per second and finally monitored using a software control display.

2.4 Scanning electron microscope (SEM) and focussed ion beam (FIB)- dual beam platform

Scanning electron microscopy (SEM) is an imaging technique that uses electrons as probe instead of photons or light as used in a conventional optical microscopes. With this instrument, an ultimate resolution of the order of 1 nm can be achieved as a result of fine-tuning the electron energy and aperture control. It is mainly used to study the surface topography of materials and detection of the phase distinction as color contrast due to the variation in average atomic number. An SEM equipped with an EDS detector can also quantify an average value of phase composition. The basic structure of a simple SEM can be describe in different parts- (1) electron column, (2) condenser lenses, (3) scanning coil lenses, (4) motorized stage, and (5) various detectors [see Fig. 2.3]. An electron column contains an electron emitter and a few electromagnetic lenses. Electric field-assisted thermally generated electrons from the electron gun are accelerated to attain final energy in the range of 0.2-40 KeV. A series of electrostatic condenser lenses control the beam divergence and spot diameter on the specimen. A side-wise deflection of the scanning beam is controlled by sending the current to the scanning coil placed below the condenser lens. An aperture selector is placed below the scanning coil to decide the width of the beam aperture. The focused/directed beam scans the specimen in a raster fashion to acquire an image. The sample placed on a motorized stage can be rotated and tilted, which enables to get a flavor of the 3-D surface topography of the specimen. The incident beam of electron interacts with the sample surface and generate various kind of signal depending on the type of interaction and depth at which the interaction takes place. Generally, the surface morphology of the specimen is obtained by detecting the secondary electrons (SE) generated due to the inelastic scattering. The elastically scattered electrons, called backscattered electrons (BSE), are used to distinguish the phase homogeneity of the materials. The phases with different average atomic numbers cause different energy to the BSE, which are then detected

in a BSE detector. The electrons with high energy can dislodge the inner shell electrons resulting in a characteristic X-ray, which is then detected by an energy dispersive X-ray energy detector (EDS) for the compositional analysis. Different detectors with specific purposes are being used once at a time to collect the signal and send it to monitor after electrical amplification. The electron gun works at very high vacuum of the order of 10^{-9} mbar, and the system vacuum is kept around 10^{-6} mbar. There are different kinds of SEM that can work under different conditions, such as ambient to cryogenic temperature as well.

A dual beam platform, i.e., electron and focused ion beam (FIB) column installed with other options like electron back scattered diffraction (EBSD), EDS, gas injection system (GIS), and micromanipulator, etc., possesses versatile applications in different branches of science. Such a multifunctional system provides multiple utility in an in-situ environment. The FIB also can be used for imaging purposes similar to the SEM image acquisition process. Usually, the FIB column is placed with some angle (54°) with respect to the SEM column [see Fig. 2.4]. So, the sample stage needs to be tilted at an angle of 54° , as at this position the FIB delivers maximum efficiency both in deposition and milling. At this condition, the image of the SEM and the FIB may not be the same. So, in order to make the particular specimen the same appearance in both FIB and SEM, one needs to bring the focal point of both FIB and SEM to the same point by using the fourth axis adjustment called M-correction. This method enables the simultaneous visualization of the process performed using FIB, such as deposition or sputtering, etc., in SEM. The FIB has multiple applications starting from mask-free lithography, deposition of elements, milling, micro and nano-fabrication, micro engineering, device fabrication, nanometer-thin lamella preparation for TEM use, etc. Here, it is used for the TEM lamella preparation from a polycrystalline bulk sample. First of all, the desired grain of requirement is fixed using an EBSD detector installed at 70° to the SEM column. This is a widely used technique to detect, quantify, and map the distribution of crystalline grains in the materials. The high-energy electron beam interacts with the materials to generate different types of signals. The electron,

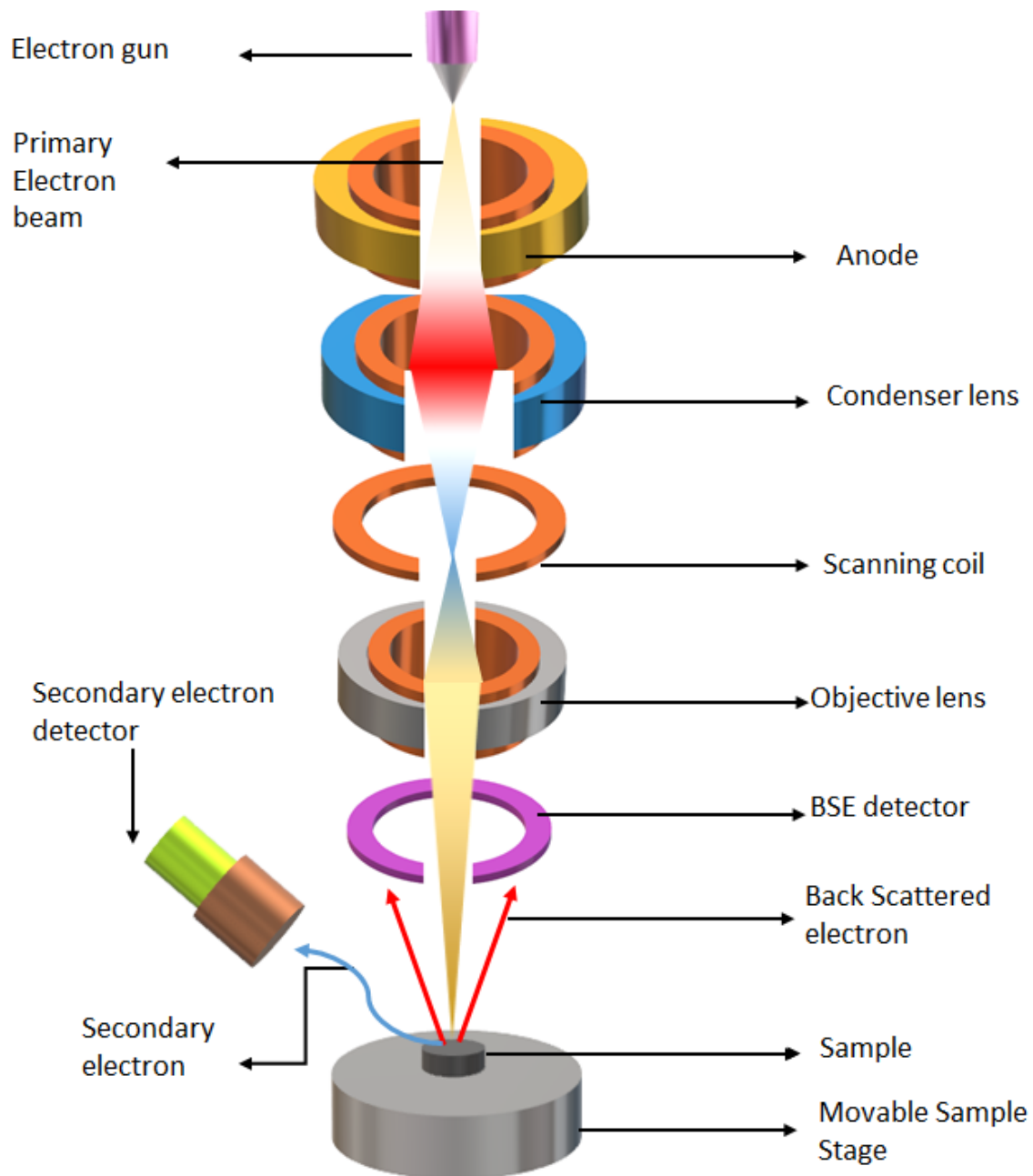


Figure 2.3: (Color online) A pictorial description of the different components of the Scanning Electron Microscope (SEM).

which is scattered from the atoms sitting on the lattice plane, forms a diffraction pattern and is detected upon falling on the phosphor screen of the detector. The detected optical signal is modulated and transferred to the computer display. The obtained Kikuchi band are matched with the Kikuchi band generated by simulation

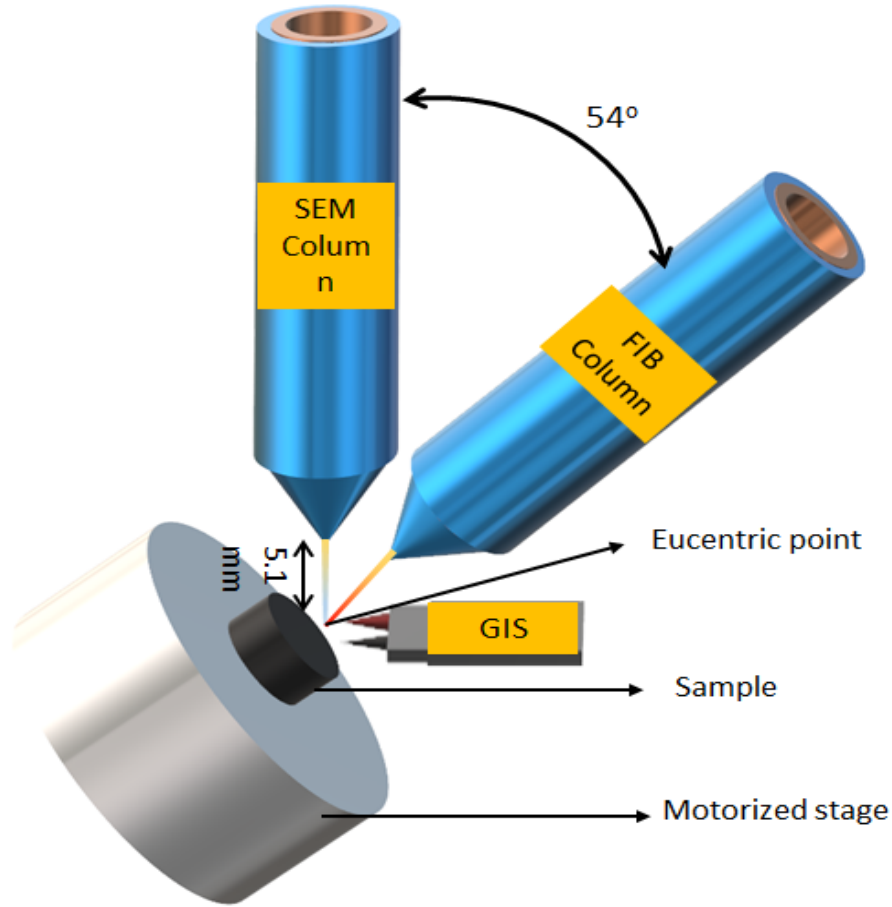


Figure 2.4: (Color online) The dual-beam platform of SEM and focus ion beam (FIB) column is equipped with a Gas Injection system (GIS). The FIB column is arranged at an angle of 54° with respect to the SEM column.

providing the prior information to the software. From there, the sample stage is slowly brought to 54° while keeping a close eye on the point of interest. After that, a $1\ \mu\text{m}$ thick, $1\text{--}1.5\ \mu\text{m}$ breadth, and $10\text{--}15\ \mu\text{m}$ long layer of Pt is deposited from the organic composite of elemental metallic precursor gas through a gas injection system. This is required to protect the site of interest from getting damaged. Then, a substantial area beside the deposited portion being trenched out using FIB milling. The high-energy incident beam of ions first sputter removes the surface materials by the process of milling. The sequence of the different stages is shown in Fig. 2.5(a)-(e). Then attached with the Omni probe TEM grid [Fig. 2.5(f) and (g)]. Afterwards, the lamella is being polished from sideways to thin down to transmissible

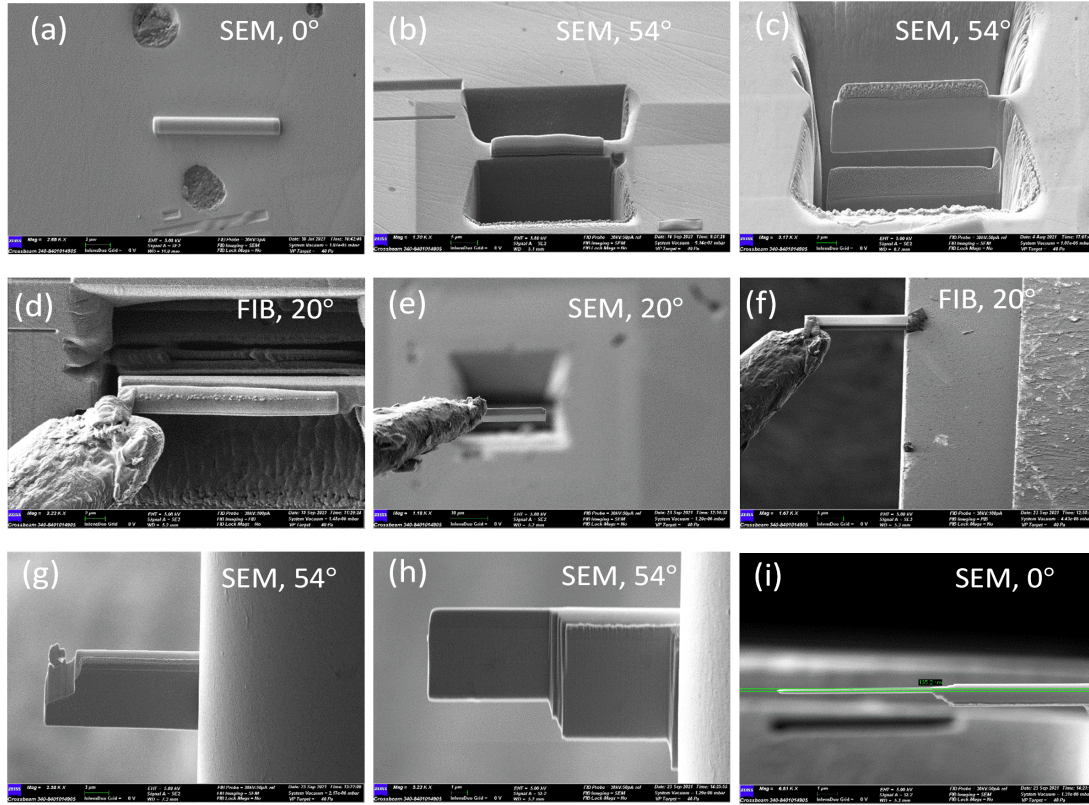


Figure 2.5: (Color online) Different steps of preparation of TEM lamella. (a) One micrometer width and a thick layer of PtC_x protection cap. (b) Trench out of the material from two sides of the capped portion. (c) One side of the thick lamella is attached to the bulk portion of the sample. (d) Joining of the micromanipulator with the floating lamella. (e) Detachment and lift off of the lamella by the manipulator. (f) Joining of one side of the lamella with TEM grid. (g) Detaching the manipulator after joining the lamella with the TEM grid. (h), (i) Side and top view of the thinned lamella taken with SEM. The images taken using SEM or FIB at a particular angle are mentioned in the respective images.

electron thickness [Fig. 2.5(h) and (i)]. The final polishing needs to be done at low current and low energy ion beam to remove any residual dust deposited during the subsequent previous milling. Figure 2.5(h) and (i) show the top and side views of the final lamella, respectively.

2.5 SQUID vibrating sample magnetometer (VSM)

Determination of magnetic properties of the requisite materials is crucial for fundamental study as well as practical applications. Since, several other properties of the magnetic materials also have a strong correlation with the magnetic characteristics, it is essential to understand the temperature and field-dependent response of the magnetic moment. Super Conducting Quantum Interference Device (SQUID) based vibrating sample magnetometer (VSM) have been widely used for quantifying the magnetization of the system. It is one of the most sensitive instruments for measuring the magnetic moment of material to indirectly detects the magnetic field generated from the sample. When a magnetic sample moves through the superconducting coils, it induces a current in the circuit due to the change in the magnetic flux. The induced current is fed to the input coil of the SQUID. Any small amount of change in the induced current in the input coil causes a change in the flux through the SQUID loop. This, in turn, generates a voltage that is linearly proportional to the change in the current. Therefore, the magnetic moment of the sample is measured by measuring the voltage and calibrating it with the known magnetic moment system. A pictorial description of a SQUID VSM is shown in Fig. 2.6. A superconducting magnet, i.e., a solenoid wound with superconducting wire is used to generate a magnetic field (in the range of ± 7 T, ± 15 T etc.) by passing an appropriate amount of current. The variation or desired magnetic field can be attained by sending the required current to the superconducting solenoid. A high level of noise arises in the SQUID detection system due to the fluctuation in the current provided by the power supply. To avoid this, the SQUID detection system is placed underneath the sample space with proper magnetic shielding. Also, the second order gradiometric configuration [as shown in Fig. 2.6, a single wire with top and the bottom coil is one turn wound counter-clockwise and the middle coil is two turn wound clockwise] of the detection coil improves the signal-to-noise ratio.

For the temperature variation in the range of 2 to 400 K, a controlled flow of cold Helium gas is maintained and a heater is placed suitably in the system. DC magnetization curves $M(H)$ and/or $M(T)$ are taken by measuring the voltage generated in this inductive method. A constant magnetic field is applied to magnetize the sample, and the movement of the sample through the set of pickup coils results in the measured voltage. In ac magnetic measurement, an ac field is superimposed on a dc magnetic field. Application of the ac field causes a time-dependent moment in the system without altering the sample position. In this scenario, a magnetic field produced from the time-dependent moment of the sample induces a current in the pickup coils. Magnetic susceptibility is the quantity of interest in ac magnetic measurement.

2.6 Hall effect measurement

In 1879 Edwin H. Hall discovered the historic ‘electricity pressing’ effect towards one side of the conductor placed in the external magnetic field, now famously known as the ‘Hall effect’ [102]. The Hall effect used to call as the queen of solid state transport experiments in the middle of the 19th century due to its important role in developing semiconductor physics and solid state electronics. At present, the Hall effect experiment provides a simple and elegant tool to explore various intriguing properties and characterize the magnetic materials. In Hall effect experiment, a constant current is sent through the material placed in a constant magnetic field ($\mathbf{B}=\mu_0\mathbf{H}$), which is perpendicular to the current direction, and the transverse voltage is measured, i.e., the voltage in the direction perpendicular to both the current and magnetic field. The schematic diagram given in Fig. 2.7 describes a simple Hall effect measurement configuration. The applied current is in the x direction (I_x), magnetic field in z , and the Hall voltage (V_y) is measured across y direction. The electrons moving with velocity v in x direction experience a force along positive y direction due to Lorentz force [$F_L = -e(\mathbf{v} \times \mathbf{B})$]. In steady-state conditions, i.e., when there is no further electron flow in the y direction, an electric field appears due to

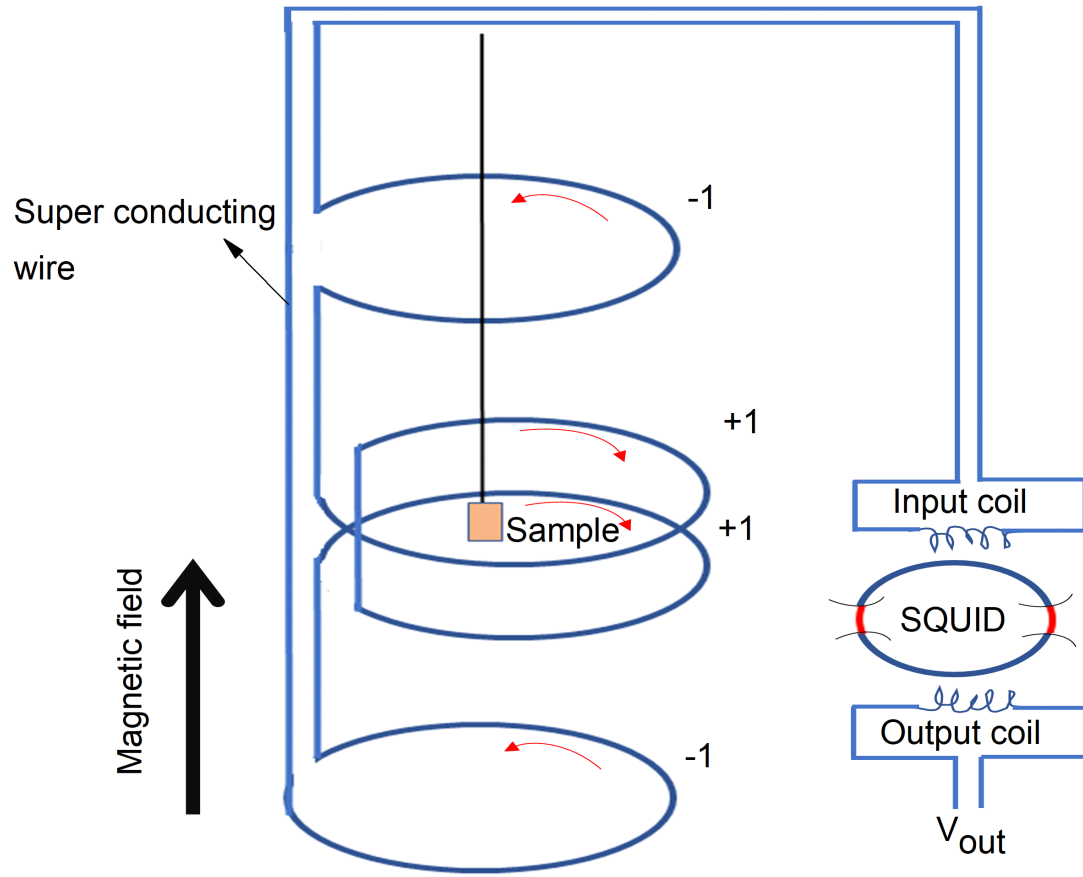


Figure 2.6: (Color online) (a) Arrangement of second-order gradiometer superconducting coils. The sample space is within the gradiometer coil, and the whole system is placed within the liquid Helium bath.

the charge accumulation in this direction. As a result, a potential will develop in the y direction, known as Hall voltage. The Hall resistance is given by $R_{yx} = V_y/I_x$. The longitudinal resistance is defined as $R_{xx} = V_x/I_x$. Now, it should be noted that the material's resistance is a tensor quantity whose diagonal and off-diagonal elements are resistance measured along and perpendicular to the current direction, respectively.

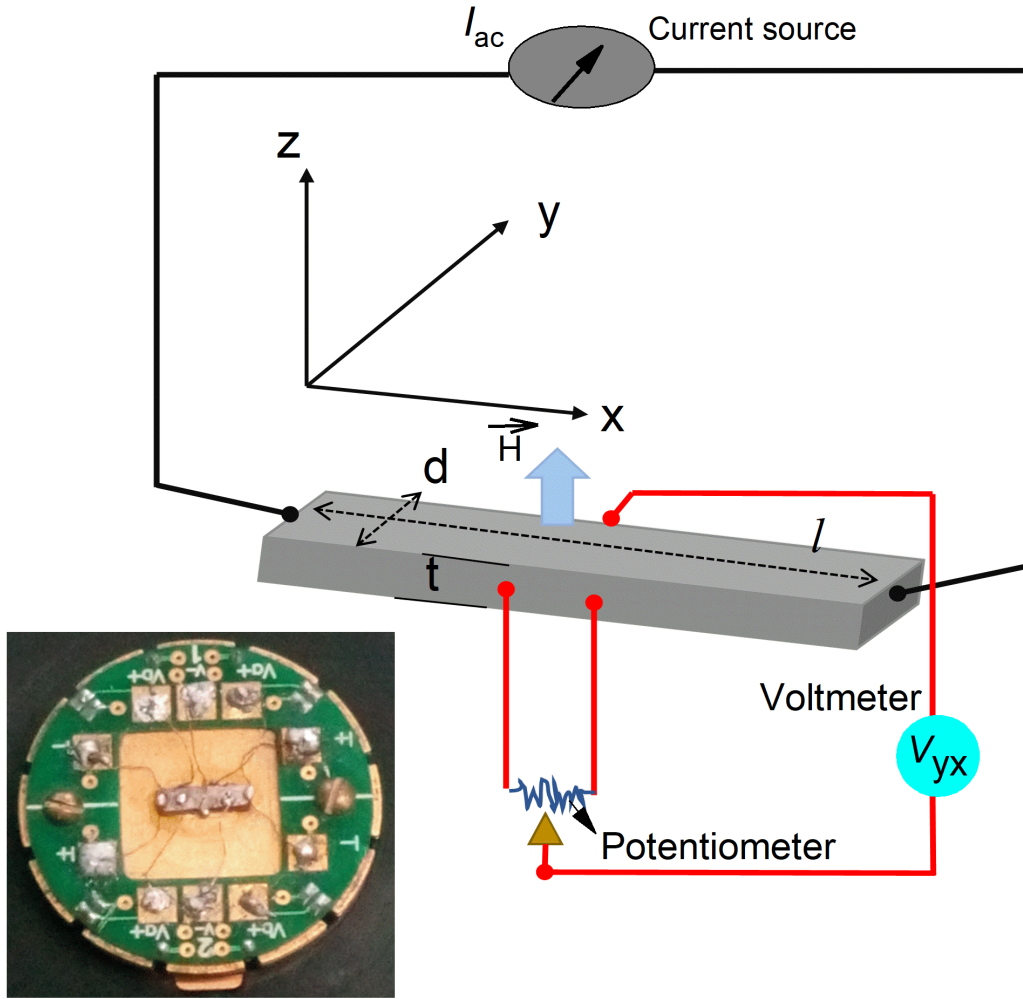


Figure 2.7: (Color online) Circuit diagram for the five probe Hall effect measurement on a rectangular sample. A potentiometer is used to nullify the offset voltage due to misalignment of the voltage lead. The lower inset shows the circuit fabrication of such rectangular Hall bar on a ACT puck.

2.7 Lorentz transmission electron microscope (LTEM)

A transmission electron microscope (TEM) provides a broad range of characterization techniques for materials from atomic limit (~ 1 nm) to the micrometer scale. Specially designed sample holder and maintaining the actual features of the specimen along with high spatial and analytical resolution makes it a versatile tool in

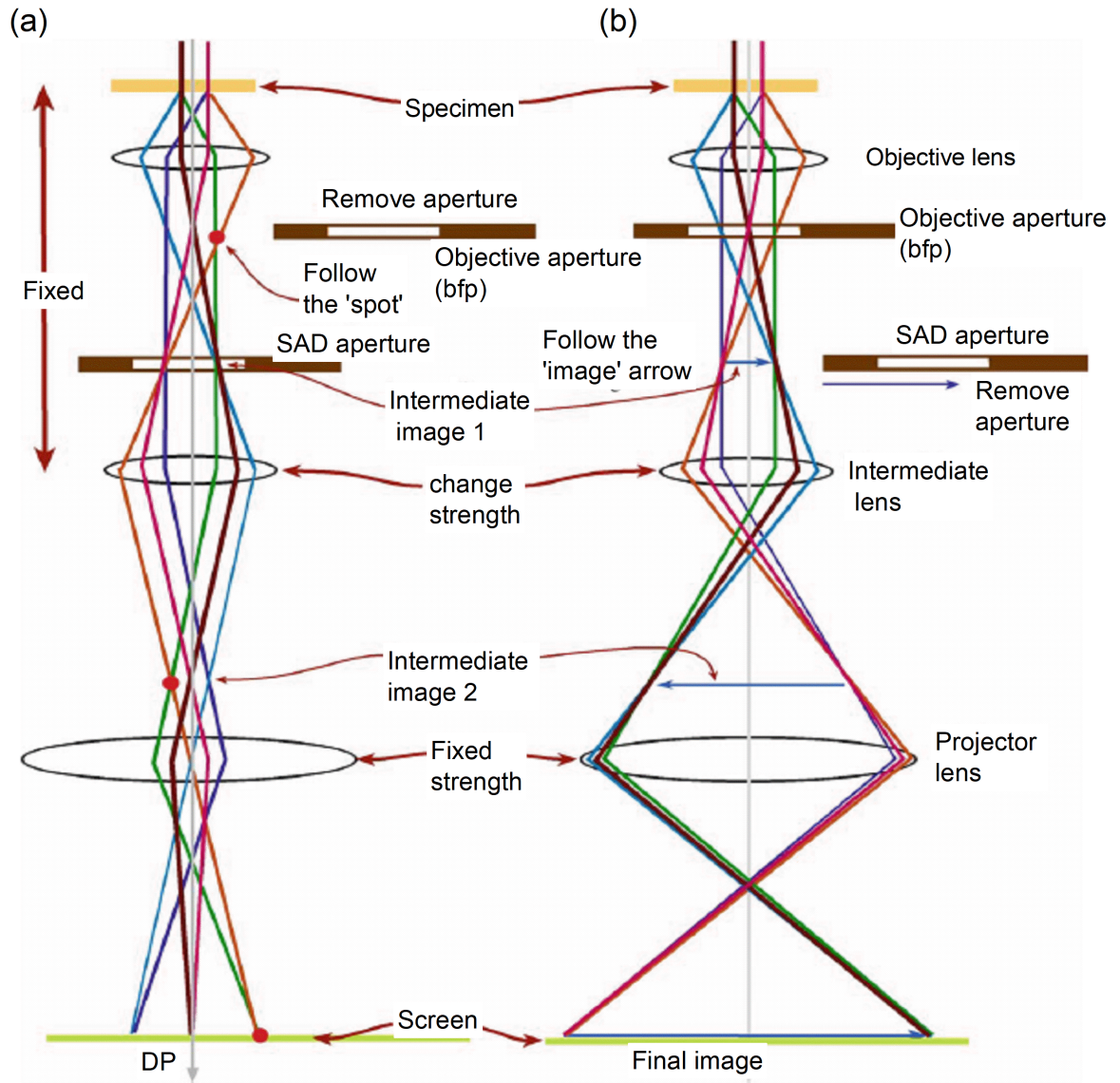


Figure 2.8: (Color online) Two basic modes of operation of a TEM (a) Diffraction mode, and (b) Image mode. In case of diffraction pattern (DP) and image mode the objective aperture at the back focal plane (BFP) is removed and inserted, respectively. Selected area diffraction (SAD) aperture is inserted for DP mode only. This is simplified ray diagram of DP and image formation. Real TEM may contains more number of intermediate lenses for greater flexibility of focusing and magnification purpose for DP and image formation. Image taken from ref-[103].

various branches of science. Thanks to the electrons for their dual properties (wave and particle) and different modes of interaction with the materials, which generate

required signals enabling us to capture images. Therefore, the basic structure of the TEM can be divided into - generation of the electrons, control of the generated electrons, specimen area, detection of the generated and transmitted signal, processing and visualization/quantifying of the detected signal. Based on different criteria, such as better resolution, and aberration-free image, there are two types of electrons source mainly employed, namely thermionic and field emission (FE) electron sources. FE source produces electron beam which has better spatial coherence, the smallest energy spread of the beam therefore mainly employed to high resolution TEM (HRTEM), Lorentz microscopy, analytical electron microscopy, electron energy loss spectroscopy, etc. A field emission electron gun emits an almost monochromatic electron beam. The emitted electrons then are accelerated to very high energy on passing through the predetermined voltage gradient region. The accelerated beam passes through a pair of condenser lenses and optional upper objective lenses, which control the beam to be parallel or convergent to illuminate the specimen. The TEM employs electromagnetic lenses, where, by controlling the current the magnetic field can be manipulated and hence the control over the electron trajectories, focus position, convergence of the beam, etc can be achieved. Also, TEMs are furnished with a scanning coil that can tilt and side-wise translate the electron beam to better impinge the specimen. On transmitted through the specimen, the electrons interact with it and scatter in different ways like elastic, in-elastic, diffuse scattered, etc. Finally, the electrons emerging from the final surface of the specimen carry full of information guided by the objective lens situated just below the specimen to form a diffraction pattern (DP) at the back focal plane (BFP) or image at the image plane. Two basic operation modes of the TEM can be handled upon selection of different apertures equipped with the lower objective lens and the projector lens. At last, the images or the diffraction pattern form in the BFP or image plane of the objective lens are guided and projected to the respective detector for visualization. It is noteworthy to mention that our eyes cannot observe the direct electron. Therefore we need to convert the information carried by the beam of electron which incident on the detector and produces the signal in the visible range. This resultant signal

basically mimics the spatial distribution of intensity of the electron upon passing through the specimen. Most of the recent TEM instruments are fabricated with either semiconductor or charge-coupled device (CCD) detectors. The detected signal is then processed and sent to the viewing screen of the computer display, which can be summarized/analyzed further.

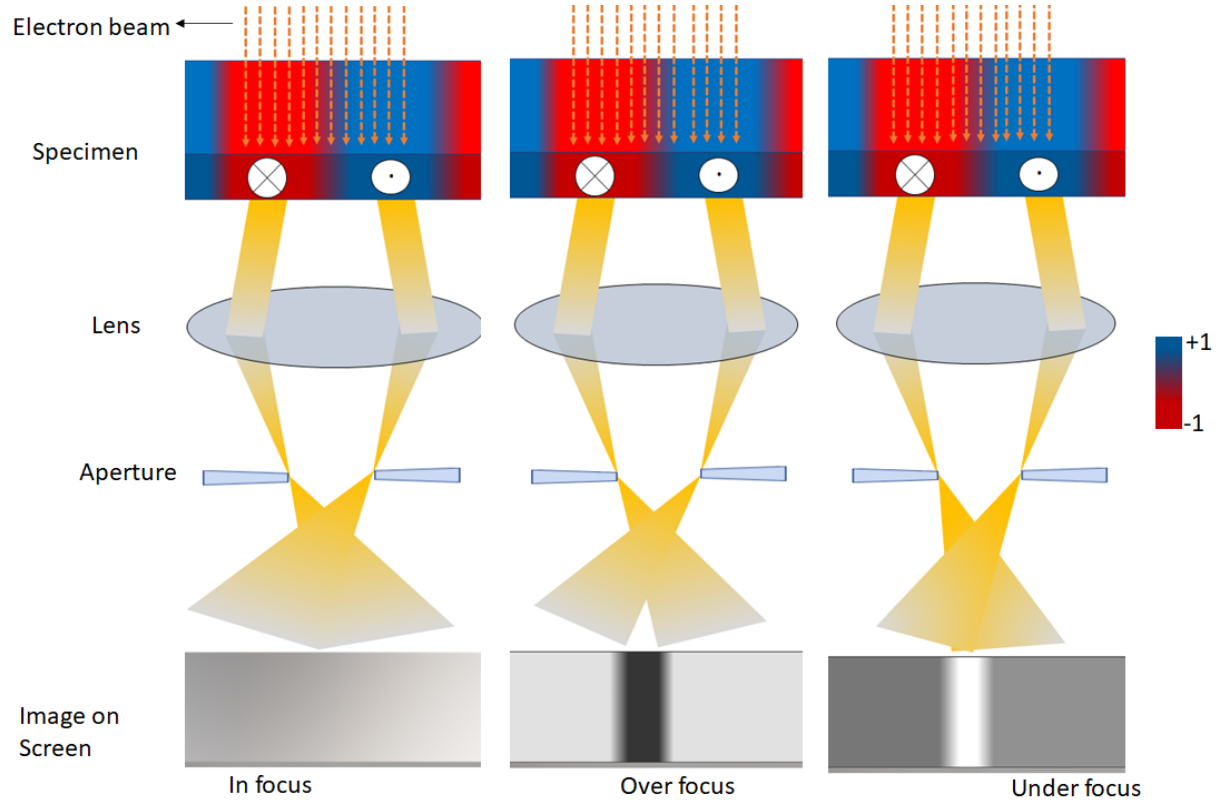


Figure 2.9: (Color online) Schematic ray diagram of electron through the magnetic sample in Fresnel mode of Lorentz TEM. The domain wall contrast appears as a dark and bright line in over and under focused condition, respectively. \otimes and \odot represent the magnetization direction into and out of the plane of the page, respectively. The color bar represents two oppositely magnetization directions (blue and red).

The above-mentioned DP and image formation is shown with a very simple ray diagram in Fig. 2.8(a) and (b), respectively. As it can be seen, this ray path description is for the emerging ray from the specimen to the detector component. This region, i.e., sample space and objective lens together called the heart of the TEM. The upper diagram is not shown here as it is similar to that of SEM discussed earlier, which constitutes the anode, condenser lens, scanning coil, etc. [see Fig.

2.3]. The actual instrument is much more complicated and may furnish with more number of lens at various parts of the lens system for a special purpose. As a part of the magnetic imaging technique, a brief discussion is given for the Lorentz Transmission Electron Microscopy (LTEM). The mode of operation of the LTEM is similar to that of conventional TEM with a specially designed objective lens and sample area. The main idea is to map the information carried out by the electrons due to the interaction with the magnetic field of the sample. This is a kind of phase contrast imaging, which is available in two different modes: Foucault and Fresnel modes. In Foucault mode, one can image the domain, whereas, in the Fresnel mode, one can image the domain wall. Figure 2.9 describes the image formation of the magnetic domain wall. The electrons coming from different domains get deflected in a different directions according to the Lorentz force that they experience in the sample. When the electrons converges, it appears as bright spot, whereas and divergence of electrons gives a dark spot. Therefore, the domain wall region appears as dark and bright contrast depending on the defocus condition. The dark (bright) region becomes bright (dark) in under and over-focused conditions or vice versa. It is worth quoting the text from ref-[103]- ‘Fresnel imaging is named for another famous Frenchman whose TEM images would never be in focus’. However, one should maintain a high level of caution while performing magnetic imaging with the magnetic sample. Especially the loss of the magnetic sample due to the application of the magnetic field in the objective lens, which can stick to the objective pole pieces. As a result, it can tremendously hinder aberration and astigmatism correction and even can cause more expensive damage to the instrument.

2.8 Neutron diffraction (ND)

Neutron scattering experiment has been widely used to address the various phenomena in condensed matter physics. Being uncharged and having a small magnetic moment, neutrons are found to be a valuable probe to determine the magnetic structure and dynamics of the magnetic materials. They have the ability to provide

direct information at the microscopic level, such as magnetic ordering and moments associated with the constituent atoms in the specimen [104]. Nonetheless, depending on the energy of neutrons, a wide range of de Broglie wavelengths is associated with them. Mainly the thermal neutrons have wavelengths of the order of atomic spacings in crystals, thus enabling to carry out diffraction experiments. Neutrons scatter from the nucleus due to the strong nuclear force, as well as by the magnetic field within the crystal via electromagnetic interaction as they carry a magnetic moment. The latter interaction makes the neutron a useful tool to probe the magnetic properties of materials. Here we first discuss nuclear scattering and then extend our discussion in terms of magnetic scattering. In a neutron scattering event, the short-range repulsive nuclear force of atoms acts as a scattering center. And the range of the nuclear force, which is of the order of $10^{-14} - 10^{-15}$ m, is much smaller than the wavelength of the thermal neutrons. Hence it justifies to assume the incident neutrons beam as a plane wave $\Psi_i = e^{i\mathbf{K}\cdot\mathbf{r}}$ and the scattered wave function can be taken in the form of a spherically symmetric wave function $\Psi_f = e^{i\mathbf{K}'\cdot\mathbf{r}} - \frac{b}{r} e^{i\mathbf{K}'\cdot\mathbf{r}}$. Here b is the scattering length, its value depends on the nucleus and the spin state of the nucleus-neutron system (which can be $I + 1/2$ or $I - 1/2$ for a nucleus of spin I). The incoming and outgoing wave vectors are denoted by \mathbf{K} and \mathbf{K}' , respectively. The scattering amplitude does not vary in a particular manner with the atomic number (Z); in fact it can be positive and negative because the nuclear scattering of the neutron arises from the interaction with the nucleus rather than the electron cloud (as neutron is charge less) of the atom. This makes the neutron advantageous over the X-ray in the sense that it can easily detect light atoms in an environment of heavier atoms and even distinguishes the isotope.

The scattered neutrons from a periodic system can produce the Bragg reflection when the scattering vector is equal to a reciprocal lattice vector. Figure 2.10(a) depicts the scattering of the neutron from a set of the parallel planes. For an incoming (\mathbf{K}) and outgoing \mathbf{K}' wave vector the scattering vector is defined as $\mathbf{Q} = \mathbf{K} - \mathbf{K}'$ [Fig. 2.10(b)]. As it carries the momentum, the interaction with electron's magnetic moment also leads to the scattering of the neutron. In a similar way,

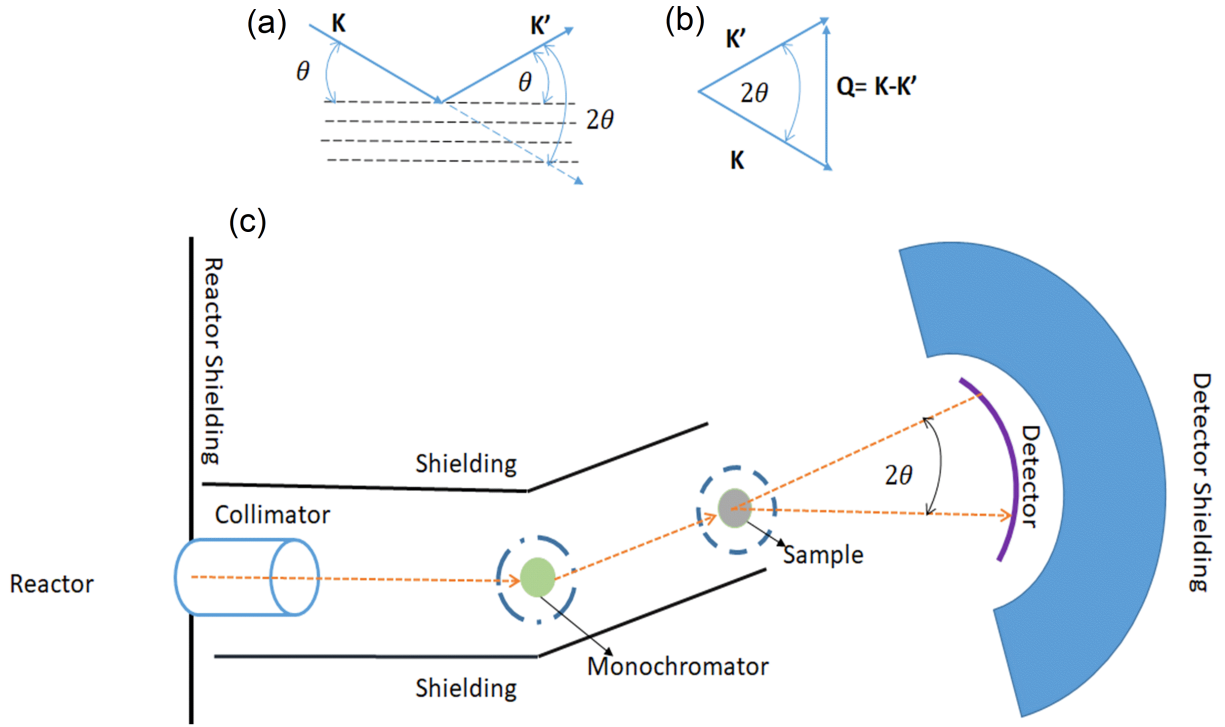


Figure 2.10: (Color online) (a) Incident neutrons with wave vector \mathbf{K} gets scattered by the crystal planes and propagate with wave vector \mathbf{K}' through a scattering angle of 2θ . (b) For elastic scattering; the scattering vector is defined as $\mathbf{Q} = \mathbf{K} - \mathbf{K}'$. (c) A schematic picture of the neutron diffraction experimental set up.

the magnetic scattering event also produces the Bragg reflections. The magnetic scattering amplitude ($\mathbf{a}(\mathbf{Q})$) is a vector quantity given by-

$$\mathbf{a}(\mathbf{Q}) = pf(Q)\mathbf{m}_{\perp} \quad (2.1)$$

$$= \frac{1}{2}r_e\gamma f(Q)(\mathbf{m} - \frac{\mathbf{m}(\mathbf{m} \cdot \mathbf{Q})}{Q^2}) \quad (2.2)$$

$$= \frac{1}{2Q^2}r_e\gamma f(Q)(\mathbf{Q} \times \mathbf{m} \times \mathbf{Q}). \quad (2.3)$$

where, $p = r_e \gamma / 2$ is the conversion factor for Bohr magnetons to scattering length in units of 10^{-12} cm. Other constants like, r_e is classical radius of electron, γ ($=1.9132 \mu_N$) is the neutron moment. Function $f(Q)$ is the atomic magnetic form-factor,

which, basically a Fourier transformation of the unpaired electron charge density. \mathbf{m}_\perp is the component of the atomic moment perpendicular to the scattering vector \mathbf{Q} . This tells that, only the perpendicular component of moment (\mathbf{m}) contributes to the magnetic scattering amplitude. Also, it gives an idea about the magnetic moment direction with respect to the crystal lattice.

For a given magnetic Bragg peak, the only contribution comes from the magnetization component perpendicular to the scattering vector. Depending on the magnetic ordering, some satellite peaks may also occur along with the nuclear Bragg peaks. When the nuclear and magnetic unit cell is the same, the magnetic Bragg peaks appear on top of the nuclear Bragg peaks. In such cases, the total intensity is the sum of the intensity arising from nuclear and magnetic scattering. So, there will be a gain in intensity in some of the peaks.

Chapter 3

Tunable topological Hall effect in inverse tetragonal Mn-Pt-In ferrimagnetic system

“There is no treasure equal to
contentment and no virtue equal
to fortitude.”

Maa Sarada Devi

3.1 Introduction

Over the last two decades, the non-collinear magnets have attracted a shift of focus on research involving next-generation spintronic devices. The easiness associated with controlling/switching the magnetic state of non-collinear magnets over the collinear ones is one of the important parameter going forward. For example, the topologically stable magnetic skyrmions, which are nanometric size localized non-collinear magnetic objects, can be moved at significantly low current densities [2, 3, 6, 105]. Therefore, the information stored in the skyrmion-based logic/spintronic

devices can be efficiently manipulated with less consumption of power. In most of the cases, a basic ingredient for the stabilization of these non-collinear magnetic states is the presence of chiral magnetic interaction, the Dzyaloshinskii-Moriya interaction (DMI), that arises from the broken inversion symmetry in certain classes of chiral magnets [9, 57, 58, 106, 107] and layered thin films [13, 108, 109]. The presence of such non-trivial topological configurations gives rise to a large topological Hall effect (THE) [10, 11, 13, 14, 15]. The basis of the THE is related to a non-zero scalar spin chirality (SSC) $\chi_{ijk} = \mathbf{S}_i \cdot (\mathbf{S}_j \times \mathbf{S}_k)$, that corresponds to the solid angle Ω subtended by three non-coplanar spins \mathbf{S}_i , \mathbf{S}_j and \mathbf{S}_k on a unit sphere. Although measurement of THE has been extensively used to characterize topological magnetic objects, the manipulation of THE for its direct use in spintronics is never demonstrated. Therefore, the systems exhibit a non-vanishing scalar spin chirality, which can appear in magnetic materials with non-collinear and/or non-coplanar spin structures, ideal for the realization of THE [16, 17, 19]. However, the absence of chiral magnetic symmetry can lead to a net vanishing THE in most of the systems. There are only limited examples of nonzero SSC induced THE [16, 34, 35]. Such systems hold a special type of lattice structures, e.g., pyrochlore, triangular lattices, etc., with distinctive types of spin configurations. Recent observation of THE by Wang et al. in a perpendicularly magnetized system with interfacial DMI indicates the importance of chiral magnetic interaction to achieve a nonzero THE [18]. Only limited experimental findings are reported in recent literature. In this direction, Mn-based inverse tetragonal Heusler materials can be a suitable candidate to realize the goal. Magnetic properties of Heusler materials such as, magnetization, magnetic anisotropy and Curie temperature (T_C) can be tuned by suitably engineering the chemical composition. In addition, the tetragonal $\text{Mn}_2 \text{YZ}$ compounds (where $Y = \text{Pt, Rh, Ir and Ni}$) crystallizing in the non-centrosymmetric space group $\bar{I}4m2$ are plausible candidates to host DMI in the system [48, 57, 93, 110]. To achieve the goal, i.e., the tuning of THE, an inverse tetragonal Heusler compound Mn_2PtIn is selected as a starting compound. It consists of two magnetic sublattices of Mn atoms. A systematic changing of Mn concentration leads to the degree of non-collinearity

of the magnetic moments in the system. The direct consequence of the different degrees of non-collinearity is reflected through THE.

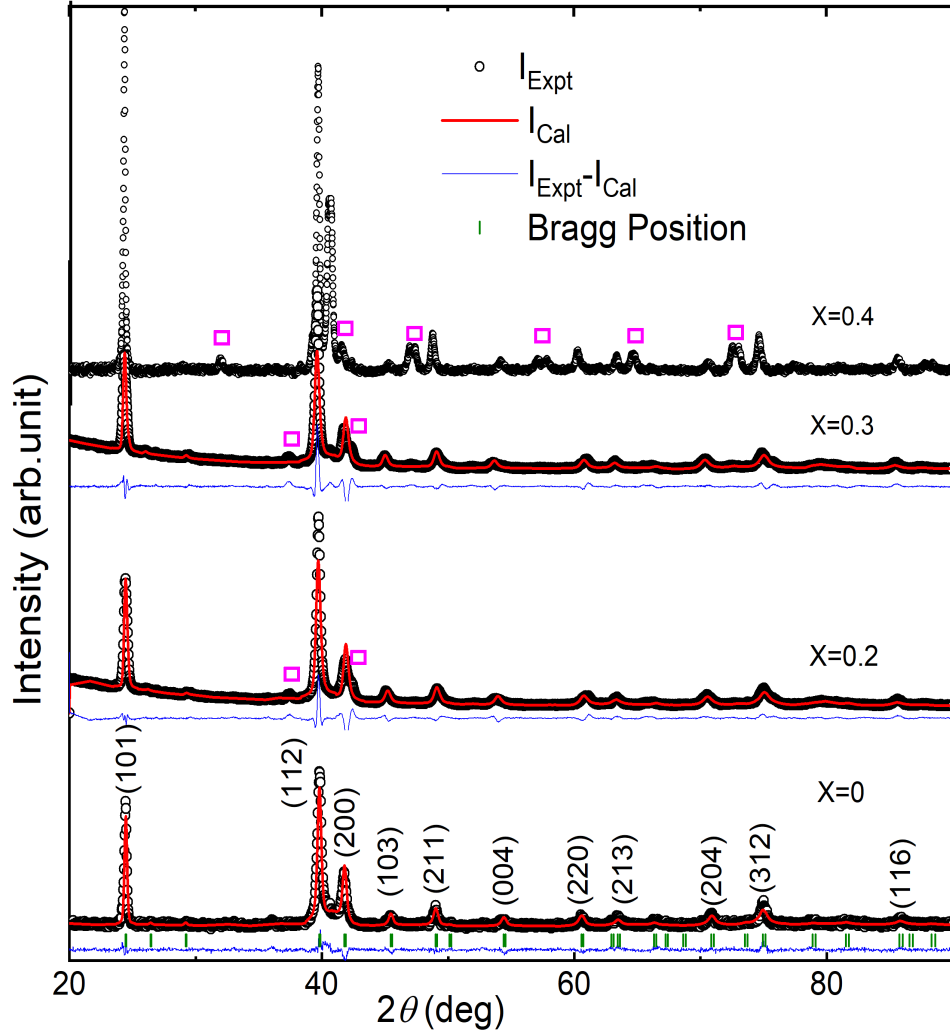


Figure 3.1: (Color online) Powder XRD patterns for $\text{Mn}_{2-x}\text{PtIn}$ for $x = 0.0$ to 0.4 taken at room temperature. The open black circles in the figure represent the experimental data, and the red color solid lines are the simulated data. The solid blue line shows the difference between the experimental and simulated lines. The $(h\ k\ l)$ value for all major reflections is shown for $x = 0$ by vertical dark green lines. The magenta square boxes in the top three panels represent the extra Bragg peak outside $I\bar{4}m2$.

3.2 Sample preparation

Polycrystalline ingots of $\text{Mn}_{2-x}\text{PtIn}$ with $x= 0.0$ to 1.0 were prepared by arc melting the stoichiometric amounts of constituent elements in a high-purity argon atmosphere. For better homogeneity, the samples were melted multiple times by flipping them upside down. The ingots were sealed in an evacuated quartz tube and subsequently annealed at 1023 K for seven days, followed by quenching in the ice-water mixture.

3.3 Characterisation

3.3.1 Structural analysis (XRD)

Room temperature powder XRD patterns with their corresponding Rietveld refinement for $\text{Mn}_{2-x}\text{PtIn}$ with $x= 0.0$ to 1.0 are presented in Fig. 3.1 and Fig. 3.2. The parent compound Mn_2PtIn crystallizes in the inverse Heusler tetragonal structure which belongs to the space group (SG) $\bar{I}4m2$. The corresponding crystal structure of Mn_2PtIn and $\text{Mn}_{1.5}\text{PtIn}$ are shown in the Fig. 3.3(a) and (b), respectively. In Mn_2PtIn , the Mn atoms sits at the Wyckoff positions 2b $(0, 0, 0.5)$, and 2d $(0, 0.5, 0.75)$, whereas, In and Pt atoms occupy the 2a $(0, 0, 0)$ and 2c $(0, 0.5, 0.25)$, respectively [see Fig. 3.3(a)]. Samples with the composition ranges $x=0.5$ to 1.0 also crystallize in the tetragonal structure and belong to the space group $\bar{I}4_2m$ (SG No. 121). Within this structure the Mn atoms occupy four different Wyckoff positions, i.e. Mn_I at 2a $(0, 0, 0)$, Mn_{II} at 2b $(0, 0, 0.5)$, Mn_{III} at 4d $(0, 0.5, 0.25)$ and Mn_{IV} at 8i (x, x, z) [see Fig. 3.3(b)]. Pt atoms occupy two Wyckoff sites 4c $(0, 0.5, 0)$ and 4e $(0, 0, 0.26473)$, whereas, In sits at the 8i (x', x', z') [see Fig. 3.3(b)]. Samples with composition $x=0.2$ to 0.4 show a structurally mixed phase due to the composition-dependent structural transition from SG $\bar{I}4m2$ to $\bar{I}4_2m$. Here it can be mentioned that a small fraction of the MnPt phase (CuAu- I type tetragonal structure) is observed for $x = 0.9$ and 1.0 samples [111]. The MnPt phase fractions were

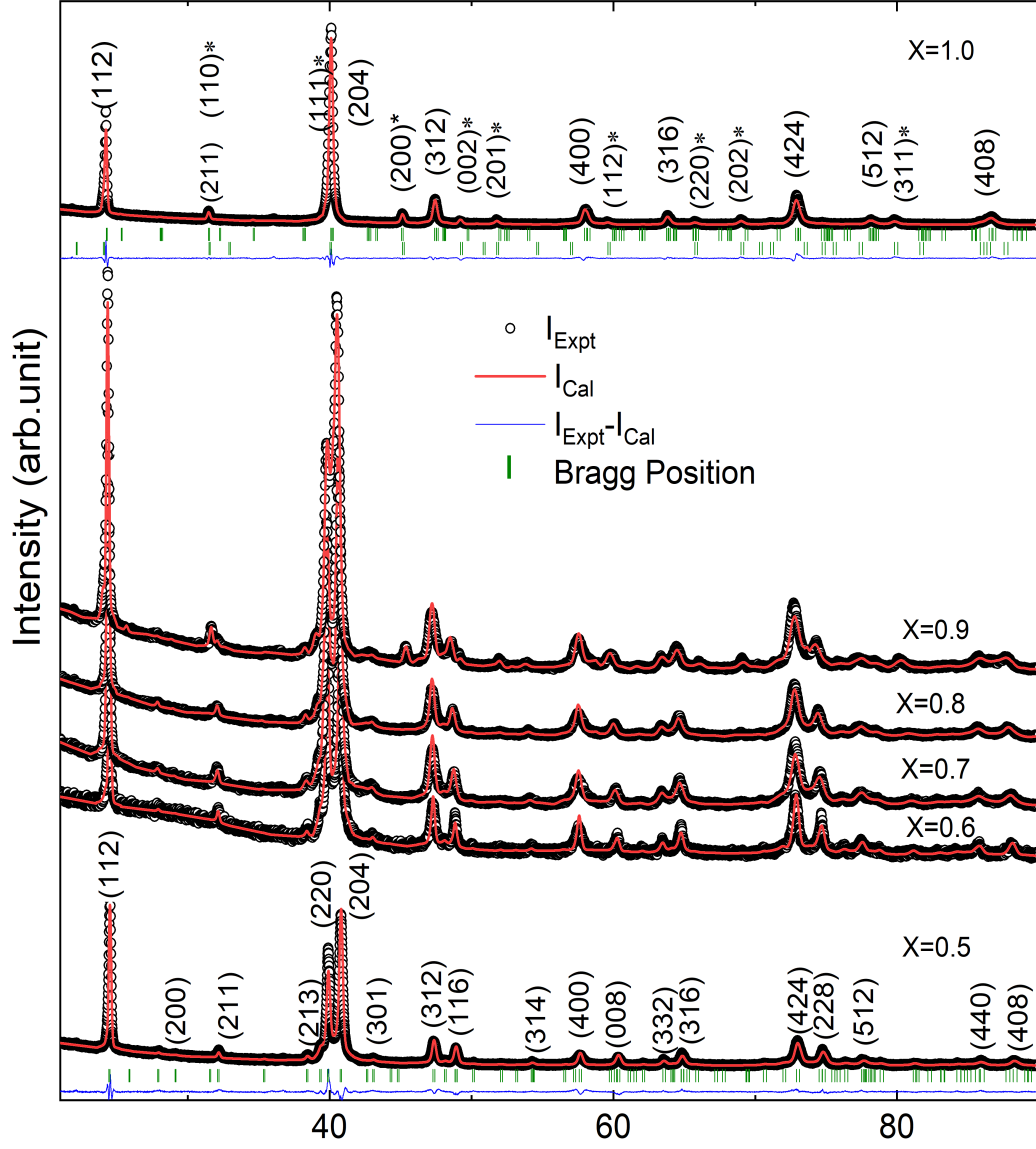


Figure 3.2: (Color online) Room temperature powder XRD patterns for $\text{Mn}_{2-x}\text{PtIn}$ for $x = 0.5$ to 1.0 . The open black circles represent the experimental data, and the red solid lines are the simulated data. The solid blue line shows the difference between the experimental and simulated lines. The $(h\ k\ l)$ values for all major reflections are shown only for $x=0.5$ and 1.0 . The * marked $(h\ k\ l)$ indexes for $x = 1.0$ belongs to the MnPt secondary phase.

estimated to be approximately 13% and 16% in the case of $\text{Mn}_{1.1}\text{PtIn}$ and MnPtIn , respectively.

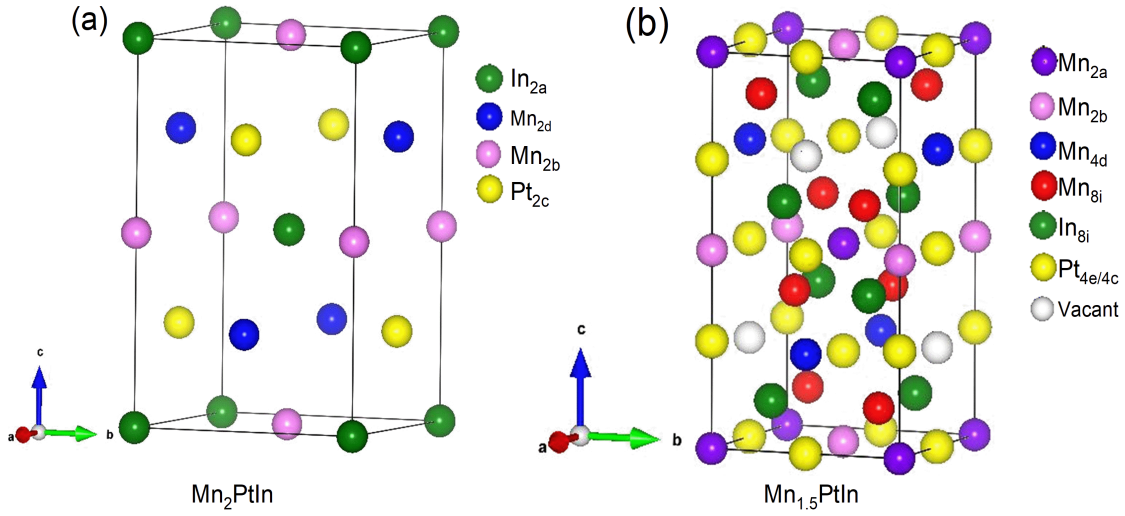


Figure 3.3: (Color online) (a) Crystal structure of Mn_2PtIn belongs to $\bar{I}4m2$ space group. (b) Crystal structure of $\text{Mn}_{1.5}\text{PtIn}$ belongs to $\bar{I}42m$ space group. The distinctive atoms occupy the different Wyckoff positions are mentioned and represented by different color balls in each figure.

3.3.2 SEM and EDS study

The presence of the multiple phases can be distinguished in the SEM images with different color contrast, such as dark and bright regions. The compositional homogeneity in the present samples was determined with the help of scanning electron microscopy (SEM). The SEM images for three samples that are mostly used for topological Hall effect measurement are shown in Fig. 3.4. The single-phase nature of the samples can be clearly seen from the SEM images. Small black spots in Fig. 3.4(a) are due to the presence of small holes on the sample surface. To know the chemical composition of these samples, energy dispersive X-ray analysis (EDS) measurement is performed at several places on the sample. As can be seen from Table- 1, the chemical composition obtained from the EDS analysis nearly matches the starting composition of the samples.

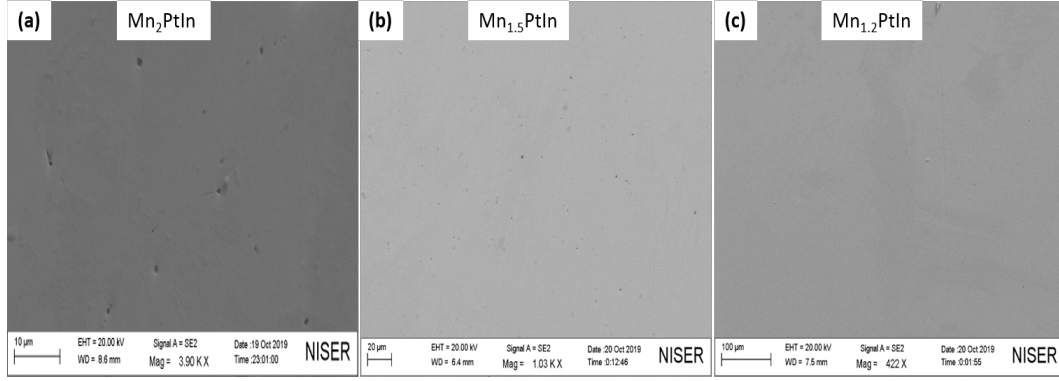


Figure 3.4: SEM images of (a) Mn_2PtIn , (b) $\text{Mn}_{1.5}\text{PtIn}$ and (c) $\text{Mn}_{1.2}\text{PtIn}$.

Table 3.1: EDS data of $\text{Mn}_{2-x}\text{PtIn}$

Composition (x)	Exact atomic ratios of Mn, Pt, In (in %) respectively	Obtained values of Mn, Pt, In from EDS (in %) respectively
x= 0.0	50.00, 25.00, 25.00	52.03, 25.62, 22.34
x= 0.5	42.85, 28.57, 28.57	42.53, 29.38, 28.06
x= 0.8	37.5, 31.25, 31.25	40.74, 30.45, 28.80

3.3.3 Magnetic properties study

Temperature and field dependent magnetization measurements are performed to map out the magnetic state in the present samples. Figure 3.5(a)-(g) depict the temperature-dependent magnetic moment variation for the $\text{Mn}_{2-x}\text{PtIn}$ samples. The Curie temperature (T_C) systematically decreases with decreasing Mn concentration [see Fig. 3.5(h)]. A spin re-orientation kind of transition appears around 150 K for Mn_2PtIn sample only [see Fig. 3.5(a)]. However, we do not observe any such feature in rest of the samples. The isothermal magnetization $M(H)$ loops measured at 2 K for different $\text{Mn}_{2-x}\text{PtIn}$ samples are plotted in Fig. 3.6(a)-(g). The saturation magnetization (M_s) initially increases for $x = 0$ to 0.3 before decreasing systematically with decreasing Mn concentration [see Fig. 3.6(h)]. The value of the saturation moment in these samples suggests a ferrimagnetic ordering. A very small magnetic moment and a linear kind of hysteresis loop is observed for the MnPtIn sample, indicating a fully compensated magnetic state. As previously mentioned, the samples with $x = 0.9$ and 1.0 contain a small fraction of MnPt phase. Since MnPt shows

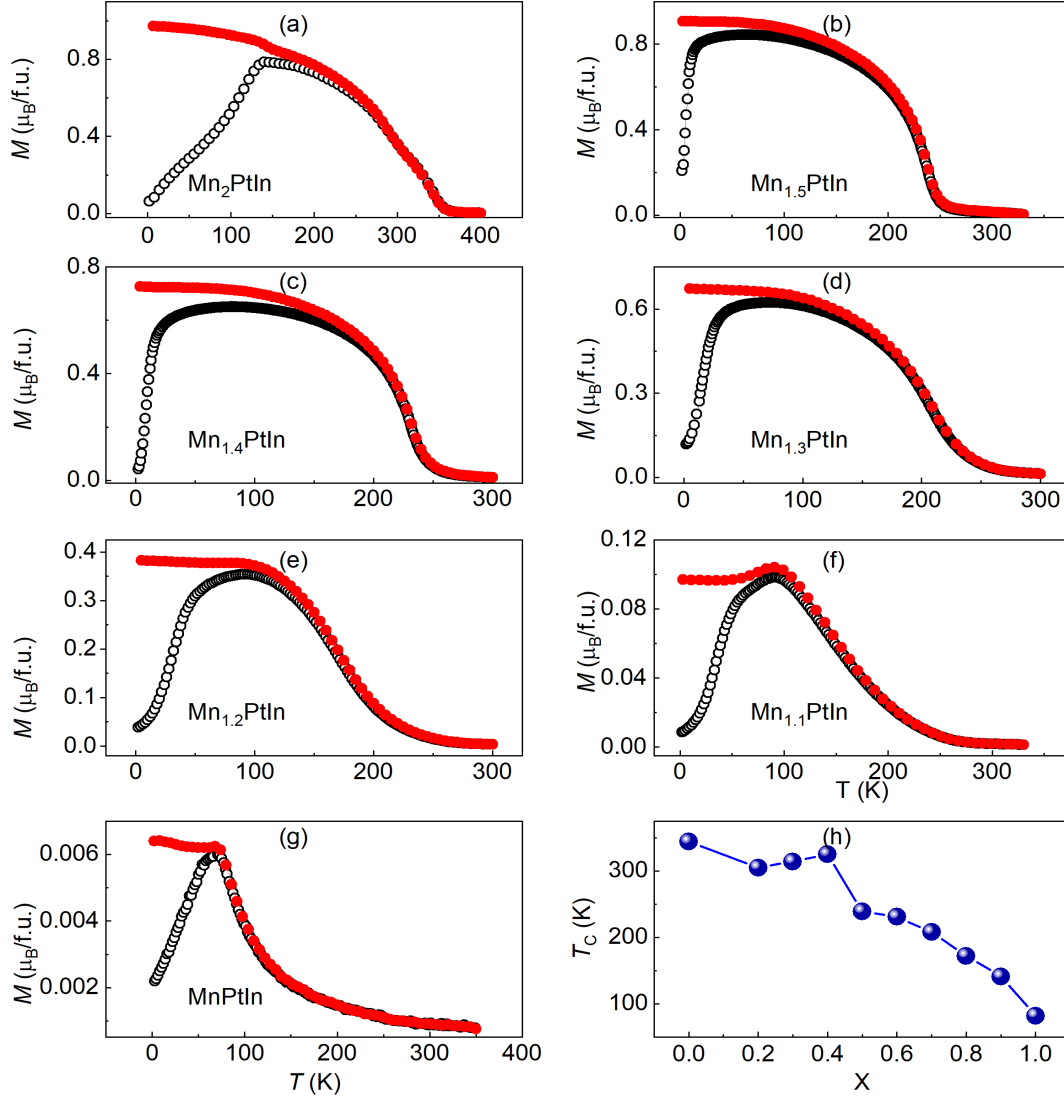


Figure 3.5: (a)-(g) Temperature dependence of magnetization $M(T)$ measured in zero field cooled (ZFC, open symbols) and field cooled (FC, filled symbols) modes in an applied field of 0.1 T for $\text{Mn}_{2-x}\text{PtIn}$. (h) Variation of Curie temperature (T_C) with Mn concentration (x) in $\text{Mn}_{2-x}\text{PtIn}$.

an antiferromagnetic [111] ordering with zero net magnetic moments, it should not affect the magnetic properties of $\text{Mn}_{1.1}\text{PtIn}$ and MnPtIn samples. The structural and magnetic parameters of $\text{Mn}_{2-x}\text{PtIn}$ are summarized in Table-2.

The density functional theory (DFT) calculation confirms the ferrimagnetic ordering of the Mn sub-lattices [please refer to the theoretical calculations parts in Phy. Rev. B 102, 014449 (2020)]. The calculated moment value for Mn_2PtIn , $\text{Mn}_{1.5}\text{PtIn}$,

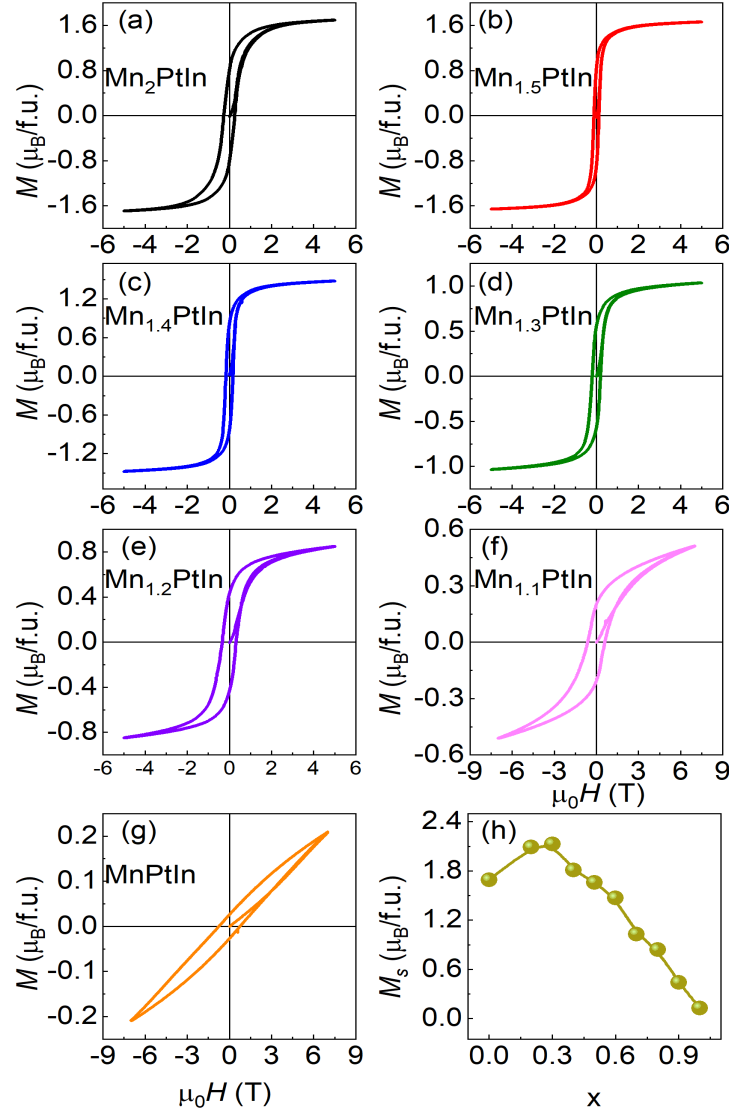


Figure 3.6: (a)-(g) Field dependence of magnetization loops measured at 2 K for $\text{Mn}_{2-x}\text{PtIn}$. (h) The composition-dependent saturation magnetization (M_s) taken at a field of 5 T.

and MnPtIn is close to the saturation magnetization obtained from the $M(H)$. The details of the magnetic ordering in this system shall be discussed later. As the present system are noncentrosymmetric in nature and belongs to the crystallographic D_{2d} class, it provides the platform for realizing anisotropic DMI. The compatibility of Heisenberg energy, and DMI can lead to the formation of complex magnetic states including helical magnetic ordering. In application of magnetic field, helical state

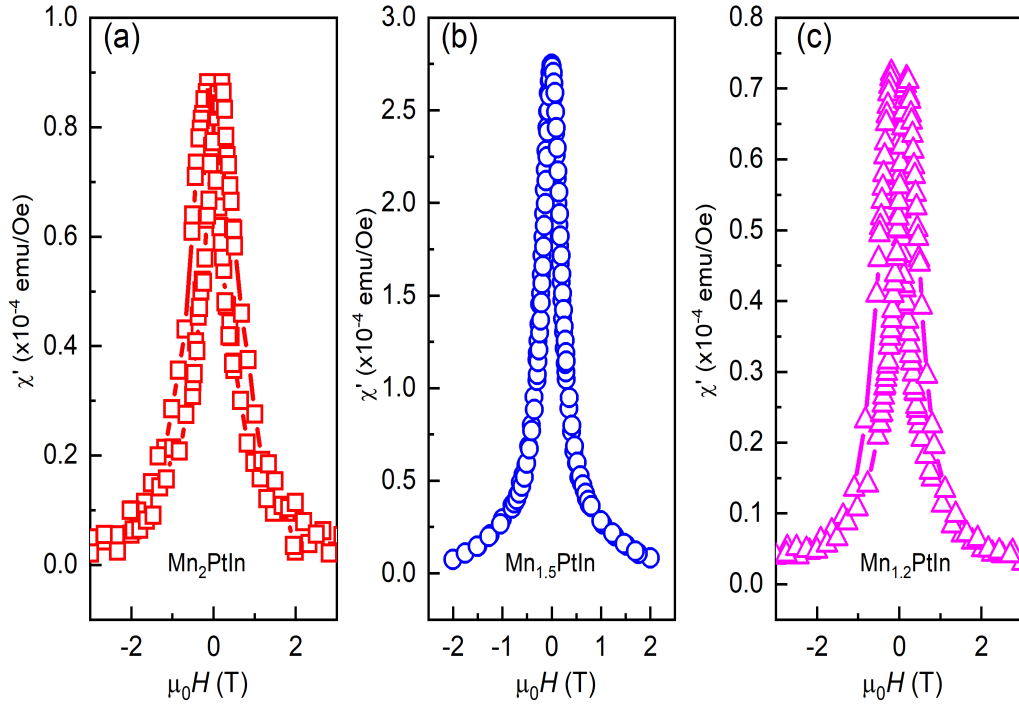


Figure 3.7: (a)-(c) Plot of ac-susceptibility data with respect to the applied DC-magnetic field at a constant temperature of 5 K for Mn_2PtIn , $\text{Mn}_{1.5}\text{PtIn}$, and $\text{Mn}_{1.2}\text{PtIn}$, respectively.

can transform into a magnetic antiskyrmion state. Ac susceptibility measurement is the easiest and quickest method to identify the signature of antiskyrmion. Therefore, field-dependent ac-susceptibility measurements at 5 K for all three samples is performed [Fig. 3.7(a)-(c)]. The $\chi'(H)$ data do not exhibit any anomaly up to a field of ± 5 T. It can be mentioned here that all skyrmion/anti-skyrmion hosting bulk materials display dip/kink kind of features in the ac-susceptibility measurements [106, 110, 112, 113, 114]. In addition, the first derivative of magnetization with respect to the field for the $M(H)$ loops also do not exhibit any unusual behavior. Therefore, it is very unlikely that the present samples possess any kind of antiskyrmionic phase.

Table 3.2: Structural and magnetic parameters

Composition (x)	structure (Space Group)	$a = b$ (in Å)	c (in Å)	c/a ra- tio	T_C (K)	M_S (μ_B /f.u.) Experi- mental (at 5T field)
x= 0.0	<i>Tet.</i> ($\bar{I}4m2$)	4.32(1)	6.74(3)	1.56	344	1.69
x= 0.2	<i>Tet.</i> ($\bar{I}4m2$)*	4.30(8)	6.79(0)	1.57	305	2.09
x= 0.3	<i>Tet.</i> ($\bar{I}4m2$)*	4.30(7)	6.82(4)	1.58	314	2.13
x= 0.4	<i>Tet.</i> ($\bar{I}4m2$)*	4.42(8)	6.32(4)	1.43	325	1.81
x= 0.5	<i>Tet.</i> ($\bar{I}42m$)	6.39(6)	12.27(0)	1.91	239	1.66
x= 0.6	<i>Tet.</i> ($\bar{I}42m$)	6.40(1)	12.28(2)	1.92	231	1.47
x= 0.7	<i>Tet.</i> ($\bar{I}42m$)	6.40(6)	12.30(7)	1.92	208	1.03
x= 0.8	<i>Tet.</i> ($\bar{I}42m$)	6.40(8)	12.33(0)	1.92	172	0.84
x= 0.9	<i>Tet.</i> ($\bar{I}42m$) [†]	6.40(3)	12.37(1)	1.93	141	0.44
x= 1.0	<i>Tet.</i> ($\bar{I}42m$) [†]	6.36(0)	12.67(2)	1.99	82	0.13

* signifies a structurally mixed phase. † represents the presence of secondary MnPt phase.

3.4 Tunable topological Hall

The preliminary magnetic measurement suggests the presence of tunable magnetic properties in the present system. To explore the magneto transport response, detailed Hall resistivity (ρ_{yx}) measurements are carried out for Mn_2PtIn , $\text{Mn}_{1.5}\text{PtIn}$, and $\text{Mn}_{1.2}\text{PtIn}$. Fig. 3.8(a)-(g) depict the Hall resistivity (ρ_{yx}) data for Mn_2PtIn . The experimental data are represented by the open (+5 T to -5 T) and filled (-5 T to +5 T) blue circles to distinguish the different field sweep directions. The ρ_{yx} data exhibit a negative hysteresis loop for the temperature range of 5 K to 100 K. At 150 K and above temperature, we observe normal hysteresis, as can be seen from the inset of Fig. 3.8(d) and (g). It is noteworthy to mention that the inequality in the highest value of the ρ_{yx} at $T = 5$ K at the first and fourth quadrant due to a small magneto-resistance contribution at this temperature, whereas no such effect is found for $T \geq 50$ K. A hump-like behavior in Hall resistivity data apparent in low temperature as well as 300 K requires additional explanation. In general the total Hall resistivity in a system can be written as $\rho_{yx} = \rho_{OHE} + \rho_{AHE} + \rho_{yx}^T$, where ρ_N ,

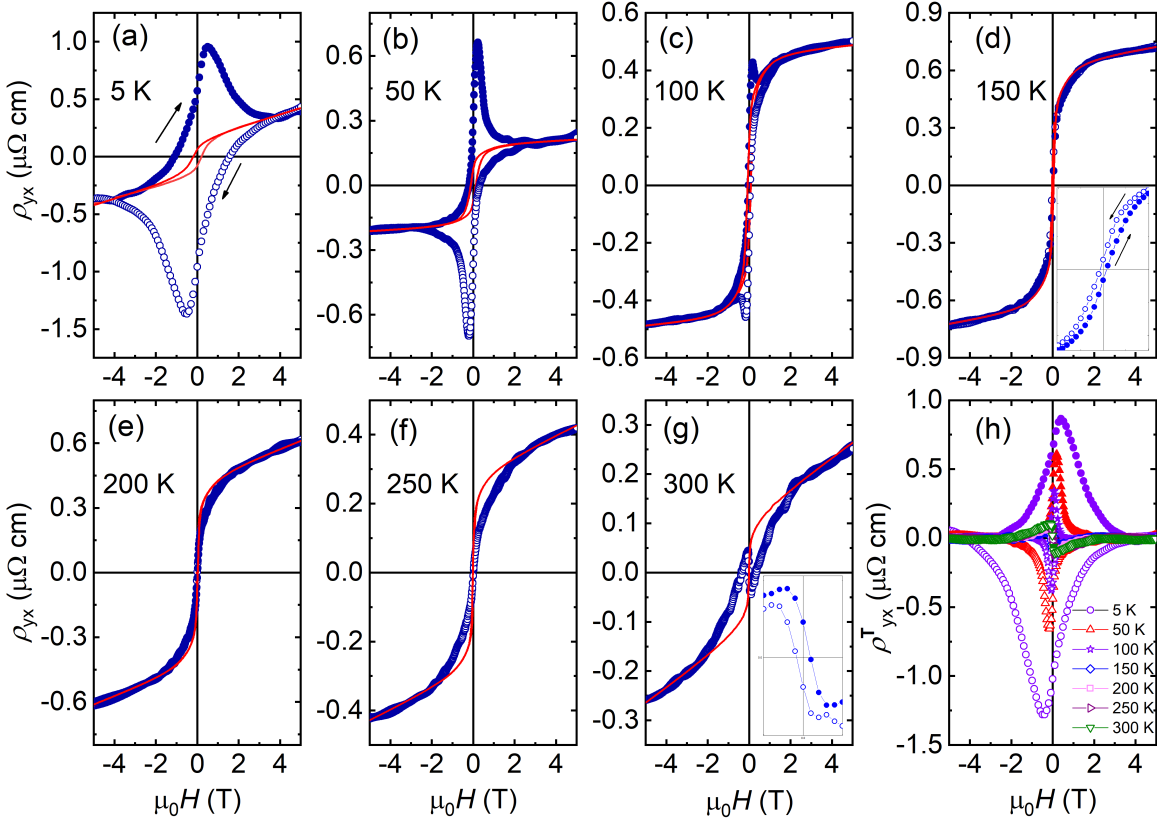


Figure 3.8: (Color online) (a)-(g) Experimentally obtained and calculated Hall resistivity plot of Mn_2PtIn at different constant temperatures. The experimental data are shown in open and filled blue circles, and the solid red lines correspond to the fitted data. Open and filled symbols correspond to the +5 T to -5 T and -5 T to +5 T, respectively. (h) Extracted topological Hall resistivity at different temperatures. Open and filled symbols corresponds to same meaning as stated before. The inset of (d) and (g) shows the usual field reversal of Hall resistivity data.

ρ_{AH} and ρ_{yx}^T are ordinary, anomalous and topological Hall resistivity, respectively. The ordinary Hall resistivity, which is linearly proportional to the magnetic field, can be expressed as $\rho_{OHE} = \mu_0 R_0 H$, where R_0 is the normal Hall coefficient and H is the magnetic field. In an FM/FiM system, the intrinsic contribution to the anomalous Hall effect can be illustrated as $\rho_{AHE} = b\rho_{xx}^2 M$, where b is a constant, ρ_{xx} is the longitudinal resistivity and M is the magnetization. As can be seen from the experimental Hall resistivity data, at higher fields, ρ_{yx} almost saturates with fields. So, it can be assumed that the high field data only consists of the normal

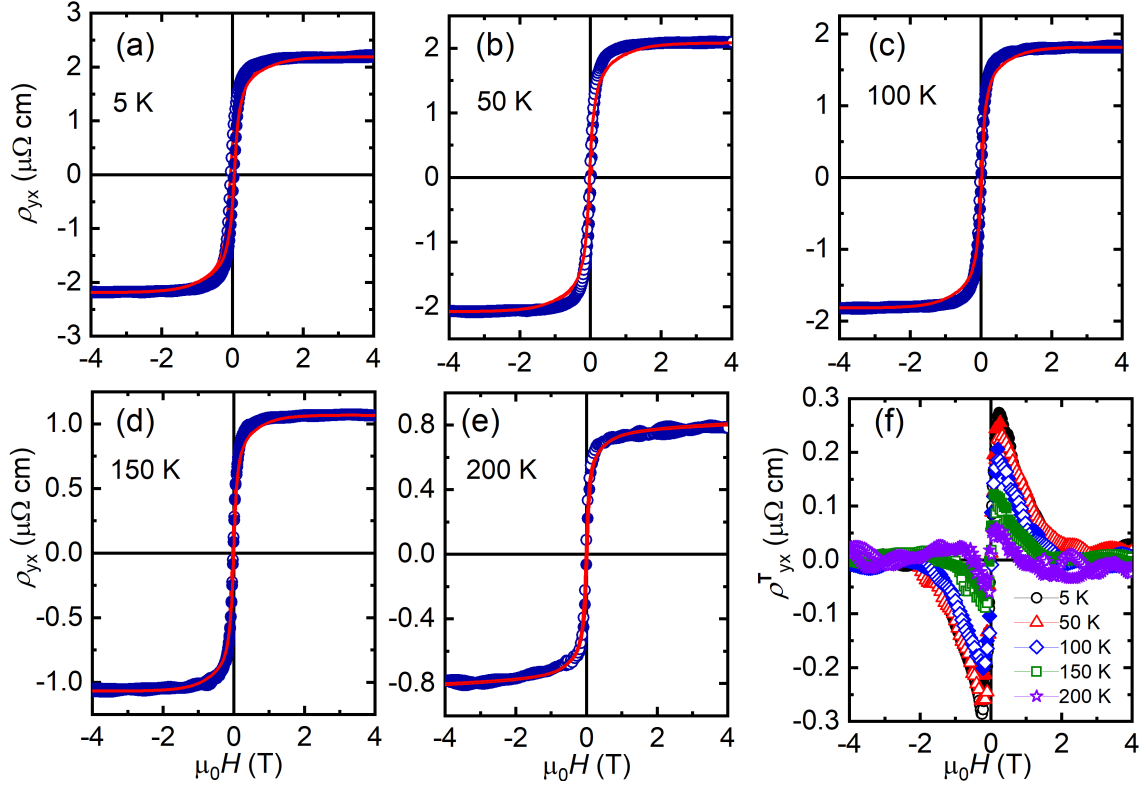


Figure 3.9: (Color online) (a)-(e) Experimental and fitted Hall resistivity data of $\text{Mn}_{1.5}\text{PtIn}$ at different constant temperatures. The experimental data are shown in open and filled blue circles, and the solid red lines correspond to the fitted data. Open and filled symbols represent the field sweep direction of +5 T to -5 T and -5 T to +5 T, respectively. (f) Extracted topological Hall resistivity for different temperatures.

and anomalous Hall components. Therefore, ρ_{yx} at high fields can be written as $\rho_{yx} = \mu_0 R_0 H + b \rho_{xx}^2 M$. The calculated Hall resistivity curves for different temperatures are shown by red solid lines [Fig. 3.8(a)-(g)]. The difference between the experimental and calculated Hall resistivity data of various temperatures is plotted in Fig. 3.8(h). Now, it can be said that the additional scattering of the conduction electrons takes place opposite to that of normal and anomalous Hall contribution for temperatures up to 100 K [Fig. 3.8(a)-(c)], where the ρ_{yx} data exhibit a negative hysteresis loop. We also observe a reasonable difference between the experimental and calculated Hall resistivity data for $\text{Mn}_{1.5}\text{PtIn}$, as shown in Fig. 3.9(a)-(e). The extracted THE for different temperatures can be seen in Fig. 3.9(f). However, both

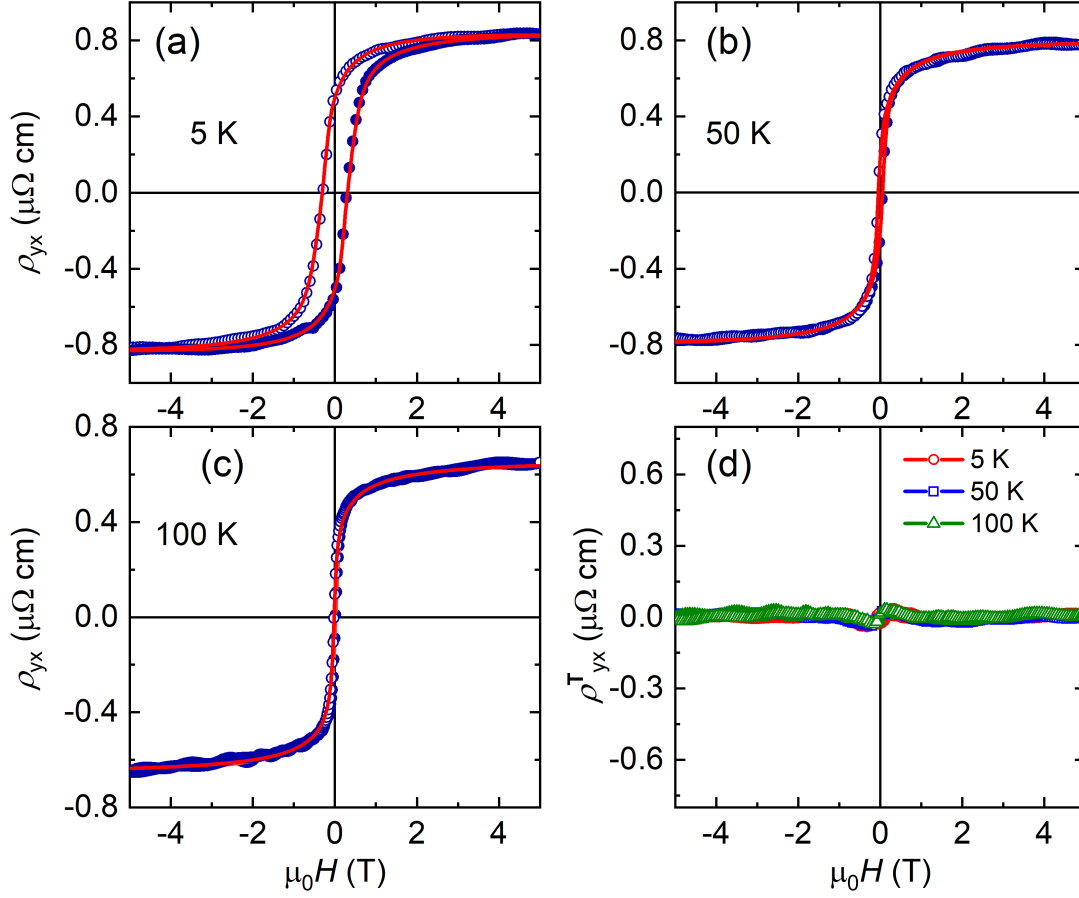


Figure 3.10: (Color online) (a)-(c) Experimental Hall resistivity plot of Mn_{1.2}PtIn at different temperatures. The experimental data are shown in open and filled blue circles, and the solid red lines correspond to the fitted data. Open and filled symbols correspond to the +5 T to -5 T and -5 T to +5 T, respectively. (d) Extracted topological Hall resistivity at different temperatures.

curves (experimental and calculated) matches well for Mn_{1.2}PtIn [see Fig. 3.10(a)-(c)]. The extracted THE, which is almost zero plotted in Fig. 3.10(d). This signifies the absence/vanishingly small component of any additional ρ_{yx} for this sample.

The calculated ρ_{yx} ($=\rho_{OHE} + \rho_{AHE}$) is subtracted from the experimental total Hall resistivity to obtain the topological Hall ρ_{yx}^T . For Mn₂PtIn, it is found that for $T \leq 100$ K, the maximum value of ρ_{yx}^T lies in the first and the third quadrants, whereas the maxima lie in the second and fourth quadrants for $T \geq 150$ K [Fig. 3.8(h)]. The maximum value of ρ_{yx}^T taken from the field sweep $-H \rightarrow +H$ at

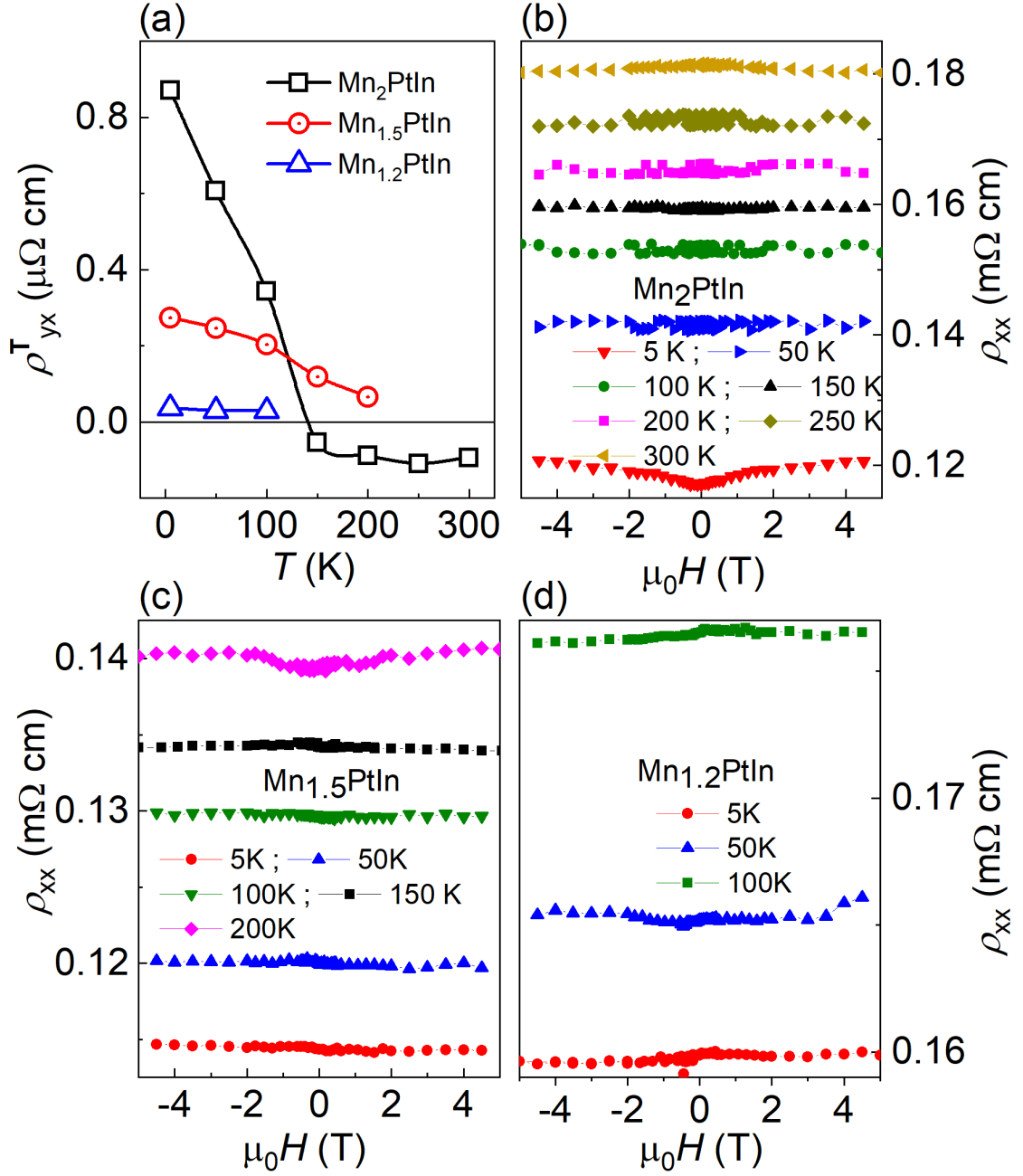


Figure 3.11: (Color online) (a) The temperature variation of THE (for three different samples as mentioned by different colors and symbols). (b)-(d) The external magnetic field dependence of longitudinal Hall resistivity of Mn_2PtIn , $\text{Mn}_{1.5}\text{PtIn}$, and $\text{Mn}_{1.2}\text{PtIn}$ respectively. The temperature values are indicated in the respective plot.

different temperatures [Fig. 3.11(a)]. A large ρ_{yx}^T of about $1\ \mu\Omega\text{-cm}$ can be found at 5 K in Mn_2PtIn . The ρ_{yx}^T drastically decreases to about $0.3\ \mu\Omega\text{-cm}$ in case

of $\text{Mn}_{1.5}\text{PtIn}$ before vanishing for $\text{Mn}_{1.2}\text{PtIn}$, as depicted in Fig. 3.11(a). Also, it is observed that a change in the sign of THE with the temperature in Mn_2PtIn [Fig. 3.11(a)]. The origin of the change in sign of the ρ_{yx}^T can be attributed to the existence of a spin-reorientation-like transition at 150 K as can be visualized in ZFC and FC $M(T)$ curves shown earlier in Fig. 3.5(a). In the case of $\text{Mn}_{1.5}\text{PtIn}$, the maximum value of ρ_{yx}^T monotonically decreases with temperature, whereas it remains almost close to zero at all temperatures for $\text{Mn}_{1.2}\text{PtIn}$. It is important to mention here that the $M(T)$ data for both $\text{Mn}_{1.5}\text{PtIn}$ and $\text{Mn}_{1.2}\text{PtIn}$ do not exhibit any kind of anomaly [see Fig. 3.5(b) and (e)]. However, there is no commendable magnetoresistance for all the samples studied here. Figure 3.11(b)-(d) represent the magnetic field dependence of longitudinal resistivity for Mn_2PtIn , $\text{Mn}_{1.5}\text{PtIn}$, and $\text{Mn}_{1.2}\text{PtIn}$, respectively.

3.5 Probing the non-collinear magnetic ordering in $\text{Mn}_{1.5}\text{PtIn}$

A clear hump-like feature is seen in the Hall resistivity for Mn_2PtIn . Also, a clear difference in the experimental and calculated Hall data is visible for $\text{Mn}_{1.5}\text{PtIn}$. The neutron diffraction study on Mn_2RhSn , which have similar structural and magnetic properties to that of Mn_2PtIn , showed a large non-collinearity in the spin structure[48]. However, the spin state of $\text{Mn}_{1.5}\text{PtIn}$ is unknown. Therefore, to experimentally verify the existence of the non-collinear magnetic structure in the present system, powder neutron diffraction (ND) experiment is performed on the $\text{Mn}_{1.5}\text{PtIn}$. The ND patterns taken in the temperature range of 1.5 K to 300 K at different 2θ values are depicted in Fig. 3.12(a). The temperature-dependent ND patterns show an increase in the scattering intensity below the ordering temperature at the nuclear Bragg peaks (101), (200), and (004), suggesting a commensurate magnetic structure. This can be clearly seen from the temperature variation of normalized intensities, which decrease significantly with increasing temperature [Fig.

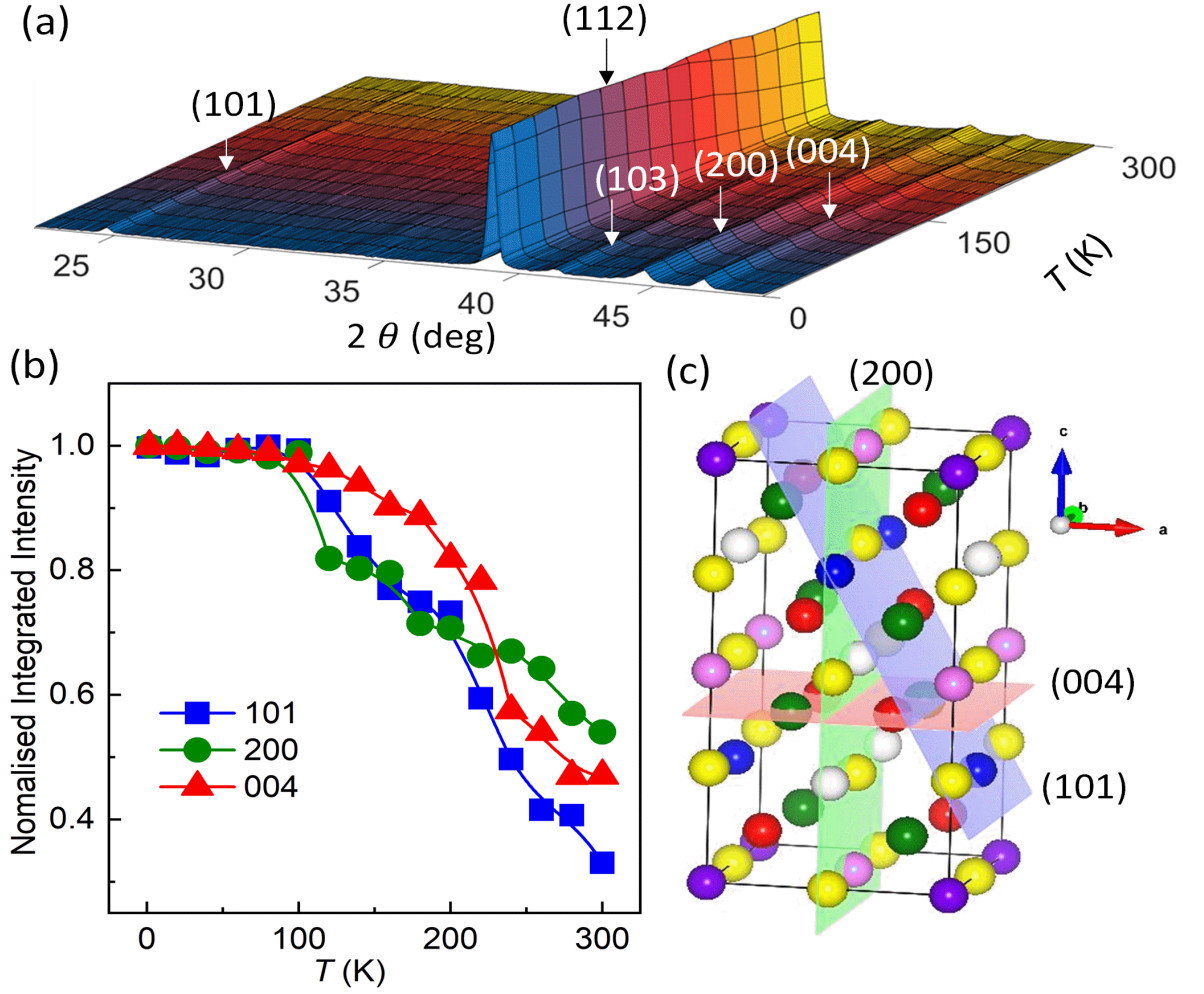


Figure 3.12: (Color online) (a) Intensity plot of the powder neutron diffraction performed on $\text{Mn}_{1.5}\text{PtIn}$ sample. The x- and y-axis correspond to the diffraction angle (2θ) and temperature (T). (b) Temperature dependence of the normalized integrated intensity for Bragg peaks (101), (200), and (004). (c) The respective Bragg planes are indicated in the unit cell of $\text{Mn}_{1.5}\text{PtIn}$.

3.12(b)]. In Fig. 3.12(c), the (101), (200), and (004) planes are highlighted. The increase in the intensity of the Bragg peaks (101), (200), and (004) below the ordering temperature (240 K) suggests the presence of contribution from both in-plane and out-of-plane magnetic components.

Since $\text{Mn}_{1.5}\text{PtIn}$ exhibits a T_C of about 240 K, the ND pattern at 300 K used for the nuclear refinement by utilizing the previously determined space group $\text{I}\bar{4}2\text{m}$ (SG No. 121) and related structural parameters [Fig. 3.13(a), upper panel]. A magnetic

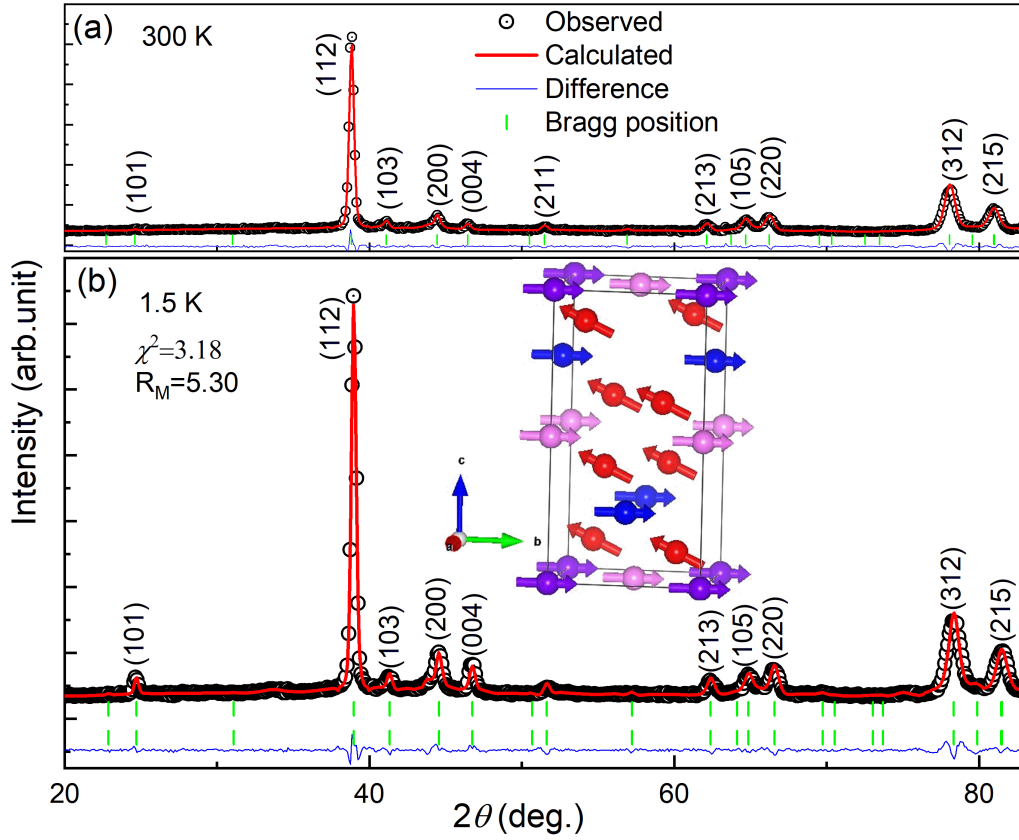


Figure 3.13: (Color online) (a), (b) Reitveld refinement of 300 K and 1.5 K ND pattern, respectively. The open black circles correspond to the experimental data, and the solid red line represent the calculated intensity. The solid blue line is the difference between experimental and calculated intensity. The green vertical lines are Bragg peak positions. The magnetic structure obtained from the refinement is shown in the inset of (b).

propagation vector $k = (0, 0, 0)$ is found with best agreement factors from the k -search program included in the Fullprof-suite package. The Rietveld refinement of 1.5 K ND data convincingly demonstrate magnetic contribution in $\text{Mn}_{1.5}\text{PtIn}$ [Fig. 3.13(b), lower panel]. The magnetic structure depicted in the inset of Fig. 3.13 (b) describes the corresponding magnetic model. The temperature dependence of absolute values of the magnetic moments for Mn sitting at different sublattices are shown in Fig. 3.14(a). The Mn atoms sit at 2b, 4d, and 8i and display almost equal magnitudes of magnetic moments with similar temperature dependency. The Mn moments at 2a, 2b, and 4d exhibit a complete in-plane orientation, whereas 8i

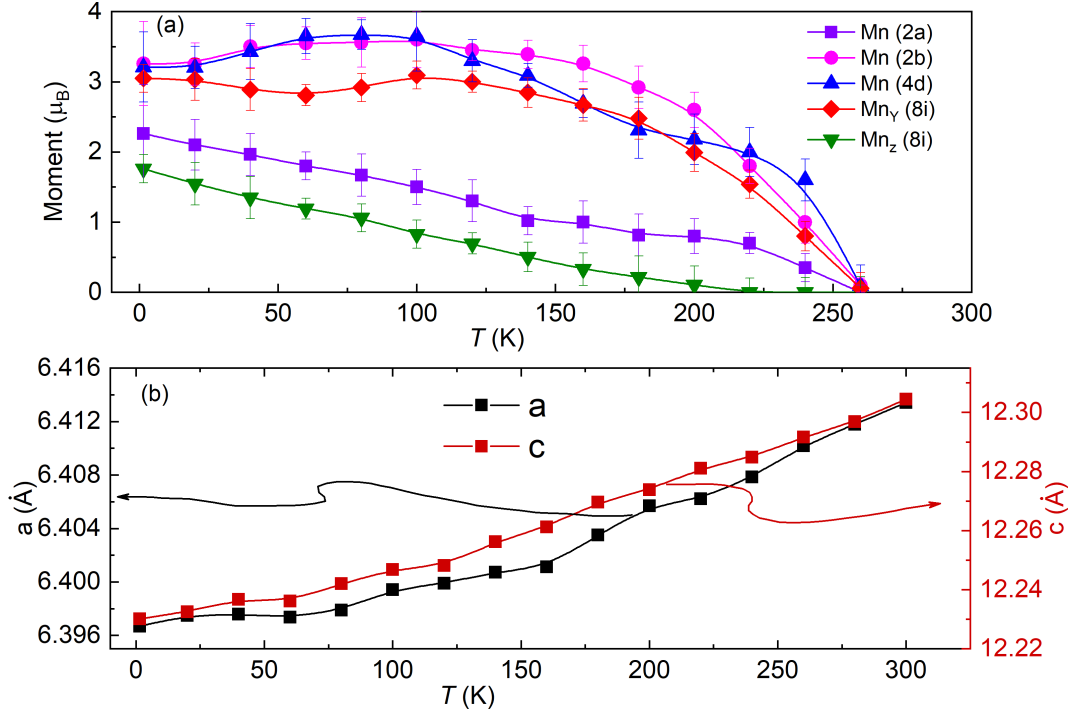


Figure 3.14: (Color online) (a) Temperature dependence of the sub-lattice moment in $\text{Mn}_{1.5}\text{PtIn}$ indicated by different color symbols. Here, $\text{Mn}_Y(8i)$ is the absolute value of the y component of the Mn(8i) sub-lattice moment. (b) Variation of lattice constant a and c with temperature.

Mn atoms possess both in-plane and out-of-plane magnetic components. A smaller magnitude of 2a Mn moment is due to the fact that the 2a site is comparatively less occupied in the present sample. The temperature dependence of the lattice constant is shown in Fig. 3.14(b). Therefore, our Neutron diffraction measurements provide a clear evidence of non-coplanar magnetic state in the present system.

3.6 Origin of THE

The theoretical calculation and experimental results have convincingly established the presence of non-collinear magnetic state in the Mn_2PtIn system. For a better understanding of the present THE, which originates from the non-vanishing scalar spin chirality, let's considered one Mn spin (\mathbf{S}_1) in the Mn-In plane (magenta plane) and two Mn spins (\mathbf{S}_2 and \mathbf{S}_3) from two different Mn-Pt planes (blue plane) as

shown in Fig. 3.15(a). For simplicity, first, consider the components of the canted spins \mathbf{S}_2 and \mathbf{S}_3 lie in the yz plane. The magnetic moment of Mn atoms sitting in upper blue, lower blue plane, and magenta plane can be described by $\mathbf{S}_1 = Z_1 \mathbf{k}$, $\mathbf{S}_2 = Y_2 \mathbf{j} - Z_2 \mathbf{k}$, $\mathbf{S}_3 = -Y_2 \mathbf{j} - Z_2 \mathbf{k}$, respectively. Here Y_2 is the component of Mn moment in the y direction, and Z_1 and Z_2 are that of z direction. $\mathbf{i}, \mathbf{j}, \mathbf{k}$ are the unit vectors. For the said configuration the scalar spin chirality can be calculated as $\chi_{123} = \mathbf{S}_1 \cdot (\mathbf{S}_2 \times \mathbf{S}_3) = 0$. However, the competing antiferromagnetic interactions along with the chiral DMI in the system and/or the external magnetic field can tilt the in-plane component of the \mathbf{S}_2 and \mathbf{S}_3 in any direction in the ab plane. Hence, with a small x component δ , $\mathbf{S}_2 = \delta \mathbf{i} + Y_2 \mathbf{j} - Z_2 \mathbf{k}$ and $\mathbf{S}_3 = \delta \mathbf{i} - Y_2 \mathbf{j} - Z_2 \mathbf{k}$. As a result, a non-vanishing $\mathbf{S}_1 \cdot (\mathbf{S}_2 \times \mathbf{S}_3) = -2Y_2 Z_1 \delta$ is obtained that can give rise to the observed topological Hall effect. Similarly, for the non-collinear magnetic structure of the $\text{Mn}_{1.5}\text{PtIn}$, a non-vanishing SSC can be obtained by attributing a small x component alternate sequentially layer-wise for the Mn8i atoms [Fig. 3.15(b)]. As schematically depicted in Fig. 3.15(c), any three non-coplanar spins \mathbf{S}_i , \mathbf{S}_j and \mathbf{S}_k can subtend a solid angle Ω , thereby resulting in a non-zero scalar spin chirality with a fictitious magnetic field as shown by purple arrow. In the absence of any fixed chirality, this magnetic field will act in all possible directions resulting in a net vanishing THE. However, the D_{2d} symmetry of the present materials ensures a chiral magnetic state, thereby, a non-vanishing THE in the system. At very high magnetic fields, the Zeeman energy can easily overcome the chiral DMI energy, suppressing the chirality as well as THE.

The assertion of large topological Hall resistivity at low temperatures as a result of finite scalar spin chirality instead of any skyrmion/antiskyrmion phase is supported by several facts. (i) Absence of any kind of kink/peak behavior in the ac-susceptibility measurements as discussed earlier. (ii) The isostructural Heusler compounds $\text{Mn}_{1.4}\text{Pt}_{0.9}\text{Pd}_{0.1}\text{Sn}$ [57] and $\text{Mn}_2\text{Rh}_{0.9}\text{Ir}_{0.1}\text{Sn}$ [115] found to exhibit anti-skyrmion phase with antiskyrmion size of about 150 nm and 200 nm, respectively. Since the magnitude of THE is inversely proportional to the skyrmion size, it is expected that the antiskyrmion phase in these systems will result in topological Hall

resistivity in the order of 1 n Ω –cm or less. (iii) It can be clearly seen that Mn₂PtIn displays a spin-reorientation transition around 150 K. The previous studies on similar systems show the existence of the antiskyrmion phase, if any, only above the spin-reorientation transition [114, 116]. The non-coplanar spin structure with finite

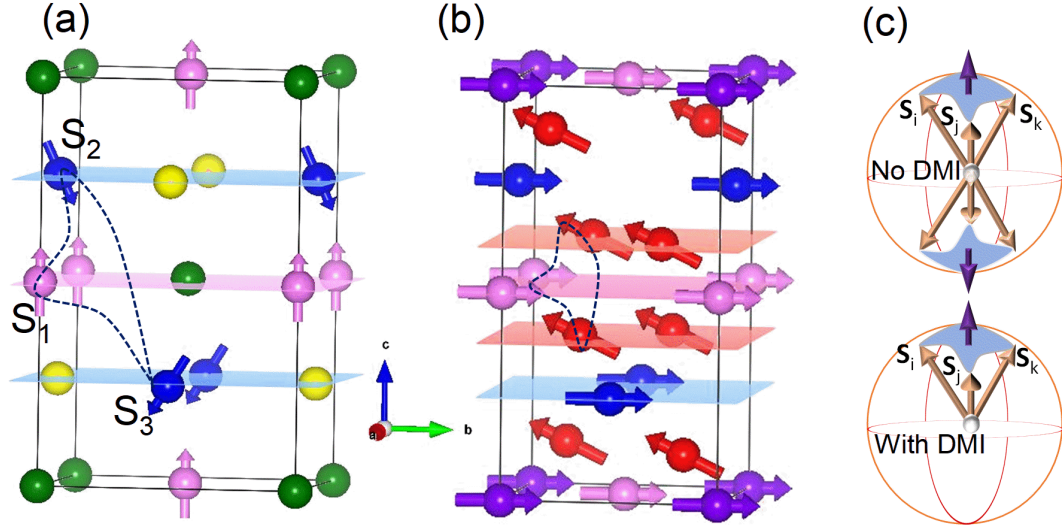


Figure 3.15: (Color online) (a) Non-collinear magnetic ordering of Mn₂PtIn system. (b) Non-collinear magnetic ordering in Mn_{1.5}PtIn as obtained from powder ND experiment. The black dashed loop connecting different Mn sub-lattice moments in (a) and (b) is used to calculate SSC. (c) Upper panel: cancellation of fictitious magnetic field directed in both upward and downward directions (purple arrows) due to the absence of any chiral DMI. The fictitious magnetic field associated with the solid angle subtended by three noncoplanar spins S_i , S_j , S_k . Lower panel: Fixed chirality and non-vanishing fictitious field in the presence of DMI.

scalar spin chirality as a source of THE has been recently observed in FM systems [18], as well as in antiferromagnetic systems (AFM) [117]. Although THE arises in systems hosting skyrmions/antiskyrmions or comprised of non-coplanar spin structures, a very basic difference lies in the length scale of the periodicity associated with their magnetic structure. A crossover between a long periodic magnetic structure to a comparatively shorter scale non-coplanar magnetic state is about the interplay between the energy contributions from various energy terms [118]. In case of the present system under study, it might be possible to stabilize an incommensurately modulated helical/cycloid ground state with a modulation period of up to a few

hundred. This helix/cycloid can transform into skyrmions/antiskyrmions under the external magnetic field. This can cause very small THE due to the large size of the skyrmions. In a recent study, Kumar *et al.* have assigned the low temperature THE in some of their samples to the presence of antiskyrmions, although these samples display a large canting angle below the spin-reorientation transition [116]. However, THE is only found when there is a large canting angle, indicating its probable origin from the non-vanishing scalar spin chirality coming from the non-coplanar magnetic state. This scenario is supported by the nonexistence of any THE in the well-established antiskyrmion phase, probably due to the large size of the antiskyrmions in these materials.

3.7 Summary

In summary, the experimental findings convincingly establish the presence of non-collinear magnetic ground states, resulting in a robust THE. We show a controlled tuning of the topological Hall effect by modifying the canted magnetic state in the system. The magnitude of the spin canting achieved by tuning the Mn composition is associated with a slight change in lattice parameters that eventually control various fundamental parameters such as the exchange interactions, the DMI, and the magnetocrystalline anisotropy (MCA). Hence, the competition among these parameters determines the underlying magnetic texture of the present system. Therefore, THE, in the present case, can be controlled electrically by inducing strain in the system. Hence, the present study on the realization of tunable THE possesses great potential in all electrical switching-based memory applications. A very recent study on electrical control of anomalous Hall state corroborates the importance of the present study that can motivate further research in this direction [119].

Chapter 4

Role of non-collinear magnetic ordering on antiskyrmion phase in Mn-Pt(Pd)-Sn-In

“Be the change that you wish to see in the world.”

Mahatma Gandhi

4.1 Introduction

Magnetic skyrmions are topological defects consisting of a bunch of swirling spins within a homogeneous magnetic background [7, 8, 9]. In recent times, magnetic skyrmions (skx) have been at the center of intense research in the field of spintronics for their potential practical implications, such as binary-based magnetic storage and information processing system [3, 120, 121, 122], bit for neuro-morphic computation [123], random number generator for computer simulation [124], etc. Also, the ease of decoupling the skx from the underlying lattice by applying a small electronic current makes it advantageous to be implicated in the race-track memory devices,

whose original proposition was based on the conventional domain wall motion [5]. However, the ‘skyrmion Hall effect’ is a major drawback for the current driven motion of skx [125, 126]. Several models have been proposed to suppress this intriguing problem associated with the skx motion [127, 128, 129, 130, 131]. Moreover, the micromagnetic simulation study have shown that the antiskyrmions (askx) could be free from such difficulties [132]. The inhomogeneous spin distribution within askx (twofold rotational symmetry of askx) leads to the anisotropic ‘skx Hall effect’ and becomes zero under certain conditions [132]. Therefore, the study of askx is important from the application as well as fundamental physics points of view.

Till now, there are only limited number of systems that exhibit antiskyrmion phase. The first observation of magnetic antiskyrmion was found in inverse tetragonal Heusler system $\text{Mn}_{1.4}\text{Pt}_{0.9}\text{Pd}_{0.1}\text{Sn}$ belongs to D_{2d} crystal class [57]. The underlying crystal symmetry in this system restricts the opposite sign of DM vector ($D_x = -D_y$) to lie along the two principal axes within a tetragonal basal plane. Such anisotropic DMI generates an opposite sense of twisting in the spins along two orthogonal directions in the basal plane. The anisotropic DMI competes with the isotropic exchange interaction that governs the helical modulation propagation along (100) and (010) directions. Under the application of a magnetic field in the direction of the tetragonal axis (001), which is an easy axis of magnetization, transform the helical phase into the askx phase. Recent theoretical study also shows that the askx can be stabilized in a magnetically frustrated system [133]. The search for skx/askx in frustrated magnetic systems has drawn special attention recently. The reason is that the size of the skx/askx can be very small compared to the DM-assisted system. A small size of skx/askx is necessary for the realization of high-density storage media. Secondly, a given topological spin texture within this mechanism is energetically independent of the helicity in contrast to the DMI stabilize case.

This work is focused on the effect of exchange frustration on the stabilization of askx phase in the Mn-Pt(Pd)-Sn-In system. Exchange frustration drives the extinction of the askx phase instead of forming nano-scale askx. Using magnetic ac susceptibility measurement, Lorentz transmission electron microscopy (LTEM)

imaging, and neutron diffraction study, it is found that the askx phase is stable in the temperature region where there is a collinear magnetic ordering. They do not stabilize where there is a non-collinear ordering of the spin. Therefore, this study elucidates the consequence of the exchange frustration in the presence of DMI and plays a decisive role in stabilizing the askx phase in Mn-Pt(Pd)-Sn-In system.

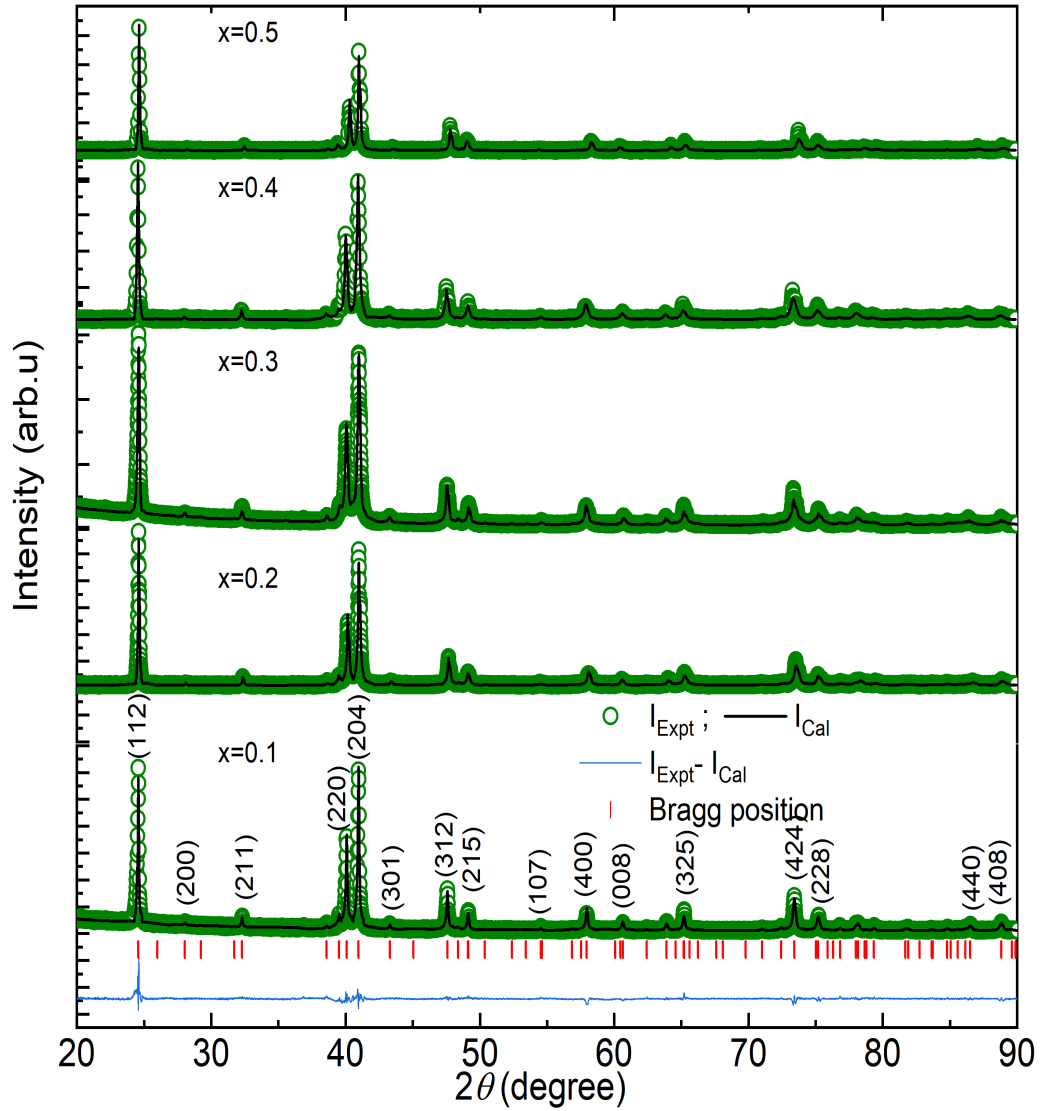


Figure 4.1: (Color online) Powder XRD patterns for $\text{Mn}_{1.4}\text{Pt}_{0.9}\text{Pd}_{0.1}\text{Sn}_{1-x}\text{In}_x$ where $x = 0.1$ to 0.5 . The open green circles in the figure represent the experimental data, and the black color solid lines are the simulated data. The blue color solid line shows the difference between the experimental and simulated lines. The $(h\ k\ l)$ value for all major reflections is shown only for $x=0.1$.

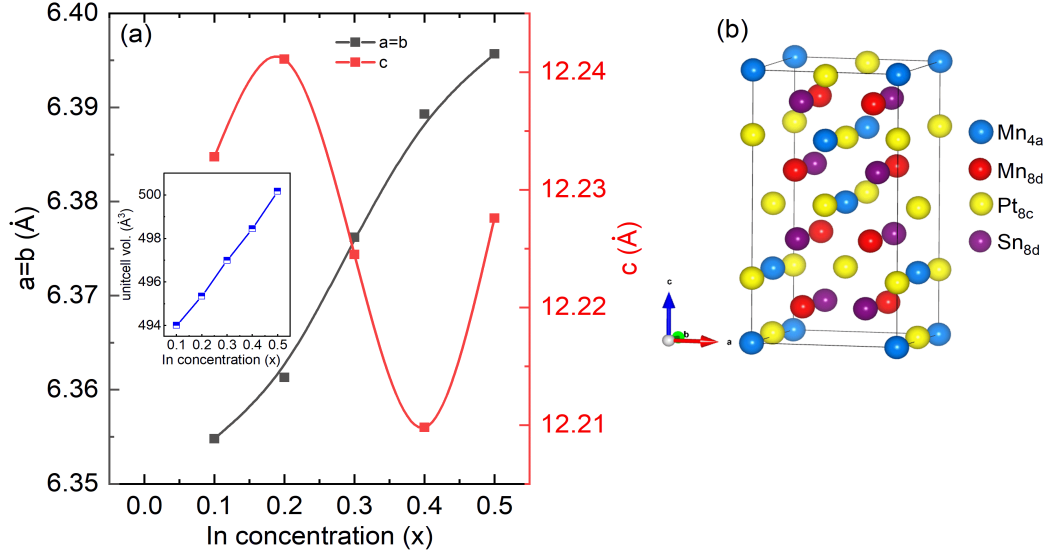


Figure 4.2: (Color online) (a) Variation of lattice parameters with the Indium concentration (x) in $\text{Mn}_{1.4}\text{Pt}_{0.9}\text{Pd}_{0.1}\text{Sn}_{1-x}\text{In}_x$. The inset is the unit cell volume with Indium concentration (x). The lines are guides to the eye. (b) Crystal structure of $\text{Mn}_{1.4}\text{PtSn}$. The distinct atoms in the unit cell are represented by different color balls, as mentioned on the right side.

4.2 Motivation

The antiskyrmion phase in $\text{Mn}_{1.4}\text{Pt}_{0.9}\text{Pd}_{0.1}\text{Sn}$ was only found above the spin reorientation temperature ($T_{SR} \sim 130$ K) [57]. Powder neutron diffraction study has revealed the presence of a collinear and a non-collinear spin ordering above and below T_{SR} , respectively [95]. Therefore, it is not clear the effect of thermal and exchange fluctuation in this system. Furthermore, the dipolar energy associated with the large magnetic moment of the system also plays a vital role in controlling the shape and size of the askx in this system [94]. A previous study shows the presence of a pure non-collinear state in $\text{Mn}_{1.4}\text{PtIn}$ with a small magnetic moment ($1.5 \mu_B/\text{f.u.}$) [see sec-3.3 of Chapter-3]. Therefore, a systematic decrement of the moment from $5 \mu_B/\text{f.u.}$ to a $1.5 \mu_B/\text{f.u.}$ can be expected by substituting In in place of Sn, which has one less valence electron. The finding of askx in a low-moment system may ensure a small stray field which is advantageous for dense packing within the device. Also, the

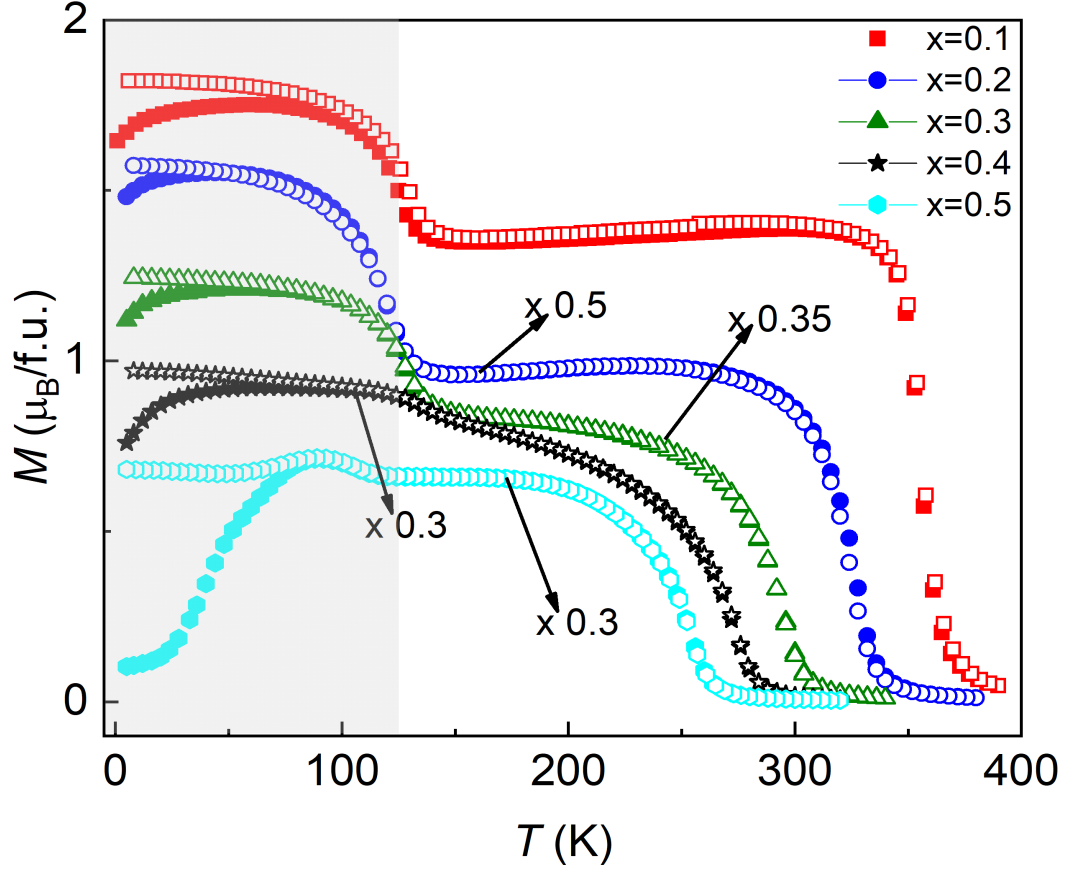


Figure 4.3: (Color online) (a) Magnetization plot with respect to varying temperature (T) measured at a constant field of 1000 Oe for different compositions of x as indicated by different colors and symbols. The solid and open symbols correspond to the zero field-cooled (ZFC) and field-cooled (FC) data. The light gray shaded region mark the temperature region below T_{SR} .

effect of spin transfer torque can be enhanced in a system with a reduced moment. Therefore, the present chapter focuses on the askx phase in $\text{Mn}_{1.4}\text{Pt}_{0.9}\text{Pd}_{0.1}\text{Sn}_{1-x}\text{In}_x$ system and understanding the effect of exchange frustration on the askx stability.

4.3 Experimental details

Polycrystalline samples of $\text{Mn}_{1.4}\text{Pt}_{0.9}\text{Pd}_{0.1}\text{Sn}_{1-x}\text{In}_x$ for $x=0.1$ to 0.5 are prepared using arc-melting technique under argon atmosphere by taking the appropriate ratio of the constituent element. The prepared ingots are then sealed in quartz tubes

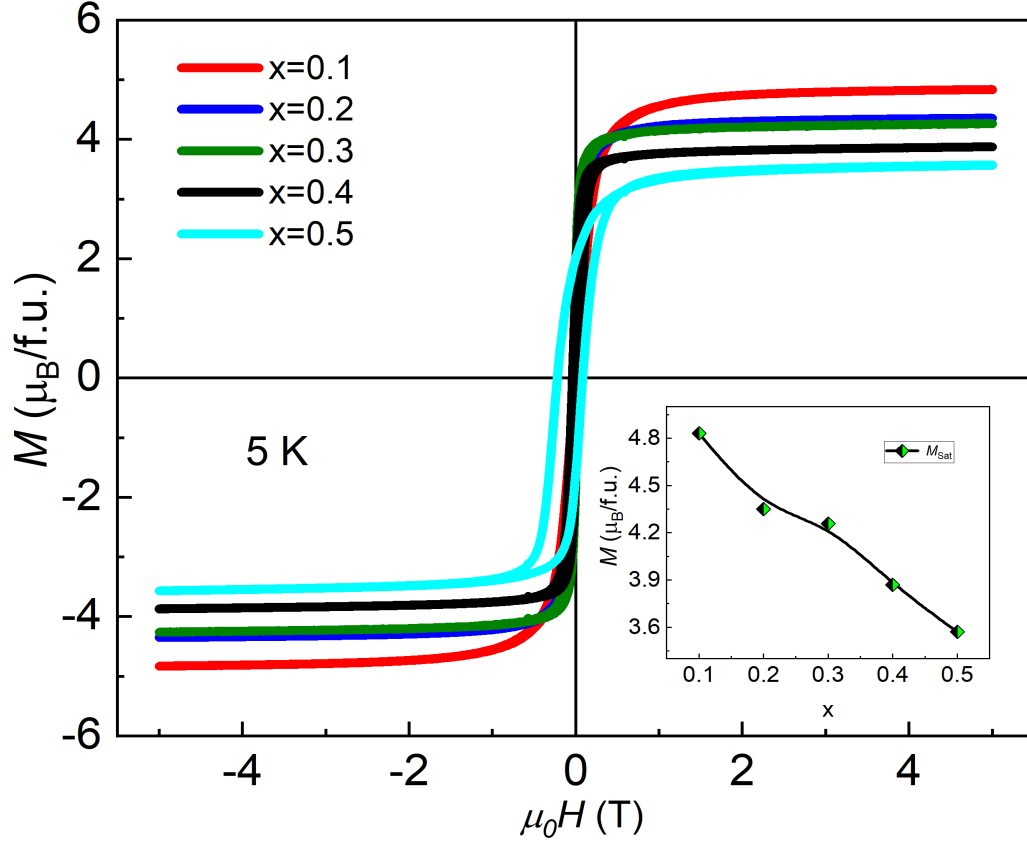


Figure 4.4: (Color online) (b) Isothermal magnetization data taken at a constant temperature of 5 K. The inset shows the M_{sat} with respect to x .

under an argon atmosphere and annealed for eight days at 1023 K. Powder X-ray diffraction (XRD) is performed in Rigaku smart x-ray diffractometer with Cu-K α source. Magnetization measurements are done in the superconducting quantum interference device vibrating sample magnetometer (SQUID VSM, Quantum Design). The ac susceptibility measurements are performed in PPMS with an ac field of $H_{ac} = 10$ Oe and frequency $f = 331$ Hz. Thin lamella of particular crystallographic oriented grain are prepared using the focussed ion beam (FIB, ZEISS) for Lorentz transmission electron microscopy (LTEM) imaging. The specific choice of grain was detected from the polycrystalline sample using electron back scattered detector (EBSD) equipped with a dual beam platform. LTEM is performed for magnetic imaging using JEOL, 200 KV. A liquid nitrogen sample holder of Gatan is used to

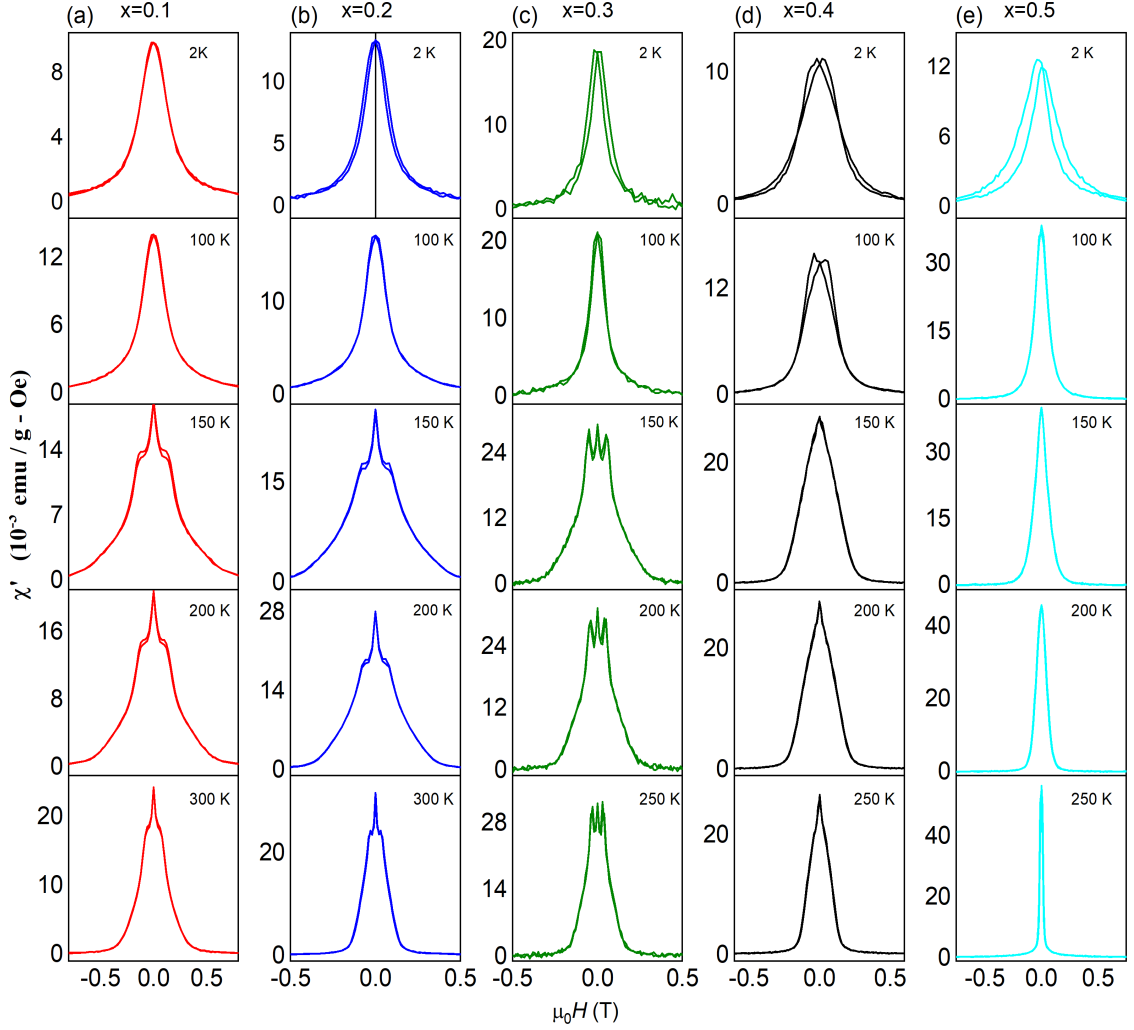


Figure 4.5: (Color online) Ac susceptibility data of $\text{Mn}_{1.4}\text{Pt}_{0.9}\text{Pd}_{0.1}\text{Sn}_{1-x}\text{In}_x$ for $x=0.1$ to 0.5 . (a)- d) Plot of the real part of ac susceptibility data with respect to dc magnetic field. The measurements are taken at selective constant temperatures above T_{SR} as mentioned in each plot. (e) χ (H) plot for $x=0.5$ at temperature 200 K, which is above the shoulder kind of feature [see $M(T)$ plot of $x=0.5$ in Fig. 1(a)]. (f)-(j) χ (H) plots taken at 2 K well below T_{SR} .

study the temperature-dependent LTEM. Powder neutron diffraction experiments are performed using a multi-position sensitive detector (PSD) based powder diffractometer (1.2443 \AA) at Dhruva reactor, Bhabha Atomic Research Centre.

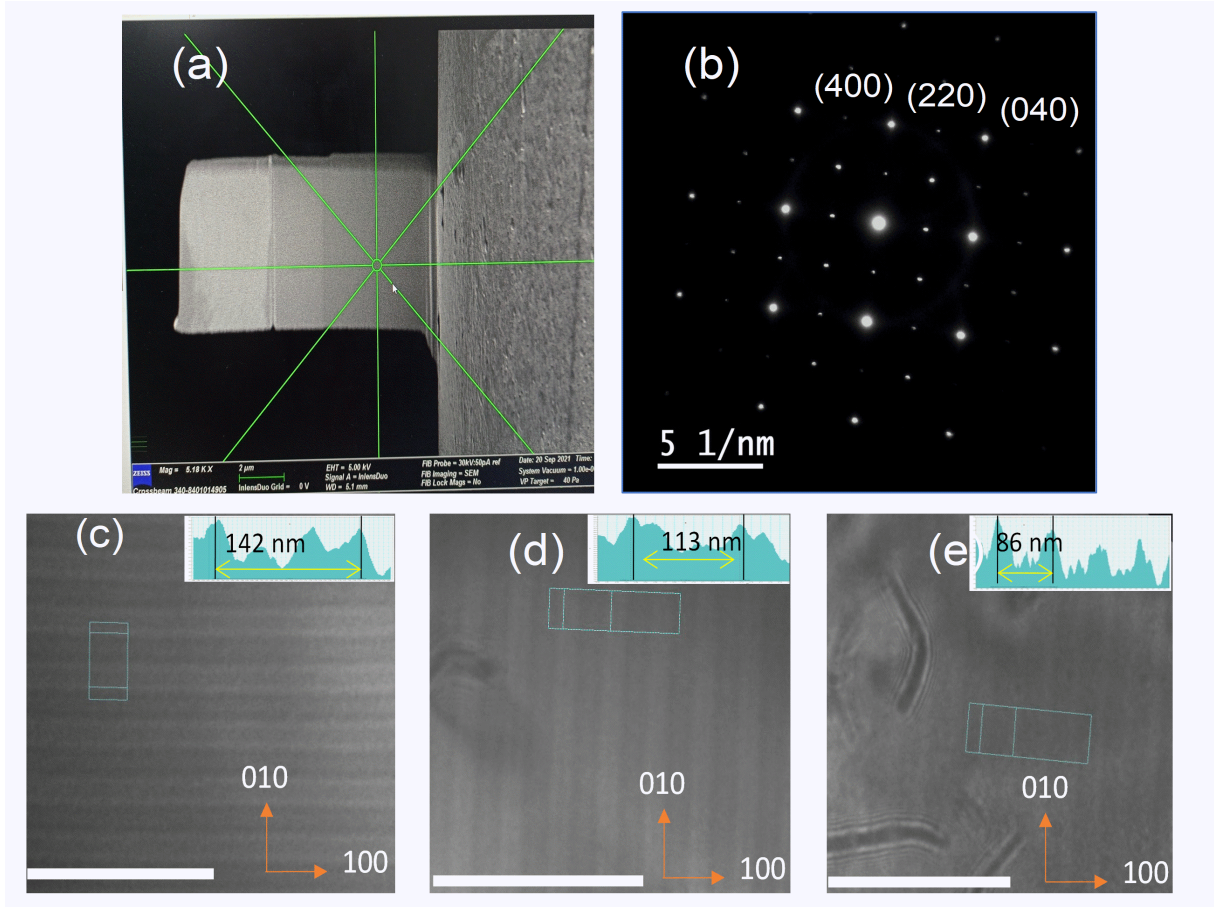


Figure 4.6: (Color online) (a) Side view of TEM lamella of $\text{Mn}_{1.4}\text{Pt}_{0.9}\text{Pd}_{0.1}\text{Sn}_{0.8}\text{In}_{0.2}$ sample with three different thickness regions as can be understood from the brightness contrast. (b) Selected area electron diffraction pattern for one of the regions. (c)-(e) Over focused LTEM images taken from the three different thickness regions. Helical modulation of the magnetic structure propagating along either (100) or (010). Right corner insets in (c)-(e) represent the intensity profile of the line scan marked in each figure. The scale bar in figure (c)-(e) is set to 500 nm.

4.4 Structural characterisation

The powder XRD measurements are performed for $\text{Mn}_{1.4}\text{Pt}_{0.9}\text{Pd}_{0.1}\text{Sn}_{1-x}\text{In}_x$ samples with $x = 0.1$ to 0.5 [see Fig. 4.1]. Rietveld refinement is performed to confirm the structural phase. It is found that all the samples crystallize in the inverse tetragonal crystal structure belonging to the space group $I\bar{4}2d$. The variation of lattice constants with the In concentration is shown in Fig. 4.2(a). It can be seen

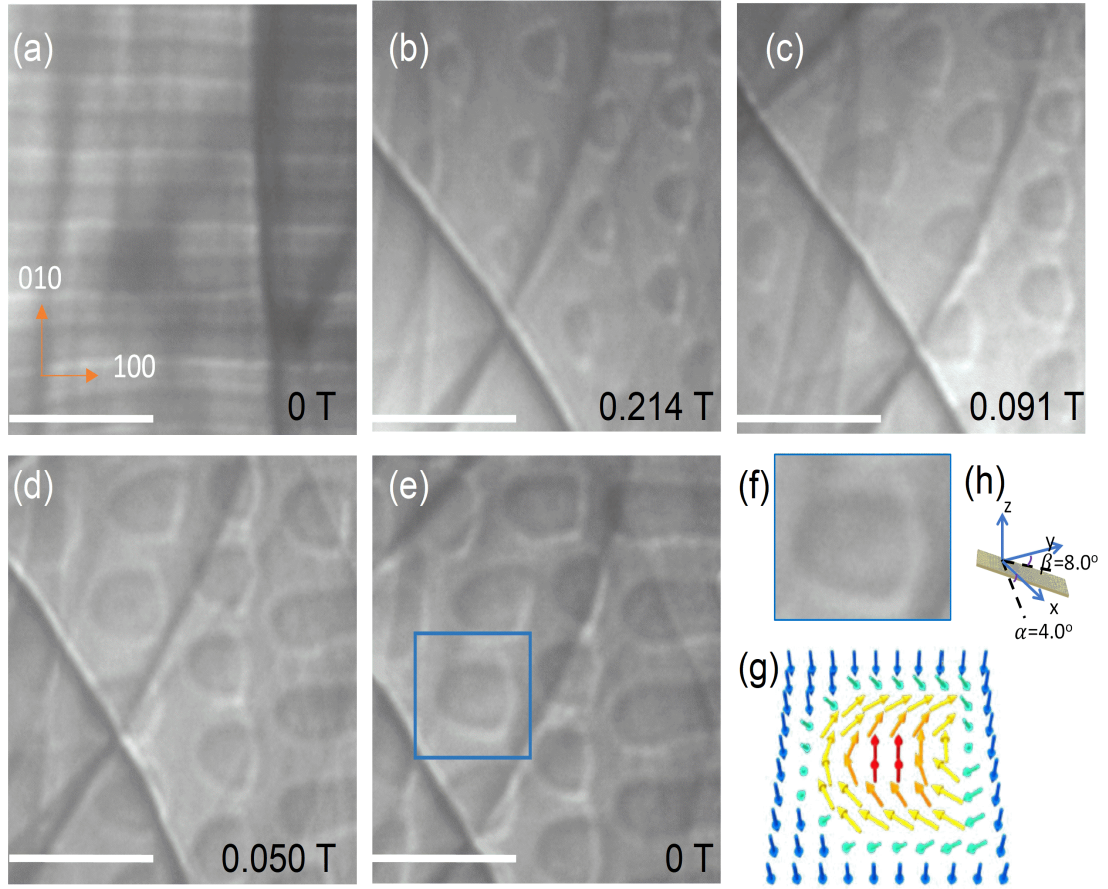
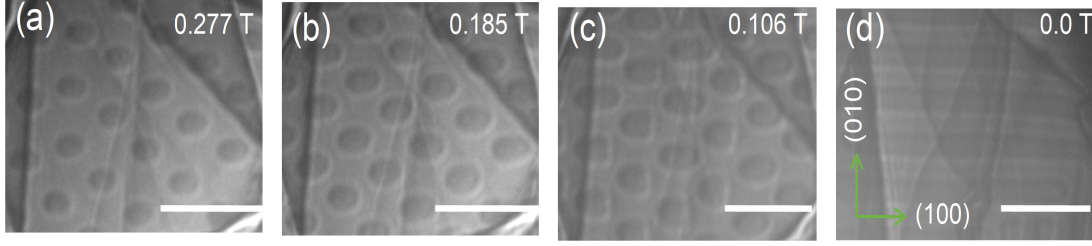


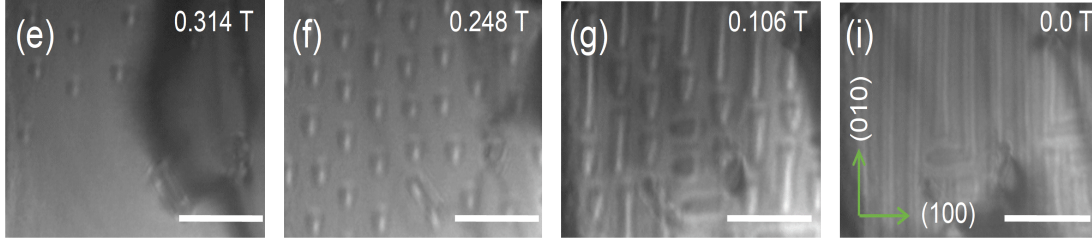
Figure 4.7: (Color online) Field evolution of non-topological bubble phase at 100 K temperature of $\text{Mn}_{1.4}\text{Pt}_{0.9}\text{Pd}_{0.1}\text{Sn}_{0.8}\text{In}_{0.2}$ sample. (a)-(e) Over-focused LTEM images captured under different magnetic fields as mentioned in each figure. (f) Zoomed view of a NT bubble selected from the marked area of (e). (g) The schematic spin texture of the NT [ref-[94]]. (h) Tilting angle from the pole position at which the images are taken. The angle α and β is the tilting angle about the X and Y axis from the pole position. The scale bar in each figure is set to 500 nm.

that there is no systematic variation of the long axis (c). However, the basal plane lattice constant ($a=b$) systematically increases with the increasing In concentration. The volume of the unit cell also increases with the In [inset of Fig. 4.2(a)]. The corresponding crystal structure is shown in Fig. 4.2(b). There are two Mn sublattice at 4a (0, 0, 0) and 8d (0.72, 0.5, 0.25) Wyckoff positions. Sn and Pt atoms occupy the 8d (0.27, 0.75, 0.125) and 8c (0, 0, z) Wyckoff positions, respectively.

$T=200\text{ K}, \alpha=12, \beta=5.6$



$T=250\text{ K}, \alpha=10, \beta=2.5$



$T=300\text{ K}, \alpha=9.7, \beta=4.6$

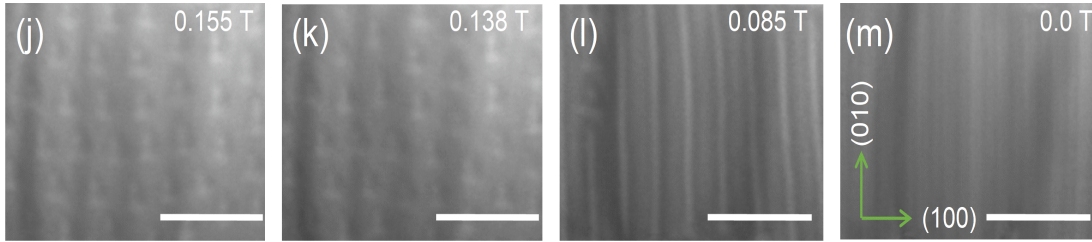


Figure 4.8: (Color online) Temperature and field evolution of skx and askx phase in $\text{Mn}_{1.4}\text{Pt}_{0.9}\text{Pd}_{0.1}\text{Sn}_{0.8}\text{In}_{0.2}$. (a)-(d) LTEM images taken at 200 K and different values of the magnetic fields as mentioned in each figure. (e)-(i) and (j)-(m) LTEM images of the askx phase and their field-dependent transformation at 250 K and 300 K, respectively. All the images presented here are captured in over-focused mode. The scale bar in each figure corresponds to 500 nm. The angle α and β is the tilting angle about the X and Y axis from the pole position.

4.5 Magnetic properties study

To study the magnetic properties of $\text{Mn}_{1.4}\text{Pt}_{0.9}\text{Pd}_{0.1}\text{Sn}_{1-x}\text{In}_x$ samples, the magnetization versus temperature $[M(T)]$ measurement is carried out in zero field cooled (ZFC) and field cooled (FC) modes as shown in Fig. 4.3. It can be seen that the Curie temperature (T_C) systematically decreases with increasing In concentration. However, the low-temperature spin re-orientation temperature (T_{SR}) remains

almost the same for In concentration up to $x=0.4$. For $x=0.5$, a hump kind of feature is observed around the 100 K. So, the range of $x=0.1$ to 0.4 shows a typical $M(T)$ plot as that of parent compound $Mn_{1.4}Pt_{0.9}Pd_{0.1}Sn$. Isothermal magnetization $M(H)$ measurements show a systematic decrement of the saturation magnetization M_S [see Fig. 4.4]. Also, ac susceptibility measurement is performed for all the samples. Figure 4.5(a)-(j) depicts the real part of ac susceptibility χ' data recorded at different selective temperatures. A dip and kink kind of feature is observed for $x=0.1$ to 0.3 sample for temperatures above T_{SR} [Fig. 4.5(a)-(c)]. For $x=0.4$, a broad shoulder-like signature is present [Fig. 4.5(d)]. However, below T_{SR} , there is no such anomaly in χ' (H) data for $x=0.1$ to 0.4 [Fig. 4.5(f)-(i)]. In the case of the $x=0.5$ sample, no anomaly is evident throughout the ordered phase [Fig. 4.5(e) and (j)]. Therefore, it is expected that the $skx/askx$ phase is present only above T_{SR} for samples up to $x=0.4$.

4.6 Lorentz transmission electron microscopy study

For the real space visualization of $skx/askx$ phase in the above-mentioned samples, first the sample with $x=0.2$ having a T_C more than 300 K is selected for LTEM the imaging. For this purpose, TEM transparent thin lamella of (001) oriented grain are prepared using FIB. Three different thickness regions of 180, 150, and 120 nm thin are prepared to see the effect of the dipolar interaction as a function of the thickness. The details of the different steps employed to prepare the lamella is described in chapter -2. Figure 4.6(a) shows the side view of the lamella captured in SEM during the preparation stage. The variation in the thickness of the lamella can be understood from the color contrast. The (001) orientation of the grain is confirmed by performing selected area electron diffraction (SAED), as can be seen from Fig. 4.6(b). Figure 4.6(c)-(e) depict the room temperature over focused LTEM images collected from three different thickness areas in zero field. As it can be seen, a helical magnetic state is present in the sample propagating in the (100) [Fig. 4.6(d) and (e)] and (010) [Fig. 4.6(c)] direction. It can be seen that the helical modulation

period strongly depends on the thickness of the lamella due to the dipolar field effect. In the present case length of the helical period increases with increasing thickness of the lamella.

Absence of antiskyrmion below T_{SR} : To understand the effect of temperature on the antiskyrmion phase stability, first the sample is cooled down to the lowest possible temperature of 100 K under zero-field condition. A helical-like state can be seen at 0 T field and propagating along (010) direction [Fig. 4.7(a)]. The application of magnetic field destroys the particular orientation of the helical state and creates a stripe domain-like structure. Further increasing the field creates few isolated non-topological (NT) bubbles. The initial helical magnetic state could not be restored after the removal of the magnetic field. To generate a dense NT magnetic bubbles in the sample, we first brought the sample to the pole position and applied a magnetic field until saturation. In this saturation field condition, the sample is tilted away from the zone axis by $\alpha = 15$ -17 and $\beta = 10$ -12 degree. Then started slowly tilting back towards the pole position and decreasing the field by small steps as well. The process is continued until some of the isolated NT bubbles are formed. At this condition, we fixed the sample position and took the images by decreasing the field only. Fig. 4.7(b)-(e) depicts the field evolution of the NT bubble phase. In this process, at zero field, a mixed state of stripe domain and NT bubbles is obtained. Figure 4.7(f) and (g) are the zoomed view of a NT bubble and the corresponding spin texture, respectively. Figure 4.7(h) depicts the tilt condition of the lamella at which the images are collected.

Skyrmion and antiskyrmion above T_{SR} : To observe the askx and skx in $\text{Mn}_{1.4}\text{PtSn}_{0.8}\text{In}_{0.2}$ sample, LTEM imaging is performed above T_{SR} . At zero field a helical state is found as discussed before. The application of magnetic field only nucleates very few numbers of isolated askx/skx depending on the temperature. So, to form a dense skx or askx lattice, we have followed the same step as discussed in the previous paragraph. Figure 4.8(a)-(d) depicts the field evolution of the hexagonal lattice of elliptical Bloch skx phase at 200 K. With decreasing field a mixed phase of the non-topological bubble (triangular shape) and skx also appeared [Fig. 4.8(c)]. A

helical phase is retrieved in the zero magnetic field [Fig. 4.8(d)]. A triangular lattice of askx is formed at elevated temperatures. Figure 4.8(e)-(i) and Fig. 4.8(j)-(m) describe the field evolution of askx phase at 250 K and 300 K, respectively. With decreasing magnetic field, a mixed phase of non-topological magnetic bubbles and askx are observed at these temperature [Fig. 4.8(f) and Fig. 4.8(k)]. In all cases, the helical phase can be obtained by reducing the magnetic field to zero.

4.6.1 Spontaneous meron and antimeron formation

Merons (antimerons) are distinctive type of topological non-coplanar objects with a topological charge of $-1/2$ ($+1/2$). They are categorically different quasi particles in comparison to the fractional skx/askx, which are found at the sample edge [134]. Basically, the fractional skx/askx are the diametric bi-section of full skx/askx with peripheral spin directed in the opposite way to the core. Unlike skx, the peripheral spins in meron remain in-plane [see Fig. 4.9(a) and (b)]. The spin curling mechanism in both meron and skx can be of the same origin, i.e., competing Heisenberg exchange and DMI. However, their stability can be separated by the finite energy barrier introduced through variation in anisotropy [135, 136], and Zeeman energy [137], etc. The transformation from an integer topological charge to a fractional value occurs through a first-order phase transition. However, recent observations of continuous transformation of topological charge can be regarded as the counteracting forces due to the twist of the edge spin and the repulsive forces from the interior lattice part of the sample [134]. In this system, the energy landscape is more important than the topology of the spin structure. Therefore, a delicate balance between various magnetic interactions can be a standard pathway for such a control on the topological spin structures.

From ac-susceptibility data, it is understood that the $\text{Mn}_{1.4}\text{Pt}_{0.9}\text{Pd}_{0.1}\text{Sn}_{0.6}\text{In}_{0.4}$ is the border sample between an skx hosting and trivial non-collinear ordered system. Therefore, this sample can be regarded as a junction of topological ambiguity. Indeed we observe the formation of merons and antimerons chains within the helical stripe.

It should be noted that the formation of the meron/antimeron chain is spontaneous and at a temperature below T_{SR} [see Fig. 4.9(c) and (d)]. The spin texture of the bright dot, as shown in Fig. 4.9(d), is speculated from the intuition of different literature surveys. The actual spin texture can be understood after analysing the transport of intensity equation (TIE).

It is important to check their stability and spin modulation against the external magnetic field. Figure 4.10(a)-(h) depicts the field evolution of the pair of a chain of merons and antimerons. It can be seen that they remain stable up to a field value of 0.07 T [see Fig. 4.10(f)]. Above that, only the stripe helical phase converted to a field polarized state. Unlike the skx hosting samples, here, at 102 K temperature, we do not observe the formation of any non-topological bubbles. It can be noticed that the merons/antimerons chain pairs, (1,2) and (3,4), are well separated at the lower fields. With increasing field, both the pairs (1,2) and (3,4) come closer before they disappear. It can be mentioned here that the antimerons chain (black dot marked with blue dashed lines) only moves and comes closer to the meron chain (black dot marked with red dashed lines). The meron chains are rigid because the core spin points downward, which costs extra energy to alter the direction. It can be noticed that the antimerons move through the black stripe portion of the helical state towards the meron chain with the increasing field before they vanish. The formation of merons and antimerons within the helical stripe possesses a huge potential from the application point of view. The findings of domain wall skx and its constrained motion along the domain wall provide an alternate way to escape the much-debated skx Hall effect [138]. As merons/antimerons also hold the fractional topological charge with particular helicity, they can be treated on an equal footing for data processing. In a similar way, it is also found that the antimerons move in the stripe pattern with application of magnetic fields.

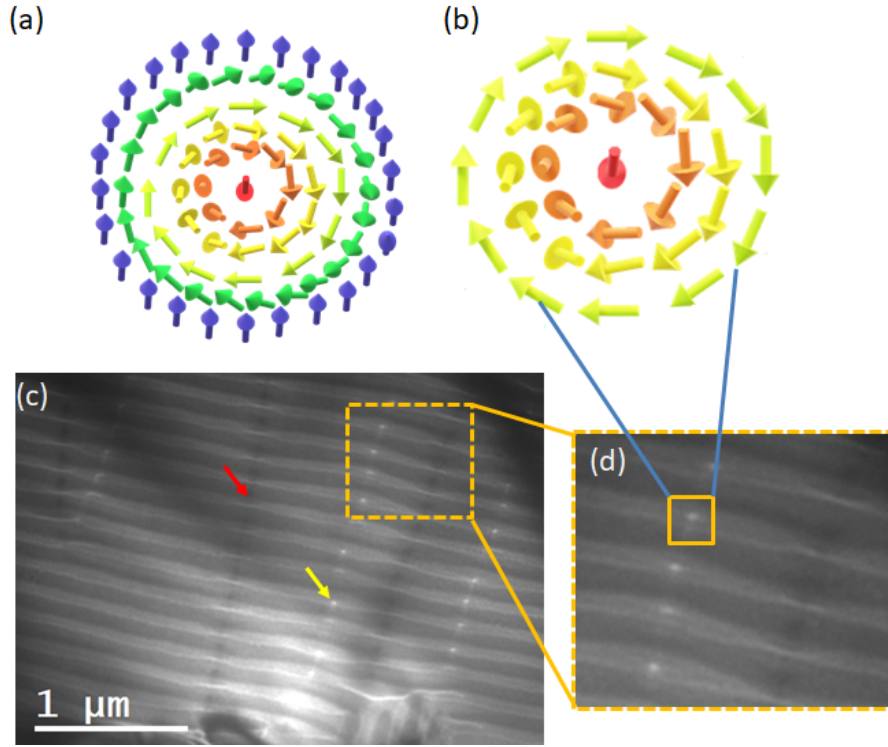


Figure 4.9: (Color online) (a) Core down skyrmion. (b) Core down meron. (c) Over focus LTEM image taken at 102 K. The chain of meron and antimeron evident in the $\text{Mn}_{1.4}\text{Pt}_{0.9}\text{Pd}_{0.1}\text{Sn}_{0.6}\text{In}_{0.4}$ sample are indicated by yellow and red arrow, respectively. (d) Enlarge view of the highlighted region in yellow dashed rectangle of (c).

4.7 Neutron diffraction (ND) study

4.7.1 Neutron diffraction study of $\text{Mn}_{1.4}\text{PtSn}_{0.8}\text{In}_{0.2}$

So far, the ac susceptibility data and the LTEM measurements confirm the presence of topological phase like skx/askx above T_{SR} and $x = 0.1$ to 0.3 samples and merons/antimerons for $x = 0.4$. To understand the underlying ground of magnetic states in these samples, first we have performed temperature dependent powder neutron diffraction measurements for $\text{Mn}_{1.4}\text{PtSn}_{0.8}\text{In}_{0.2}$. As can be seen from Fig. 4.11(a), the scattering intensities of the nuclear Bragg peaks (101), (200), and (004) increase with decreasing temperature. The intensity of the Bragg peak (101) enhances only below the T_{SR} . Enhancement of the intensity on top of the nuclear

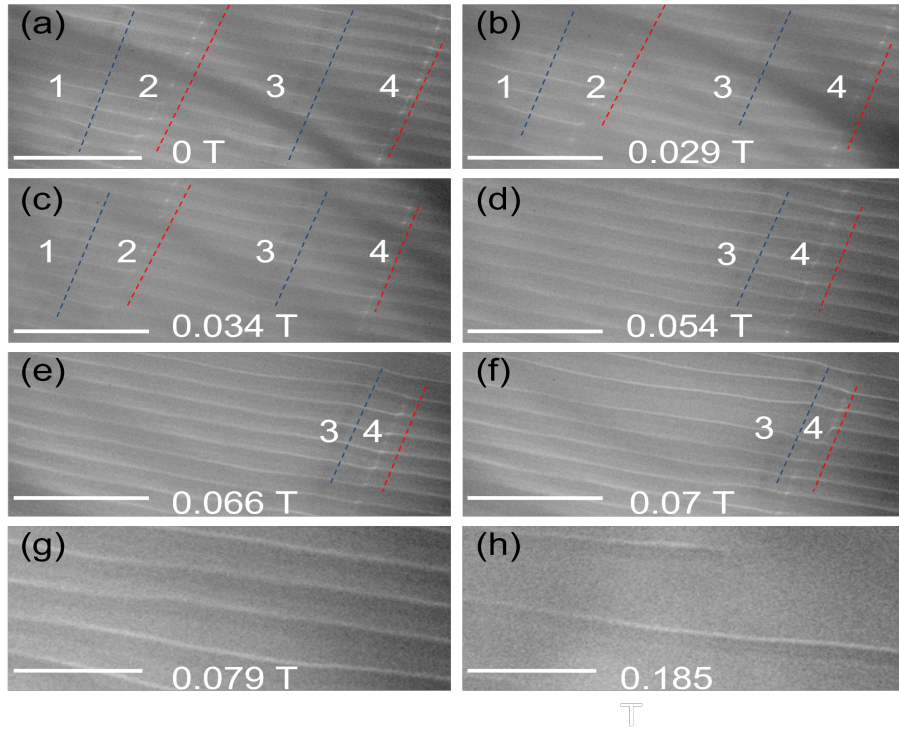


Figure 4.10: (Color online) Field evolution of two pairs of chain of meron and anti-meron. (a)-(h) OF LTEM images taken at $T = 102$ K and at different field value as mentioned in the each figure. The meron anti-meron chain pair are indicated by blue and red dashed lines for visual guidance. Scale bar in each figure is $1 \mu\text{m}$.

Bragg peak suggests a commensurate magnetic structure with propagation vector $\mathbf{k}(0, 0, 0)$. To extract the magnetic structure, we have performed the Rietveld refinement, including the structural and magnetic phases. Figure 4.11(b) and (c) depicts the Rietveld refinement of 5 K and 300 K ND data. The underlying magnetic structure obtained after the refinement is shown in Fig. 4.12(a) and (b), respectively. A non-collinear ferrimagnetic ordering is observed at 5 K [see Fig. 4.12(a)]. However, a collinear ferromagnetic ordering of the constituent Mn atoms is found at 300 K [see Fig. 4.12(b)]. Rietveld refinement is also performed for all the ND data taken at different temperatures. It is observed that the non-collinear ordering exists up to the $T \leq T_{SR}$. The collinear ordering among the constituent spin is found in the temperature window $T_{SR} \leq T \leq T_C$. Figure 4.13(a) and (b) describe the temperature variation of the component of the sub-lattice moments. It can be noticed that

all the magnetic sub-lattices exhibit in-plane component of the moment below T_{SR} . This in-plane components of the magnetic moment couples antiferromagnetically. However, only the M_Z component of the magnetic moments for all the magnetic sublattices is observed for above T_{SR} . The release of the in-plane component may be associated with the sudden change in the lattice parameters around the T_{SR} as can be seen from Fig. 4.13(c). Most possibly, the onset of competing exchange interaction below T_{SR} causes the formation of a non-collinear magnetic structure. Above T_{SR} , the thermal energy may be enough to overcome the competing exchange fluctuation and resulting a collinear ordering.

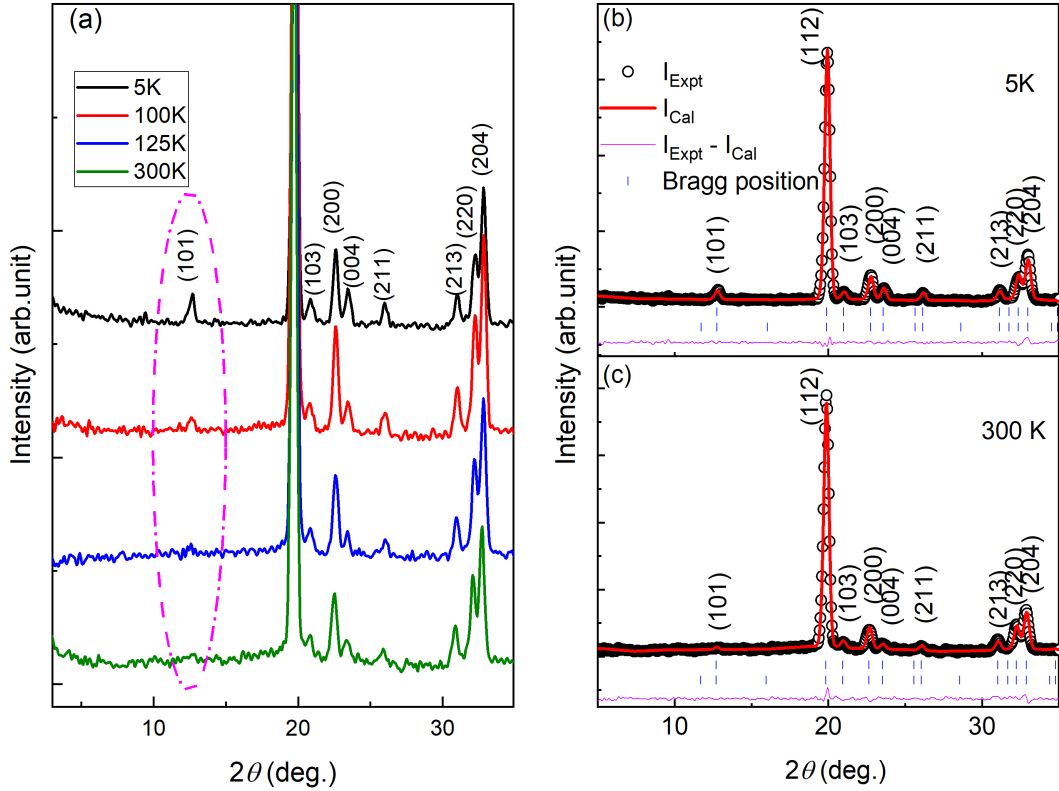


Figure 4.11: (Color online) (a) Intensity plot of powder neutron diffraction data with respect to diffraction angle 2θ . The various color lines represents ND data recorded at different constant temperature indicated in the inset. For a clear view of the major magnetic reflections, the patterns are magnified in the range of 3 to 35 degrees. The Bragg peak (101) is highlighted by a magenta color dash line ellipse. (b) and (c) Rietveld refinement of the 5 K and 300 K ND data by taking the magnetic contribution into account.

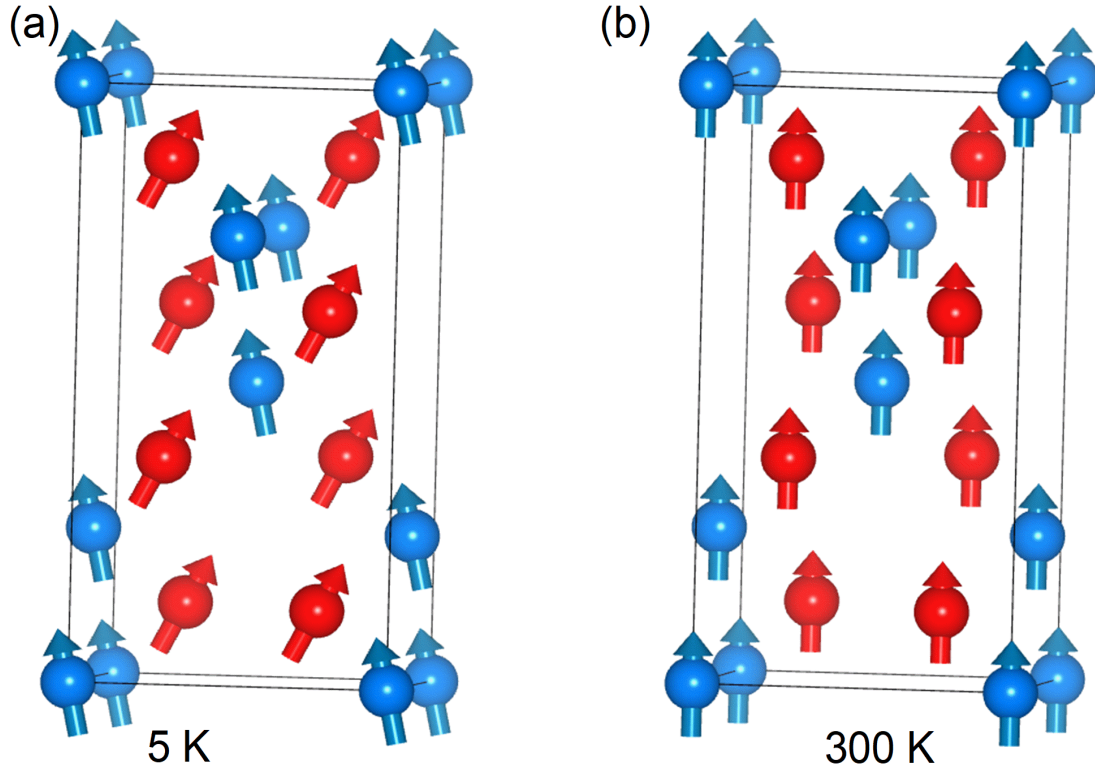


Figure 4.12: (Color online) (a) and (b) Simulated magnetic structure of $\text{Mn}_{1.4}\text{PtSn}_{0.8}\text{In}_{0.2}$ at 5 K and 300 K, respectively.

4.7.2 Neutron diffraction study of $\text{Mn}_{1.4}\text{PtSn}_{0.4}\text{In}_{0.6}$

To understand the nature of magnetic ground state in $\text{Mn}_{1.4}\text{PtSn}_{0.4}\text{In}_{0.6}$, we have performed the powder neutron diffraction experiments at different temperatures for $\text{Mn}_{1.4}\text{PtSn}_{0.4}\text{In}_{0.6}$. Figure 4.14(a) depicts the ND data taken at different temperatures. The intensity of the nuclear Bragg peaks (101), (200), and (004) increases consistently with decreasing temperature. In the present system, the intensity of (101) starts enhancing below the ordering temperature itself, in contrast to $\text{Mn}_{1.4}\text{PtSn}_{0.8}\text{In}_{0.2}$ case where it gains intensity only below T_{SR} . To get the information of the underlying magnetic structure, we take the non-collinear magnetic structure model similar to the 5 K magnetic structure of $\text{Mn}_{1.4}\text{PtSn}_{0.8}\text{In}_{0.2}$. Figure 4.14(b) and (c) shows the Rietveld refinement, including the structural and mag-

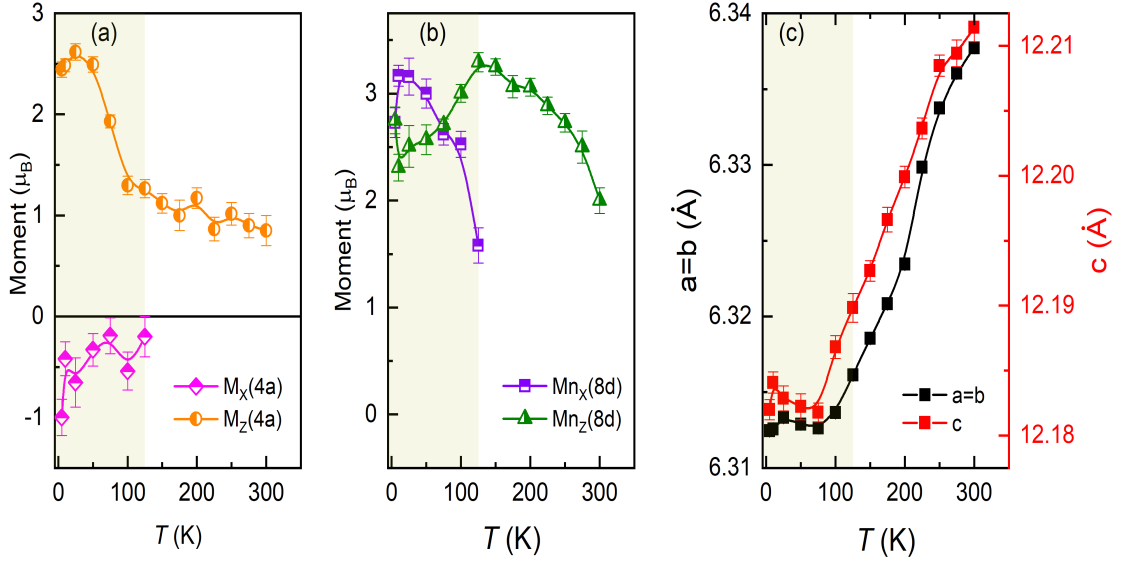


Figure 4.13: (Color online) (a) and (b) Variation of component of the sub lattice moment with temperature. (c) Temperature variation of lattice constant (a and c).

netic phases. The inset in Fig. 4.14(b) is the obtained magnetic ordering of the Mn atoms at 5 K. It is found that the magnetic moments for the Mn atoms at 8d Wyckoff position are aligned completely in-plane. However, the Mn atoms sitting at 4a position show both in-plane and out-of-plane components of the magnetic moment. The in-plane components of Mn moments at 4a and 8d form an antiferromagnetic alignment. The temperature variation of different components of the Mn_{4a} and Mn_{8d} moments are shown in Fig. 4.14(a) and (b). Figure 4.14(c) describes the temperature dependency of the lattice constants a and c .

4.8 Discussion

The ac susceptibility data shows the existence of $skx/askx$ phase only above the T_{SR} for $x=0.1-0.4$. Lorentz transmission electron microscopy (LTEM) measurements confirm the presence of skx and $askx$ in this system only above T_{SR} . Below T_{SR} , non-topological bubbles can be found. Powder ND analysis performed on the $Mn_{1.4}PtSn_{0.8}In_{0.2}$ sample reveals a non-collinear and collinear magnetic ordering

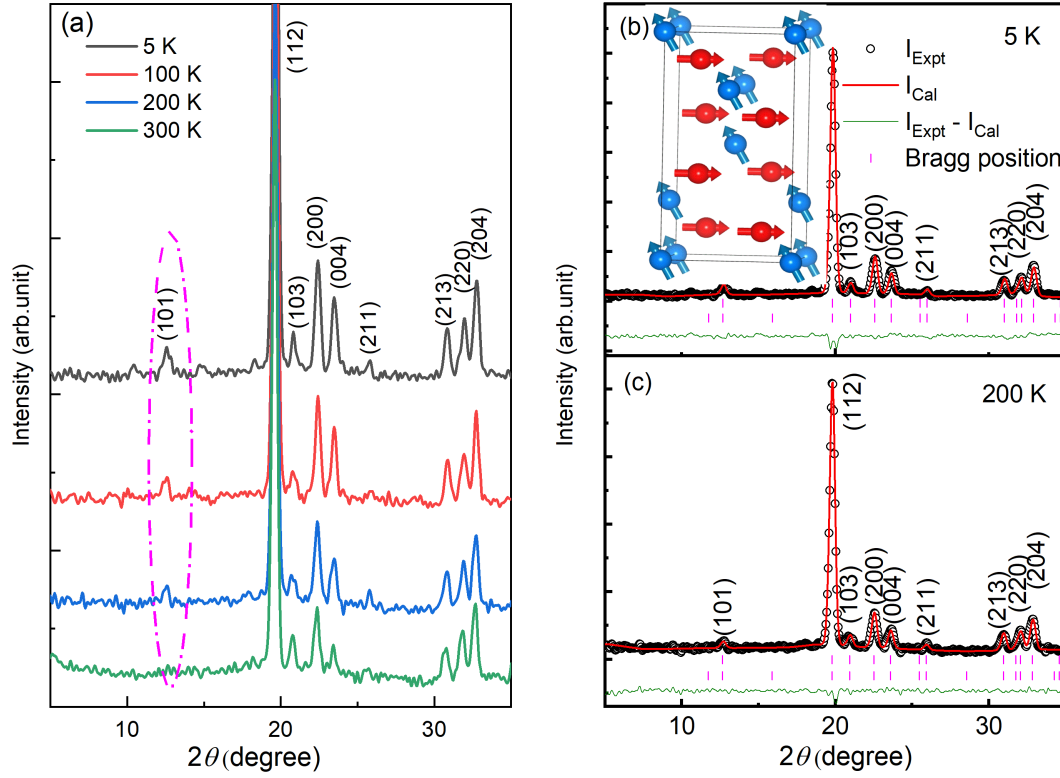


Figure 4.14: (Color online) (a) Intensity plot of powder neutron diffraction data of Mn_{1.4}PtSn_{0.4}In_{0.6} sample with respect to diffraction angle 2θ . The various color lines represent ND data recorded at the different constant temperatures indicated in the inset. For a clear view of the major magnetic reflections, the patterns are magnified in the range of 3 to 35 degrees. The Bragg peak (101) is highlighted by a magenta color dash line ellipse. (b) and (c) Rietveld refinement of the 5 K and 200 K ND data by taking the magnetic contribution into account. The inset magnetic structure corresponding to 5 K ND data.

of the Mn spin below and above T_{SR} , respectively. The powder ND experiment performed on higher In doped samples shows a non-collinear magnetic ordering throughout the temperature range in their ordered phase. Interestingly, this system does not show any signature askx/skx over the whole temperature range of the order phase. It is a well-known fact that thermal stability plays an important role in stabilizing the skx/askx in all skyrmion hosting materials. In fact, the first experimental evidence of magnetic skx in the MnSi system appeared within a narrow temperature pocket near T_C . In contrast, a thermal equilibrium skx phase is evident in an achi-

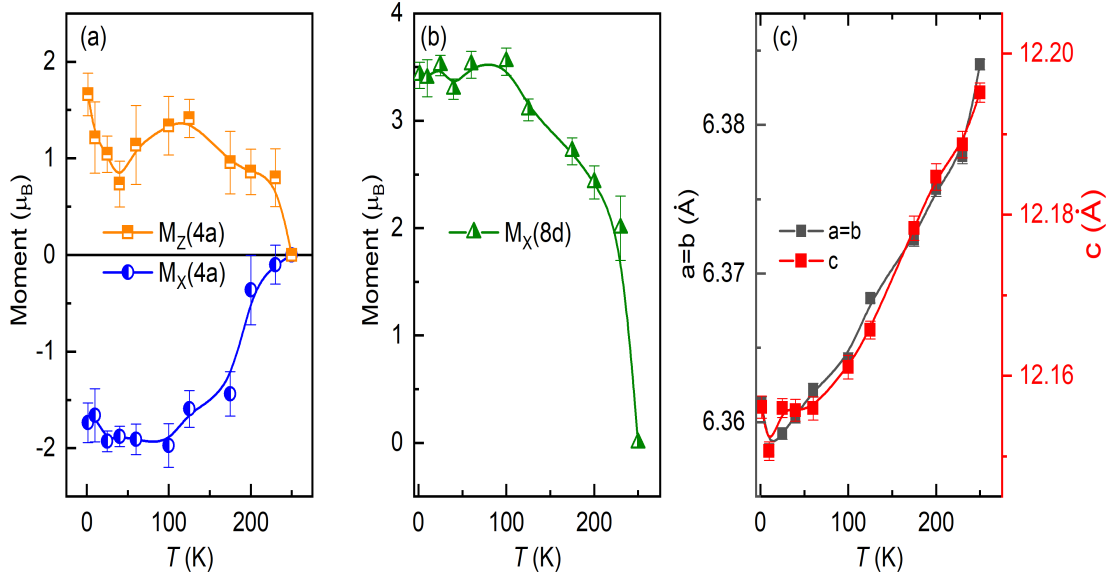


Figure 4.15: (Color online) (a) and (b) Variation of component of the sub lattice moment with respect to temperature. (c) Temperature variation of lattice constant a and c .

ral geometrically frustrated system [15]. Therefore it is necessary to consider the exchange and thermal fluctuation in the system. Mainly in the metallic system, the effective exchange strength may not be limited to the nearest neighbor site only. The itinerant electron can give an oscillatory Ruderman–Kittel–Kasuya–Yosida (RKKY) type interaction extended beyond the nearest neighbor. With temperature, the system may evolve through the grip of varying effective exchange strength. Therefore, the competing exchange interaction can have an intriguing effect on the formation of different nontrivial phases. For instance, exchange frustration leads to the development of novel disorder and local clustering of skx phase in β -Mn structure-type Co-Zn-Mn alloys [139]. Furthermore, the magnetic ground state in inverse tetragonal Mn_2RhSn , Mn_2IrSn , and Mn_2PtIn is extensively shown to be non-collinear as a result of exchange frustration[48]. These systems also show a similar kind of spin-reorientation transition to that of the present systems under study. Moreover, the askx phase found in the Mn_2RhSn system above T_{SR} only [115]. Again, Swekis et al. showed that the origin of the spin re-orientation in $\text{Mn}_{1.5}\text{PtSn}$ is associated with

the exchange frustration [140]. The description of the low temperature non-collinear state was explained using an atomistic spin model with the competing classical exchange interaction given by the equation-

$$H = -J_1 S_i^1 \cdot S_j^2 - J_2 S_k^1 \cdot S_l^1 - J_3 S_m^2 \cdot S_n^2. \quad (4.1)$$

J_1 is the inter sub-lattice interaction, J_2 and J_3 are the Mn_{8d} and Mn_{4a} intra-site interactions for each sub-lattices, respectively. It exemplified the role of all interactions in achieving a non-collinear spin texture in this system. Therefore, in the present systems, the low temperature (below T_{SR}) formation of a non-collinear state is most likely due to the exchange frustration. However, the non-collinearity in the higher Indium doped system may arise from the higher order exchange interaction and need a rigorous study. Because the addition or reduction in valence electron counts through Indium doping can maximally impact the interaction, which is linked to the higher power of moments such as RKKY, biquadratic ($\propto (S_i \cdot S_j)^2$), and topological-chiral interaction ($\propto [S_i \cdot (S_j \cdot S_k)]^2$). Therefore, below the certain Indium concentration, either the exchange frustration or the higher order interactions may drive the system to a non-collinear magnetic ordering throughout the order phase. Therefore, the combined ac susceptibility results, LTEM imaging, and ND study establish that the formation of the asks phase requires a collinear arrangement of background spin for the present systems. Most possibly, the exchange frustration-driven non-collinearity hinders the formation of askx in the Mn-Pt(Pd)-Sn-In system in the low-temperature region (below T_{SR}).

4.9 Conclusion

In summary, this chapter includes an extensive study of effect of exchange frustration on the stability of skx/askx phase in Mn-Pt(Pd)-Sn-In system. Most possibly, the exchange frustration favor a non-collinear magnetic ground state below T_{SR} and avert the formation of askx in the Mn-Pt(Pd)-Sn-In system. This result is in sharp

contrast to the theoretical prediction of smaller sk_x/ak_x in centro-symmetric system due to exchange frustration. Therefore, this study reveal the effect of magnetic frustration in presence of DMI in Mn-Pt(Pd)-Sn-In inverse tetragonal system. Moreover, we observe the presence of a fractional topological object like meron and antimeron within the helical stripe pattern, which may have special importance for the spintronics application perspective.

Chapter 5

Large exchange bias and non-trivial interface spins in compensated ferrimagnets

“Facts are many, but the truth
is one.”

Rabindranath Tagore

5.1 Introduction

The exchange bias (EB) field can be described as an asymmetrical offset of the magnetic hysteresis loop $[M(H)]$ [20, 78]. The phenomena of EB was first observed by Meiklejohn and Bean in 1956 [78]. It is believed that the EB phenomena originates from the interfacial exchange coupling between a ferromagnetic (FM) and an anti-ferromagnetic (AFM) material. Although the FM/AFM interface is the inseparable element for realizing EB, its microscopic origin is the subject of discussion even today. In this context, various models, e.g. rough FM-AFM interface [83], uncompensated interface spin [84], and domain state model [85], etc., have been developed

to through more insight into the phenomena. An essential requirement for most of the microscopic models is the finite magnetization at the interface from the AFM layer, which plays a crucial role in the interface exchange field and causes asymmetry in the hysteresis loop. The exchange field H_E , which is in general inversely proportional to the magnetization M_{FM} of the ferromagnet, can be controlled by tuning the M_{FM} and nature of the interface. In corroboration, very recently, Nayak *et al.* have demonstrated a protocol and simultaneously obtained a very high exchange bias field in bulk polycrystalline tetragonal Heusler compounds Mn-Pt-Ga, where the antisite disorder results in an FM cluster embodied in the compensated ferrimagnetic host [47, 82]. Over the last few decades, the exchange bias effect has been studied extensively due to its utmost application in spintronics, e.g., setting up the pinning layer in giant magneto-resistance (GMR) based devices [24, 25, 26, 27] and to beat the super-paramagnetic limit in magnetic nano-particles based in ultra-high density recording media [141].

The finding of extremely large EB as well as large coercive field (H_C) in anti-site disorder induced magnetic inhomogeneous systems demands a comprehensive understanding of their origins. It has been proposed that the magnitude of the EB field can attain several Tesla by considering anisotropic exchange, the Dzyaloshinskii-Moriya interaction (DMI) in the system [21, 22, 23]. The DMI assisted by the inversion symmetry breaking at the interface can drastically modify the interfacial coupling as it prefers a perpendicular spin alignment of the neighboring spins. In the case of a bulk inhomogeneous magnetic systems, the presence of anti-site disorder can easily break the local inversion symmetry resulting in a non-zero DMI, even in a centrosymmetric material.

The present chapter is focused on the existence of a large tunable EB and related phenomena on the basis of the combined effect of symmetric and antisymmetric interface exchange between FM cluster and compensated ferrimagnetic host in the cubic compounds $Mn_{3-x}Pt_xIn$ and $Mn_{3-y}Ni_yIn$. Using THE measurement, it is found that there exists a non-trivial magnetic structure at the interface. The formation of such a non-trivial structure of the uncompensated interface spin causes a

large exchange bias field in this system.

5.2 Motivation

Mn₃In crystallizes in a cubic structure with 52 atoms in a unit cell, which can be divide into two atomic clusters, each containing 26 atoms and centred at (0, 0, 0) and (0.5, 0.5, 0.5) [99, 100]. For a better understanding of the exact nature of the atomic arrangement, the unit cell of Mn₃In system decomposed into several parts based on the general symmetry analysis as depicted in Fig. 5.1(a)-(f). Each cluster (labeled as A and B) contain an inner tetrahedron (IT), an outer tetrahedron (OT), an octahedron (OH), and a cuboctahedron (CO). All the atomic sites of cluster-A are fully occupied by Mn atoms only [Fig. 5.1(d)]. In the case of cluster-B, IT and OT are completely occupied by Mn atoms, whereas OH and CO sites are mostly filled by the Mn and In atoms, respectively (with OH containing two In and rest Mn while CO involves one Mn and rest In atoms), as shown in Fig. 5.1(e). The mixed occupancy between Mn and In atoms at the OH and CO sites of cluster B intrinsically induces antisite disorder in the system. It provides the advantage of the complex/unique atomic arrangement and the presence of intra-unitcell clusters to tune the EB in the system. The assessment is based on the fact that the magnitude of antisite disorder can be readily modified by the substitution of non-magnetic/magnetic atoms, thereby tailoring the long-range magnetic order to formulate an inhomogeneous magnetic ground state. Interestingly, doping with non-magnetic heavy metals with strong spin-orbit coupling gives us the luxury to play with local crystalline symmetry to induce Dzyaloshinskii-Moriya interaction (DMI). Therefore, the present material platform [Pt and Ni-doped cubic Mn₃In alloys] can simultaneously host the existence of large EB and FCF behavior. This study mostly concentrates on the Pt and Ni-doped Mn₃In alloys to facilitate tunable exchange bias field.

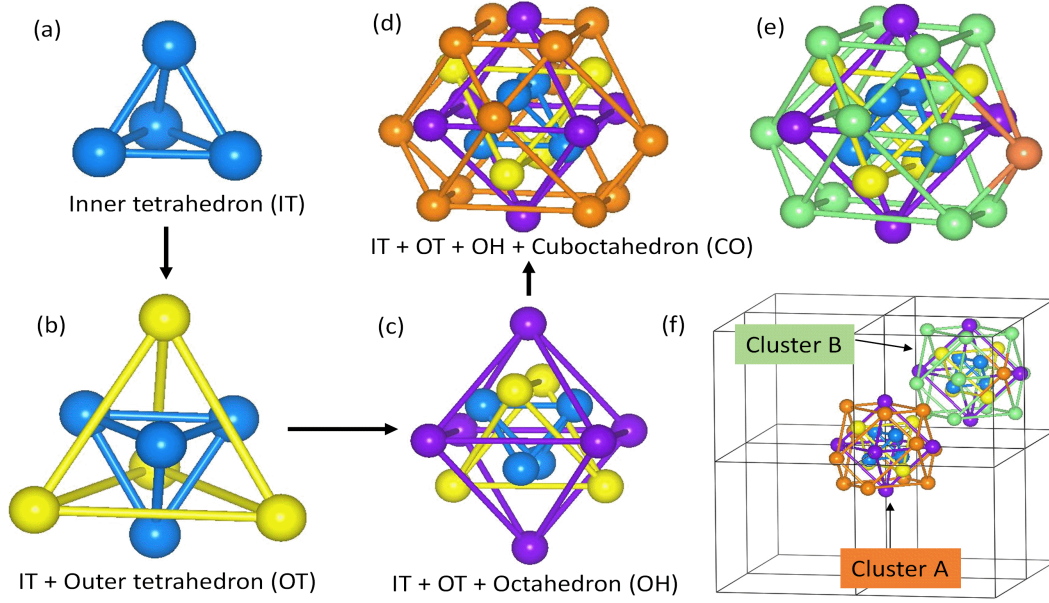


Figure 5.1: (Color online) Mn₃In crystal structure. (a) Four Mn atoms (blue balls) connected to each other, forming an inner tetrahedron (IT). (b) Four Mn atoms (yellow balls) form an inverted outer tetrahedron (OT), which is rotated by 30 degrees with respect to the IT. (c) Six Mn atoms (violet balls) form an octahedron (OH) in a way such that each OH atom is close to two IT and two OT atoms. (d) The IT, OT, and OH atoms held inside the cuboctahedron (CO) are formed by twelve Mn atoms (orange spheres). Altogether, the arrangement of IT + OT + OH + CO is called cluster-A. (e) cluster-B: It is also formed in a similar way to that of cluster-A. The only difference is that here the CO contains eleven In atoms (light-green balls) and one Mn atom (orange ball), and the OH is composed of four Mn atoms (violet balls) and two In atoms (light-green balls). Atomic composition/geometry for the IT and OT are the same as of cluster-A. (f) Extended view of Mn₃In unit cell with cluster-A centered at (0, 0, 0) and cluster-B at (0.5, 0.5, 0.5).

5.3 Experimental details

Polycrystalline samples of Mn_{3-x}Pt_xIn for $x = 0.1$ to 0.3, and Mn_{3-y}Ni_yIn for $y = 0.1$ and 0.2 were prepared by arc-melting technique. The desired constituent elements were taken and melted under an Ar gas atmosphere within the arc melt chamber. As prepared samples were vacuum sealed within a quartz tube. Under this condition, a heat treatment for eight days at 1073 K temperature was completed and subsequently quenched in the ice water mixture. Room temperature

x-ray diffraction measurements were performed on powder sample using a Rigaku SmartLab x-ray diffractometer with a Cu-K α source to characterize the structural phase.

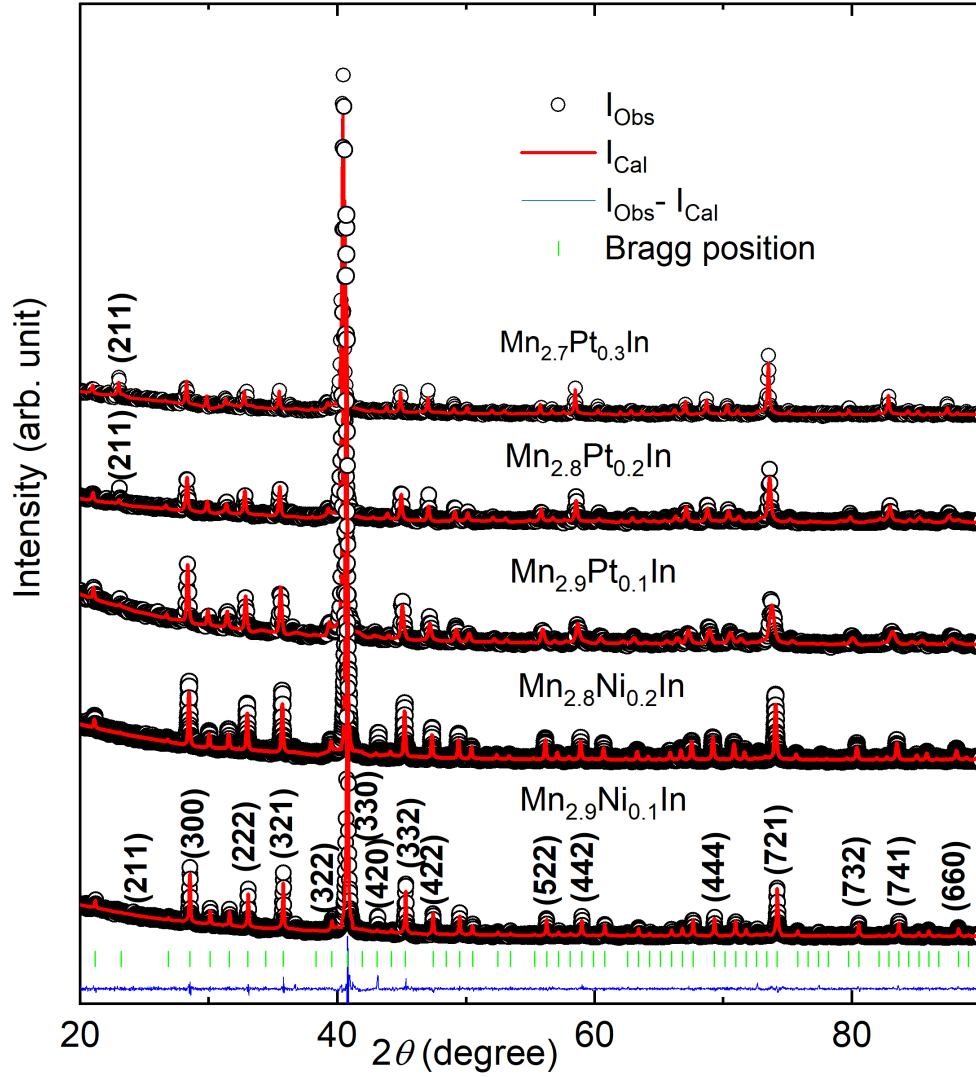


Figure 5.2: (Color online) Room temperature powder XRD patterns for $\text{Mn}_{3-x}\text{Pt}_x\text{In}$ and $\text{Mn}_{3-y}\text{Ni}_y\text{In}$ for $x = 0.1$ to 0.3 . and $y = 0.1$ and 0.2 . The open black circles in the figure represent the experimental data, and the red solid lines correspond to the simulated data. The difference between the experimental and simulated data is shown by the blue color solid line. The green vertical lines indicate the Bragg positions. The (h k l) values for all major reflections are shown for $\text{Mn}_{2.9}\text{Ni}_{0.1}\text{In}$ in the sample.

A field emission scanning electron microscope (FESEM) equipped with an energy dispersive x-ray (EDS) analysis detector was utilized to confirm the composition

homogeneity. Low-field magnetic measurements were carried out using a SQUID vibrating sample magnetometer (MPMS-3, Quantum Design) and VSM option in Quantum Design Physical Property Measurement System (PPMS). Transport measurements were performed using Quantum Design PPMS. Pulsed-field magnetization measurements up to 60 T were carried out at the Dresden High Magnetic Field Laboratory HLD-HZDR. The 32 T static magnetic field measurements were performed using a vibrating sample magnetometer at the High Field Magnet Laboratory HFML-RU/FOM in Nijmegen.

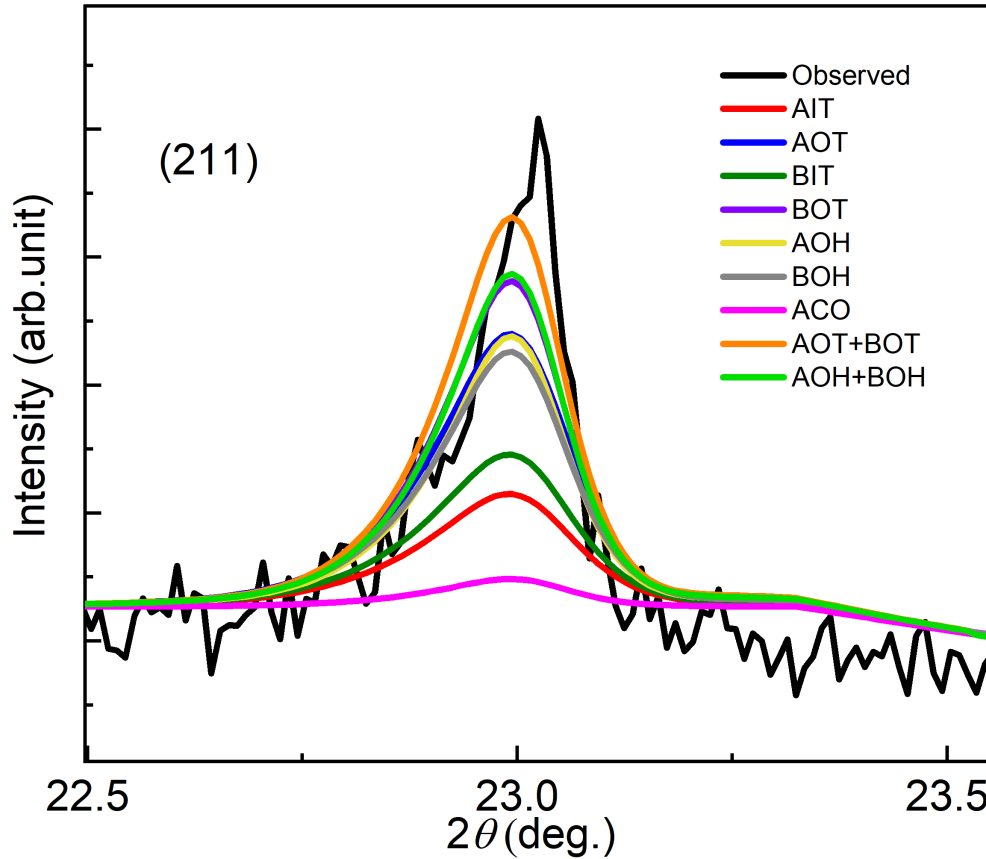


Figure 5.3: (Color online) Zoomed view of the variation of (211) peak intensity for the substitution of Pt atoms at distinctive/combination of Wyckoff positions in $\text{Mn}_{2.7}\text{Pt}_{0.3}\text{In}$.

5.4 Characterisation

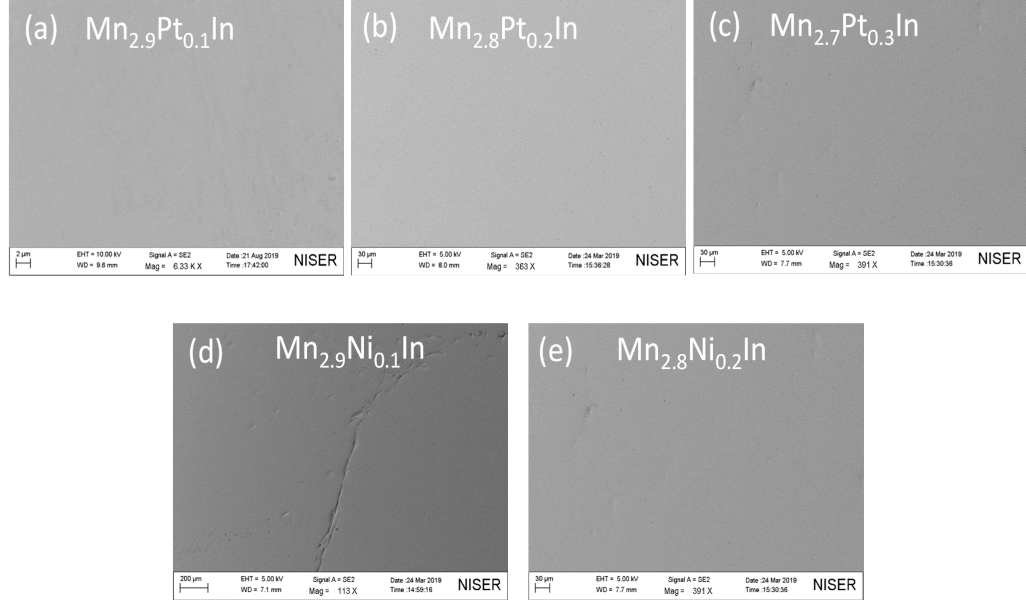


Figure 5.4: (Color online) (a)- c) SEM images of $\text{Mn}_{3-x}\text{Pt}_x\text{In}$ for $x = 0.1$ to 0.3 . (d) and (e) SEM images of $\text{Mn}_{3-y}\text{Ni}_y\text{In}$ where $y = 0.1$ and 0.2 .

5.4.1 Structural characterization

Polycrystalline $\text{Mn}_{3-x}\text{Pt}_x\text{In}$ and $\text{Mn}_{3-y}\text{Ni}_y\text{In}$ samples with $x = 0.1$ to 0.3 and $y = 0.1$ to 0.2 are synthesized for the present study. The doped samples outside the specified concentration of Pt and Ni were not possible to stabilize in a single structural phase of Mn_3In by the present arc-melting technique. The structural phase purity of all the doped samples can be seen from the Rietveld refinement of the room temperature x-ray diffraction (XRD) data as shown in Fig. 5.2. All the samples crystallize in the cubic structure that belongs to the space group $P\bar{4}3m$. A thorough investigation is performed with the XRD data to find any site-specific preference of the doping element. As can be seen from the Pt composition-dependent XRD patterns [Fig. 5.2], the Bragg peak (211) is absent in $\text{Mn}_{2.9}\text{Pt}_{0.1}\text{In}$. With the increase of Pt concentration, the intensity of the Bragg peak (211) increases; in fact, it is very

Table 5.1: Averaged EDS data of $\text{Mn}_{3-x}\text{Pt}_x\text{In}$ and $\text{Mn}_{3-y}\text{Ni}_y\text{In}$

Composition (x/y)	Exact atomic ratios of Mn, Pt/Ni, In respectively (in %)	Obtained values of Mn, Pt/Ni, In from EDS respec- tively (in %)
x= 0.1	72.50, 2.50, 25.00	71.60, 2.61, 25.71
x= 0.2	70.00, 5.00, 25.00	67.90, 5.21, 26.89
x= 0.3	67.50, 7.50, 25.00	66.12, 7.50, 26.33
y= 0.1	72.50, 2.50, 25.00	70.84, 2.57, 25.00
y= 0.2	70.00, 5.00, 25.00	68.89, 5.04, 25.07

prominent in case of $\text{Mn}_{2.7}\text{Pt}_{0.3}\text{In}$. Therefore, a systematic substitution of Pt atoms in all the possible Wyckoff positions was done to find out any preferential site occupation. The variation of simulated intensity of the (211) peak for substitution of Pt at different Wyckoff positions in the $\text{Mn}_{2.7}\text{Pt}_{0.3}\text{In}$ is shown in Fig. 5.3. In particular, the Pt and Ni atoms preferentially sit at AOH and BOH sites.

5.4.2 Homogeneity and composition study

To check the sample homogeneity and phase purity, we have performed the SEM study on all the samples. Figure 5.4(a)-(c) depict the SEM images of $\text{Mn}_{3-x}\text{Pt}_x\text{In}$. Usually, any spatial chemical inhomogeneity appears as a color contrast (dark and bright). Since only a single SEM image contrast is found for all the samples, they are believed to be chemically homogeneous. Figure 5.4(d) and (e) is the SEM image of $\text{Mn}_{3-y}\text{Ni}_y\text{In}$. The EDS analysis gives the compositional value around the exact stoichiometric requirement, as can be seen in Table - 5.1.

5.5 Theoretical understanding

The density functional theory (DFT) calculation on the stabilization mechanism of different magnetic phases in Mn_3In is performed in collaboration [please refer to the theoretical calculations parts in Phy. Rev. B 104, 014413 (2021)]. A summary of the DFT outcome is necessary for the completeness of the present chapter. It is found that a compensated ferrimagnetic (FiM) state is energetically the most favor-

able one. We also find the presence of a partially compensated magnetic state with a net uncompensated magnetic moment of $1.84 \mu_B/\text{f.u.}$ and a very small energy difference relative to the compensated FiM. It is evident that the substitution of Pt and Ni in Mn_3In does not alter the fully compensated ferrimagnetic behavior. Importantly, for all the cases, the individual cluster pertains a large net magnetic moment. The resulting fully compensated magnetic state can be regarded as the anti-parallel alignment of the net magnetic moment in cluster-A and cluster-B. Due to the large number of magnetic atoms Mn_3In , the degree of frustration around each Mn-sites is quite obvious. The degree of frustration is defined as the deviation from the antiferromagnetic coupling between the two nearest neighboring Mn spins. The percentage of the total number of nearest neighbors which are frustrated divided by the total number of nearest neighbors for all Wyckoff sites gives the percentage (%) of degree of frustration for a given configuration. The degree of frustration corresponding to the compensated ground state and uncompensated state with a small energy difference is almost same. Therefore, it might be possible to stabilize some uncompensated FiM magnetic clusters within the fully compensated ferrimagnetic host. As a result, the exchange bias phenomena can be occurred due to the interaction between the fully compensated FiM host and the uncompensated magnetic clusters.

5.6 Magnetic properties

Mn_3In is a special type of FCF system, where the magnetic compensation is achieved by AFM alignment between two atomic clusters (as opposed to the individual atomic moment in conventional AFM) in a single unit cell. The presence of a long-range FiM/AFM ordering in Mn_3In with Néel temperature $T_N \sim 75 \text{ K}$ has been reported earlier [99, 100]. To study the magnetic properties of the Pt/Ni doped samples, temperature dependent and isothermal magnetization measurements are performed. Figure 5.5 (a) and (b) describe the temperature (T) dependent magnetization ($M(T)$) for the $\text{Mn}_{3-x}\text{Pt}_x\text{In}$ and $\text{Mn}_{3-y}\text{Ni}_y\text{In}$ samples, respectively. All

Table 5.2: Structural and magnetic parameters for the $\text{Mn}_{3-x}\text{Pt}_x\text{In}$ and $\text{Mn}_{3-y}\text{Ni}_y\text{In}$ samples.

Composition (x/y)	structure(Space Group)	Lattice constant (in Å)	T_N (K)	M Experi- mental (at 5 T field) (in $\mu_B/\text{f.u.}$)
x= 0.1	<i>Cubic</i> ($\text{P}\bar{4}3\text{m}$)	9.430864	97	0.21
x= 0.2	<i>Cubic</i> ($\text{P}\bar{4}3\text{m}$)	9.449223	102	0.21
x= 0.3	<i>Cubic</i> ($\text{P}\bar{4}3\text{m}$)	9.460003	107	0.18
y= 0.1	<i>Cubic</i> ($\text{P}\bar{4}3\text{m}$)	9.398867	88	0.15
y= 0.2	<i>Cubic</i> ($\text{P}\bar{4}3\text{m}$)	9.386379	92	0.14

the samples exhibit typical AFM type $M(T)$ curves. A strong bifurcation between the zero field cooled (ZFC) and field cooled (FC) $M(T)$ curves appears below the Néel temperature (T_N). The Néel temperature (T_N) increases monotonically with increasing x . The low-temperature irreversibility between the ZFC and FC $M(T)$ data hints at the presence of coexisting magnetic phases. This might be the formation of FM clusters within the compensated FiM matrix during the field cooling process. The $M(T)$ data taken at different constant magnetic field are shown in Fig. 5.6(a) and (b) for $\text{Mn}_{2.8}\text{Pt}_{0.2}\text{In}$ and $\text{Mn}_{2.8}\text{Ni}_{0.2}\text{In}$, respectively. Large irreversibility between the ZFC and FC $M(T)$ data persists even at the 5 T field. The sharp peak around the T_N takes a broader hump-like shape and the corresponding maxima shifts towards the higher side of the temperature. Such behavior is in contrast to the spin glass feature. Also, the ac susceptibility measurement ($\chi'(T)$) taken at different drive field frequency support the above conclusion. The variation of the real part of ac susceptibility ($\chi'(T)$) with respect to temperature at various drive frequencies are shown in Fig. 5.7(a) and (b) for $\text{Mn}_{2.8}\text{Pt}_{0.2}\text{In}$ and $\text{Mn}_{2.8}\text{Ni}_{0.2}\text{In}$ samples, respectively. The ($\chi'(T)$) shows a peak around the ordering temperature T_N . The structural and magnetic parameters for all the samples are summarized in Table 5.2.

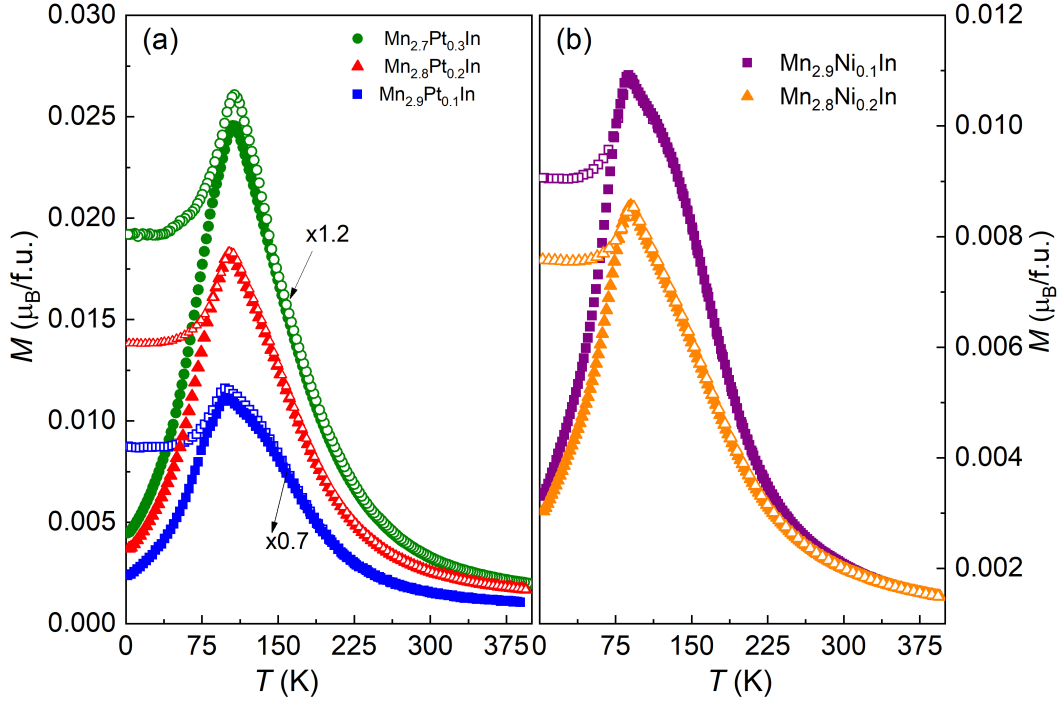


Figure 5.5: (Color online) Temperature-dependent magnetization plot, $M(T)$, measured at an applied field of 0.1 T. (a) For $\text{Mn}_{3-x}\text{Pt}_x\text{In}$ and (b) for $\text{Mn}_{3-y}\text{Ni}_y\text{In}$. Solid (open) symbols represent the ZFC (FC) data. The data for $x = 0.2$ and $x = 0.3$ are multiplied by factors of 1.3 and 1.5, respectively, for visual clarity.

5.7 Tunable EB

The exchange interactions between two different coexisting magnetic phases can be mapped out using FC hysteresis loop measurements. Therefore, the ZFC and FC isothermal magnetization measurements are performed at 2 K. Figure 5.8(a) and (b) depicts ZFC (open symbols) and FC (filled symbols) magnetic hysteresis loops for $\text{Mn}_{3-x}\text{Pt}_x\text{In}$ and $\text{Mn}_{3-y}\text{Ni}_y\text{In}$, respectively. Before the measurement, the samples are cooled down to the desired temperature from 300 K either in the absence (ZFC) or in presence (FC) of the specified applied field. The ZFC $M(H)$ loops for all the samples show a nearly linear field dependency up to the measured field of 14 T. However, a hysteretic behavior can be seen for all the loops with a large coercive field (H_C). These results support the assumption of the presence of FM and FiM phases. The linear nature of $M(H)$ loops may be attributed to the compensated FiM

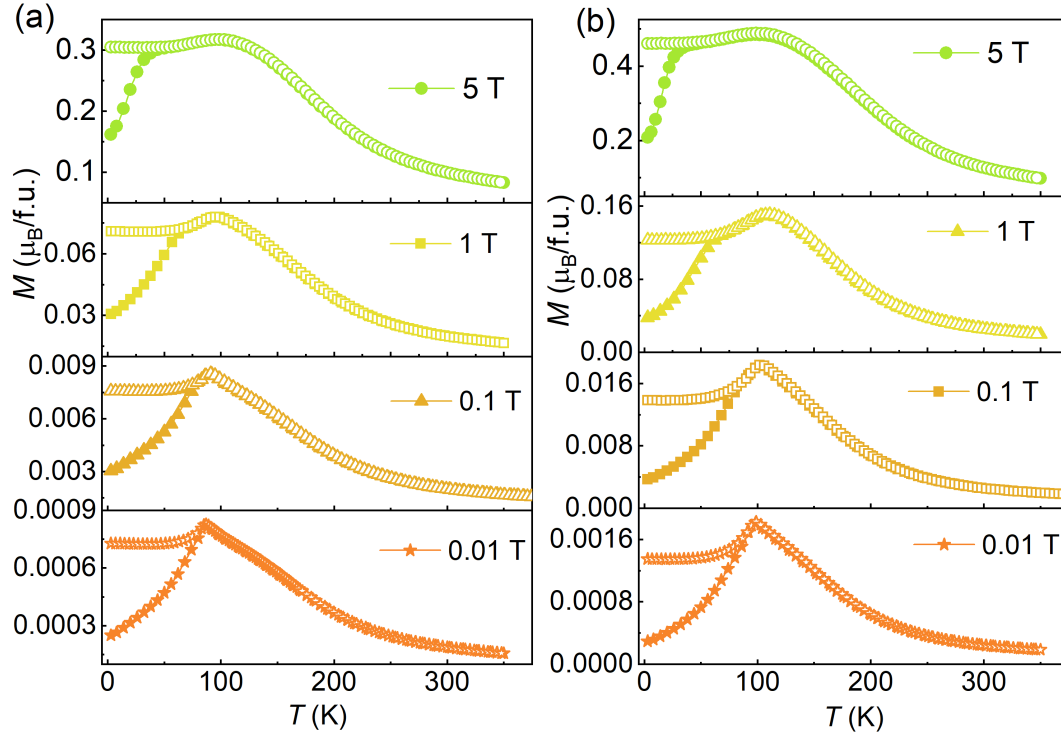


Figure 5.6: (Color online) Temperature dependent magnetisation $M(T)$, measured at different value of constant magnetic fields. (a) For $\text{Mn}_{2.8}\text{Pt}_{0.2}\text{In}$ and (b) for $\text{Mn}_{2.8}\text{Ni}_{0.2}\text{In}$. Solid (open) symbols represent the ZFC (FC) data.

background, whereas the hysteretic behavior can arise due to the existence of FM clusters. The FC isothermal magnetization loops are measured at 2 K to examine the presence of any exchange interaction between the FM and FiM phases, as shown in Fig. 5.8(a) and (b) (solid symbols). A large shift along the negative field axis can be seen for all the FC $M(H)$ loops. This particular behavior demonstrates the existence of a large unidirectional exchange anisotropy in the system. Note that the FC loops of $\text{Mn}_{3-y}\text{Ni}_y\text{In}$ display a spontaneous magnetization behavior with the loop closing around the 5 T field. The value of EB and coercive fields are obtained by using the formula $H_{EB} = -(H_L + H_R)/2$ and $H_C = |H_L - H_R|/2$ respectively, where H_L and H_R are the lower and upper critical field at which the magnetization becomes zero. A large EB field (H_{EB}) of 0.8, 1.6, and 1.8 T for $x = 0.1, 0.2$, and 0.3 , respectively [Fig. 5.9]. The field cooled H_C also increases to 2.33 T, 2.67 T and 3.37 T for $x = 0.1, 0.2$, and 0.3 , respectively. For the Ni-doped samples, large H_{EB} of 2.68 T is obtained for

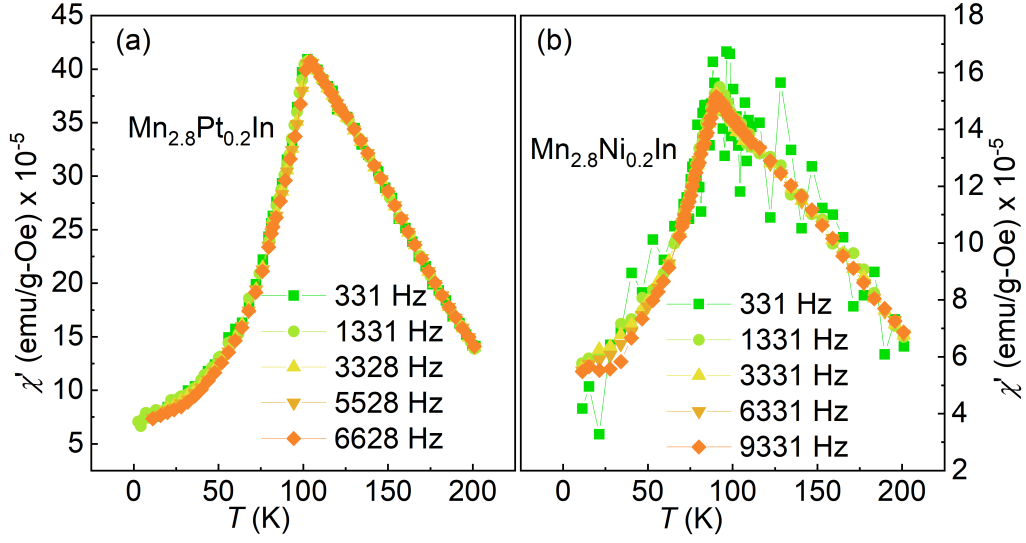


Figure 5.7: (Color online) Temperature-dependent real part of ac susceptibility (χ') taken at different ac field frequencies for (a) $\text{Mn}_{2.8}\text{Pt}_{0.2}\text{In}$ and (b) $\text{Mn}_{2.8}\text{Ni}_{0.2}\text{In}$ sample. An ac drive field of 10 Oe amplitude is used.

$\text{Mn}_{2.8}\text{Ni}_{0.2}\text{In}$ [see inset of Fig. 5.9].

It can be noticed that the FC loops for the Ni substituted samples close at a moderate field of about 5 T. However, it is intangible for the Pt-doped samples where the FC $M(H)$ loops really close at about 14 T. Furthermore, the finding of large EB with dissimilar characteristics of the FC hysteresis in Pt and Ni-doped samples needs a comprehensive understanding of the underlying mechanism. Also, it is important to confirm that the observed EB phenomena do not arise from the minor loop measurement. Hence pulsed field magnetization measurements are carried out up to 60 T field at 1.8 K for the Pt substituted samples, as depicted in Fig. 5.10(a). All the loops close at a field of about ~ 15 T. For all, the $M(H)$ curves do not saturate even up to the maximum applied field, suggesting a strong exchange strength between the sub-lattice moment. A hysteretic feature in the field range of 0-15 T with a remnant magnetization of $0.16\text{-}0.23 \mu_B/\text{f.u.}$ is also found in all the three samples. In addition, the presence of a step-like signature around 10 T indicates a field-induced metamagnetic type of transition. In addition, field cooled (in 15 T) hysteresis loops measurements are carried out up to ± 30 T for $\text{Mn}_{3-x}\text{Pt}_x\text{In}$ samples, as shown in

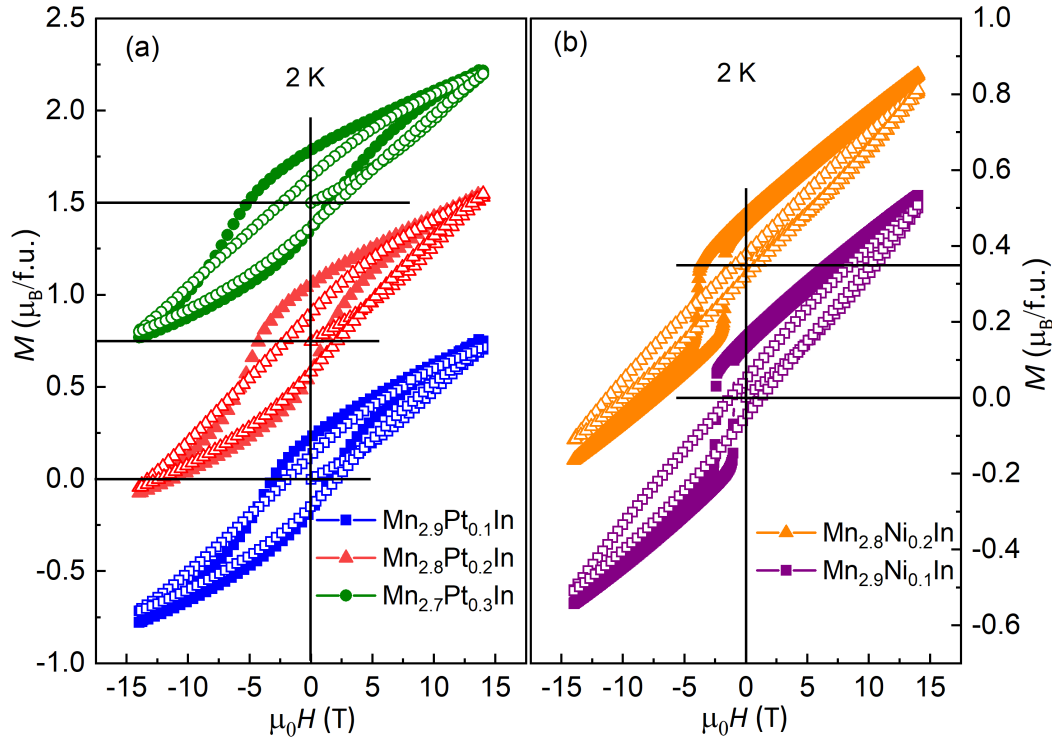


Figure 5.8: (Color online) $M(H)$ loops measured at $T = 2$ K in ZFC (open symbol) and +5 T FC (solid symbol) mode. (a) For $\text{Mn}_{3-x}\text{Pt}_x\text{In}$ and (b) for $\text{Mn}_{3-y}\text{Ni}_y\text{In}$ sample. The $M(H)$ loops corresponding to the sample $x = 0.2$ and 0.3 are shifted by 0.75 and $1.5 \mu_B/\text{f.u.}$, respectively, along the magnetization axis. $M(H)$ loops for $y = 0.2$ is shifted by $0.35 \mu_B/\text{f.u.}$

Fig. 5.10(b). The 15 T FC $M(H)$ loops (measured up to 30 T) show a smaller EB field in comparison to that of the 5 T FC loops shown in Fig. 5.8. As evident, all the $M(H)$ loops close at about 15 T. Therefore, the FC hysteresis loops measured up to the field of ± 14 T in Fig. 5.8 categorically fall in the major loop category. Hence, it can be readily confirmed that the large exchange bias obtained in the present case is intrinsic in nature.

The findings of large EB in the present system firmly advocates the existence of exchange coupling between two different types of magnetic phases. Most reasonably, in the present system, it is the exchange coupling between the FCF background and the FiM clusters. The present conjecture can be understood as follows. The FCF as the lowest energy state is found from the DFT calculation. In a recent report, Chatterjee *et al.* has proposed an uncompensated ferrimagnetic ordering in Mn_3In

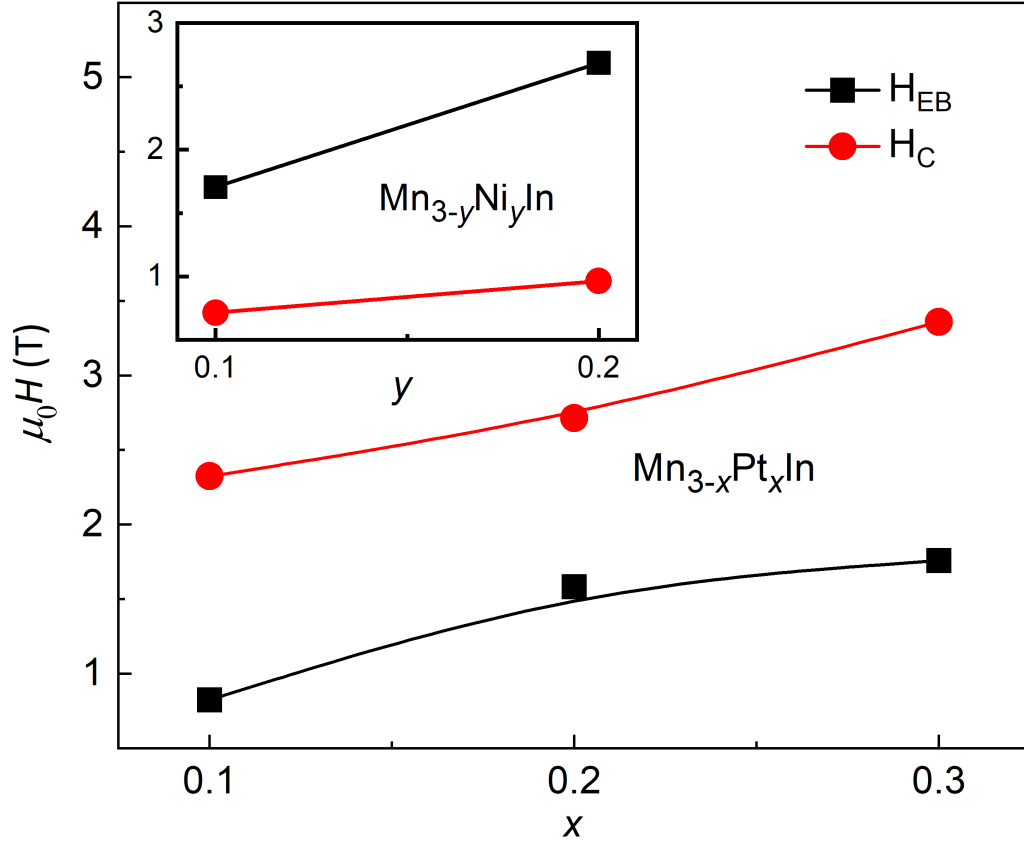


Figure 5.9: (Color online) Dependence of exchange bias fields (H_{EB}) and coercive fields H_C on Pt concentration (x) for $Mn_{3-x}Pt_xIn$ systems. The inset plot shows the dependence of H_{EB} and H_C on Ni concentration (y) in $Mn_{3-y}Ni_yIn$.

as the lowest energy state [142]. The stabilization of uncompensated FiM state in Mn_3In is possible due to negligible energy difference with respect to the FCF state. However, the theoretical proposition of FCF as the lowest energy state in the present system is strongly supported by the experimental results. Therefore, it is most likely that the exchange coupling between the coexisting FCF and the uncompensated FiM phases is responsible for the observation of large EB phenomena. Figure 5.11(a) and (b) schematically describe the possible mechanism of the EB.

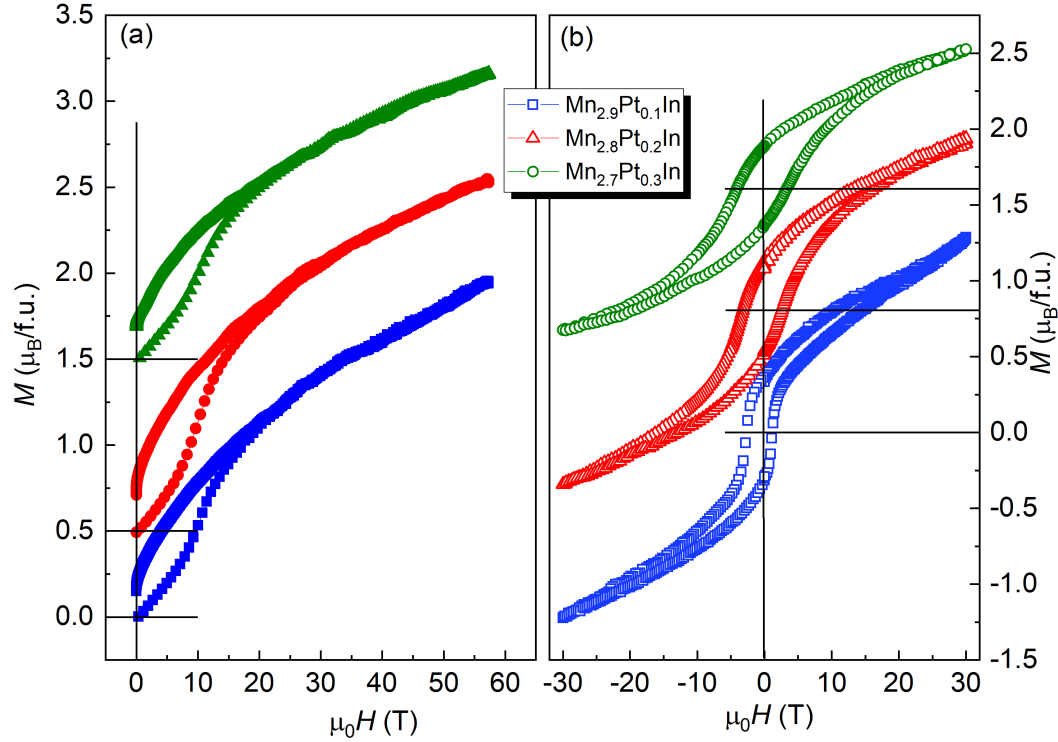


Figure 5.10: (Color online) (a) ZFC pulsed field magnetisation data ($M(H)$) measured up to 60 T for $\text{Mn}_{3-x}\text{Pt}_x\text{In}$. Magnetization data for the sample $x = 0.2$ and 0.3 are shifted along M axis by 0.5 and $1.5 \mu_B/\text{f.u.}$, respectively. (b) 15 T FC $M(H)$ loops measured up to ± 30 T. The $M(H)$ loops of $x = 0.2$ and 0.3 are vertically shifted by 0.8 and $1.6 \mu_B/\text{f.u.}$, respectively.

5.8 Transport measurement and discussion

The electrical transport measurements are carried out with a rectangular shaped Hall bar to understand the nature of interfacial exchange interaction in the system. Figure 5.12(a) and (b) represents the temperature dependence of longitudinal resistivity (ρ) of $\text{Mn}_{3-x}\text{Pt}_x\text{In}$ and $\text{Mn}_{3-y}\text{Ni}_y\text{In}$, respectively. For $x=0.1-0.2$ and $y=0.1-0.2$ the resistivity decreases with increasing temperature, i.e., a negative temperature coefficient of the resistivity. Whereas the parent Mn_3In sample shows similar behavior only above the spin-glass transition temperature and below that it shows a metallic behavior [100, 142]. A metallic behavior is found for $\text{Mn}_{2.7}\text{Pt}_{0.3}\text{In}$ sample only [Fig. 5.12(a)]. The Hall measurements are performed to get an idea of

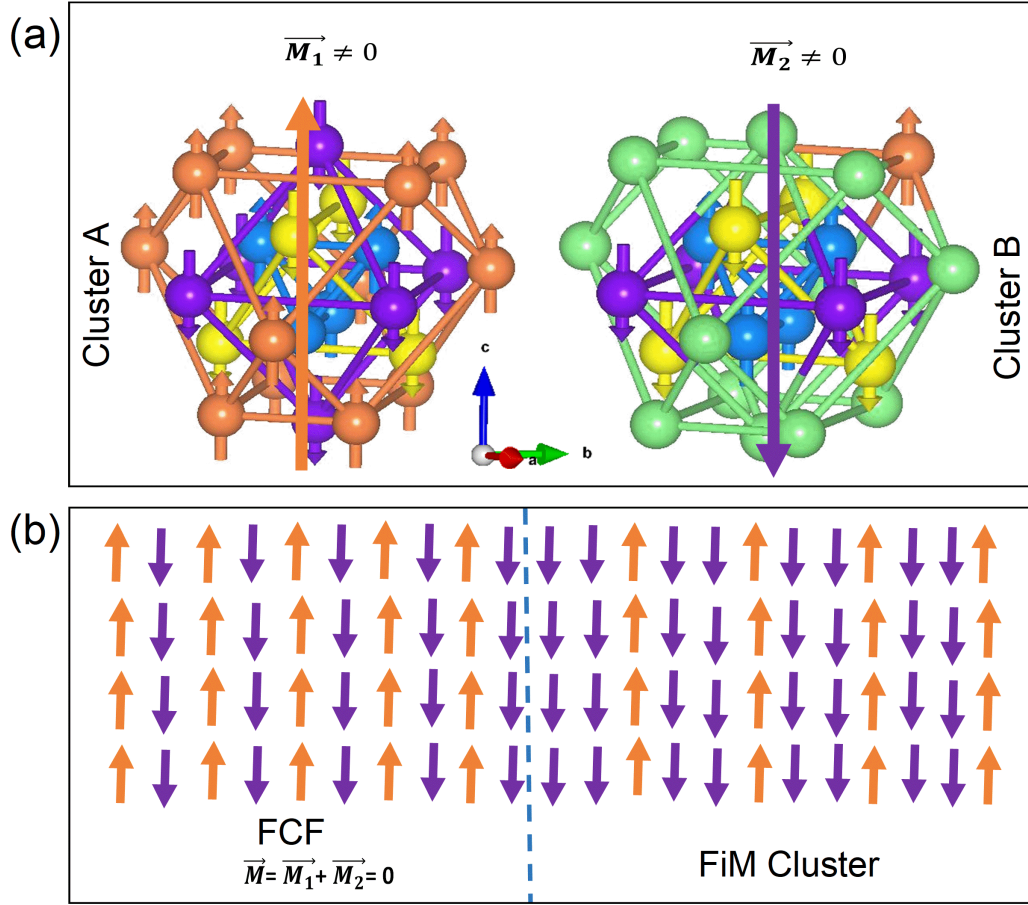


Figure 5.11: (Color online) (a) Cluster-A and cluster-B with finite staggered magnetization \vec{M}_1 and \vec{M}_2 aligned anti-parallel. (b) Left panel: fully compensated FiM background as a result of cancellation between the staggered magnetization \vec{M}_1 and \vec{M}_2 of cluster-A (orange arrows) and cluster-B (violet arrows). Right panel: Possible FiM cluster due to a finite magnetic moment; as one of the uncompensated magnetic state has small energy difference with the FCF ground state. The dashed line stands for the interface between the FCF background and the FiM cluster with finite moment.

the interface spin texture at the FCF background and the FiM cluster. The sample $\text{Mn}_{2.8}\text{Ni}_{0.2}\text{In}$ is used as it needs a moderately low field (~ 5 T) to close the hysteresis loop. Figure 5.13 depicts the field dependence of Hall resistivity (ρ_{yx}) measured at 5 K, taken after cooling the sample in the field of +7 T and -7 T. To extract any extra contribution in addition to the conventional normal and anomalous Hall in the total Hall resistivity data, the experimental ρ_{yx} data fitted with the calculated one. The total ρ_{yx} can be written as $\rho_{yx} = \rho_{OHE} + \rho_{AHE} + \rho_{yx}^{EHE}$. Here, ρ_{OHE} , ρ_{AHE} and

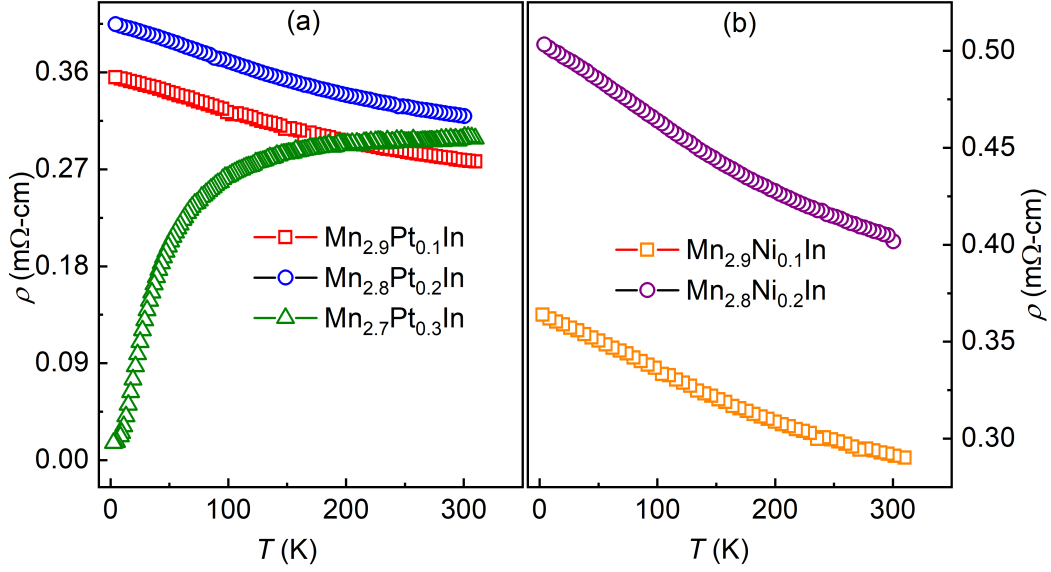


Figure 5.12: (Color online) (a) Temperature dependence of longitudinal resistivity (ρ) for $\text{Mn}_{3-x}\text{Pt}_x\text{In}$, and (b) for $\text{Mn}_{3-y}\text{Ni}_y\text{In}$.

ρ_{yx}^{EHE} are ordinary, anomalous and extra Hall resistivities, respectively [19]. ρ_{OHE} can be expressed as $\rho_{OHE} = \mu_0 R_0 H$, where R_0 is the normal Hall coefficient and H is the magnetic field. The ρ_{AHE} can be written as, $\rho_{AHE} = b\rho_{xx}^2 M$, where b is a constant, ρ_{xx} is the longitudinal resistivity and M is the magnetization. It can be seen from Fig. 5.13 that the FC loop closes for a field above 5 T. Therefore, it can be considered that the spin structure saturates for the field larger than 5 T. Hence, the high field ρ_{yx} data only contains ρ_{OHE} and ρ_{AHE} . With this assumption, the ρ_{yx} at field greater than 5 T written as $\rho_{yx} = \mu_0 R_0 H + b\rho_{xx}^2 M$. The calculated Hall resistivity is plotted as solid lines in Fig. 5.13. As can be seen for the +7 T FC data, the experimental and calculated lines overlap each other everywhere except at the magnetization reversal point for +9 T to -9 T cycle. This unusual behavior is present for the -7 T FC data and arises at the magnetization reversal point for -9 T to +9 T field sweep curves. This extra Hall effect (EHE) at the field reversal region is marked by dotted circles in Fig. 5.13. Note that for the +7 T and -7 T FC loop, the measurement is done by sweeping the field from +9 \rightarrow -9 \rightarrow +9 T and -9 \rightarrow +9 \rightarrow -9 T, respectively. In the case of the ZFC Hall data, no such anomaly is

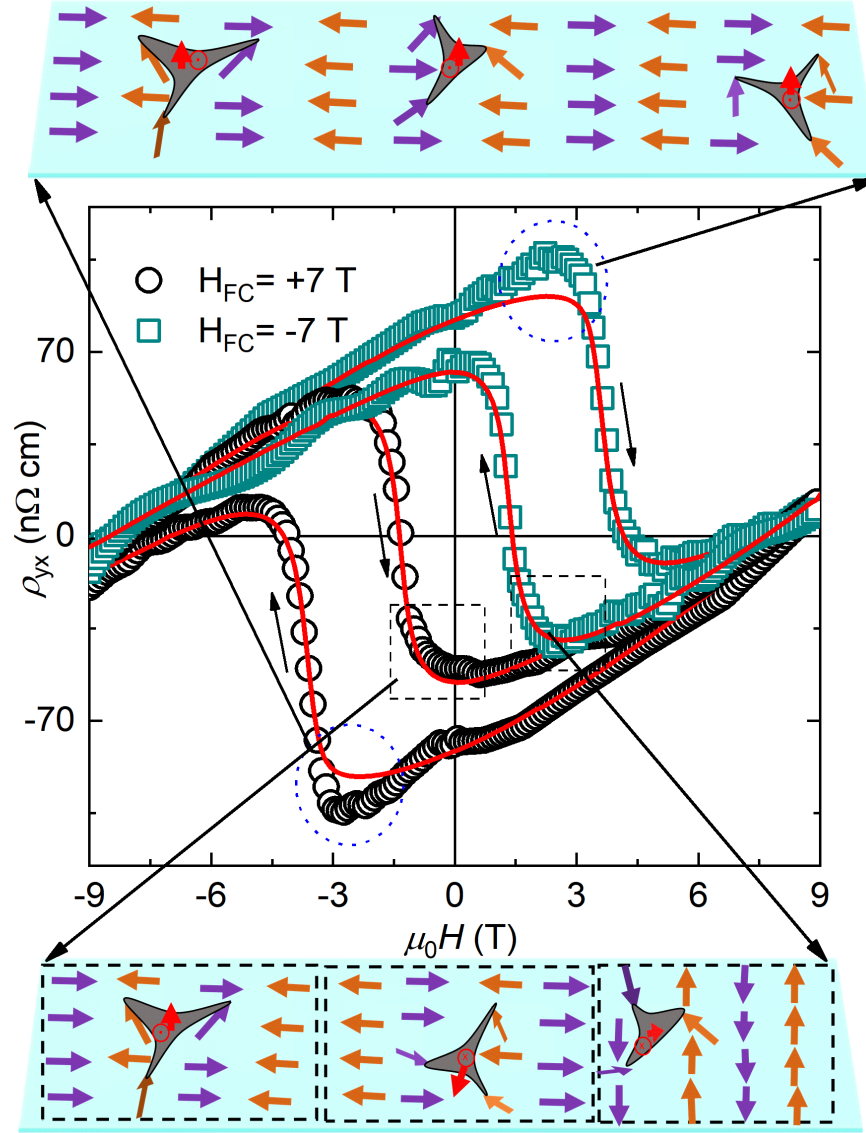


Figure 5.13: (Color online) Field dependence of Hall resistivity (ρ_{yx}) measured at 5 K for $\text{Mn}_{2.8}\text{Ni}_{0.2}\text{In}$. The open circles and open squares represent the ρ_{yx} measured after field cooling the sample in an applied field of +7 T and -7 T, respectively. The solid lines correspond to the total calculated Hall resistivity. The schematic spin configuration at the top and bottom panels represent the possible interfacial FCF magnetic texture at the field reversal point, which are marked in dotted circles and dotted squares, respectively. The solid angle subtended by the noncoplanar spins in the schematic diagrams is marked by a shaded dark grey region, and the red arrows indicate the direction of the fictitious magnetic field.

found [see Fig. 5.14]. This suggests that the appearance of extra Hall is related to the interface phenomena. Therefore, in the present system, the EHE is most likely

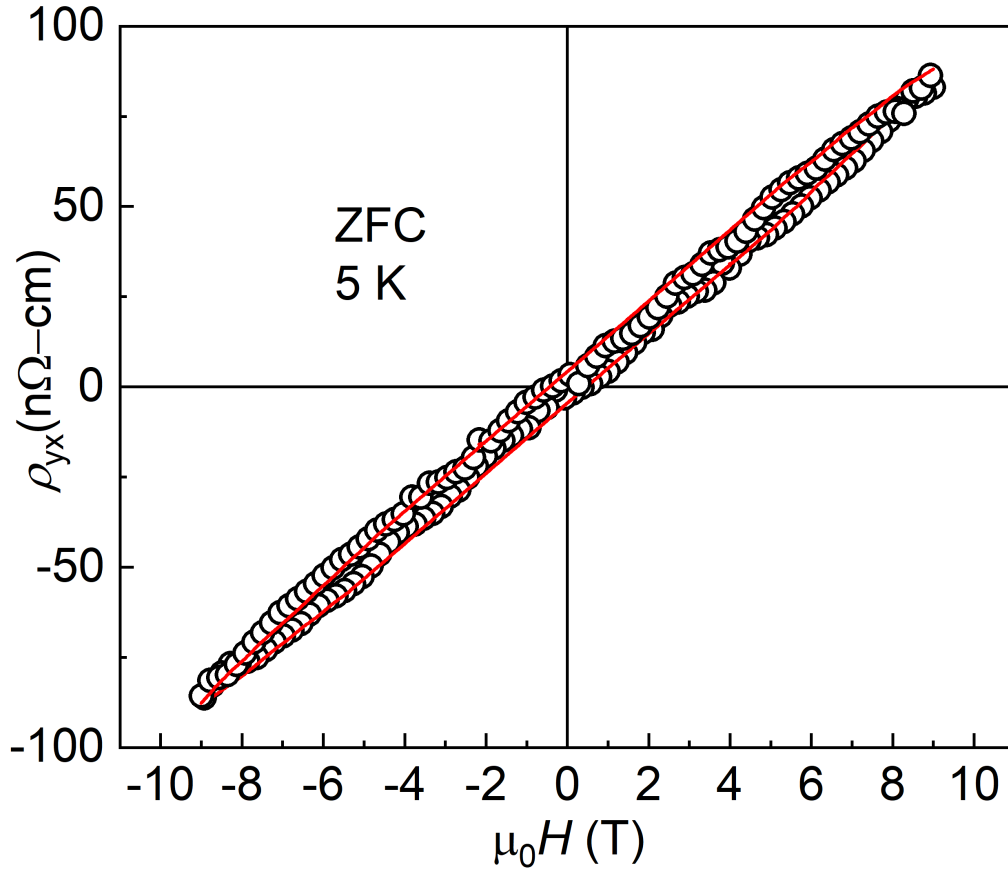


Figure 5.14: (Color online) Field dependence of ZFC Hall resistivity (ρ_{yx}) measured at 5 K for $\text{Mn}_{2.8}\text{Ni}_{0.2}\text{In}$. The open circles and solid lines correspond to the experimental data points and calculated Hall resistivity, respectively.

originated from the non-vanishing scalar spin chirality governed by the non-coplanar spin structure within a single domain AFM arrangement [18, 19, 117]. A possible schematic spin texture is illustrated in the top panel of Fig. 5.13. It should be noted that the extra Hall contribution in the present system arises only in the field decreasing and increasing path of the Hall measurement for +7 T and -7 T FC cases, respectively. This disparity in the Hall resistivity data in the opposite cycle of the field sweep indicates a different mechanism of magnetization reversal through the lower and upper critical field in exchange coupled system. Such asymmetry in the hysteresis curve appears in the vicinity of magnetization reversal associated with domain wall motion, or magnetization rotation [143, 144, 145]. Therefore, the ob-

served extra Hall contribution can only be attributed to the interfacial non-coplanar spin structure in an exchange bias system. Most likely, the non-coplanar spin state stabilized by interfacial DMI arising from the breaking of inversion symmetry at the interface. As a result, an extra component of Hall resistivity appears in the vicinity of the magnetization reversal through magnetization rotation. The absence of an extra Hall component in the reverse cycle marked by dashed squares is shown in Fig. 5.13. The corresponding spin texture is represented schematically in the bottom panel of Fig. 5.13., indicating the formation of the multi-domain state in the AFM layer. Moreover, the nucleation of domain states is favorable while moving from a negative saturated field to positive one for the positive field cooled case and vice versa. In fact, the existence of AFM domain at the interface in an EB system has also been reported earlier [144, 146, 147].

5.9 Conclusion

This chapter deal with a Pt and Ni-doped Mn_3In system. A classic example of composite quantum material that shows the co-existence of fully compensated ferrimagnet (FCF) and large exchange bias (EB). The FCF state is realized as the antiferromagnetic coupling between the intra-cluster staggering moment. The high degree of frustration in the energetically most stable FCF state and the small energy barrier of this state with respect to other uncompensated magnetic states is the most plausible reason for giving an inhomogeneous magnetic state. As a result, a large exchange bias arises in the present system, demonstrated as the exchange interaction between the FCF and the uncompensated ferrimagnetic clusters. An EB field of 0.8–2.7 T can be achieved in this cubic system. The observed EHE in such systems indicates the presence of interfacial DMI along with the symmetric exchange interaction. As a result, the uncompensated inter-facial spins forms non-coplanar spin texture at the field reversal region. Moreover, it establishes the importance of magnetic compensation to achieve large EB regardless of the crystalline anisotropy.

Chapter 6

Summary and future perspective

“And miles to go before I sleep”

Robert Frost

6.1 Summary of the thesis work

In this thesis, efforts have been made to understand different mechanisms that govern non-trivial magnetic states in Mn-based In-rich ferrimagnetic materials. Magnetic and magneto-transport properties are extensively studied to understand the electron correlation associated with the complex spin structures. The concept of topology is introduced to understand the unconventional behaviors found in the magnetic and magneto-transport phenomena. It also highlights the dynamic character of the Mn rich ferrimagnetic materials on achieving desired magnetic states. Moreover, topologically non-trivial ferrimagnetic materials can provide the fertile grounds to explore various aspects of spintronic device requirement. Therefore, this thesis is in line with the current trends in search of topological quantum materials with exotic properties. In this regard, a short description of topology in magnetism is introduced. Specially, the the notion of Berry phase is advertised to illustrate the exotic topological Hall effect. In addition, different non-trivial magnetic systems

and their underlying origin are mentioned through a brief literature survey. A preamble of the ferrimagnetic materials under this thesis study is highlighted. A separate chapter is dedicated to the basic understanding of the methods and working principle of different instruments employed in this thesis. The whole thesis work is presented in three different chapters.

In the third chapter, a scheme of tuning of the topological Hall effect (THE) is displayed. For this purpose a series of inverse tetragonal Heusler alloys $\text{Mn}_{2-x}\text{PtIn}$ were synthesized. Magnetic measurements are carried out to show a systematic variation of Curie temperature (T_C) and saturation magnetization. The DFT calculations reveal a systematic change in the degree of non-collinearity among the constituent spins. The origin of the non-collinear magnetic state is attributed to the exchange frustration arising from the competing ferromagnetic and antiferromagnetic exchanges. The evidence of non-collinear magnetic states are also obtained from the neutron diffraction measurements. A detailed Hall effect experiment is performed to understand the direct consequences of the non-collinear states. Robust signature of THE is found for Mn_2PtIn system. This THE decreases for a system with lower degree of non-collinearity and vanishes for a collinear state. The magnetic ac susceptibility data rule out the existence of skyrmions/antiskyrmions in this system. Therefore, the source of the THE in the present system is attributed to the non-vanishing scalar spin chirality (SSC). The presence of SSC is then elaborated in connection to the underlying magnetic ground states. The DMI in this system favor a particular spin chirality.

The effect of such non-collinear magnetic ordering on the stability of skyrmions is studied in the fourth chapter. To this direction, a series of inverse tetragonal $\text{Mn}_{1.4}\text{Pt}_{0.9}\text{Pd}_{0.1}\text{Sn}_{1-x}\text{In}_x$ samples were synthesized. The D_{2d} symmetry in this system provides the base for anisotropic DMI, which is an essential requirement for the formation of antiskyrmions. Magnetic measurements show a systematic decrease in the T_C and saturation magnetization (M_s). Magnetic ac susceptibility study reveals the signature of antiskyrmions only in the temperature range $T_{SR} \leq T \leq T_C$. Lorentz transmission electron microscopy (LTEM) measurements also provide

a direct evidence of the antiskyrmions formation only in this temperature regime. Above T_{SR} , a collinear magnetic state is observed from the powder neutron diffraction experiment. A non-collinear magnetic ground state is found below T_{SR} . Most possibly, the exchange frustration leads to the non-collinear magnetic states in the system. The exchange frustration suppresses the effect of the Dzyaloshinskii–Moriya interaction (DMI), hence hindering the formation of the antiskyrmions. The powder neutron diffraction experiment is performed on the higher In doped samples to further support the conjecture. In this case, a non-collinear magnetic ordering is observed throughout the temperature range in the ordered phase. The LTEM measurements and ac-susceptibility data of this sample exclude the evidence of antiskyrmions. Therefore, the combined ac susceptibility results, LTEM imaging, and neutron diffraction study establish that the formation of the antiskyrmion phase requires a collinear arrangement of the ground magnetic state sans DMI in the present system. This study also sheds some light on the effect of exchange frustration in the DMI-assisted antiskyrmion system. Moreover, here we present a spontaneous formation of fractional topological object like meron and anti-meron in the $\text{Mn}_{1.4}\text{Pt}_{0.9}\text{Pd}_{0.1}\text{Sn}_{0.6}\text{In}_{0.4}$. This findings reveal a new kind of nontrivial topological phase as a result of delicate balance between the underlying magnetic interaction.

The fifth chapter of this thesis work is focused on the role of non-coplanar spin structure at the interface in exchange coupled systems. The THE measurement is used to find the existence of a non-trivial interfacial spins state. The development of such an interfacial spin structure stems from the interfacial DMI and symmetric exchange. A large exchange bias field arises as a combined effect of the symmetric and anti-symmetric (DMI) exchanges at the interface. For the experimental evidence, a series of polycrystalline samples of $\text{Mn}_{3-x}(\text{Pt}, \text{Ni})_x\text{In}$ are prepared. Structural characterization shows that all the samples form in the cubic structure belonging to the space group $P\bar{4}3m$. A rigorous magnetic measurement suggests a nearly compensated FiM state in the systems. The DFT calculations support the experimental conjecture. A fully compensated FiM (FCF) state is found to be energetically most

stable. The magnetic compensation occurs due to the antiferromagnetic coupling between the effective moment of two clusters situated at $(0, 0, 0)$ and $(0.5, 0.5, 0.5)$. An uncompensated FiM state is also possible due to a small energy difference from the FCF state. Therefore, the magnetic phase coexistence in this system showcases a very large exchange bias (EB) field. The origin of the large EB is attributed to the interface coupling between the uncompensated FiM cluster within an FCF background. Hall effect measurement is performed in $\text{Mn}_{2.8}\text{Ni}_{0.2}\text{In}$ to interpret the nature of exchange interactions between the FCF background and the FiM cluster. The absence and presence of THE in a zero field and field-cooled measurement indicates that it is an interfacial phenomenon. The resultant THE arises as a result of the non-coplanar spin state stabilized by the interfacial DMI. Therefore, the large exchange bias phenomena in this system are associated with the formation of a noncoplanar spin state at the interface due to the competition between symmetric exchange and interfacial DMI.

6.2 Future perspective

This thesis introduces various types of non-trivial magnetic states in Mn-rich ferromagnetic systems. The first part represents a classic example of a large and robust topological Hall effect, which is being tuned by modifying the canted magnetic state. The second part describes the effect of exchange frustration on the stability of the antiskyrmion phase in the Mn-Pt(Pd)-Sn-In system. In the third part, the presence of a non-coplanar spin state at the interface is mapped out through the topological Hall effect measurement. Moreover, the non-trivial magnetic materials showcase various exotic phenomena with rich physics.

In the first chapter, a systematic tuning of THE is presented. Tuning of the Mn concentration basically causes a change in the lattice parameter, which in turn affect various magnetic interactions. Hence, growing a thin film of Mn_2PtIn on a piezoelectric substrate can be an effective platform to realize tunable THE. The electrical control of THE can be used as an electrical switching-based memory device.

The second part represents the effect of exchange frustration on the stability of antiskyrmions. This study is important contribution towards the basic understanding on the nature of magnetic frustration to induce nano-scale antiskyrmions. A further study may be proposed before making a general statement on the role of magnetic frustration in a DMI system. Further chemical tuning can lead to the observation of other topological spin textures like meron, anti-meron, etc.

The third part reveals the presence of symmetric and anti-symmetric exchange interactions in an exchange coupled system. This system is a special type of compensated ferrimagnet. The compensation is achieved through cluster-cluster coupling. The observation of large exchange bias in a cubic compensated system demonstrates the role of compensation irrespective of crystalline anisotropy. Moreover, this thesis also presents several compensated ferrimagnetic systems and/or reduced moment systems. This can be of interest in zero-moment base spintronics applications.

Reference

- [1] C. Lacroix, P. Mendels, and F. Mila, *Springer Series in Solid State Sciences*, **vol. 164**, (2011).
- [2] Naoto Nagaosa and Yoshinori Tokura, *Nature Nanotechnology*, **8**, 899–911 (2013).
- [3] Albert Fert, Vincent Cros, and João Sampaio, *Nature Nanotechnology*, **8**, 152–156 (2013).
- [4] Yoshinori Tokura, Masashi Kawasaki, and Naoto Nagaosa, *Nature Physics*, **13**, 1056–1068 (2017).
- [5] Stuart S. P. Parkin, Masamitsu Hayashi, and Luc Thomas, *Science*, **320**, 190–194 (2008).
- [6] F. Jonietz et al., *Science*, **330**, 1648–1651 (2010).
- [7] A. Bogdanov and A. Hubert, *Journal of Magnetism and Magnetic Materials*, **138**, 255–269 (1994).
- [8] U. K. Rößler, A. N. Bogdanov, and C. Pfleiderer, *Nature*, **442**, 797–801 (2006).
- [9] S. Mühlbauer et al., *Science*, **323**, 915–919 (2009).
- [10] S. R. Saha et al., *Phys. Rev. B*, **60**, 12162–12165 (1999).
- [11] A. Neubauer et al., *Phys. Rev. Lett.*, **102**, 186602 (2009).
- [12] N. Kanazawa et al., *Phys. Rev. Lett.*, **106**, 156603 (2011).

-
- [13] M. Raju et al., *Nature Communications*, **10**, 696 (2019).
 - [14] J. C. Gallagher et al., *Phys. Rev. Lett.*, **118**, 027201 (2017).
 - [15] Takashi Kurumaji et al., *Science*, **365**, 914–918 (2019).
 - [16] Y. Taguchi et al., *Science*, **291**, 2573–2576 (2001).
 - [17] Hiroaki Ishizuka and Naoto Nagaosa, *Science Advances*, **4**, eaap9962 (2018).
 - [18] Wenbo Wang et al., *Nature Materials*, **18**, 1054–1059 (2019).
 - [19] Pradeep K. Rout et al., *Phys. Rev. B*, **99**, 094430 (2019).
 - [20] J Nogués and Ivan K Schuller, *Journal of Magnetism and Magnetic Materials*, **192**, 203–232 (1999).
 - [21] Y. Ijiri et al., *Phys. Rev. Lett.*, **99**, 147201 (2007).
 - [22] Shuai Dong et al., *Phys. Rev. Lett.*, **103**, 127201 (2009).
 - [23] R. Yanes et al., *Phys. Rev. Lett.*, **111**, 217202 (2013).
 - [24] P. Grünberg et al., *Phys. Rev. Lett.*, **57**, 2442–2445 (1986).
 - [25] M. N. Baibich et al., *Phys. Rev. Lett.*, **61**, 2472–2475 (1988).
 - [26] G. Binasch et al., *Phys. Rev. B*, **39**, 4828–4830 (1989).
 - [27] B. Dieny et al., *Phys. Rev. B*, **43**, 1297–1300 (1991).
 - [28] J. S. Moodera et al., *Phys. Rev. Lett.*, **74**, 3273–3276 (1995).
 - [29] S. M. Bhattacharjee, M. Mj, and A. Bandyopadhyay eds., *Springer Singapore*, **19**, (2017).
 - [30] Michael Victor Berry, *Proceedings of the Royal Society of London. A. Mathematical and Physical Sciences*, **392**, 45–57 (1984).
 - [31] Y. Aharonov and D. Bohm, *Phys. Rev.*, **115**, 485–491 (1959).
 - [32] A. A. Burkov and Leon Balents, *Phys. Rev. Lett.*, **107**, 127205 (2011).

- [33] C. L. Kane and E. J. Mele, *Phys. Rev. Lett.*, **95**, 146802 (2005).
- [34] Y. Machida et al., *Phys. Rev. Lett.*, **98**, 057203 (2007).
- [35] Hiroshi Takatsu et al., *Phys. Rev. Lett.*, **105**, 137201 (2010).
- [36] C. G. Shull, W. A. Strauser, and E. O. Wollan, *Phys. Rev.*, **83**, 333–345 (1951).
- [37] A Anane et al., *Journal of Physics: Condensed Matter*, **7**, 7015–7021 (1995).
- [38] I. Dzyaloshinsky, *Journal of Physics and Chemistry of Solids*, **4**, 241–255 (1958).
- [39] Tôru Moriya, *Phys. Rev.*, **120**, 91–98 (1960).
- [40] M. Binder et al., *Phys. Rev. B*, **74**, 134404 (2006).
- [41] C. D. Stanciu et al., *Phys. Rev. B*, **73**, 220402 (2006).
- [42] Kohei Ueda et al., *Phys. Rev. B*, **96**, 064410 (2017).
- [43] S. Becker et al., *Phys. Rev. Applied*, **16**, 014047 (2021).
- [44] Andy Quindeau et al., *Advanced Electronic Materials*, **3**, 1600376 (2017).
- [45] Rolf Stinshoff et al., *Phys. Rev. B*, **95**, 060410 (2017).
- [46] Roshnee Sahoo et al., *Advanced Materials*, **28**, 8499–8504 (2016).
- [47] Ajaya K. Nayak et al., *Nature Materials*, **14**, 679–684 (2015).
- [48] O. Meshcheriakova et al., *Phys. Rev. Lett.*, **113**, 087203 (2014).
- [49] Satoru Nakatsuji, Naoki Kiyohara, and Tomoya Higo, *Nature*, **527**, 212–215 (2015).
- [50] Ajaya K. Nayak et al., *Science Advances*, **2**, e1501870 (2016).
- [51] Charanpreet Singh et al. *Higher order exchange driven noncoplanar magnetic state and large anomalous Hall effects in electron doped kagome magnet Mn_3Sn* . 2022.

-
- [52] W. C. Koehler, *Journal of Applied Physics*, **36**, 1078–1087 (1965).
- [53] T. H. R. Skyrme and Basil Ferdinand Jamieson Schonland, *Proceedings of the Royal Society of London. Series A. Mathematical and Physical Sciences*, **260**, 127–138 (1961).
- [54] M. C. Cross and P. C. Hohenberg, *Rev. Mod. Phys.*, **65**, 851–1112 (1993).
- [55] David C. Wright and N. David Mermin, *Rev. Mod. Phys.*, **61**, 385–432 (1989).
- [56] S. L. Sondhi et al., *Phys. Rev. B*, **47**, 16419–16426 (1993).
- [57] Ajaya K. Nayak et al., *Nature*, **548**, 561–566 (2017).
- [58] X. Z. Yu et al., *Nature*, **465**, (2010).
- [59] Y. S. Lin, P. J. Grundy, and E. A. Giess, *Applied Physics Letters*, **23**, 485–487 (1973).
- [60] T. Garel and S. Doniach, *Phys. Rev. B*, **26**, 325–329 (1982).
- [61] Suzuki Takao, *Journal of Magnetism and Magnetic Materials*, **31-34**, 1009–1010 (1983).
- [62] Xiuzhen Yu et al., *Proceedings of the National Academy of Sciences*, **109**, 8856–8860 (2012).
- [63] Dola Chakrabartty et al., *Communications Physics*, **5**, 189 (2022).
- [64] Kirsten von Bergmann et al., **9**, 396–396 (2007).
- [65] Stuart Parkin and See-Hun Yang, *Nature Nanotechnology*, **10**, 195–198 (2015).
- [66] Masamitsu Hayashi et al., *Science*, **320**, 209–211 (2008).
- [67] Ioan Mihai Miron et al., *Nature Materials*, **10**, 419–423 (2011).
- [68] Kwang-Su Ryu et al., *Nature Nanotechnology*, **8**, 527–533 (2013).

-
- [69] See-Hun Yang, Kwang-Su Ryu, and Stuart Parkin, *Nature Nanotechnology*, **10**, 221–226 (2015).
- [70] Christian Pfleiderer and Achim Rosch, *Nature*, **465**, 880–881 (2010).
- [71] E.H. Hall Ph.D., *The London, Edinburgh, and Dublin Philosophical Magazine and Journal of Science*, **12**, 157–172 (1881).
- [72] E. M. Pugh and T. W. Lippert, *Phys. Rev.*, **42**, 709–713 (1932).
- [73] Naoto Nagaosa et al., *Rev. Mod. Phys.*, **82**, 1539–1592 (2010).
- [74] Yuan Tian, Li Ye, and Xiaofeng Jin, *Phys. Rev. Lett.*, **103**, 087206 (2009).
- [75] S. X. Huang and C. L. Chien, *Phys. Rev. Lett.*, **108**, 267201 (2012).
- [76] Kentaro Ueda et al., *Nature Communications*, **9**, 3032 (2018).
- [77] Minhyea Lee et al., *Phys. Rev. B*, **75**, 172403 (2007).
- [78] W. H. Meiklejohn and C. P. Bean, *Phys. Rev.*, **105**, 904–913 (1957).
- [79] William C. Cain and Mark H. Kryder, *Journal of Applied Physics*, **67**, 5722–5724 (1990).
- [80] Mannan Ali et al., *Nature Materials*, **6**, 70–75 (2007).
- [81] German Salazar-Alvarez et al., *Journal of the American Chemical Society*, **129**, 9102–9108 (2007).
- [82] Eran Maniv et al., *Nature Physics*, **17**, 525–530 (2021).
- [83] A. P. Malozemoff, *Phys. Rev. B*, **35**, 3679–3682 (1987).
- [84] Kentaro Takano et al., *Phys. Rev. Lett.*, **79**, 1130–1133 (1997).
- [85] P. Miltényi et al., *Phys. Rev. Lett.*, **84**, 4224–4227 (2000).
- [86] Meng Meng et al., *Applied Physics Letters*, **112**, 132402 (2018).
- [87] K. Chen et al., *Phys. Rev. Applied*, **12**, 024047 (2019).

-
- [88] Tanja Graf, Claudia Felser, and Stuart S.P. Parkin, *Progress in Solid State Chemistry*, **39**, 1–50 (2011).
- [89] J. C. Slonczewski, *Journal of Magnetism and Magnetic Materials*, **159**, L1–L7 (1996).
- [90] L. Berger, *Phys. Rev. B*, **54**, 9353–9358 (1996).
- [91] L. Berger, *Journal of Applied Physics*, **93**, 7693–7695 (2003).
- [92] P. Baláž, M. Gmitra, and J. Barnaś, *Phys. Rev. B*, **80**, 174404 (2009).
- [93] Ajaya K. Nayak et al., *Applied Physics Letters*, **100**, 152404 (2012).
- [94] Licong Peng et al., *Nature Nanotechnology*, **15**, 181–186 (2020).
- [95] Praveen Vir et al., *Phys. Rev. B*, **99**, 140406 (2019).
- [96] Jürgen Winterlik et al., *Phys. Rev. B*, **77**, 054406 (2008).
- [97] E. Krén and G. Kádár, *Solid State Communications*, **8**, 1653–1655 (1970).
- [98] Feng Wu et al., *Applied Physics Letters*, **94**, 122503 (2009).
- [99] J. D. Browne et al., *physica status solidi (a)*, **49**, K177–K179 (1978).
- [100] Q. Zhang et al., *Journal of Applied Physics*, **106**, 113915 (2009).
- [101] D. B. Cullity and S. R. Stock, *ADDISON-WESLEY*, (1977).
- [102] E. H. Hall, *American Journal of Mathematics*, **2**, 287–292 (1879).
- [103] David B. Williams and C. Barry Carter, *Springer-Verlag US 2009*, **2 Edition**, (2009).
- [104] Juan Rodríguez-Carvajal, *Physica B: Condensed Matter*, **192**, 55–69 (1993).
- [105] X. Z. Yu et al., *Nature Communications*, **3**, 988 (2012).
- [106] S. Seki et al., *Science*, **336**, 198–201 (2012).
- [107] Chiming Jin et al., *Nature Communications*, **8**, 15569 (2017).

-
- [108] Stefan Heinze et al., *Nature Physics*, **7**, 713–718 (2011).
 - [109] Anjan Soumyanarayanan et al., *Nature Materials*, **16**, 898–904 (2017).
 - [110] Subir Sen et al., *Phys. Rev. B*, **99**, 134404 (2019).
 - [111] L. Pál et al., *Journal of Applied Physics*, **39**, 538–544 (1968).
 - [112] H. Wilhelm et al., *Phys. Rev. Lett.*, **107**, 127203 (2011).
 - [113] A. Bauer and C. Pfleiderer, *Phys. Rev. B*, **85**, 214418 (2012).
 - [114] Sk Jamaluddin et al., *Advanced Functional Materials*, **29**, 1901776 (2019).
 - [115] Jagannath Jena et al., *Nano Letters*, **20**, 59–65 (2020).
 - [116] Vivek Kumar et al., *Phys. Rev. B*, **101**, 014424 (2020).
 - [117] Christoph Sürgers et al., *Nature Communications*, **5**, 3400 (2014).
 - [118] A. N. Bogdanov et al., *Phys. Rev. B*, **66**, 214410 (2002).
 - [119] Hanshen Tsai et al., *Nature*, **580**, 608–613 (2020).
 - [120] R. Tomasello et al., *Scientific Reports*, **4**, 6784 (2014).
 - [121] Shijiang Luo et al., *Nano Letters*, **18**, 1180–1184 (2018).
 - [122] Christina Psaroudaki and Christos Panagopoulos, *Phys. Rev. Lett.*, **127**, 067201 (2021).
 - [123] Kyung Mee Song et al., *Nature Electronics*, **3**, 148–155 (2020).
 - [124] Kang Wang et al., *Nature Communications*, **13**, 722 (2022).
 - [125] Wanjun Jiang et al., *Nature Physics*, **13**, 162–169 (2017).
 - [126] Kai Litzius et al., *Nature Physics*, **13**, 170–175 (2017).
 - [127] Pramey Upadhyaya et al., *Phys. Rev. B*, **92**, 134411 (2015).
 - [128] Joseph Barker and Oleg A. Tretiakov, *Phys. Rev. Lett.*, **116**, 147203 (2016).
 - [129] Kyoung-Whan Kim et al., *Phys. Rev. B*, **97**, 224427 (2018).

-
- [130] Yuushou Hirata et al., *Nature Nanotechnology*, **14**, 232–236 (2019).
- [131] Chen Cheng et al., *Phys. Rev. B*, **104**, 174409 (2021).
- [132] Siying Huang et al., *Phys. Rev. B*, **96**, 144412 (2017).
- [133] Xichao Zhang et al., *Nature Communications*, **8**, 1717 (2017).
- [134] Jagannath Jena et al., *Nature Communications*, **13**, 2348 (2022).
- [135] Shi-Zeng Lin, Avadh Saxena, and Cristian D. Batista, *Phys. Rev. B*, **91**, 224407 (2015).
- [136] Zhuolin Li et al., *Nature Communications*, **12**, 5604 (2021).
- [137] X. Z. Yu et al., *Nature*, **564**, 95–98 (2018).
- [138] Paul Jennings and Paul Sutcliffe, *Journal of Physics A: Mathematical and Theoretical*, **46**, 465401 (2013).
- [139] Kosuke Karube et al., *Science Advances*, **4**, eaar7043 (2018).
- [140] Peter Sweekis et al., *ACS Applied Electronic Materials*, **3**, 1323–1333 (2021).
- [141] Vassil Skumryev et al., *Nature*, **423**, 850–853 (2003).
- [142] Snehashish Chatterjee et al., *Phys. Rev. B*, **102**, 214443 (2020).
- [143] M. R. Fitzsimmons et al., *Phys. Rev. Lett.*, **84**, 3986–3989 (2000).
- [144] J. McCord et al., *Journal of Applied Physics*, **93**, 5491–5497 (2003).
- [145] Steven Brems et al., *Phys. Rev. Lett.*, **95**, 157202 (2005).
- [146] F. Nolting et al., *Nature*, **405**, 767–769 (2000).
- [147] H. Ohldag et al., *Phys. Rev. Lett.*, **86**, 2878–2881 (2001).